UNIVERSITY OF SOUTHAMPTON

FACULTY OF ENGINEERING AND APPLIED SCIENCE

SCHOOL OF ENGINEERING SCIENCE

SOLID PARTICLE EROSION OF CVD DIAMOND COATINGS

David William Wheeler

Thesis submitted for the degree of Doctor of Philosophy

January 2001

ABSTRACT

This document constitutes the PhD thesis of the author's project *Solid Particle Erosion of CVD Diamond Coatings*. It details the experimental work carried out over the period October 1997 to September 2000. The project was undertaken at the University of Southampton under the auspices of an Engineering and Physical Sciences Research Council CASE award, in collaboration with De Beers Industrial Diamonds (UK) Ltd. The objective of this project was to investigate the behaviour of CVD diamond coatings when subject to high velocity impact from sand particles as well as relating damage mechanisms to microstructure.

In the experimental work, diamond coatings deposited on both tungsten and tungsten carbide-cobalt substrates were investigated. The thickness of the coatings ranged from 10 to 200μm and the samples were supplied in both as-grown and lapped forms. The coatings were characterised using a number of techniques including X-ray diffraction, Raman spectroscopy, indentation, surface profilometry as well as optical and electron microscopy. The grain size and surface roughness were also measured for comparison with the size of damage features generated in the erosion studies. The results revealed that the coatings were close to natural diamond in both chemical (i.e. negligible graphite content) and mechanical (i.e. hardness and elastic modulus) characteristics.

In the erosion studies, two test facilities were used: a water-sand slurry rig and a high velocity air-sand rig. The erodent used was silica sand with average diameters 135μm, 194μm and 235μm with the velocities in the range 16 to 268 m s^{-1} and 90° nominal impact angle. The erosion rates were plotted against particle kinetic energy and compared with those for cemented tungsten carbide and stainless steel. At 268 m s^{-1}, the most erosion-resistant coating was a 120μm lapped sample, which had an erosion resistance more than 10 times that of cemented WC-7Ni. The coatings were examined both pre- and post-test by scanning electron microscopy in order to determine the degradation mechanisms. Ultrasonic imaging and taper polishing of eroded samples were also performed to reveal sub-surface damage and to elucidate its contribution to coating degradation. The results suggest that the erosion mechanism consists of a three-

stage process consisting of micro-chipping, development of pin-holes and interfacial debonding, followed by catastrophic failure.

The principal damage features, the circumferential cracks and pin-holes, were examined in detail in an attempt to identify the mechanism responsible for their formation. When compared with Hertzian impact theory the measured circumferential crack diameters were found to be at least double the diameter predicted by Hertz. Moreover, a trend of increasing circumferential crack diameter with coating thickness, which is not predicted by Hertzian impact theory, was found. The diameters of the circumferential cracks were closer to that predicted by the theory of stress wave reinforcement, which is more commonly associated with damage in brittle materials subjected to liquid impact. This suggested that stress wave reinforcement was responsible for the formation of the pin-holes. This hypothesis was supported by work using scanning acoustic microscopy, which found that circumferential cracks and pin-holes were only found on areas of the coating that had become delaminated during the erosion tests. The experiments also indicated that the coatings became delaminated under the action of sub-surface shear stresses that are generated by the particle impacts. When the maximum shear stress was located at the coating-substrate interface (i.e. $z_t/C_T = 1$) the coating failed rapidly. This work indicates that for optimum coating performance $z_t/C_T < 0.3$ and the stress field contained within the coating.

ACKNOWLEDGEMENTS

Many people have provided help and support over the last three years, without which this work could not have been accomplished. This is the place to acknowledge their contribution; I apologise if I have inadvertently omitted anyone who has not been included.

I am especially indebted to my supervisor, Dr Robert Wood, who provided much guidance and advice throughout the project, even though it wasn't always appreciated at the time! In addition, the expertise of technicians Dave Finchette and Steve Pilcher in carrying out maintenance of the erosion rigs, as well as in other areas, was indispensable. The engineers and technicians at the Automotive Design Advisory Unit (ADAU), with whom I share the building at Chilworth, also provided assistance on occasions too numerous to mention. The help and advice of Dr Terry Harvey, Dr Julian Wharton, Dr Barbara Cressey, Martin Hill, Geoff Spencer, Pete Wheeler and Dave Beckett is also acknowledged.

I am most grateful to the Engineering and Physical Sciences Research Council (EPSRC) and De Beers Industrial Diamonds (UK) Ltd for providing both financial and material support throughout the project. In particular I wish to thank Dr John Collins, Dr Jim Pickles and Dr Ricardo Sussmann at De Beers for their advice and assistance. The help of Alan Basterfield and Richard Way at Sonoscan (Europe) Ltd., Shaftesbury, who allowed me access to the acoustic microscope, is also greatly appreciated. Other people who provided help include Dr David Harrison, Edwin Smith and Joe McAleese (BP), who assisted on the valve testing, and Dave McHattie (Boart Longyear), who supplied the tungsten carbide samples for the erosion testing.

Finally, by no means the least significant, was the love and support of my parents, and Rachel. The magnitude of their contribution makes a few words of thanks on this page seem somewhat inadequate, so it is to them that this thesis is dedicated.

CONTENTS

LIST OF FIGURES

LIST OF TABLES

1

INTRODUCTION

Diamonds have long been highly prized for their aesthetic qualities and have been used as jewels and other decorative items for centuries. In the ancient world, they were invested with great mystical significance, with many magical virtues being attributed to them. One such description can be found in the *Sloane Lapidary*, written in 1243:

> Diamonde comes from Inde and some from Arabie; that which cometh from Inde is clipped males, ye other female. The male is brown appon light shininge, ye female is whit and beautifull of coulor like Cristall. Thes diamonds is very pretious to thee and of great hardnesse, for they will grave in Iron or steele, taking no harme. If a man werre it, it strengthen him and kepith him from dreming in his sleep, from faintnes and from poyson, from wroth and chiding. It sendeth and helpeth men to great worth. It defendeth a man from his enemies, and keepeth a man in good estate when he findeth him; it comforte a man witt, and support him of ritches. And though a man do fall downe from a cart or a wale he shall not break any of his bones if the stone be on him.

While belief in the more magical properties of diamonds have long since been spurned by all except cranks and some new-age believers, diamonds have continued to exert a powerful hold on the imagination of successive generations. Few other materials have been the source of such strife, both in fact and fiction. A century ago Gardner Williams, general manager of De Beers in the 1890s, summed it up thus:

> To win them, temples have been profaned, palaces looted, thrones torn to fragments, princes tortured, women strangled, guests poisoned by their hosts, and slaves disembowelled. Some have fallen on battlefields, to be picked up by ignorant freebooters, and sold for a few silver coins. Others have been cast into ditches by thieves or swallowed by guards, or sunk in shipwrecks, or broken into powder in moments of frenzy. No strain of fancy in an Arabian tale has outstripped the marvels of fact in the diamond's history.

Even today, diamonds continue to attract the attentions of the criminal fraternity. During the writing of this thesis an audacious bid to steal diamonds on display at the Millennium Dome in London was dramatically foiled by Police.

Although they have been the cause of conflict between nations, diamonds have also been used as gifts signifying goodwill, for example the 3106-carat (621 g.) Cullinan diamond, which was presented to King Edward VII by the Transvaal government in 1908 as a gesture of reconciliation following the South African War (1899-1902). Two diamonds cut from this giant stone now adorn the Imperial State Crown and the Royal Sceptre. On a more personal level diamonds are found in engagement rings, tokens of love, trust and commitment. One of the most munificent examples of this type of gift is the 189-carat (38 g.) Orlov diamond, named after Count Grigory Orlov, who proposed marriage to Catherine the Great of Russia in the 18th century. The empress graciously accepted the gift of the diamond from the unfortunate count, only to decline his offer.

The name "diamond" is derived from the Latin word *adamas*, and the earlier Greek word *διαμαντε*, which means "the invincible". At the time of the birth of Christ, *adamas* was used to describe any hard metal or stone; it was applied to diamond by the Roman poet Manilius in *Astronomica*, written in 16 AD. It was later corrupted into "diamond" and is the root of the word adamantine, the adjective applied to diamond's hard brilliant lustre [1].

The principal source for diamonds until the 18th century was India. Following the discovery there in 1726, Brazil became the largest producer of diamonds, before it was eclipsed by South Africa, where diamonds were discovered near Kimberley in 1866. Today, Australia, at 41 million carats, accounts for the largest share of world diamond production, followed by the Democratic Republic of Congo (formerly Zaire) (20 million), Botswana (16.8 million), Russia (12.5 million), and South Africa (9.1 million) (1995 figures) [2]. Diamonds are usually weighed in carats: 1 carat = 0.2 g.

However, diamond is much more than a desirable gemstone. It is, perhaps, unique among materials in being both a highly prized gemstone and a highly important engineering material. Its extreme hardness was utilised in mechanical applications by the Chinese as long ago as 150 BC, when diamond-tipped engraving tools, known as *kin-kang tsuan* ("cutting jade knives") were used to cut hard jade stone. Two centuries later, in his *Historia Naturalis*, Pliny the Elder, supplies the following description:

> They resist blows to such an extent that the hammer rebounds and the very anvil splits asunder, but this invincible element which defies nature two most violent forces, iron and fire, can be broken by ram's blood. But it must be steeped in blood that is fresh and warm and even so, many blows are needed.

Two thousand years later, this statement does not ring true. Indeed, it is questionable whether the material Pliny described was actually diamond, bearing in mind his assertion that "[it] defies... fire". In air, diamond will transform to graphite at temperatures of approximately 600 K. Nevertheless, there are similarities between Pliny's description and the behaviour of diamond in tribological situations. One consequence of its hardness is that most other materials in contact with diamond will suffer greater damage than the diamond itself.

The high hardness and strength of diamond make it an attractive material for components in which friction and wear are prominent degradation mechanisms. The second half of the 20^{th} century has witnessed the advent of synthetic diamond, first by the high pressure high temperature (HPHT) and more recently by chemical vapour deposition (CVD) [3]. This has enabled researchers to exploit its unique properties in new applications, for instance aircraft and missile domes and mechanical seals.

The properties of diamond also make it a potentially attractive material for use in applications where erosion is a significant problem, for instance choke valves. These valves are used in the offshore oil industry to regulate the flow of hydrocarbon fluids extracted from offshore oil wells. A schematic diagram of a plug-in-cage type choke valve is shown in Figure 1.1. Sand is often present in these flows, owing to the geological composition in which the reservoir is located. The presence of sand can result in erosion of the valves, particularly as high particle velocities can be generated (300 - 500 m s^{-1}) when the valves are operated at large pressure drops (300 - 400 bar) and the process stream is partially or wholly gaseous. In the North Sea there are approximately 300 oil wells; of these, half the failures of subsea choke valves can be attributed to erosive wear. The high costs associated with unscheduled replacement of damaged subsea valves (approximately £300,000) has led offshore operators to consider ways in which valve life can be extended. One way in which this can be done is to coat the internal components of the valves with wear-resistant hard facings.

The most widely used trim material in choke valves is cemented tungsten carbide; however, the typical operating life of the valves is still only 3 years, though in some oil wells more frequent valve replacement is required. In extreme cases, in the North Sea, WC-6Co plugs have been eroded at rates of up to 1mm per hour. As a result, critical components intended to last 18-24 months, have been destroyed within a few weeks, or even hours. In the search for more erosion resistant materials the high hardness, strength and wear resistance of diamond made it an obvious candidate.

1.1 Background to the present project

The concept of coating valve trim components with CVD diamond was initiated in 1989 at BP. CVD coating technology, which is used in the electronics industry to produce diamond films for use as heat sinks for micro-chips on Si substrates, was applied to other substrates. Substrates included SiC, Si_3N_4 and partially-stabilised ZrO_2 (PSZ) at BP, Warrensville, Ohio. Both planar samples and cylindrical / cone samples were coated. The planar samples were tested in a slurry erosion rig while the cylindrical / cone samples were tested in the BP valve loop test rig within a needle-and-seat choke valve. Both types of test showed excellent erosion resistance for CVD diamond coatings greater than 15μm in thickness. Other, similar, candidate materials, most notably polycrystalline diamond (PCD) and diamond-like carbon (DLC) could not match CVD diamond in erosion performance.

This work was continued in the DTI/EPSRC-sponsored LINK surface engineering project, *Valvelink*. The objective of *Valvelink* was to identify and develop suitable hard coatings for use in gate and choke valves. One aim of the project was to develop suitable coatings that would deliver a three-fold increase in operating life. The project consortium included representatives drawn from all sides of the industry, from valve manufacturers and coating companies to end users, as well as three universities.

The work at the University of Southampton focused on the erosion and abrasion testing of materials and coatings. The results from these tests provided tribological data to aid the selection process for wear-resistant materials. Examination of the tested samples also provided information on the damage mechanisms that cause them to degrade while subject to the different regimes of wear.

1.2 Objectives of the present project

The current project continued the work begun in the *Valvelink* project. Where it differed from that project was that instead of being concerned with general performance data and ranking of different coatings, it focused on one material: CVD diamond. The mechanistic aspect of erosive wear was to be investigated in greater detail and related to the microstructure of the material.

In addition to the work described in this thesis, diamond-coated choke valves were tested in the valve loop test facility at the BP Research Centre, Sunbury-on-Thames, and compared with uncoated WC trims. The tests found that the trims containing diamond exhibited significantly lower levels of erosion damage. This work is described in detail elsewhere [4].

1.3 Thesis Structure

This document constitutes the PhD thesis of the author's project *Solid Particle Erosion of CVD Diamond.* It details the experimental work carried out over the period October 1997 to September 2000.

Chapters 2 to 4 examine previous work reported in the published literature in order to provide the context for the present project. Subjects include solid particle erosion, diamond, as well as the erosion and mechanical behaviour of diamond and related materials.

The experimental work is introduced in Chapter 5, which explains the different equipment used in the project. Chapter 6 describes the results of the experiments used to characterise the diamond coatings used in the project. Residual stress is an important factor to consider when studying coating systems; for this reason Chapter 7 is devoted to an examination of the residual stress of the diamond coatings.

The main part of the work concerns the erosion behaviour of the diamond coatings and this is described in Chapters 8 to 11. Initially, the tests focused on the erosion performance of CVD diamond coatings and how they compared with materials currently used in choke valves, principally tungsten carbide. Of more importance, though, is the behaviour of the coatings and the damage mechanisms that are observed

in coatings subjected to high velocity sand impact. The circumferential cracks and pin-holes that were observed were of particular interest as they had not been previously reported in the literature. Chapter 9 attempts to explain the mechanisms that generate these features.

This work is augmented by Chapter 10, in which the development of sub-surface damage at the coating-substrate interface is described. The use of novel techniques such as ultrasonic scanning and acoustic microscopy to probe this damage is described in this chapter. Chapter 10 has shown that the development of sub-surface coating delamination is necessary before circumferential cracks and pin-holes can form. The mechanisms of coating delamination are discussed in Chapter 11; one important aspect of this work is that conditions are identified in which delamination, and hence pin-hole formation, is not seen. This chapter demonstrates that knowledge of the impact conditions and the associated stress field is required in order to select the optimum coating thickness. The conclusions drawn from the present work are summarised in Chapter 12, together with suggestions for further work.

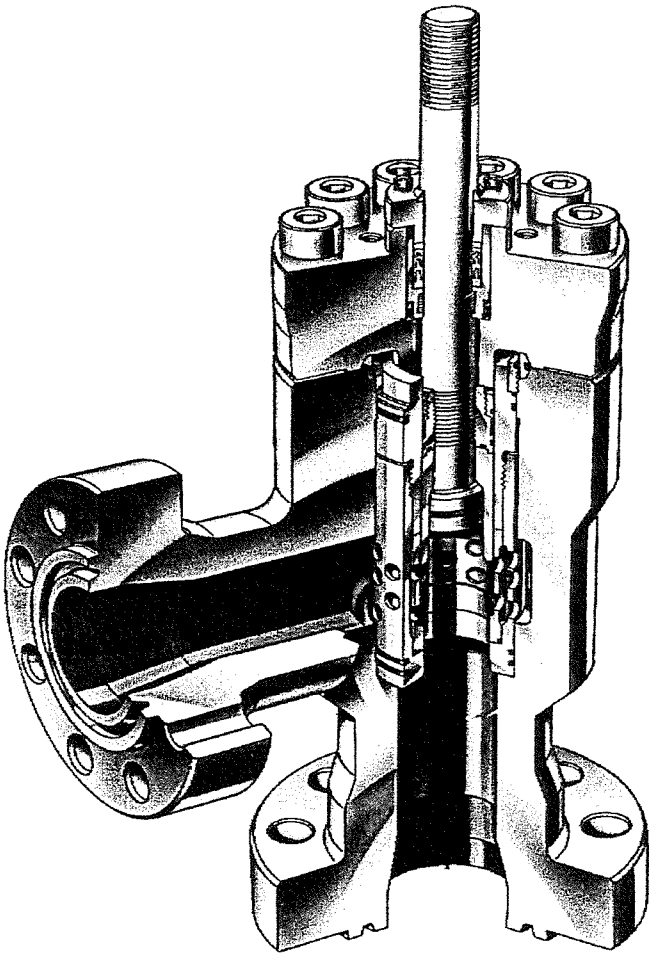

Fig. 1.1: Schematic diagram of a plug-in-cage type choke valve (ABB Kent Introl Type 74).

2

WEAR

Wear can be defined as "damage to a solid surface, generally involving the progressive loss of material due to the relative motion between that surface and a contacting substance or substances" [1]. It can lead to the deterioration in the performance and possible premature replacement of a component that is subject to wear. However, not all forms of wear are regarded as undesirable: in some situations the initial stages of wear will result in a smoother surface, which is beneficial for the running-in of components. Another beneficial aspect of wear is polishing.

There are many different types of wear depending upon the nature of the conditions in which the components operate. Eyre [2] has reviewed the different types and their contribution to the total number of failures attributable to wear-related degradation. At 50%, abrasion accounts for the largest share, followed by adhesive wear (18%). Erosion ranked joint-third (8%), along with fretting, followed by chemical wear (5%). The results are shown in Figure 2.1. A more recent industrial wear survey has been carried out as part of the DTI project *CAM8* in 1997 [3]. The survey included 1800 questionnaires and 22 industrial visits and estimated that the total losses to British industry, which were attributable to wear, amounted to £650 million per annum. The survey also divided the total number of failures into the different types of wear to determine the share of each as a percentage of the total. The results, also shown in Figure 2.1, are similar to the previous survey, with abrasion (63%) and adhesion (19%) still the most prominent degradation mechanisms. However, in certain circumstances, more than one mechanism can operate simultaneously; in others, one mechanism can change to another. Because erosion is the principal mechanism that forms the subject of this thesis the next section will be taken up with a discussion of the salient features of this form of wear.

2.1 Erosion

Erosion is a process by which discrete projectiles strike the surface of a material (known as the "target") causing damage to its surface. Though only accounting for 2% of total failures in the most recent survey, this figure is considerably higher in certain industries, notably the offshore oil industry as already described in Chapter 1. In addition to valves and missile domes, erosion can also be a problem for components such as turbine blades, pipelines and fluidised bed combustion systems. The cost of erosion can be measured in many ways, including loss of performance, control and reliability, as well as lost production as a result of unscheduled shutdowns, and the necessity of replacing damaged equipment. Safety can also be affected by components that have been eroded. However, as in the case of running-in of mechanisms mentioned above, erosion does have its beneficial applications, notably for cleaning surfaces by grit-blasting and cutting of rocks using abrasive water jets.

There are three categories of erosion depending on the nature of the erodent. They are:

- Cavitation erosion
- Liquid droplet erosion
- Solid particle erosion

Each form of erosion will now be described in turn.

2.1.1 Cavitation Erosion

In liquids, when the local pressure falls below the saturated vapour pressure, bubbles, or cavities, can be generated. When these bubbles collapse onto an adjacent solid surface the pressure pulse associated with the collapse can rapidly damage the surface leading to cavitation erosion. Cavity collapse has been studied by Bourne and Field [4], who used high-speed photography to view the process. It is a particular problem for liquid circulation equipment (i.e. pumps, valves and pipes) as well as bearings and cylinder linings of high-speed reciprocating engines. No work on cavitation erosion of CVD diamond has been found in the literature. Although cavitation can be a problem in offshore valves it will not be included as part of this project and, for this reason, will not be discussed further.

2.1.2 Liquid Droplet Erosion

In liquid droplet erosion, the impact of fast-moving liquid droplets onto a solid surface can result in damage to the target material. It is a particular problem in high-speed aircraft, missiles, steam turbine blades and wet gas wells. As there are similarities between liquid impact and some of the work described in this thesis it will be examined further.

In liquid droplet erosion, the damage resulting from the impact is caused by the propagation of stress waves that are generated in the material. Figure 2.2 shows a schematic diagram [5] of the initial stage of impact, while Figure 2.3 shows a high-speed photographic sequence of a liquid droplet impacting a surface of PMMA [6,7]. The key to understanding liquid droplet impact is the realisation that it takes a finite time after initial impact before outflow of water away from the impact site occurs; prior to this, compressible flow occurs and the water behaves like a solid. This causes pressures in the area of the target immediately beneath the impact. This pressure, known as the "water hammer pressure", is defined as:

$$P_i = \rho_e c_e V \tag{2.1}$$

where P_i is the pressure, ρ_e the density of the liquid, c_e the compression wave velocity for the liquid, and V the impact velocity.

In a short time after impact, the edge of the contact area moves outwards at high velocity. The exact value of this velocity is dependent on the impact velocity and the radius of the drop. Initially it is travelling faster than the shock velocity; this prevents any free outflow from taking place. It is only when the speed of the contact edge falls below that of the shock velocity that the shock in the liquid moves up the free surface of the liquid and the high pressures are reduced by jetting [8]. In the period before jetting takes place the liquid behaves in a compressible manner, giving pressures of the order $\rho_e c_e V$ [9]. However, the pressures at the expanding contact edge are much higher, reaching a value of $3\rho_e c_e V$ just prior to the shock envelope overtaking the contact edge. However, the contact edge pressure is less significant because of its short duration of impact. Once this has occurred, stress waves are released into the target material. These

waves can take three forms: longitudinal, transverse or Rayleigh waves. Figure 2.4 shows these three types of waves propagating into a solid following impact. They are also shown in Figure 2.5 [10].

The classical damage features that are generated by liquid impact on brittle materials consist of rings of discontinuous cracks surrounding the area of impact. The central region of impact is usually largely undamaged. This is because the compressive strength of brittle materials is often greater than that in tension. It is often high enough to resist deformation caused by the high pressures generated by the initial impact. The circumferential cracks are caused by the interaction between Rayleigh surface waves and pre-existing surface flaws larger than a certain critical size in the target material [11]. They are short because the stress pulse forming them is itself short, typically less than 1μs [12]. An additional mechanism by which damage can occur in thin samples is by interaction between Rayleigh waves and reflected bulk waves [11]. Following impact, compression waves are propagated into the body of the material. When they reach the rear surface they are reflected back and return to the front surface as tensile waves. At certain radii from the initial impact zone the position at which the reflected wave returns to the front surface will coincide with the position of the Rayleigh surface wave resulting in stress reinforcement generating even higher stresses at these locations. It should be noted that longitudinal waves travel faster than Rayleigh waves. The stress reinforcement can lead to the nucleation of further cracks at the front surface.

The nucleation of these cracks in the target material leads to strength degradation and, when cracks intersect, material removal. Liquid droplet impact is a significant problem in the rain erosion of infra-red transmitting domes for aircraft and missiles and has been the subject of numerous studies. Many currently used infra-red transparent materials, such as ZnS, have poor strength properties and this has led to the development of CVD diamond as a viable dome material to reduce the incidence of rain erosion suffered by these components. The liquid impact studies of CVD diamond will be discussed in a later section.

The impact of particles of lower hardness than the target material has also been shown to create similar damage features as those generated by liquid impact. Particles used in

these cases include polyethylene [13], PTFE [13], lead [13], ice [14,15], and nylon [14-16]. In most cases the target materials have been PMMA [13-15] and ZnS [16]. High-speed photographic sequences have shown these particles to undergo plastic deformation during impact. In contrast, the damage in the target material remained purely elastic.

2.1.3 Solid Particle Erosion

Solid particle erosion is the final category in this discussion and the one on which this project will focus. It is caused by the impact of particles on solid surfaces. The particles can be entrained in a liquid (known as a slurry) or gas and can be present either intentionally, as in powder or mineral handling facilities, or as contaminants, such as oxide debris from the inside of pipelines or sand from hydrocarbon reservoirs. Whatever their origin, their impact with solid surfaces can cause considerable damage and is a problem with fluidised bed combustion systems, helicopter blades (especially in desert environments), pipelines and valves carrying particulate matter.

The parameter by which solid particle erosion is measured is the erosion rate. This is usually defined as the volume loss, V_l, of the material divided by the mass of erodent used in the test The usual unit of measurement for this is $mm^3\ g^{-1}$. The volume loss is obtained by dividing the mass loss of the material by its density. However, the number of impacts is often considered to be more useful and $mm^3\ g^{-1}$ is of little use in comparing the erosion rates of materials subjected to erodents of different sizes. For a constant volume fraction of particles, an increase in the diameter of the erodent means a reduction in the number of particles. Consequently, the number of individual particle impacts is also fewer.

By using an alternative definition of volume loss per impact, V_u this complication can be eliminated. V_u is usually expressed in units of $\mu m^3\ impact^{-1}$. Its advantage over volume loss per erodent mass is that it can be considered to be independent of sand size. It is calculated by obtaining E_v, the erodent volume, and by dividing this into the volume loss:

$$E_v = \frac{Qxt}{\rho_e} \tag{2.2}$$

where Q is the volumetric flow rate, x the fraction of the erodent, t the duration of the test and ρ_e the density of the erodent. If the volume loss V_l, is divided by E_v, the result is V_s, the specific volume loss. V_u is then obtained by using the following formula:

$$V_u = \frac{V_s \pi d_p^{\ 3}}{6} \tag{2.3}$$

where d_p is the average particle diameter.

Plots of V_u (μm^3 $impact^{-1}$) vs. kinetic energy of impact, E_k (J) are used to generate an erosion map. These maps, proposed by Moore and Wood [17], enable comparisons to be made between materials at a wide range of impact energies independent of particle size. E_k is defined as:

$$E_k = \tfrac{2}{3}\pi R^3 \rho_e V^2 \tag{2.4}$$

where R is particle radius, ρ_e the erodent particle density and V the impact velocity.

When quoting erosion rates it is important to ensure that these are "steady state" values, i.e. the target material is being eroded at a constant rate. In the early stages of an erosion test, there is often a discernible period prior to the establishment of steady state erosion conditions. This period is known as the "incubation period", the length of which is dependent on the material being tested and the test conditions employed. For ductile materials, processes taking place during this period could include embedding of particles in the target (resulting in a mass gain), surface roughening and work hardening of the surface. This is particularly marked at higher impingement angles. In brittle materials, chipping of prominent grains is one process that is thought to take place.

2.2 Factors affecting the solid particle erosion of materials

There are a number of factors that affect the behaviour of materials when they are subjected to erosive flows. These can be placed in four categories: (i) nature of the fluid transporting the particles (liquid or gaseous); (ii) nature of the particles; (iii) the flow

field; (iv) target parameters. They are summarised in Table 2.1. It should be noted that the barriers separating these categories are slightly artificial as some of the factors discussed below can be placed in more than one category. Those factors that are most applicable to the contents of this thesis are discussed in more detail below.

Category	Factor
Nature of the fluid	Viscosity Density Corrosivity (erosion/corrosion synergy) Temperature
Nature of the particles	Size Density Friability Shape Particle – Target hardness ratio
Flow Field	Particle velocity Particle kinetic energy Impact angle Particle flux Particle impingement efficiency Particle drop out
Target parameters	Hardness Elastic modulus Fracture toughness Residual stress Surface roughness Surface treatment Size and distribution of microstructural flaws

Table 2.1: Factors affecting the solid particle erosion of materials

2.2.1 Nature of the fluid transporting the particles

Particles entrained in viscous slurries, for instance crude oil, are generally less erosive than gas-borne particles. This is because a squeeze film, which forms between particle and surface, can reduce the impact velocity, which in some cases can be as low as 10% of the nominal impact velocity [18]. The existence of the squeeze film serves to cushion the target material from the full energy generated by the impact. For impact to occur this squeeze film must be displaced by the particle. The important factors

affecting the severity of impact are the Reynolds number, which is a function of the ratio of solid and liquid densities. The greatest effect (retardation) is seen for the particles of low Reynolds number. For the same reason, the retarding effect of the squeeze film in gas-solid erosion is negligible.

2.2.2 Nature of the particles

The three factors of size, density and relative velocity can be considered together as they all have a bearing on the kinetic energy of the particles that will affect the erosion rate. The erosion rate, E_{er}, increases with velocity, V, and the two are related by the following relationship:

$$E_{er} \propto V^{u} \tag{2.5}$$

where u is the velocity exponent, the value of which usually falls between 2 and 3. This is a general term: in reality E_{er} has independent dependency on both d_p and V, hence many published papers plot separate graphs of E_{er} vs. d_p and E_{er} vs. V.

The shape of the eroding particle (i.e. its sharpness) is significant. It is well known that highly angular particles cause greater wear than rounded particles due to the higher contact stresses on impact. Sharp particles can cause wear rates to be between 10-100 times greater than rounded ones of the same material. Most erosion tests have employed erodents with an average diameter in the range 5-500μm. In ductile materials, the erosion rate increases dramatically with size up to 100μm, beyond which little variation is seen. For particles larger than 100μm, the erosion rate can be considered to be essentially independent of size [19]. For brittle materials, the dependence of erosion rate on particle size is more pronounced and a plateau does not exist. The impact of larger particles results in the generation of larger cracks in the surface. As a consequence, an increase in strength degradation caused by these impacts is seen, causing more material to be removed from the surface and, hence, increased erosion rate.

The brittleness of the erodent must be considered in assessing its effect on the erosion of a material. In the present work, it will be shown in a later chapter that in the erosion

of CVD diamond, the silica sand erodent will undergo considerably more degradation than the diamond. In some cases smearing of the erodent on the target has been reported, usually on hard ceramics. It has been suggested that this is caused by the transformation of mechanical or frictional energy into thermal energy sufficient to cause localised melting [20]. This is usually only seen with softer erodents such as silica and occasionally alumina, rather than SiC or diamond.

As in abrasive wear, it has been shown that the erosion rate reduces considerably below a relative hardness ratio of 1.2 [21], and below this figure, less damaging erosion mechanisms are seen. [22-24]. Hutchings [25] has attempted to construct maps of particle size against impact velocity, which identify the transitions between the different modes of damage, for instance elastic-plastic fracture, chipping etc.

2.2.3 Flow field

The influence of impact angle on erosion rate has been investigated by a number of workers [26-30]. This is shown in Figure 2.6. For ductile materials, it has been found that the maximum erosion is seen at angles of about 20-30° before declining at higher angles [30]. The erosion rate at 90° is typically one third to one half that of the figure at 30°. The erosion rate for ductile materials at near-normal angles is often higher in practice than those values predicted theoretically. This is due to two factors. The first is due to the effect of surface roughening produced by previous impacts, which reduces the true impact angle. The other cause of this is that ductile materials subjected to this type of erosion can often assume a more brittle character as a result of work hardening due to repeated impacts and high strain rates which can result in fracture rather than plastic deformation. This behaviour contrasts with that seen in brittle materials, where the loss of material due to erosion rises steadily with angle, reaching a peak at 90° [26-29]. Other materials, such as cemented tungsten carbides, behave in a manner that reflects their microstructure. In these cases, the maximum erosion rates are often seen at impact angles of about 60°.

The concentration of erodent, also known as the particle flux, is important. The erosion rate is usually considered to be independent of flux rate as it is expressed as volume loss per erodent mass, i.e. it has already been taken into account. However, beyond a certain flux a decline in the erosion rate is seen [31]. Shipway and Hutchings used long

exposure photography to study the shape of the erosion plume in a gas-blast rig [32]. They found that significant levels of particle-particle interaction were taking place in the region between the end of the nozzle and the target; many of these interactions are with particles rebounding from the target surface. This reduced the number of impacts on the target surface, and hence the "erosion efficiency". They suggested that for 212-250μm particles, increasing the flux beyond 0.76 kg m^{-2} s^{-1}, the inter-particle interactions start to reduce the erosivity of the flow. In slurry erosion, this figure is 5 wt. % [33].

In other cases, more usually seen in real components rather than erosion test rigs, particles can drop out of suspension from the fluid carrying them. They can settle and act as a protective barrier to inhibit further erosion in that location. In other components subject to erosive wear a worn component or part of a component can cause a change in the flow patterns. In offshore choke valves erosion of the ports can change the flow into the cage. Consequently mutual jet impingement, and hence energy dissipation, will be less and as a result the turbulence of the flow will be increased. This will result in more erosive conditions and lead to acceleration in the degradation of the valve.

2.2.4 Target parameters

One of the most significant factors in determining the erosion response of a material is whether it is ductile or brittle in nature. In the previous section, it was noted that different relationships between erosion rate and impact angle are seen for ductile and brittle materials. The difference between them can be explained by the difference in erosion mechanism. Ductile materials undergo mass loss by a process of direct micro-cutting or plastic deformation, followed by cutting, in which material is displaced by impact with the eroding particles. In brittle materials, the energy transfer associated with repeated particle impacts results in a fatigue process. Radial and lateral cracks, both surface and sub-surface, are formed. These cracks are similar to those seen in abrasive wear and it is assumed that material is removed by intersection of the lateral cracks with each other and with the surface [21].

Some materials, for instance sintered tungsten carbides, which contain both ductile and brittle constituents, defy such neat categorisation as "ductile" or "brittle". In this family of materials the microstructure consists of a brittle WC matrix and a more ductile

binder, usually Co or Ni-Cr. Work on evaluating the erosion behaviour of sintered WC-Co [34] revealed that erosion takes place by four competing mechanisms. These are (1) loss of binder; (2) ductile erosion of carbides; (3) brittle erosion of carbides by chipping and/or fracture; (4) pullout of carbides, often following removal of binder material. The relative importance of each mode is dependent on the erosive conditions, and the composition and microstructural condition of the material [35]. In these materials, a reduction in grain size has been found to increase the erosion resistance. This is because the strength is known to increase with $d_g^{-1/2}$, where d_g is the grain size (the Hall-Petch relationship). Larger grains contain larger intrinsic flaws present within them.

The next influence on erosion rate is that of hardness. Because microstructure, heat treatment and work hardening alter the value of a metal's hardness they will be discussed here as well in order to avoid repetition of certain facts. As might be expected, there is a relationship between target hardness and erosion resistance. As with abrasion there is a linear relationship between erosion and *annealed* hardness. However, most engineering alloys are unlikely to be in the annealed state; consequently the correlation must not be taken too far. Hardness, by itself, is not an accurate indicator of erosion resistance. One of the reasons for this statement is that certain treatments which can result in increasing the hardness of a material by as much as a factor of 2, for instance heat treatment and cold working, have had no significant improvement in erosion resistance [36]. However, it was noted that the profile of erosion rate versus impact angle began to assume a more "brittle" shape due to the reduction in ductility.

This finding is repeated in harder materials, too. For sintered tungsten carbides, it has been found that for the same level of hardness, the wear resistance of different alloys within the same family may differ by up to 80%. Therefore, within one alloy system, indentation hardness is not a valid parameter to describe erosion differences. A better approach is to consider a number of parameters that include hardness, proof stress and fracture toughness [37] bearing in mind that in most materials, high hardness and high fracture toughness are mutually exclusive. The price of an improvement in one is a reduction in the value of the other. Therefore, a trade-off is required in the selection process of materials for service in erosive environments.

The other primary parameter that influences the erosion resistance of a material is that of fracture toughness. Because brittle materials often erode by elastic-plastic processes, fracture toughness plays an important role in the wear of brittle materials. It is thought that dynamic values of fracture toughness would be the most appropriate parameter [38]. Anton and Subhash [39] have recently carried out static and dynamic Vickers indentation on a number of brittle materials (Pyrex glass, AlN, Al_2O_3, PSZ and TZP) to examine the influence of loading rate on hardness, fracture toughness and the resulting crack morphologies. The dynamic hardness was consistently greater than the static hardness for all materials, while the trend for dynamic fracture toughness was less clear: PSZ and TZP exhibited higher dynamic values while the dynamic toughness of glass was lower than its static equivalent. This discrepancy between static and dynamic values may partially explain the poor agreement of some erosion models.

2.3 Factors influencing the erosion performance of coatings

The factors influencing the erosion of materials described in the preceding section were for both bulk materials and coatings. However, there are additional factors that are also particular to hard coatings, which will be discussed in this section.

The primary function of a coating is to separate the substrate from the counterface in order to protect the former. Therefore, it may be imagined that the greater the distance from the counterface to the substrate (i.e. the thicker the coating) the more protection will be offered by the coating. However, the reality is usually more complex. Other factors, such as residual stress, microstructural defect levels and adhesion can also vary with thickness. As a result it is not usually possible to vary one of these elements without affecting the others. This section will focus on those factors that are most applicable to coatings operating under erosive conditions; however, they are also pertinent to other tribological situations, for instance abrasion and adhesive wear. The main factors will be considered below. While primarily considering erosion studies, this section will also use other related studies of coatings, for instance indentation, where they are relevant.

2.3.1 Coating thickness

Figure 2.7 shows the effect of coating thickness in schematic form. The thin coating does not support the load and deflects in accordance with that of the substrate. In

contrast, thicker coatings can support a greater proportion of the load, thereby reducing the deformation of the substrate.

The coating thickness is one of the most important factors. It has been shown theoretically, using a Finite Element (FE) model [40], that coatings reduce the stresses at the coating-substrate interface. If the coating is of a sufficient thickness all the stresses can be contained within it. However, in some coating systems the erosion resistance decreases with thicker coatings because of increased residual stresses. The influence of residual stress on coating performance is examined in Section 2.3.3.

In one study of erosion, thicker coatings have been shown to confer enhanced protection against solid particle attack. Hedenqvist and Olsson [41] investigated PVD TiN coatings on high speed steel with coating thicknesses of 0.4, 1.3 and 3 μm. The coatings were tested in a centrifugal erosion tester using 62-125μm Al_2O_3 particles at 20 m s^{-1}; the impact angle was 90°. The results showed that the critical particle dose required to cause coating removal on the 3μm coating was as much as 180 times greater than for the 0.4 μm coating.

In an indentation study assessing the effect of thickness on coating performance, Brookes *et al* [42] have proposed the concept of Integrity Ratio (IR) as a measure of protection provided by a coating to the substrate. It is defined as:

$$IR = \frac{P''_m}{P'_m} \tag{2.6}$$

Where P''_m is the threshold pressure to initiate failure in the coating and P'_m the corresponding pressure necessary to promote failure in the uncoated substrate. In a study of CVD diamond coatings deposited on Si, the threshold mean contact pressure required to cause any type of failure of the coating system increased with coating thickness up to 48μm, beyond which no further improvement was observed. The reason for this was thought to be residual stresses, which caused coating failure to occur following indentation.

The improved protection offered to substrates by a thin hard coating has been found with other materials. In one study of germanium coated with amorphous carbon films,

van der Zwaag and Field [43] reported that the critical load for spherical indentations to form ring cracks could be increased by up to 200%. The largest improvement was offered by the thickest coating. The coating was also found to have reduced the damage generated by liquid droplet impact, though the superiority of the coating over the uncoated Ge was less marked. The damage caused by the impacting droplets was less severe though it was not thought that these coatings could deliver a significant improvement in Damage Threshold Velocity (DTV). The study did not include a quantitative assessment of DTV for the specimens.

For thin coatings subjected to point loading, when the stress field extends into the substrate, yielding of the substrate can be the result. Pajares *et al* [44] studied the nature of sub-surface damage in plasma-sprayed Al_2O_3-TiO_2 coatings deposited on mild steel substrate and indented with a 6.36 mm diameter tungsten carbide sphere at a load of 1500N. Metallographic sections of indented regions revealed extensive micro-cracking and plastic deformation in the substrate as well as some delamination at the interface. The thinner coating (170μm) exhibited considerably more plastic deformation and delamination than the thicker coating (425μm), though the free-standing "coating" exhibited an even lower incidence of plastic deformation.

It is often instructive to define the coating thickness relative to the stress field to give the normalised coating thickness C_T / a_m, which is the ratio of the coating thickness to the Hertzian contact radius. Komvopoulos [45] used the finite element method to study the elastic contact of a substrate coated with a film of greater stiffness. Part of the work involved examining the effect of normalised coating thickness. The results showed that thicker coatings offered better protection to the substrate. Thick coatings resulted in lower and more uniformly distributed strains. When $C_T / a_m > 1$ significantly enhanced resistance against deformation was provided by the coating. Furthermore, thicker coatings also greatly reduce the shear stress at the coating-substrate interface. In contrast, for coatings where $C_T / a_m < 1$ the stresses in the substrate are predicted to be even higher than those that are uncoated. The dominant deformation mechanism was also found to be dependent on the normalised coating thickness: for thin coatings (C_T / a_m <0.45) surface micro-crack initiation dominates, while on thicker coatings ($C_T / a_m >$ 0.45) interfacial micro-crack initiation was the dominant damage mechanism.

In a later paper Komvopoulos [46] examined the effect of coating thickness on the contact pressure, sub-surface stresses and strains, as well as the location, size and shape of the plastic zone. It was found that the thickness of the coating influenced the extent of the plastic zone as well as its location. Thinner coatings provided less resistance to plastic deformation. The plastic zone was predicted to initiate at the coating-substrate interface directly beneath the indenter. Increasing the coating thickness reduced the extent of substrate yielding. If the stress field could be completely contained within the coating, plastic deformation of the substrate could be eliminated.

As will be seen in Chapter 3, the columnar nature of the CVD diamond microstructure means that the grain size increases as the coating thickness increases. It has already been seen that larger sized grains contain micro-fractures approaching the size of the grain [47]. This can lead to differences in the fracture strength, which will be described in Chapter 4.

In summary, thicker coatings provide enhanced protection to the substrate because the coating-substrate interface is further away from the impacting particle. The result of this is that the sub-surface shear stress at the interface is reduced and the vertical deflection of the coating at the point of impact is also diminished, thus decreasing the likelihood of surface tensile cracking. However, the influence of the substrate, residual stress and adhesion and defect levels must also be taken into account. They will now be considered in turn.

2.3.2 Nature of the coating-substrate combination

In any coating-substrate combination there exists a discontinuity at the coating-substrate interface, the magnitude of which is dependent upon the respective properties of coating and substrate. The combination of coating and substrate is also a significant factor in determining the resistance of a coating to deformation. For example, the difference in thermal expansion coefficient can have a direct influence on the nature and magnitude of residual stress, which in turn can affect the adhesion of the coating.

One way in which this mismatch can be reduced is the use of one or more interlayers between the coating and substrate. The mechanical and thermal properties of these interlayers are usually between those of the coating and substrate; therefore, they can

result in a more gradual change in properties across the interface. This can reduce residual stresses as well as improve adhesion. Both residual stress and adhesion are considered in later sections of this chapter. This section will examine the effect of the difference in mechanical properties, in particular hardness and elastic modulus, on the behaviour of coatings.

The substrate hardness affects the erosion resistance of the coating. Harder substrates increase the load required to initiate fracture in the coating because the vertical deflection in the coating is reduced. Large deflections create greater strains in the coating and increase the likelihood of tensile fracture at the coating surface. Moreover, if the substrate is not hard enough to support the load, the sub-surface shear stress may cause plastic deformation of the substrate beneath the contact. Coating delamination, caused by interfacial crack propagation, can also occur at the interface in these situations. The coating-substrate stiffness ratio can govern substrate failure. The substrate is not weakened but subject to higher and more localised stresses when stiff coatings are used [48]. Therefore, under these circumstances there is a higher probability of sub-surface plastic deformation.

In the work of Hedenqvist and Olsson (discussed above) [41], the effect of substrate hardness on erosion was also investigated. This was done by subjecting the substrate to three different heat treatments prior to coating deposition. The 3μm coatings deposited on the hardest substrate (1,000 H_v) displayed a critical particle dose approximately 14 times greater than a coating of the same thickness coating deposited on the softest substrate (290 H_v). This is mirrored in the work of Valli [49] using the scratch test found that the critical normal force required to cause coating removal increases with increasing substrate hardness.

This influence of substrate properties can lead to a coating having good erosion resistance on one substrate but poor on another. In one study, Burnett and Rickerby [50] examined PVD TiN coatings, 3-10μm in thickness, on carbon and stainless steel substrates. They found that TiN on stainless steel exhibited much lower erosion resistance and tended to spall under impact. The cause of this was thought to be high levels of elastic strain energy present in the coating as a result of high residual stresses, estimated to be 1.5 times higher than TiN-coated carbon steel.

Wuttiphan *et al* [51] examined the effect of substrate hardness on the indentation behaviour of plasma sprayed ZrO_2 coatings 300μm in thickness deposited on steel and Ni-based superalloy substrates. Indentation tests were carried out using a 6.36 mm diameter WC sphere at a load of 1500N. Metallographic examinations of the indented regions revealed greater interfacial delamination and more extensive yielding of the softer substrates. This was a consequence of the larger elastic-plastic mismatch stresses between the steel and the other material components. Therefore, a significant increase in resistance to deformation can be procured when the elastic-plastic mismatch between coating and substrate is minimised.

2.3.3 Residual stress

Residual stress, arising from the mis-match in properties between coating and substrate as well as coating microstructure, is commonly found in many coated systems. Its effects are particularly pronounced when the coating-substrate combination is composed of materials with a large difference in thermo-mechanical properties. In many cases the difference in thermal expansion coefficient is the dominant influence on the nature and magnitude of the residual stress. For ceramic coatings on metal substrates the residual stresses are typically in the range of 1-3 GPa [52]. These residual stresses can be either tensile or compressive depending on the nature of the coating and substrate.

The sign (i.e. tensile or compressive) of the residual stress can also influence the mode of deformation of the coating. Coatings under a tensile stress have an increased tendency to surface cracking, while those containing large residual compressive stresses are susceptible to delamination and spalling [53]. This delamination process can also be assisted by the presence of small flaws in the coating [54]. Excessive levels of residual stress will lead to complete removal of the coating from the substrate. Such coatings will, therefore, offer poor protection to substrates in applications where mechanisms such as solid particle erosion pose a threat to the integrity of the coating. Other workers have shown that increased residual compressive stress in coatings reduces the measured scratch and adhesion parameters [55].

In CVD diamond coatings there are two sources of residual stress: thermal stresses and intrinsic stresses. The total residual stress, σ_{rs}, is the sum of the two:

$$\sigma_{rs} = \sigma_{th} + \sigma_{in} \tag{2.7}$$

where σ_{rs} is the thermal stress and σ_{in} is the intrinsic stress.

The thermal stress is a consequence of the mis-match in thermal expansion coefficients between the coating and the substrate. It is usually compressive in nature owing to the greater contraction of most substrates on cooling to room temperature following deposition.

The intrinsic stress in the coating is due to a number of microstructural influences. Formed during the deposition process, they are usually tensile, though can also be compressive, in nature. The first source of these stresses lies in the differences in lattice parameter between the coating and the substrate. The second source is due to the microstructure of the coating and the presence of impurities and structural defects in the film. These include grain boundaries, as well as dislocations, twins, stacking faults and vacancies. Higher grain boundary densities result in a higher intrinsic stress. The nature of microstructural defects in CVD diamond coatings will be discussed in Chapter 4.

The geometry of the substrate can also influence the residual stress. Gunners and Alahelisten [56] have modelled thermal stresses in diamond coatings deposited on WC substrates. They looked at the effect of the radius of curvature of the substrate, expressed as r_e / C_T, where r_e is the edge radius and C_T the coating thickness. This has an influence on the coating integrity as intense concentrations of normal and shear stresses may lead to coating failure by interfacial spalling. The magnitude of these stresses can be reduced by increasing the r_e / C_T ratio. This has important implications for diamond coatings deposited on curved components, such as machine tools and choke valve trims.

A number of methods have been used to determine the level of residual stress in CVD diamond and are reviewed by Windischmann and Gray [57]. The most widely used

methods are x-ray diffraction (XRD) and Raman spectroscopy. However, interpretation of the results is a complex task and the results themselves are dependent on the location in the sample at which the analysis took place.

One of the most widely used methods is Raman spectroscopy. In this method, an intense monochromatic light source - usually a laser - is directed onto the sample surface. The interactions of the light with the sample cause the lattice to be excited (vibrationally and rotationally). This scatters the laser beam from the original wavelength. The degree of scattering (the Raman shift) is a function of the resonant molecular energy of the excited molecular vibrations. Every molecular species has a characteristic Raman shift, which enables its identification when analysed. Single crystal diamond exhibits a single sharp peak at a wave number of 1332.5 cm^{-1}. This makes it easily distinguishable from graphite, the main peak of which can be found at ~1580 cm^{-1} [58]. It is, therefore, a useful tool for characterising diamond films grown by chemical vapour deposition.

In addition to its ability to distinguish between the different forms of carbon, Raman spectroscopy has also been used to measure the levels of residual stress in CVD diamond coatings. The presence of a residual stress in the film has been shown to affect the position of the fundamental phonon line, which is located at 1332.5 cm^{-1}. Tensile stresses cause a downward shift in the wave number while an upward shift indicates the presence of a compressive residual stress [59]. This line varies linearly in pressure with a shift of 2.87 cm^{-1} / GPa [60].

Though Raman measurements can appear to give an indication as to the level of residual stresses present in the coating, the reality is somewhat more complicated. The degree to which the 1332.5 cm^{-1} peak shifts (positive or negative) is position sensitive. The exact extent to which the peak shifts depends on the location on the sample where the analysis took place. Even within the individual grains the degree of shift observed can vary considerably. Burton *et al* [61] found that on square {100} facets tensile stresses were found at the grain boundaries, while at the centre of the grains the stresses were predominantly compressive.

Raman mapping across an area of a diamond coating can overcome such localised variations to give a more representative indication of the stress state of the coating. Pickard *et al* [62] have used a Raman spectrometer attached to a confocal microscope to map the crystalline quality in diamond films on a micron scale and to correlate the findings with the pattern of defect densities previously observed with transmission electron microscopy (TEM). The same authors have also used the same technique to map the profiles of crystals that have been deliberately damaged by electron irradiation and also mechanically damaged by soft impressors and sliders made from TiB_2 [63].

2.3.4 Adhesion

Adhesion is related to the nature and strength of the bonding forces at the interface of the coating and substrate where they are in physical contact with each other [64]. It is dependent upon many factors, the most important being:

- Residual stress;
- Nucleation Density;
- Level of porosity at the interface;
- Pre-deposition treatment of substrate;
- Lattice constant mis-match between coating and substrate;
- Chemical nature and cleanliness of substrate;

In coated systems, the "weakest link" is often the interface between the coating and substrate and it is here that failure will often be initiated. The rate at which debonding takes place, via interfacial crack propagation, is dependent on the adhesion of the coating to the substrate.

In assessing the performance of the coating system it is important to be able to have a simple and reproducible method of determining the adhesion strength of the coating to the substrate. A number of methods have been developed in which this can be assessed, most of them semi-quantitatively, and have been described by various authors [49,55,65-67].

One of the most widespread methods used in the assessment of coating adhesion has been the scratch test. This consists of a stylus being drawn across the surface of the coating under a progressively increasing normal load until detachment of the coating takes place. The normal force affecting the indenter and causing coating detachment is called the critical normal force and it is a comparative value of the coating adhesion [49,55,66,67]. However, large variations in the critical load, L_c, are often seen from identical coatings. Moreover, as the hardness of the film under test is increased, the greater the probability of damage to the stylus. The high hardness of diamond films means that this problem is particularly acute. For this reason, the scratch test will not be used in this project and will not be discussed further.

An alternative method to the scratch test is an indentation-based method. The indenter most commonly used is the Rockwell "C" ("brale") indenter [49,55,66,67], which is a spherical diamond indenter, though a Vickers indenter has also been used [65]. The test consists of indenting the coating using a number of pre-determined loads. When the load exceeds a critical level, this causes the coating around the indent to be detached. When all the loads have been done the diameter of the delaminated area is measured and plotted against load. Steeper gradients denote poorer adhesion. This information can be used to calculate the interfacial fracture toughness, the procedure for which is described in references [49,55,66,67]. The indentation method has been used to determine the adhesion of diamond coatings on titanium [68] and tungsten carbide substrates [69]. In the latter, the authors used it to examine the effect of pre-deposition treatment of WC substrates. Recently, the indentation method has received theoretical analysis in an attempt to derive the interfacial toughness, Γ_c, from measurements of the applied load, delamination radius, film thickness and film-substrate mechanical properties [70].

Erosion testing has also been used to assess diamond coatings. Schneider *et al* [71] deposited CVD diamond films onto WC-Co substrates and used a commercial sandblast unit to subject the coatings to 90-125μm diameter Al_2O_3 particles (the velocity was not specified) at an impact angle of 90°. The minimum time to detach the diamond coating from the substrate, termed the "critical blasting time", was used to compare the different coating samples.

Diamond is a very inert material and is resistant to most forms of chemical attack, except at elevated temperature. This property makes it ideal for applications where the environment is highly corrosive. However, this inertness creates difficulties in depositing diamond films of sufficient adhesion strength. This problem means that special preparation of substrates is necessary in order to promote greater nucleation densities. A general review of the methods used to enhance the nucleation, and thus the adhesion, is given in [72]. On untreated substrates the nucleation density is in the region 10^3 to 10^5 cm^{-2}. With treatment this can be increased to as high as 10^{11} cm^{-2}. Methods used to enhance nucleation densities and/or adhesion include surface scratching, seeding with diamond crystals [73], bias pre-treatment [74] surface carburisation [75] as well as surface roughening by sand blasting [76] and multiple pulse laser irradiation of the substrate [77]. The choice of substrate also affects the nucleation of diamond crystals. The diamond nucleation rate in carbide-forming substrates (e.g. Si, W, Mo) has been found to be one to two orders of magnitude higher than on substrates that do not (e.g. Cu, Au) [78].

In choke valves, the most widely used trim material is sintered tungsten carbide; this, then, will form the substrate for diamond-coated choke trim. The advantage of this system is that it combines the fracture toughness of WC with the excellent wear resistance of CVD diamond. However, several difficulties are encountered in attempting to deposit diamond on WC. One of the major obstacles is that certain elements, Co and Ni (which are used as binders) as well as Fe, have the tendency to act as catalysts for the formation of graphitic phases. It is this characteristic which inhibits the deposition of diamond on steel. This has adverse consequences on the nucleation and growth, as well as the adhesion, of the diamond film. Binderless WC does not have sufficient fracture toughness for service in offshore valves. One of the ways in which it has been attempted to overcome this problem is to remove the binder from the near-surface regions of the substrate by selective etching. However, this is not without its drawbacks, as this tends to result in sub-surface porosity, which can weaken the diamond-carbide interface. Nesladek *et al* [79] have leached Co from the surface layers of WC-Co and replaced the lost Co with Cu. This treatment was found to have significantly improved the toughness compared with a chemically leached substrate.

Alternative methods to selective etching of the binder phase are to deposit an interlayer between the coating and the substrate or to bond free-standing diamond films to the substrate by brazing. An interlayer can act as a diffusion barrier between the Co binder and the coating. It can also act as a way of reducing residual stresses by using a material with a thermal expansion coefficient between WC and diamond. Interlayers that have been found to improve the adhesion of diamond to WC include TiCN [80] and Ag [81]. Diamond films have also been successfully brazed to SUS430 steel using a Ti-containing Ag-In-Cu alloy [82]; the brazing was carried out in vacuum at 720°C. During brazing Ti was found to segregate to the diamond film, forming TiC, and this enhanced the adhesion. However, it was noted that a large compressive strength was thought to be present at the interface as evidenced by a large diamond peak shift in the Raman spectrum.

2.3.5 Microstructural defects

The nature of microscopic defects encountered in CVD diamond coatings will be examined in Chapter 4. In this section, the role of macroscopic defects is considered. The presence of porosity in the coating can be detrimental to the erosion resistance of a coating. It can act as a stress raiser and provide a nucleation site for further damage propagation. This is particularly important in thermal sprayed coatings where the microstructure is often very inhomogeneous, containing defects such as porosity, easily distinguishable splat boundaries, oxides, inclusions and contamination. Erosion damage at the surface often initiates from these features. Some coatings of this type contain high levels of micro cracking, which can act as stress raisers, thus contributing to a reduction in erosion resistance. The same is true for bulk ceramics. Some ceramics of equal chemistry and purity have unequal erosion rates, which can be explained, by different levels of porosity in each sample. For example, Hansen [83] found that the erosion resistance of a near 100% dense alumina was more than 1.5 times greater than alumina of 95-98% density. The processing route of nominally identical ceramics can also have a large effect. Hot pressed Si_3N_4 had more than ten times the erosion resistance of the (less dense) reaction-bonded Si_3N_4. In CVD diamond, it has been found that there are often significant amounts of porosity in the coating close to the coating-substrate interface. In some cases, this has been found to be as high as 5% [84]. Therefore, this could provide initiation for further interfacial cracks, which could assist the debonding process.

2.4 Impact damage and erosion modelling of brittle materials

This section considers the types of impact damage observed on brittle materials that have been described in other solid particle impact and erosion studies. It will also attempt to explain the mechanisms responsible for the generation of the various damage features as well as the factors influencing these mechanisms.

Many people have attempted to model the erosive wear process (in order to predict erosion rates) with varying degrees of success. Meng and Ludema [85] have reviewed the major general predictive models of solid particle erosion. They considered 28 general models of erosive wear, that together contain nearly 100 different parameters. The authors state that no single predictive equation or group of limited equations could be found for general and practical use.

2.4.1 Elastic-plastic damage

This type of damage is associated with impact from angular particles, which are more common in erosive conditions. It is known as "elastic-plastic" damage and is shown in schematic form in Figure 2.8 [86]. This form of damage is similar to that seen in the indentation of ceramics by a Vickers pyramid indenter. Initially, the very high stresses beneath the tip of the indenter cause the material to plastically deform. At loads greater than a critical value a radial crack, also known as a median crack, is formed which propagates into the material in a direction perpendicular to the surface. The higher the load the further the crack will grow. During unloading, further cracks, known as lateral cracks, are formed which propagate in a direction approximately parallel to the surface. They are formed by the relaxation of residual stresses in the material and often curve upwards, intersecting with the free surface. In brittle materials intersection of these lateral cracks is thought to be the principal mechanism of material removal. The median cracks cause degradation in strength of the material; however, their contribution to the overall wear rate is minimal. Subsequent particle impacts on this site will have a wedging effect on the median (radial) crack. The extent of radial fracture depends on the hardness of the target as well as the radius and velocity of the erodent. The depth of lateral cracking is dependent on the hardness of the target and the velocity, density and radius of the erodent.

2.4.2 Hertzian ring and cone cracks

When spherical particles impact with the surface of brittle materials the damage is often in the form of circular ring cracks. These cracks, which can be described by Hertz theory [87], are initiated when the impact load or velocity exceeds a critical value. They are usually found at the edge of the contact region made by the particle on the target surface, where the maximum tensile stresses occur, and their nucleation is assisted by the presence of pre-existing surface flaws. A schematic diagram of this can be seen in Figure 2.9.

The ring crack formed propagates into the material in a direction perpendicular to the surface before diverging away from the radius to form a cone crack. The angle at which the cone cracks propagate, θ_A, is dependent on the material. For glasses having a Poisson's ratio of 0.25, θ_A is approximately 68° to the vertical. This angle is usually smaller in diamond owing to the smaller Poisson's ratio (0.07) as well as the potential for cleavage (discussed further in Chapter 4). Figure 2.10 shows a cone crack in single crystal diamond.

The Hertzian approach to understanding impact processes contains a number of assumptions, which must be remembered. The first is that the elastic energy of the two bodies acquired during the collision processes is entirely reversible, the approach and recessional velocities of impact are identical making the coefficient of restitution unity [88]. Secondly, Hertzian theory, being quasi-static, is applicable for impacts so long as the contact circle expands at a rate less than the velocity of elastic waves such that the quasi-static analysis condition is satisfied. For low velocity (<60 m s^{-1}) this has been shown experimentally to provide a reasonable approximation [89], though the measured ring crack diameter is often up to 30% greater than that predicted by the theory. Johnson *et al* [90] have attributed this phenomenon to differences in the elastic properties of indenter (i.e. erodent) and target, which generated friction in the contact zone and altered the stress field. This modified stress field had the effect of increasing the diameter at which the maximum tensile stress field occurred.

There have been cases where both cone and radial cracks have been observed. This usually occurs at high loads (or velocities in the case of dynamic impact) and/or small

radius indenters. This was found by Wiederhorn and Lawn [91] in quasi-static indentation of soda-lime glass by 0.5mm WC spheres. Above loads of 180N transverse sections of the indentations revealed the presence of radial cracks propagating away from the contact zone in a direction perpendicular to the surface. At higher loads lateral cracks were also observed and the cone cracks were seen to propagate back towards the surface.

Chaudhri and Walley [92] have reported similar findings in a dynamic situation. In an examination of the impact behaviour of soda-lime and borosilicate glass they used 1mm diameter steel and glass spheres at velocities of up to 300 m s^{-1}. It was found that at velocities greater than ~100-120 m s^{-1} lateral cracks formed on unloading (rebound), and as the impact velocity was increased further the damage features were increasingly dominated by the radial and lateral cracks with the cone cracks assuming lesser prominence. At the highest impact velocity, the cone cracks could no longer be observed in the soda-lime glass, though they were still present in the borosilicate glass.

In another study Field *et al* [93] used high speed photography to observe the modes of failure of soda-lime glass, alumina and boron carbide under impact from 5mm diameter hardened steel spheres at velocities of between 30 and 1,000 m s^{-1}. Once again, this study revealed differences in damage pattern depending on the impact velocity. At 207 m s^{-1}, the main failure mode was radial cracking caused by plate bending. However, when the velocity was increased to 402 m s^{-1} the damage features consisted of short circumferential cracks surrounding the impact site. These features, similar to those generated by liquid impact (described earlier) were caused by reinforcement of the Rayleigh surface wave at the front surface and reflected tensile waves from the rear surface. Another interesting finding is that in impacts where Hertzian ring and cone cracks were generated the semi-apex angle, θ_A, was found to decrease as the impact velocity increased. Telling and Field [94] reported similar findings. The cause of this was thought to be the interaction of the reflected stress wave with the propagating cone crack. At lower velocities the amplitude of the stress waves was insufficient to alter the path of the cone crack.

Telling [95] has used high-speed photography to study the development of impact damage on diamond surfaces. An example is shown in Figure 2.11. It shows the sequence of a 2mm diameter sapphire sphere impacting upon the (100) surface of single crystal diamond. It shows the classical Hertzian damage with the propagation of a cone crack into the interior of the diamond. It is significant to note that the main fracture damage in the diamond occurs before fragmentation of the impacting ball.

The effect of impact angle on the damage features generated by spherical particles has been investigated by Chaudhri and Liangyi [96]. Using 2mm diameter WC spheres, they impacted soda-lime glass at a velocity of 150 m s^{-1}; the impact angle was varied between 15 and 90°. High-speed photography was also used to study the trajectory of the impacting sphere as well as to record the initiation and growth of damage features, in particular Hertzian cone cracks. This work was compared with quasi-static indentation of the soda lime glass at various angles. The photography showed that spheres undergoing oblique impact slid across the surface of the target at a velocity of 100-120 m s^{-1} and this altered the orientation of the cone crack. However, the authors did not discuss the surface damage features generated by the impacts of the spheres.

Akimune [97] studied the oblique impact of 1.5mm diameter partially stabilised zirconia (PSZ) spheres onto sintered silicon nitride at a velocity of 277 m s^{-1}. The damage features produced from the angles employed (30°, 45° and 60°) were compared with those from normal (90°) impact. It was found that the cone cracks tended to become less prominent at the lower angles, and at 30° they disappeared, leaving only a surface ring crack.

2.4.3 Modelling of solid particle impact damage in brittle materials

The multiplicity of experimental variables involved in erosion testing means that developing a model that accurately describes this process is no simple task. The most significant parameters that affect the erosion of brittle materials are the hardness and fracture toughness of the target, as well as the size, density, hardness and velocity of the particle. The values of hardness and fracture toughness employed in these models are usually determined by quasi-static methods. In the case of coatings, it is necessary to use values of hardness and fracture toughness that are free of any influence of the substrate. These "surface values" can be obtained by nanoindentation, which is

discussed in Chapter 4. However, dynamic parameters may be more realistic, being obtained under conditions that are more representative of in-service behaviour. No models have been found that have either been derived from the experimental results of CVD diamond or been developed to describe the erosion process of CVD diamond.

A number of models have been developed for brittle materials, utilising both the elastic-plastic as well as the Hertzian approaches, and are described in references [91, 98-103]. However, they are not considered to be applicable to the present study and will not be discussed further. There are many reasons for this. Because diamond is the hardest known material one of the central assumptions inherent in any erosion model, that the eroding particles do not deform, is no longer valid. In sand erosion studies, which will be described in a later chapter, significant degradation of the erodent has been seen, with the average sand size reducing by more than 50%. Therefore, the erodent undergoes more degradation than the target. This could give rise to damage features, which are different to those seen in other brittle materials. Moreover, as the damage in diamond is likely to be purely elastic in nature, none of the models based on the elastic-plastic median and lateral cracks will be applicable.

A number of workers have used elastic-plastic damage as a basis for modelling the erosion of brittle materials. They make a number of assumptions including: (i) the material is homogeneous and isotropic; (ii) the impact is at an angle of 90°; (iii) the eroding particles do not deform on impact. Two similar models have been developed, both utilising the same parameters, though one is based on dynamic theory and the other quasi-static theory. However, the high hardness and elastic modulus of diamond means that, with the possible exception of angular diamond grit, all other types of erodent will undergo considerable deformation on impact, the extent of which will exceed that suffered by the diamond.

2.4.4 Finite Element Modelling of indentation and impact damage to hard coatings

The erosion models described in the previous section were for bulk materials, where their response to indentation or impact is assumed to be uniform. However, such an assumption is not necessarily valid for coatings. This complexity is further magnified in a coating system, where there is often an abrupt discontinuity at the coating-substrate interface. The magnitude of this discontinuity is dependent on the mechanical

properties of both the coating and the substrate. This presents difficulties in attempting to model the mechanical behaviour of a coating system. The complexity of the stress field is usually such that finite element modelling (FEM) is required to handle the calculations. Camacho and Ortiz [104] have described FE modelling of impact damage in brittle materials. Although Finite Element Modelling (FEM) does not form part of the present work, it has been used in other impact studies; for this reason it is briefly discussed here.

Fisher-Cripps *et al* [105] used this approach to model the damage in plasma sprayed Al_2O_3-TiO_2 coatings on carbon steel substrates. Two coating thicknesses were investigated: 160μm and 470μm. The results were compared with metallographic sections of the coating following indentation using a WC sphere. An example of the FE predictions is shown in Figure 2.12. It shows extensive plastic deformation (denoted by the shaded zones) of the substrate caused by shear stresses; this was also found on the metallographic sections. Tensile stresses are also prominent at locations close to the coating-substrate interface as well as at the surface. This was more prominent in the case of the thicker coating, rather than the thin coating; in the latter, the area of greatest tensile stress was at the surface of the coating. While the surface tensile region was also present in the thick coating it was of lower magnitude; this was thought to be due to the smaller vertical deflection at the contact edge when the coating is subjected to the compressive load.

A recent study has used FEM to analyse the stresses generated in diamond coatings under indentation. Fagan *et al* [106] used FEM to predict the stress distribution in diamond coatings on silicon up to 90μm in thickness under indentation from a blunt soft impressor. The authors found that the position of maximum principal stress was dependent upon the coating thickness to contact radius ratio (C_T / a_m). For the thinnest coating ($C_T / a_m = 0.09$; $C_T = 3.5\mu m$) the maximum stress is seen to occur on the surface of the diamond near the edge of the contact. For the thickest coating (90μm) the maximum stress occurs at the diamond-silicon interface beneath the centre of contact.

The Finite Element method has also been used to model impact damage in brittle materials and coatings. Liaw and Kobayashi [107] used a solid particle impact damage model in conjunction with an elasto-dynamic axisymmetric finite element programme.

The model was based on elastic failure due to tensile or shear overloading and the coating studied was partially stabilised zirconia (PSZ) on steel impacted with 1.6mm diameter WC spheres at 71.4 m s^{-1}. The coating thicknesses studied were 150μm, 250μm and 500μm and the predicted damage in bulk materials was compared with impacted specimens tested under identical conditions. Good agreement was found between the two, the exception being the generation of cone cracks (experimentally) which the model did not predict. In the coated samples, in addition to the shear, median and lateral cracking, the model also predicted coating debonding at the interface. The debonding length was similar (800μm) in both the 150μm and 250μm thick coatings, though none was predicted in the thickest (500μm) coating. In the 250μm coating, the debonding length (800μm) and range of spalling damage (700μm) were approximately 3 and 2.5 times, respectively, of the contact radius. The 150μm coating showed a shorter spalling region than the 250μm. The debonding length was the same for the two thicknesses.

2.5 Conclusions

This chapter has examined the factors that affect the erosion behaviour of brittle materials and coatings. It is clear that the quantity of factors, as well as interactions between them, means that attempting to model the erosion process is no small task. This is complicated by the fact that some of the most important properties, such as hardness and fracture toughness, are mutually exclusive: high hardness is usually attained at the expense of low fracture toughness, and vice versa. Therefore, a compromise between the two is required. For coatings, there are the added complications of adhesion strength and residual stress, both of which can affect the integrity of the coating and assist debonding.

Following a survey of the literature, it was concluded that no existing erosion models, either those based on Hertz theory or on elastic-plastic theory, were applicable to the present study. This is because the assumption that the particles do not deform on impact is clearly no longer true in the erosion of diamond by sand or SiC, where the particle hardness is, very approximately, between 1/8 and 3/8 of the hardness of the diamond. In the case of the elastic-plastic models, there is a second reason, which is that, to date, no erosion studies of diamond report any incidence of plastic deformation (and hence lateral cracking) so a central tenet of the elastic-plastic theories remain unfulfilled.

For CVD diamond, the most important factors affecting its erosion performance are particle velocity, erodent size, erodent hardness, coating thickness, coating surface roughness, coating adhesion strength, residual stress, hardness and fracture toughness, elastic modulus as well as the size and distribution of cracks / defects.

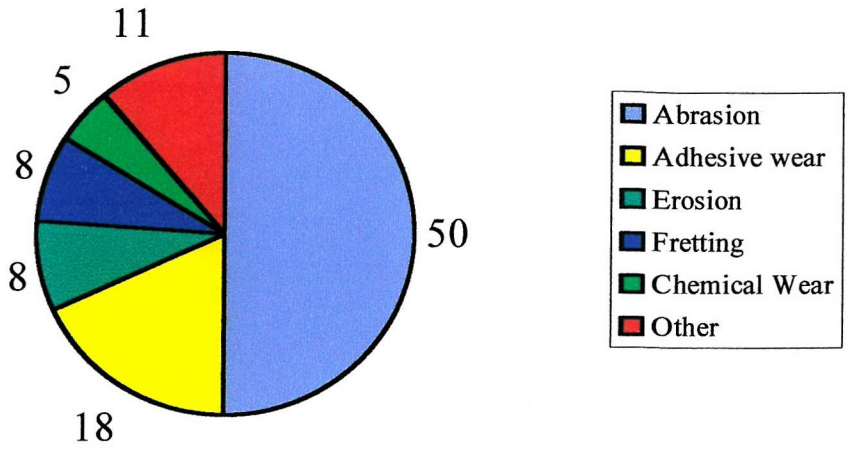

Fig. 2.1a: Results from the 1979 survey by Eyre [2] showing the contribution of the different types of wear to the total number of wear-related failures.

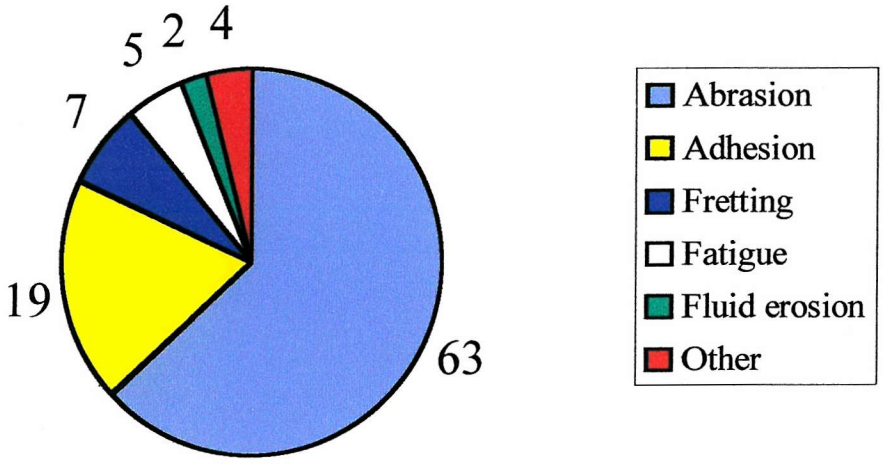

Fig. 2.1b: Results from the 1997 DTI Industrial Wear Survey showing the contribution of the different types of wear to the total number of wear-related failures.

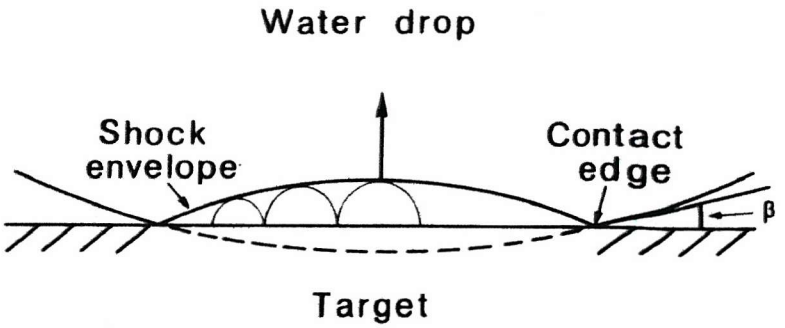

Fig. 2.2: Schematic diagram showing the process of liquid droplet impact onto a solid surface [5].

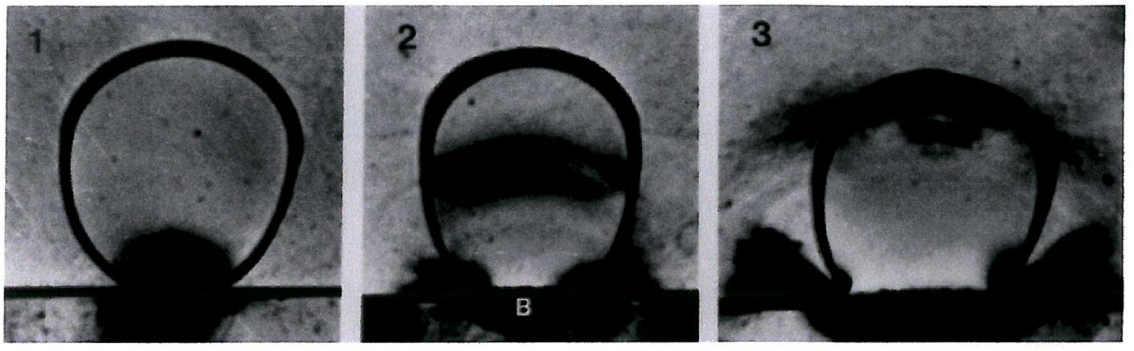

Fig. 2.3: High-speed photographic sequence showing the impact of a two-dimensional liquid droplet, 2mm in diameter, with a PMMA target at 70 m s^{-1}. The "sequence" is composed of three different experiments and the dark shaded regions denoting high stress were imaged using Schlieren optics [6,7]. Features of note include high-pressure regions in both the droplet and target at the point of impact (Frame 1), the reflected shock wave travelling through the droplet and jetting at the contact edge (Frames 2 and 3). Reproduced with the permission of Professor J.E. Field, University of Cambridge.

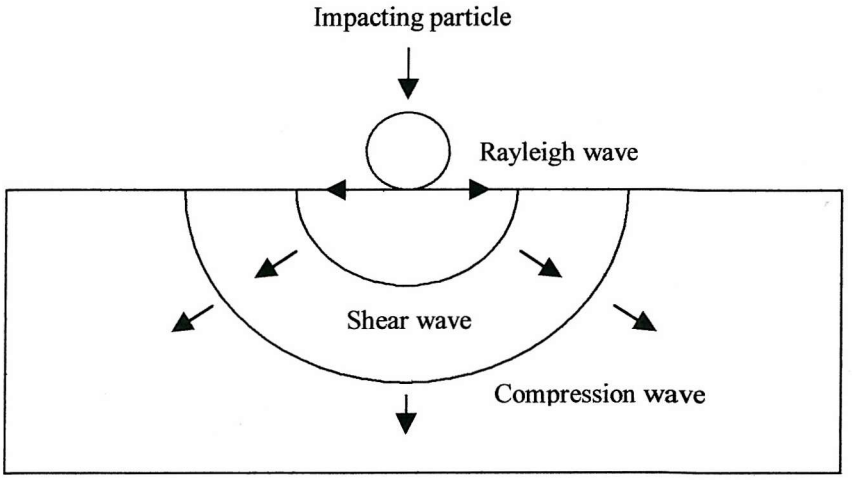

Fig. 2.4: Schematic diagram of the stress waves produced in a target material following impact by a solid or liquid erodent.

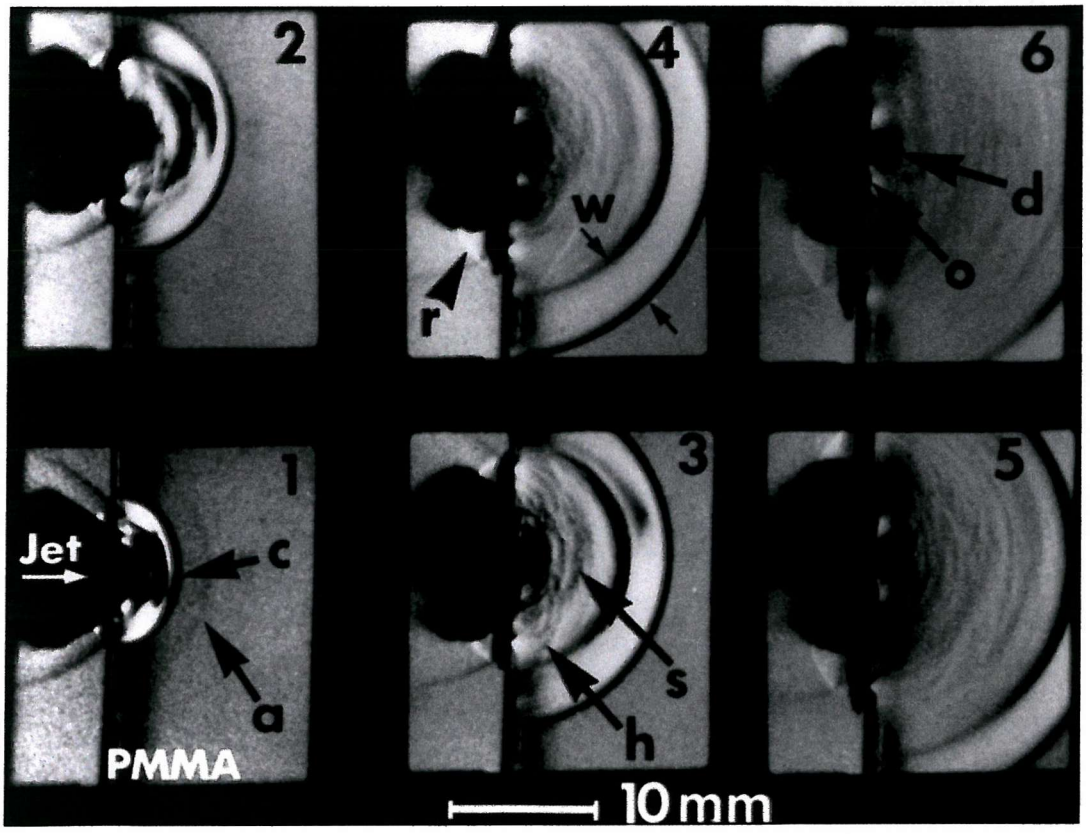

Fig. 2.5: Shadowgraph sequence of the impact of a 750 m s^{-1} water jet onto a PMMA block [10]. Duration of each frame: 1 μsec. **Key:** *a*: stress front induced by detached air shock; *r*: reflected air shock; *c*: Main compressive stress pulse of width, *w*; *h*: Head wave; *s*: Shear front (poorly defined because of the nature of the optical system); *d*: sub-surface shear failure; *o*: Main ring crack. Reproduced with the permission of Professor J.E. Field, University of Cambridge.

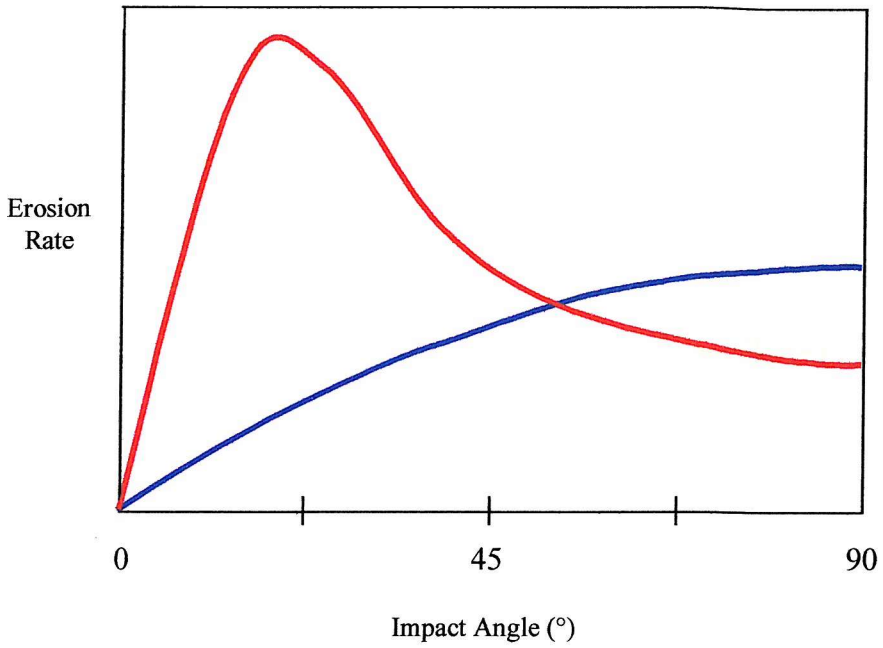

Fig. 2.6: Schematic diagram showing the variation between Erosion Rate and Impact Angle for ideal ductile (red) and brittle (blue) materials.

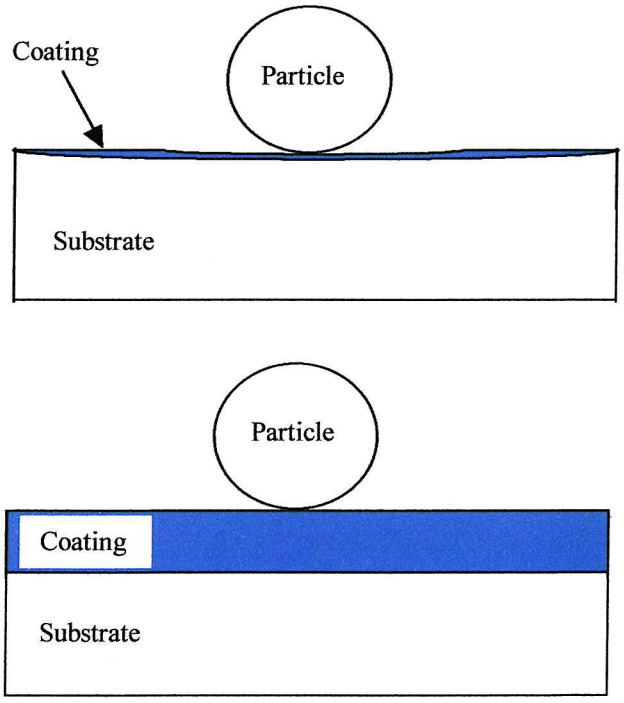

Fig. 2.7: Schematic diagram showing the influence of coating thickness on the protection offered by a coating to a substrate. The thinner coating is unable to support the load generated by the impacting particle and deflects under the impact.

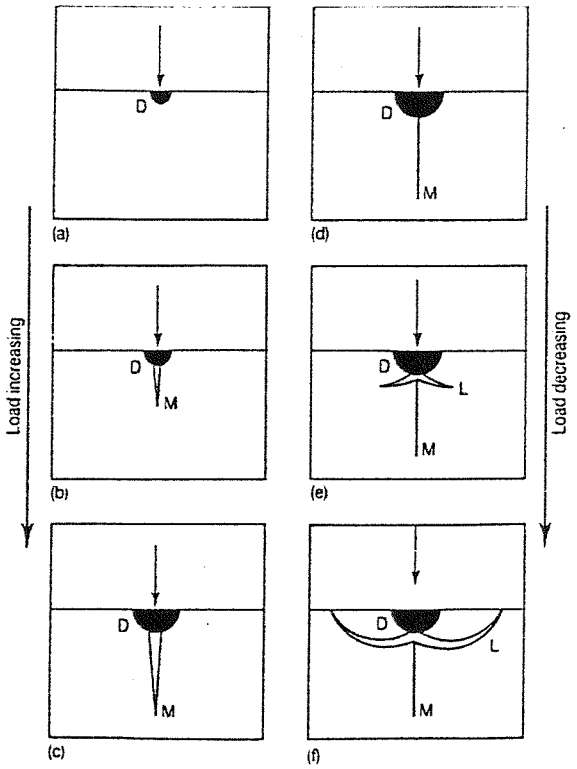

Fig. 2.8: Diagram showing the development of median and lateral cracking as a result of indentation with a sharp indenter [86]. Key: M = Median crack; L = Lateral crack; D = Area of plastic deformation beneath the indenter.

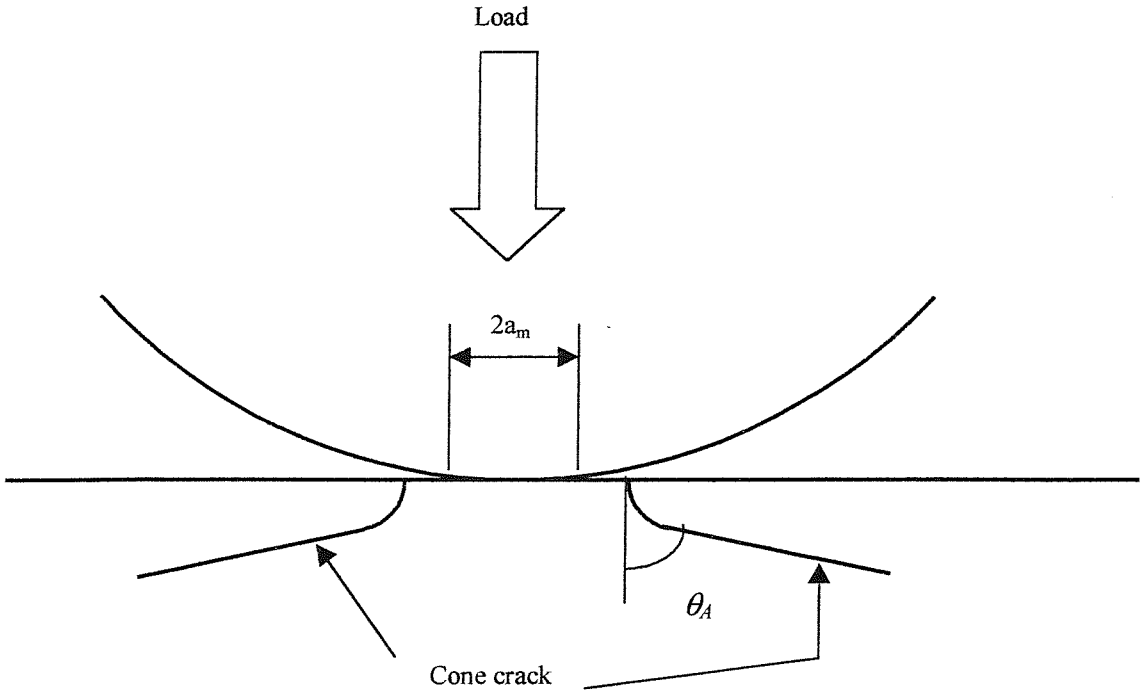

Fig. 2.9: Schematic diagram showing the formation of a Hertzian cone crack following indentation of a brittle material with a spherical indenter. Key: a_m = contact radius, θ_A = angle of propagation crack propagation.

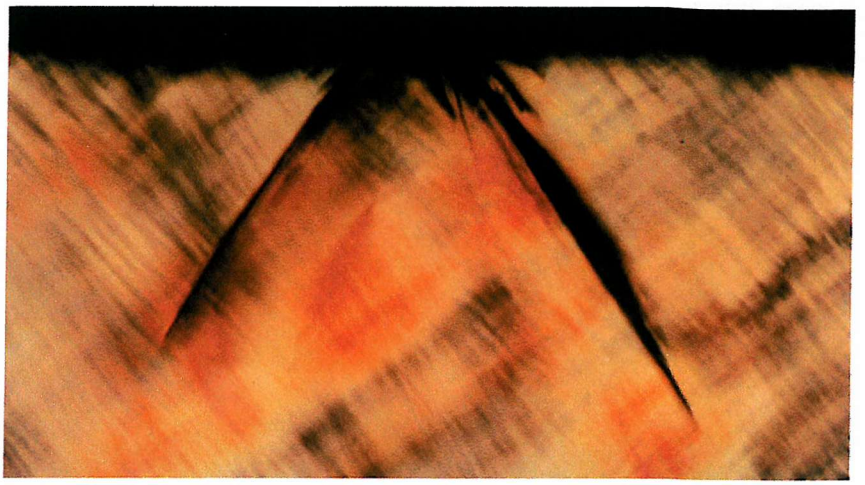

Fig. 2.10: A cone crack produced in natural single crystal diamond viewed in plane polarised light. Reproduced with the permission of Professor J.E. Field, University of Cambridge.

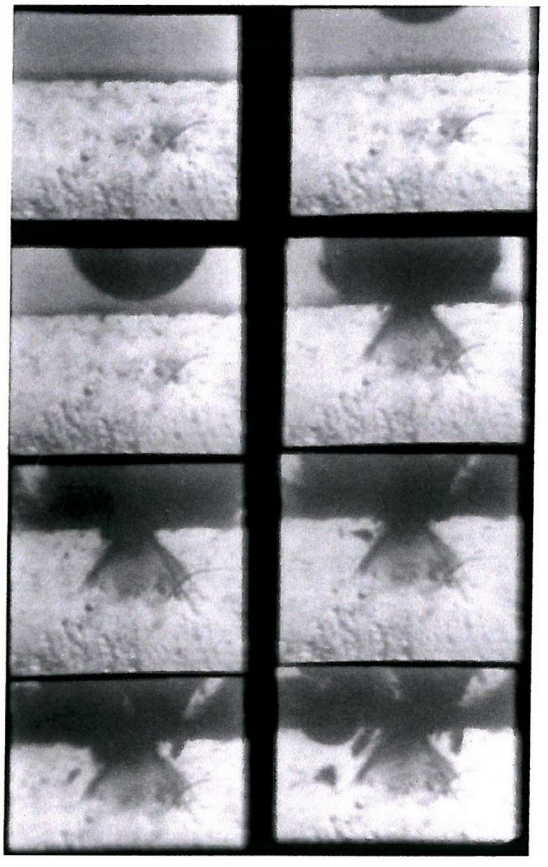

Fig. 2.11: High speed photographic sequence of a 2mm diameter sapphire sphere impacting onto a (100) single crystal diamond at 114 m s^{-1}. It shows that the main fracture damage in the diamond occurs before fragmentation of the impacting ball. The maximum crack velocity of diamond is 7200 m s^{-1} [95]. Reproduced with the permission of Professor J.E. Field, University of Cambridge.

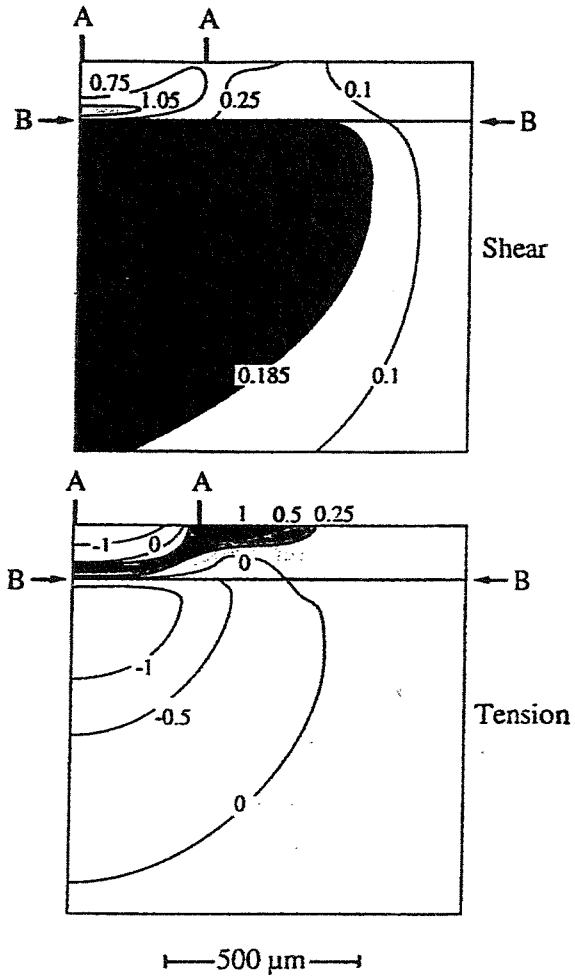

Fig. 2.12: Stress contours (in GPa), calculated by Finite Element Analysis, of a 160μm coating of Al_2O_3-40 wt% TiO_2 on steel indented by a WC sphere of 3.18mm radius at a load of 500N. The line AA is the contact radius, while BB is the coating-substrate interface. The shaded zones denote areas of yielding [105].

3

DIAMOND

3.1 Introduction

Diamond is one of the three major forms of carbon, along with graphite, which is the most stable form, and the more recently discovered Buckminsterfullerene. It has been known that diamond is a form of carbon since 1797 [1] and there have been numerous attempts since then to produce synthetic diamond from carbon-based starting material. However, it has only been in the last forty years that this has been successful, first via the high pressure / high temperature (HPHT) route, and latterly by chemical vapour deposition (CVD). Diamond is stable with respect to graphite only at high pressure (greater than 1.6GPa at room temperature) and is metastable at room temperature. However, there exists a large activation energy barrier between them, which inhibits transformation from diamond to graphite [2]. This can only be overcome at high temperatures, greater than 600 K, where under certain conditions graphitisation takes place rapidly. At room temperature the rate of transformation is negligible. Figure 3.1 shows a pressure-temperature phase diagram showing the regions where diamond and graphite are stable.

There are several categories of natural diamond, which denote the type and level of impurities present. Type Ia, the most common variety, contains approximately 0.1% nitrogen in the form of small aggregates and platelets. Type IIa has the highest purity with virtually no nitrogen present. For this reason, their thermal and optical properties are superior to other types. The third type, IIb, is often blue in colour, due to the incorporation of boron; the presence of boron also gives it its p-type semi-conductor characteristics. Synthetic diamond, such as HPHT diamond, is designated type Ib. It is often yellow in colour and contains nitrogen dispersed in substitutional form. CVD diamond is very close to type IIa in character. It is also possible to dope it with boron.

Diamond has many properties that make it an attractive option for components in a wide range of engineering, and in particular tribological, applications. It is well known that diamond is the hardest known material, though it has been predicted that crystalline carbon nitride (β-C_3N_4) may be harder [3]; this prediction, though, remains theoretical since there exists no production route. Other properties include its high elastic modulus and the highest thermal conductivity of any material at room temperature (five times that of copper). In addition to its mechanical properties, it also has excellent electrical and optical properties. It has fifteen times the average electric breakdown of common semi-conductors, five times their average hole mobility and a dielectric constant that is half that of silicon [4]. Furthermore, its high index of refraction and ability to transmit light from the far infrared to the ultraviolet range makes it an ideal material for laser windows. Diamond also exhibits a low coefficient of friction when sliding against itself in most environments, the most prominent exception being vacuum.

The exceptional properties of diamond are due to its crystal structure. The crystal lattice is cubic, though occasionally hexagonal, and consists of each carbon atom being covalently bonded to four equi-distant neighbours in a tetrahedral arrangement. This bonding is known as sp^3, with each bond length being 0.154nm. At free surfaces the absence of one of these neighbours means that there is one vacant electron, which remains unattached to a carbon atom. These are known as "dangling bonds" and, under normal atmospheric conditions, are filled by hydrogen atoms. In graphite, the structure is hexagonal with each atom having only three nearest neighbours (sp^2 bonding) resulting in a planar structure and weak bonds linking each plane. The bond length is also slightly shorter at 0.142nm. The density of graphite is significantly lower than diamond: 2,260 kg m^{-3} versus 3,520 kg m^{-3}. Figure 3.2 shows the crystal structure of all three allotropic forms of carbon. The figure also includes an example of a nanotube, which is a form of fullerene.

3.2 Chemical Vapour Deposition

Chemical Vapour Deposition (CVD) is the process by which substances in the vapour phase are decomposed and react before condensing onto a substrate to form a solid deposit. Originally developed in the semi-conductor industry, work in this area has

undergone rapid expansion over the last thirty years. It is now used in many industries for mechanical and optical, as well as microelectronic, applications.

It is now possible to deposit a large number of hard coatings by this method. These include SiC [5-8], TiC [9], TiN [9,10], GeC [11], $B_{13}C_2$ [12,13] and BP [14,15] as well as diamond. Research had been carried out on the vapour phase deposition of diamond since the 1950s. However, it was not until the early 1980s, following work by Spitsyn [16] and later by Kamo and Matsumoto [17,18], that it was possible to deposit diamond, first on diamond, and later on non-diamond, substrates. At present diamond can be deposited on a wide range of substrates including Si, SiC, W, Mo and WC. Because diamond is chemically inert difficulties can be experienced in obtaining good adhesion of coating to substrate. Much work is still needed in this field before further improvements can be obtained. Certain substrates, in particular sintered tungsten carbide, can cause problems as the binder materials, notably Co, have a tendency to catalyse the formation of graphite.

Today there are a number of methods that have been used to successfully deposit high quality diamond. The main difference between them lies in the energy source used to dissociate the reactants. These include microwave plasma, hot filament, DC arcjet and many others. The major variants of CVD diamond processes have recently been reviewed by May [19]. For brevity, this discussion will be limited to a description of just one of the more widely used methods: microwave plasma CVD.

3.3 Microwave Plasma CVD

A schematic diagram of Microwave plasma CVD (MPCVD) is shown in Figure 3.3. In this process the substrate is heated to a temperature in the range 800-1,000°C and at sub-atmospheric pressure, typically 10-100 mbar, before addition of the reactant gases into the chamber. The high deposition temperatures necessary mean that, at present, this precludes deposition on certain substrates such as steels. The reactant gases consist of a dilute mixture of a hydrocarbon, usually methane (CH_4) and hydrogen (H_2) though CO and O have also been used. In order to deposit high quality diamond the methane content must not exceed 1% of the total volume of gas. The choice of hydrocarbon gas is not limited to methane; other gases that have been used include acetylene, methanol and acetone. The exact deposition mechanism is complex and is still not fully

understood. However, what is known is that under the right conditions nucleation of diamond crystals occurs. In its basic form the reaction is:

$$CH_4 + H_2 \rightarrow C\ (Diamond) + 3H_2 \tag{3.1}$$

This reaction is initiated by a microwave source such as a magnetron generator: a commonly employed frequency in this work is 2.45 GHz. This creates a ball-shaped plasma, causing dissociation of the CH_4 and H_2 gases. Hydrogen molecules are dissociated to hydrogen radicals by electrons in the plasma, while the methane is dehydrogenated into CH_3, CH_2 and CH radicals by either the hydrogen radicals or by electrons in the plasma [20]. These species are then transported from the activation zone to the near surface region by diffusion and/or convection. The methyl radical (CH_3) is extremely reactive and on coming into contact with the hot substrate surface a bond is formed by chemisorption. The acetylene radical (C_2H_2) is also highly reactive, owing to its triple bond, and thus also bonds easily to the substrate. On the substrate the radicals form a mixture of amorphous carbon, graphite and diamond. Care must be taken to ensure that the plasma does not come into contact with the sides of the chamber. If this occurs material from the chamber wall can be co-deposited along with the diamond, to the detriment of the film quality. It is for this reason that the substrate is located in the after-glow region and not in the plasma itself. If it is placed there the plasma will etch the substrate and little diamond will be deposited.

During the deposition process, it is essential that the non-diamond species be removed from the substrate. Graphite and amorphous carbon are formed as well as diamond because, thermodynamically, the energy difference between diamond is only 453 cal mol^{-1}, less than R_gT (600 cal mol^{-1}, where R_g is the gas constant and T is the temperature in K) at room temperature. As a consequence there is always a finite possibility that both will form while trying to synthesise one of them. The rate of graphite formation may be much greater than that of diamond. In order to produce a purely diamond deposit, these species need to be removed. This is achieved by the use of atomic hydrogen which is used to etch away the graphitic deposit, leaving a purely diamond deposit behind. Atomic hydrogen etches non-diamond carbon approximately 50 times faster than the co-deposited diamond. This happens even faster in the presence of oxygen [4]. This is because the oxygen reduces the concentration of the hydrocarbon

nutrients such as CH_3 by forming CO, which is stable and so reduces excess carbon. Trace amounts of OH and O present in the plasma react with sp^2 impurities far more readily than atomic hydrogen and this improves the purity of the diamond [21]. These etching processes also aid the growth of the diamond as hydrogen atoms, which normally attach themselves to the vacant surface sites of the diamond, are removed. This is because the H-H bond energy is greater than that for the C-H bond [22]. Thus, the outermost atoms on the free surface are always carbon atoms, thereby sustaining the growth of the diamond crystals. Nitrogen also has a beneficial effect on the growth of diamond by CVD. An addition of 400ppm of N to the gas phase reactants can deliver a sevenfold increase in the growth rate [23].

Figure 3.4 shows a diamond coating in the early stages of deposition. The early diamond crystals are small, sub-micron, equiaxed grains of very high density. They have an initially random orientation, though once complete coverage of the substrate is achieved they acquire a columnar appearance (see Figure 3.5) when the more favourably orientated crystals begin to grow at the expense of those with less favourable orientations. The bonding between the equi-axed grains is often weak in the early stages of growth leading to poor inter-granular adhesion [24]. There are also appreciable levels of film porosity present, which have been found to be as high as 5% in some studies [25]. As a consequence they have a low elastic modulus as there is very little in-plane mechanical strength. Significant levels of film porosity and graphite are also seen close to the coating-substrate interface. Their proportions in the film decline as columnar grain growth proceeds. This coincides with a rapid increase in the value of the elastic modulus before it reaches a plateau, and no further increases take place.

At the end of the deposition process the surface of the coating has an appearance like that shown in Figure 3.6. It shows the grains to have an essentially random orientation, though under conditions diamond films can be grown with a specific crystallographic texture, for instance on the (100) or (111) planes.

Two types of diamond are produced by the CVD process with both having separate and distinct applications. They are known as "white" and "black" diamond. White diamond is of very high quality and is transparent on account of the extremely low levels of graphite present within it. In order to achieve this, very low growth rates ($<1.5\mu m\ hr^{-1}$)

are required. It is used in optical and electrical applications. Black diamond is the higher growth rate variety (typically 2-10μm hr^{-1}) and, though having a similar level of non-diamond carbon present (100ppm), microstructural features such as grain size, grain boundary and crystal orientation render the material opaque. It is employed in thermal applications, such as heat spreaders, and tribological components such as cutting tools. The diamond used in this project is from the latter category.

As with any material it is important to be able to check that the coating produced is indeed diamond. The simplest technique for analysing CVD diamond is Raman spectroscopy, which has already been introduced in Section 2.3.3. Knight and White [26] have reviewed the use of Raman spectroscopy applied to diamond. The characteristic Raman shift of each molecular species enables the purity of the film to be determined on a qualitative basis. The main peaks of diamond (1332.5 cm^{-1}) and graphite (1580 cm^{-1}) are easily distinguished, making characterisation a relatively simple task. Typical spectra are shown in Figure 3.7. The scattering efficiency of graphite is approximately 50 times greater than that of diamond; this fact enables even minute amounts of graphite to be detected in a CVD diamond film. However, Raman spectroscopy cannot be used to determine the quantities of graphite present and must be regarded as a qualitative method only. The use of Raman spectroscopy for measuring the levels of residual stress in CVD diamond coatings has already been described in Section 2.3.3.

The advantages of MPCVD diamond include its stability in operation, making continuous deposition for several days possible. It can also produce good quality diamond films with a high degree of uniformity. It is now possible to synthesise CVD diamond wafers in diameters of up to 140mm and up to 2mm in thickness [27]. Its main disadvantage is that it suffers from the drawback of low growth rate, necessitating extremely long production runs except for all but the thinnest coatings, although for some applications the need for diamond films of high quality and purity is more important than the growth rate. Another technique, the DC plasma jet, is capable of growth rates of up to 100μm hr^{-1} [28]; however, the maximum area of deposition is considerably smaller: ~1cm^2 [19].

3.4 Polycrystalline Diamond

A related, though different type of diamond is polycrystalline diamond (PCD). Similar to sintered tungsten carbide in that it has a two-phase microstructure, it is produced by sintering diamond grains at high pressure in the presence of a metallic binder, usually Ni or Co. The result is a product, which though exhibiting a slightly lower hardness than natural and CVD diamond (50 GPa), has a greater fracture toughness (8.8 MPa$\sqrt{m}$ vs. 5.3 MPa$\sqrt{m}$). Furthermore, because it is polycrystalline, one of the problems of natural diamond, namely that of its anisotropy, is overcome. PCD, produced by De Beers under the trade name *Syndite*, is sintered at high temperature (~1500°C) and high pressure (~6 GPa). The pressures are often high enough to cause plastic deformation in the diamond grains and direct diamond-diamond bonding can take place. The resultant microstructure consists of a semi-continuous "skeleton" of diamond grains with a binder of cobalt or nickel. The cobalt content is typically 12 % wt. The presence of the binder also renders it electrically conductive. This makes it suitable for electric discharge machining (EDM). De Beers produce three standard grades of PCD: *Syndite* 002, 010 and 025, in which the average grain size prior to sintering are 2, 10 and 25μm respectively. The average mean free path between the diamond grains is 0.09μm. Two materials related to *Syndite* are *Amborite* and *DBC80*. *Amborite* consists of polycrystalline cubic boron nitride (PCBN) grains with a binder of aluminium nitride and aluminium diboride. *DBC80* consists of 80% PCBN with an average grain size of 6μm and 20% TiC as the binder phase. *Syndite, Amborite* and *DBC80* are all bonded to substrates, usually by brazing, for practical applications. PCD has found uses in machine tools, wire-drawing dies, saw blades, slot cutters and end mills. A detailed review of PCD has been given by Lammer [29]. *Amborite* and *DBC80* are used for machining ferrous metals where diamond and PCD cannot be used.

3.5 Diamond-Like Carbon

Another material that is related, though more distantly, to CVD diamond is Diamond-Like Carbon (DLC). Its name has been the source of much confusion and is often erroneously included in the same category as diamond. Despite possessing some similarities, DLC is not diamond but rather a form of amorphous carbon with some properties, for instance hardness, approaching those of diamond. The bonds are a mixture of sp^3, sp^2 and C-H; however, the areas of sp^3 bonding are not large enough to show up on Raman spectra. The term "DLC" does not refer to a specific material, but

rather to a category of materials. Thus, certain properties cannot be assumed to be the same over the whole range of DLC coatings. General reviews of DLC can be found in [30,31].

DLC can be produced by a number of different sputtering methods similar to physical vapour deposition (PVD) and also by CVD. It is carried out at lower temperatures than CVD diamond (~200°C); this enables it to be coated onto materials such as steel, as well as other carbide formers such as Si, Mo, Ti and W, with fewer adhesion problems experienced with diamond. DLC transforms to graphite at lower temperatures than CVD diamond and, as a result, should not be exposed to temperatures greater than 250-300°C for prolonged periods of time.

There are several types of DLC depending on the composition. It can be either amorphous (known as a-C) or hydrogenated (a-C:H or H-DLC). Hydrogenated DLC can contain up to 50 at % hydrogen. In recent years metal-containing DLC (Me-DLC) has also been developed. It is produced by employing sputter targets containing a metal such as W or Ti.

The hardness is dependent on the structure and composition of the films; as a result a wide range of values have been reported, from 2,000 to 9,000 H_v. Like diamond it has a low coefficient of friction (μ) in air, though this is dependent on the humidity: μ is seen to increase with increasing relative humidity. In contrast to diamond, some DLC coatings continue to display low frictional behaviour, even under vacuum.

DLC coatings have found use in a variety of applications and not limited to the field of tribology. These have included bearing surfaces, gears, internal combustion engine components (notably piston rings), measuring instruments, high-density magnetic recording discs, hip joints and high-power laser windows. Gillette's new Mach 3 razor blade features a coating of DLC, which it is claimed will enable vastly increased life over conventional blades. On a larger scale, the materials used for domes on the new Cathedral of Christ the Redeemer, in Moscow, are coated with a 1μm layer of DLC to confer enhanced protection against erosion from both rain and airborne dust particles.

Property	Single-crystal diamond	CVDD	PCD*	PCBN#	DLC	WC-6Co
Hardness (GPa)	57-104 [35]	84-122 [31]	50 [29]	32 [36]	20-90 [4]	15.5 [37]
Density (kg m^{-3})	3,520 [35]	3,520 [31]	4,120 [29]	3,420 [36]	1,800-2,800 [4]	14,970 [37]
Fracture toughness (MPa$\sqrt{m}$)	3.4-5.0 [35]	5.3 ±1.3 [31]	8.81 [29]	10.0 [36]	Not known	10.4 [37]
Young's Modulus (GPa)	1,141 [35]	910-1,250 [31]	776 [29]	680 [36]	120 [31]	624 [37]
Tensile strength (MPa)	1050-3000$^{+\#}$ [38]	400^{++} - 800$^{\#\#}$ [38]	1260 [38]	Not known	Not known	Not known
Compressive strength (GPa)	9.0 [38]	8.68 [36]	7.60 [36]	2.73 [36]	Not known	4.88 [37]
Transverse rupture strength (GPa)	2.9 [38]	1.3 [38]	1.26 [36]	0.57 [36]	Not known	2.07 [37]
Poisson's ratio (dimensionless)	0.07 [35]	0.07 [35]	0.07 [29]	0.22 [36]	0.3 [39]	0.21 [37]
Thermal Conductivity at 25°C (W $m^{-1}.K^{-1}$)	2,000-2,300 [38]	1,300 – 2,100 [38]	560 [36]	100 [36]	400-1,000 [31]	100 [37]
Thermal expansion coefficient @ 25-200°C	1.5-4.8 [25]	1.21 [38]	4.2 [36]	4.9 [36]	Not known	6.0 [37]

Table 3.1: Summary of CVD diamond properties and comparison with related materials. Key: * = *Syndite* 010; # = *Amborite*; +# = Orientation dependent; ++ = Growth surface in tension; ## = Nucleation surface in tension.

One of the disadvantages of DLC is that, owing to high levels of residual stress, they are limited in thickness to less than approximately 3μm. There are few reports of erosion studies of DLC in the literature. Chandra *et al* [32] used solid particle erosion to evaluate the adhesion of DLC on AISI 304 stainless steel and Ti-6Al-4V substrates following exposure to a number of biological fluids. The coating thickness was not given. Telling *et al* [33] examined the erosion performance of 1-3μm DLC coatings on Ge substrates when eroded by 40-63μm silica particles at 23 m s^{-1}. The results showed that the best performing coating was a 3μm Si-DLC multiplayer, which remained adhered and exhibited only a moderate reduction in I.R. transmittance from 55% to

45% over the course of the test (800 sec). The 1μm DLC coating offered protection up to ~100 sec after which its performance declined rapidly until 400 sec when its transmission was little better than uncoated Ge (20%). Wood [34] tested 3-5μm DLC coatings deposited on WC-6Co. The erosion test conditions employed were 135μm sand at 16.5 m s^{-1}. He found that those coatings were too thin and were too highly stressed to be useful for use in erosive applications. As DLC coatings form no part of this project, they will not be discussed further.

3.6 Conclusions

This section has considered the methods in which CVD diamond is produced as well as other materials which can be considered to be related to diamond, notably PCD and DLC. In many categories the properties of CVD diamond approach, and in some cases match, those of natural diamond. The major properties of the various types of diamond and other related materials are summarised in Table 3.1. Figure 3.8 shows a selection of industrial diamond products [40-42].

The last 15 years has witnessed improvements in deposition rates of CVD diamond of more than 3 orders of magnitude from 0.005 to 20 carats hr^{-1} [43] over the period 1987 to 1997. These improvements have enabled corresponding reductions in costs to be achieved, from \$5,000 $carat^{-1}$ to \$5 $carat^{-1}$ [43]. As these developments continue, CVD diamond will find new applications where its unique properties can be exploited.

CVD diamond has found use in many applications including radiation detectors, field emission displays, fibres for composites, as well as micro-mechanical devices and sensors. In the electronics industry, the high thermal conductivity of CVD diamond has led to its use as a substrate material for the dissipation of heat by high power micro- or opto-electronic devices such as laser diodes. Mechanical applications include wheel dressing and tools for machining metal matrix composites, where they have exhibited lower wear rates and produced better surface finishes than PCD. CVD diamond has also been used in surgical blades in ophthalmology, where they generate lower cutting forces than stainless steel, which leads to less tissue damage. It has also been the subject of development programmes to use it for mechanical seals, I.R.-transmitting windows and domes for aircraft and (of particular relevance to the present project) in choke valves, where its high erosion resistance has the potential to significantly

increase valve operating life. Over the last decade a number of investigations of the erosion behaviour and mechanical properties of CVD diamond have been reported in the literature: these are described in Chapter 4.

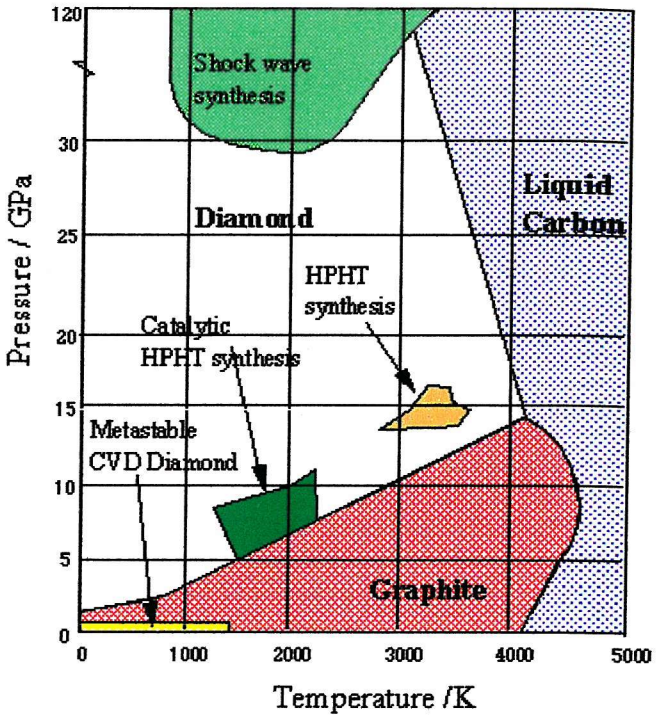

Fig. 3.1: The pressure-temperature phase diagram for carbon.

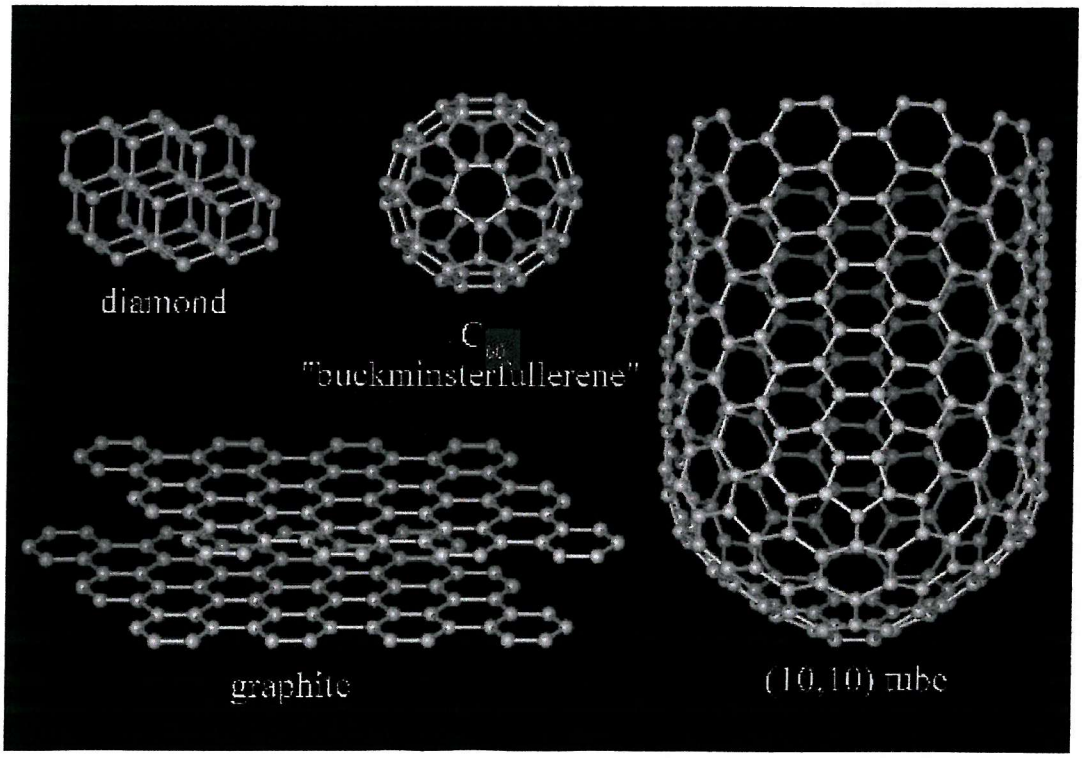

Fig. 3.2: The three crystalline allotropes of carbon.

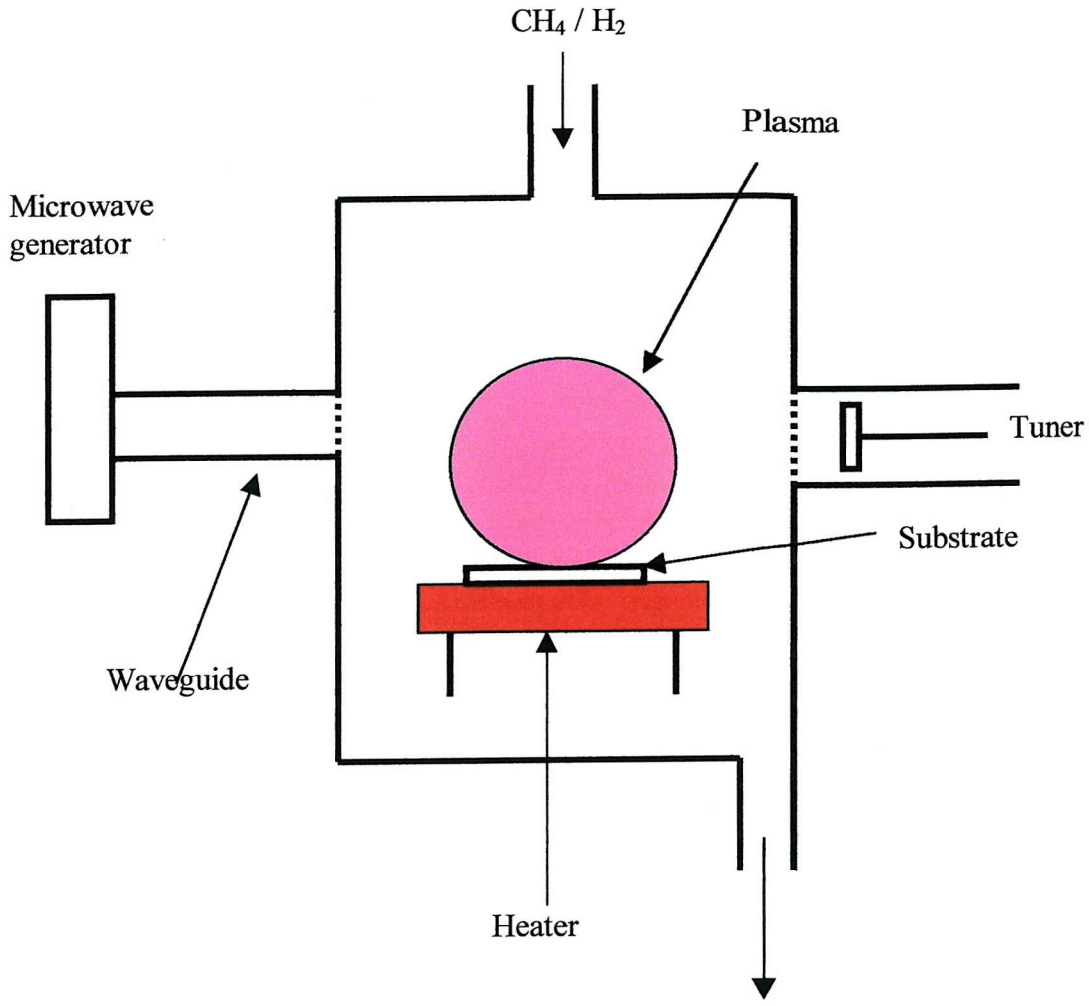

Fig. 3.3: Schematic diagram of microwave plasma CVD for the deposition of diamond

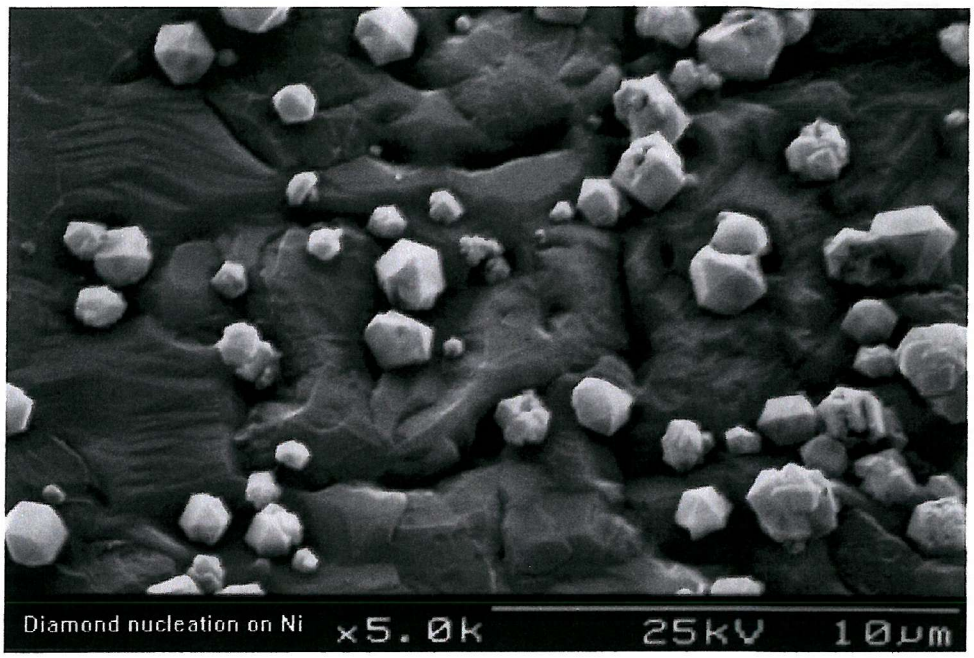

Fig. 3.4: Diamond in the early stages of growth on a Ni substrate. Reproduced with the permission of Dr. P.W. May, University of Bristol.

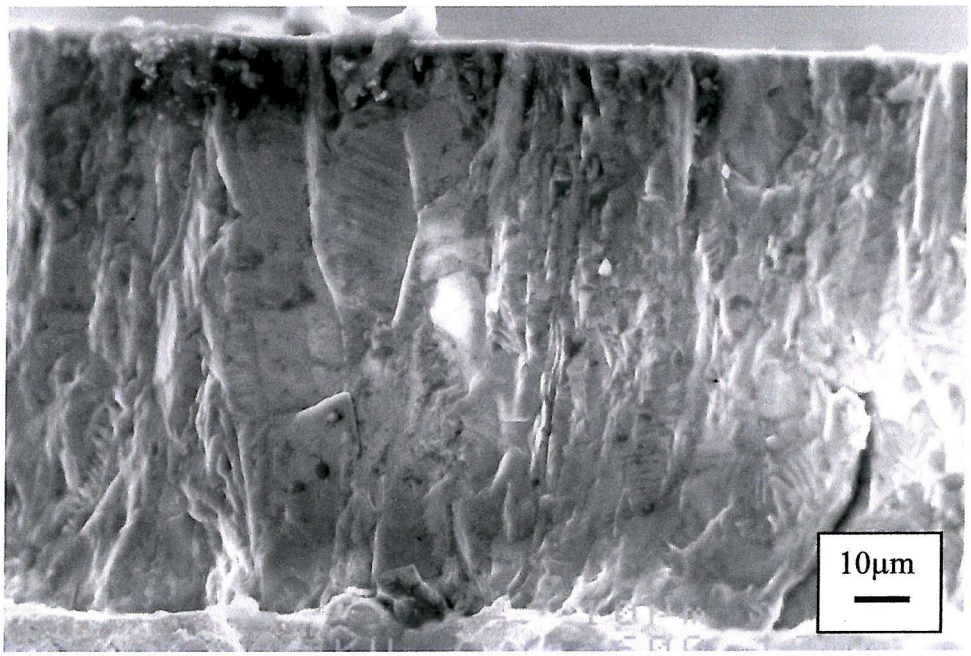

Fig. 3.5: SEM cross section of a 120µm diamond film on tungsten showing the columnar grain structure.

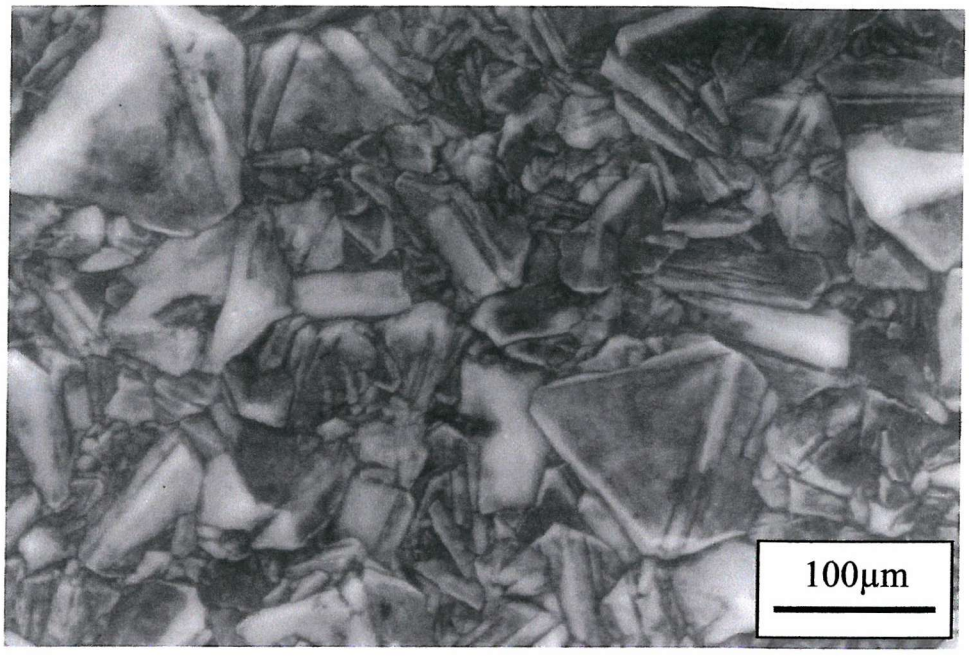

Fig. 3.6: As-grown surface of a 165μm CVD diamond film on WC-6Co.

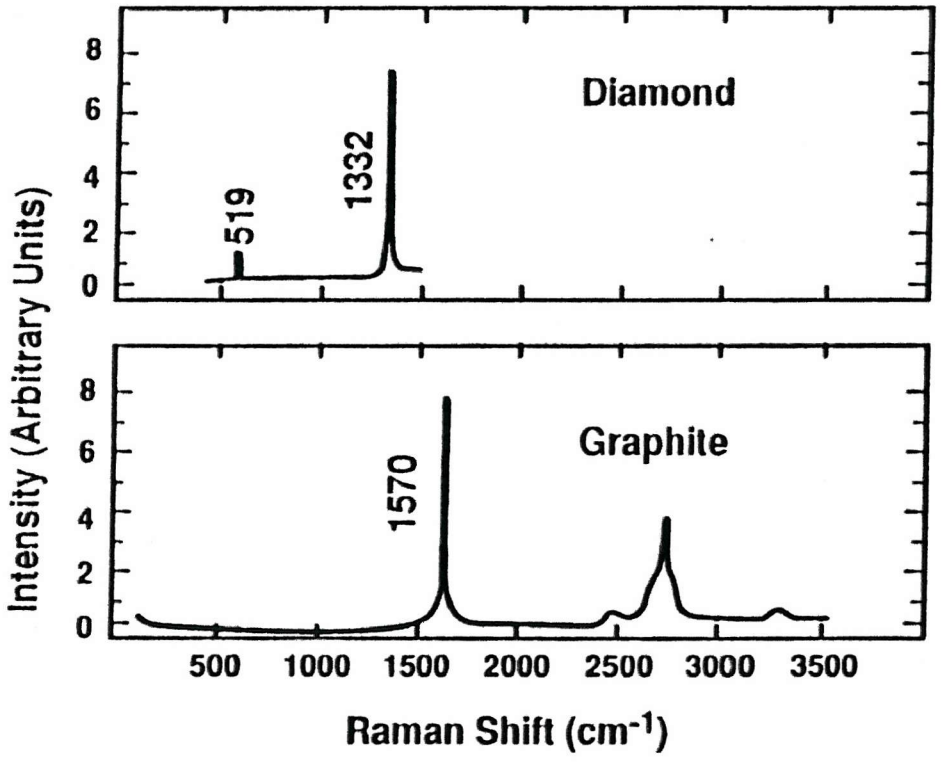

Fig. 3.7: Raman spectra of diamond and graphite [4].

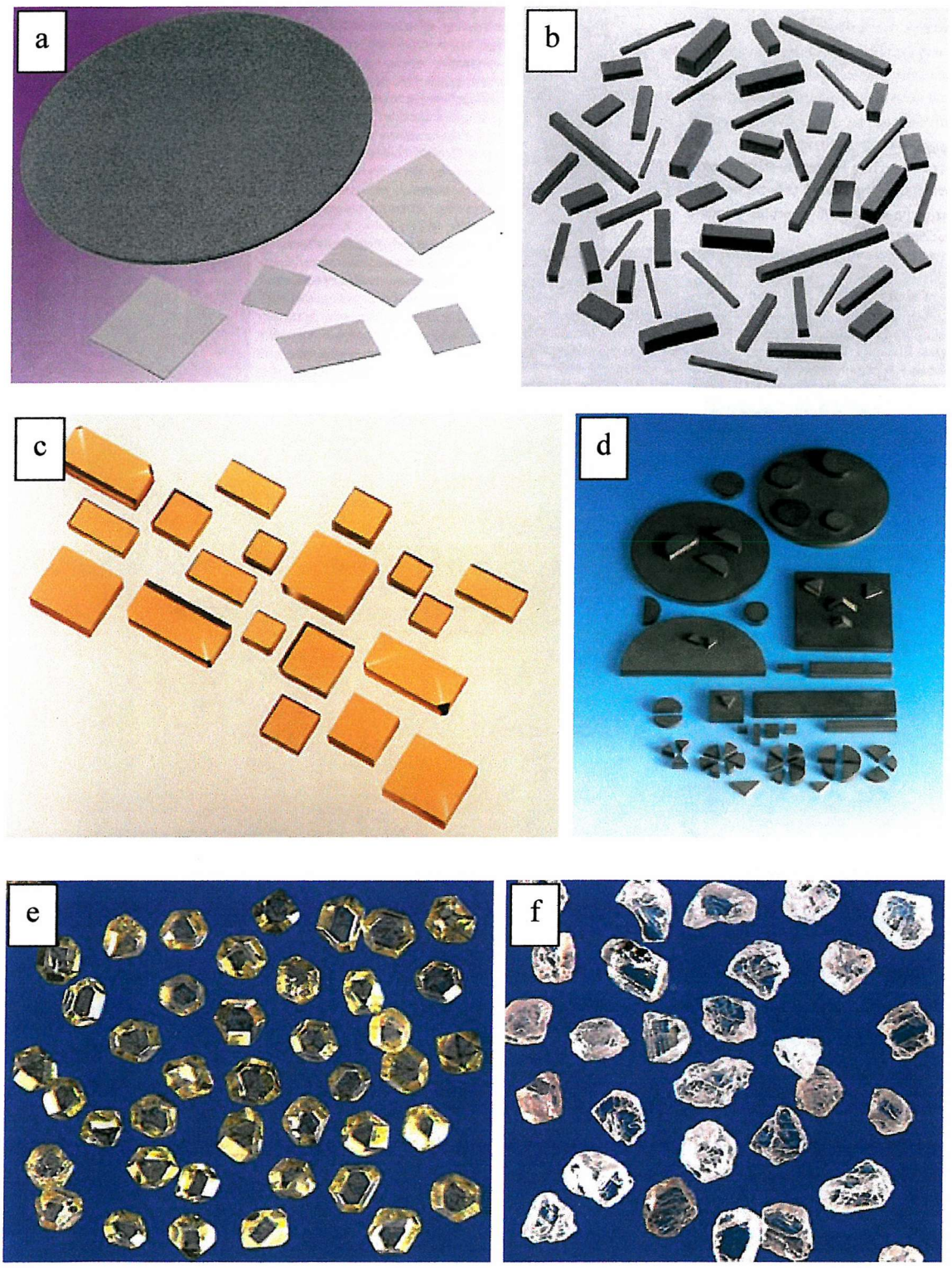

Fig. 3.8: Examples of different types of industrial diamond [40-42]: (a) CVD diamond wafers; (b) CVD diamond dressing logs; (c) synthetic single crystal diamond; (d) Polycrystalline Diamond (PCD); (e) PDA989 synthetic diamond grit; (f) PDA665 natural diamond grit. Reproduced with the permission of De Beers Industrial Diamonds (UK) Ltd.

4

EROSION AND MECHANICAL BEHAVIOUR OF DIAMOND

The high hardness and elastic modulus of diamond makes it a potentially attractive material in wear-related applications. Following on from the introduction to erosive wear in Chapter 2 this section will discuss erosion studies that have been carried out on diamond and other related materials and the damage features observed.

A number of workers have investigated the erosion behaviour of natural diamond and PCD as well as CVD diamond (CVDD). Due to their similarities with CVDD, erosion studies of both natural and polycrystalline diamond (PCD) will also be discussed in this section. Other investigations have examined the liquid droplet erosion of diamond. Though the current project will not be concerned with this type of erosion there may be similarities between erosion from liquid droplets and solid particles, notably the damage features created by the impact process and mechanisms by which they occur. For this reason, a section of this chapter will also be devoted to liquid impact studies of diamond. No instances of cavitation erosion of diamond have been found in the literature.

As has already been shown in Chapter 2, the properties of the target material that have the most important influence on its erosion performance are hardness, elastic modulus and fracture toughness. For this reason, mechanical properties of CVD diamond are also discussed in this chapter.

4.1 Solid Particle Erosion

A number of workers have investigated the solid particle erosion behaviour of diamond, looking at performance relative to other materials as well as the erosion mechanisms. These are summarised in Table 4.1, while the more significant papers are discussed in more detail below.

A general outline of the strength, fracture and erosion of CVD diamond has been given by Field *et al* [1]. Diamond is by far the most erosion resistant material compared to other ultra-hard materials. The extreme hardness of diamond means that even at high particle velocities there is no evidence of plasticity and the damage sustained is of a wholly brittle nature [2]. CVD diamond has been found to behave in a similar manner to natural diamond, the main difference being the manner in which the material is removed. In CVD diamond films, delamination of the coating from the substrate occurs whereas in natural diamond material is removed when ring or cone cracks intersect to separate small volumes of material from the bulk [1]. CVD diamond also differs in other respects from natural diamond. Like PCD, its polycrystalline nature means that some of its mechanical properties are less sensitive to crystallographic orientation. The presence of grain boundaries can be beneficial as they can, in some instances, arrest crack growth. However, the strength of CVD diamond is inferior to natural diamond due to the presence of microstructural flaws and residual stresses; it is this that prevents it from matching the latter in erosion resistance. The other main factor affecting the erosion behaviour is the properties of the bond between coating and substrate.

Hayward and Field [3] have examined the solid particle erosion of natural diamond. Using 300-600μm diameter sand at velocities between 26 and 75 m s^{-1}, they studied the erosion behaviour of two different crystallographic faces, {100} and {111}. Apart from some chipping at the edges of the specimen, the mass loss at 26 m s^{-1} was so low that it was below detectable limits.

Impact of the sand particles with the surface results in the formation of localised cracks along the {110} plane. Complete ring cracks are not produced because of the short duration of impact and the reluctance of the crack to fully deviate from the {110} to {100}. At 75 m s^{-1} cracks were seen after 2 minutes had elapsed; later further cracks formed, this time on the {111} and material was removed when intersection of cracks on the two planes took place. After 20 minutes, the material was extensively damaged.

Feng and Field [4] continued the work on natural diamond at higher velocities, up to a maximum of 200 m s^{-1}. At 140 m s^{-1}, ring and cone cracks were seen within 10 seconds. The sides of the cracks were parallel to the <110> direction, which are intersections of {111} cleavage planes with the {100} surfaces. The formation of ring

cracks took place at all velocities, though the erodent dose required to form them increased markedly at lower velocities. They were less complete at lower velocities.

To date, most work on the erosion of CVD diamond coatings has been carried out on coatings less than 20μm thick. Feng *et al* [5] subjected 6-15μm coatings on Si and Si_3N_4 to sand of velocities 34 and 59 m s^{-1} at an impact angle of 90°. The first stage of erosion is the formation of ring cracks by the generation of tensile stresses at the edge of the contact. This leads to partial debonding and penetration of the film. The propensity for ring crack formation on diamond is much greater at lower particle velocities due to the longer impact time. The reason for this is that at higher velocities there is an increased incidence of particle fragmentation on impact. The final stages of erosion are full debonding and complete removal of the film. It was found that transgranular fracture of the diamond film is common which suggests that bonding between diamond grains is as strong as that of the diamond grains themselves. The diameters of the ring cracks formed by impact were measured and compared with those produced in static tests, using a 0.39 mm diameter WC ball, in order to determine the fracture stress. The measured contact sizes were close to those predicted by Hertzian theory. It also predicted that the critical contact pressures for ring crack formation on CVD diamond were considerably less than those for natural diamond: approximately 3.2 GPa compared with 10-13.5 GPa. These correspond to tensile strengths of 1.4 GPa for CVD diamond and 4.3 - 6 GPa for natural diamond.

The choice of substrate on which the diamond is deposited also affects the erosion performance. Kral *et al* [8] deposited 10μm diamond films, using microwave plasma CVD, on Si, W and Ti-6Al-4V substrates. Compared to other investigations, the conditions were mild: 85μm alumina particles at 4 and 15 m s^{-1}, both 30° and 90° impact. While diamond conferred enhanced erosion resistance compared to the uncoated substrates, the critical factor governing the erosion performance was the coating-substrate interface. Diamond on Si was found to have the highest erosion resistance followed by W, while the lowest was found for diamond on the Ti substrate. The erosion mechanisms were also dependent on the choice of substrate. On Si and W, the diamond erodes by the accumulation of discrete chipping or cleavage of individual grains until complete penetration of the coating occurs (in the form of a circular hole),

usually at an area containing a high number of defects. The neighbouring regions close to the hole are progressively undermined leading to a steady increase in its diameter.

In contrast to the diamond coatings on Si, the diamond coating on Ti failed at the interface. The delaminated region nucleated at surface scratches that were created by pre-deposition treatment designed to enhance nucleation and improve coating adhesion. At 15 m s^{-1}, the diamond was completely removed by spalling within 10 seconds. Significantly, the substrate treatment and conditions used for deposition on Si and W had to be altered in order to improve the coating adhesion. The resultant coating was thinner and as a consequence, was less able to withstand the stresses generated by particle impact. It had a smaller grain size, thus the grain boundary density (and the flaw population) was higher. The coating may also have a higher graphite content. The result of all these changes was a weaker, and less erosion-resistant, film. Furthermore, the mismatch in thermal expansion coefficient between diamond and Ti is greater than that between diamond and Si or W. The result will be higher residual stresses in the diamond coating on Ti, which may contribute to its inferior erosion performance. In contrast, diamond coatings to the Si substrates may have benefited from better adhesion, partly due to the smaller mismatch in hardness and thermal expansion coefficient. The fact that diamond and silicon have similar crystal structures may also contribute to its better adhesion.

The slurry erosion performance of 15μm thick CVD diamond on SiC has been investigated by Wood [9] with a view to applying this coating system directly to use in offshore oil applications. In this work, no measurable mass loss was reported after it was subjected to a sand particle velocity of 31.5 m s^{-1} for 5 hours (making it over 200 times more resistant than 1mm thick polycrystalline diamond on sintered WC). CVD diamond coated SiC needle and seat choke valve trims also showed good erosion resistance when tested in the BP valve loop test rig in 1991. However, the low fracture toughness of SiC renders it unsuitable for applications where a high tolerance to shock loading and rough handling is required, for instance in offshore choke valves.

While no cases of erosion studies involving thicker CVD diamond coatings have been found to date, Field *et al* [10] have carried out some erosion tests of free-standing CVD diamond samples intended for use in diamond windows. These samples, 510-570μm

thick, were eroded at velocities of 21, 35 and 61 m s^{-1} and the infra-red transmission was analysed as a function of erosion time and velocity. Cracking of the samples was seen after approximately 50 seconds in all tests, though the damage at higher velocities was more pronounced. This damage caused a reduction in I.R. transmission, which was followed later by catastrophic failure. Other features observed included the presence of crack networks on the rear surface of the sample.

The influence of grain size on erosion rate of free-standing optical quality CVD diamond has been investigated by Telling and Field [11]. Using 300-600μm diameter sand at 100 m s^{-1} they found that lower erosion rates were observed on specimens having a larger grain size. The reason for this is the relationship between grain size and the Hertzian contact diameter, $2a_m$. When $2a_m < d_g$, the material response is closer to that seen in single crystal materials. The dependence on crystallographic orientation with diamond, mostly with regard to cleavage, is well known. When $2a_m > d_g$, there is a greater propensity for ring cracks. Statistically, there are more opportunities for cleavage. Furthermore, certain crystallographic orientations erode at a faster rate than others. Complete ring cracks were observed on {111}, while only incomplete ones were seen on {110}. In both cases $d_g > a_m$.

Other workers have eroded polycrystalline diamond (PCD) composites. As part of a wider programme of erosion studies involving a range of hard materials, Vaughan and Ball [12] used silica sand, SiC, Al_2O_3 and diamond grit at 40 m s^{-1} to examine the erosive wear mechanisms of PCD and Polycrystalline Cubic Boron Nitride (PCBN), among others. These two materials displayed negligible erosion rates; consequently, this led to difficulties in the determination of exact damage mechanisms. However, they came to the conclusion that both materials erode by removal of the softer binder phase followed by the loss of the hard skeletal material.

This view is supported by Feng and Field [4] who eroded the same materials with 300-600μm sand at velocities of up to 200 m s^{-1} for 5,000 seconds. PCD was found to have a lower erosion rate than PCBN, and at 140 m s^{-1} had an erosion resistance comparable to that of diamond. No indication of fracture of individual diamond grains was seen for PCD, though this feature was observed in PCBN. In another study, Kaye and Field [13] compared the erosion resistance of PCD, sintered WC and stainless steel at a velocity

of 250 m s^{-1}. The normalised erosion rates relative to PCD of the materials were 1, 160 and 19,500 respectively. The degree of sand degradation was a function of target hardness with the sand undergoing considerably more degradation on impact with PCD compared to WC, which itself caused more sand degradation than stainless steel. The PCD was found to erode by removal of the Co binder. In the early stages, the erosion is higher because the surface layer is rich in Co, making it less resistant to erosion. Below this surface region the microstructure is more homogeneous with an even distribution of diamond and binder. Once the erosion reaches this part of the material, the rate of material removal reduces and steady state erosion is established. No incidence of grain fracture was seen in the PCD. The small grain size (25μm) of the composite ensures the amount of diamond fracture is minimal. Grains are removed from the composite in one piece; however, the numbers involved in this were small.

To summarise, it is useful to consider the desirable properties sought in an erosion-resistant material and to compare these with the properties of diamond. Evans and Wilshaw [14] have stated that a material having good impact damage resistance will have the following attributes:

1. A target material that responds elastically as the damage in the elastic regime appears to be much less intense than that in the plastic regime. Less material is removed from the surface of the target material than is the case with elastic-plastic.
2. When the purely elastic response can be achieved, large fracture toughness and longitudinal wave velocity, and a small surface, or near-surface, flaw size are desirable.

Diamond fulfils both of the above criteria. No erosion studies of diamond have witnessed any suggestion of plastic deformation in the target material and damage is of a purely elastic nature. Diamond also has relatively high fracture toughness compared with other ceramics. Moreover, it has probably the highest wave velocity value of any material – a product of its high elastic modulus and low density. This enables any stress waves generated by the impact to be rapidly transmitted away from the impact site.

Regarding the surface, or near-surface flaw size, three-point bend tests of CVD diamond, various thicknesses, have shown that the flaws controlling fracture are located predominantly in the bulk of the material, rather than at the surface [15]. This

last characteristic will ensure that the cracking of the front surface, induced by the Rayleigh wave, is minimised. As will be seen in Section 4.7, diamond also has a relatively high Weibull modulus compared to many ceramics; this indicates that flaws are of a reasonably consistent size.

Though diamond is not used in ceramic armour, it is instructive to consider the properties required for this application as the impact processes are likely to be similar to those experienced by armour, though on a smaller scale. Previous sections of this document have discussed the propagation of shock waves through both the target and erodent following impact. The speed of the shock wave depends on the sonic velocity within each material. The greater the difference between the two values, the greater will be the ability of the target to induce fracture in the projectile [16]. This is because less energy from the waves is transmitted into the target at the point of impact and more of it is reflected back into the projectile from the interface, which will increase the likelihood of projectile fracture as a result. The Ballistic Figure of Merit, M, is used to assess the suitability of candidate materials for use as armour. It is defined as:

$$M = \frac{E_t H_t}{\rho_t} \tag{4.1}$$

where E_t is the elastic modulus, H_t the hardness and ρ_t the density of the target material. A high elastic modulus is desirable because it contributes to a high sonic velocity, which means that shock waves propagate quickly away from the impact zone. Also desirable is a high hardness, as it will increase the probability of the erodent suffering greater damage than the target. In contrast, the density should be low as possible, as this will also contribute to a high shock wave velocity. Though the weight is of no consequence for valves, in the case of armour a low density will also contribute to minimising the weight of the armour, essential if it is to be carried by either humans or on aircraft. It will also be beneficial in the case of windows and domes on aircraft or missiles, where erosion from rain and dust is a particular problem.

Ref.	Coating / Substrate	Rig Type	Surface R_a (μm)	Coating Thickness (μm)	Erodent (+ Average size (μm))	Velocities ($m\ s^{-1}$)	Impact Angle (°)	Particle Flux ($kg\ m^{-2}\ s^{-1}$)	Erodent KE (μJ)	Erosion Rate ($mg\ kg^{-1}$)	Test Time (mins)	Grain Size (μm)
3	Natural Diamond	Gas blast	Polished	N/A	Sand (450)	26 70 75	90	10.7 48.8 23.0	43 312 358	3×10^{-5}	50	N/A
4	Natural Diamond Syndite 025 Amborite	Gas blast	Polished	N/A	Sand (450)	20 34 75 140 200	90	10.5	25 74 358 1248 2546	Not known	83	25
5	CVDD/Si CVDD/Si_3N_4	Gas blast	1.0 0.008	6 15	Sand (450)	34 59	90	4.5	73 222	Not recorded	0.2-1.2	2-4
6	CVDD/WC	Centrifugal	Not known	1.5 3.0 6.0	Alumina (100-150)	46 72	45/90	Not recorded	31.6 77.3	Not recorded	Not known	Not known
7	CVDD/Ti	Gas blast	Not known	10-14	Alumina (90)	100	30 60 90	190	6.95	4 - 70	1.1	0.1-4.5
8	CVDD/Si CVDD/W CVDD/Ti	Gas blast	Not known	10	Alumina (85)	4 15	30/90	Not recorded	0.09 0.13	Not recorded	Not known	1-7
10	CVDD#	Gas blast	Polished	510-570	Sand (450)	21 35 61	90	10.5	28.1 78 237	Not measured	Not known	Not known
11	CVDD#	Gas blast	Polished	500	Sand (450)	100	90	Not known	636	0.29-4.0	Not known	30-280
13	Syndite 025 WC-6Co SS316	Gas blast	Polished	N/A	Sand (250)	250	90	20.7	682	PCD 0.088 ±0.003 WC: 14 ±2 SS: 1700 ±100	833	Not known
52	CVDD/Ge	Gas blast	Not known	7.0	Sand (20-40)	120 150	90	0.5	2.17 3.40	Not measured	Not known	Not known

Table 4.1: Previous erosion studies of diamond and related materials. Key: # = Free-standing CVD diamond

4.2 Liquid Droplet Erosion

CVD diamond is an attractive material for use in missile domes and for the leading edge areas in high speed aircraft. One of the requirements for materials to be used in these applications is a high resistance to rain erosion. A number of investigations have been carried out assessing the liquid impact behaviour of diamond and other IR-transmitting materials. The parameter used for quantifying the performance of samples subjected to liquid impact is the Damage Threshold Velocity (DTV). This has been defined as "the velocity below which the material remains undamaged regardless of the number of impacts" [2]. Table 4.2 lists typical DTV values of a range of infra-red transparent materials [17].

The nature of the damage produced by liquid impact was introduced in Chapter 2 and will not be repeated here. The damage features are more pronounced in thin free-standing samples and coatings, where most of the waves are reflected at the rear surface or, in the case of coatings, the coating-substrate interface. There are very few suitable substrate materials that can match the acoustic impedance of diamond. One of the few materials with an acoustic impedance close to diamond is gold; it, though, is not suitable for these applications. For diamond films <1 mm, the reflected tensile stresses can reflect at the interface and return to the impact zone while the high pressure phase of impact still existed and reinforce the tensile components of the stress field [18].

For thinner samples, tensile failure has been seen both at the rear surface and in the centre of the sample. This is also caused by stress wave interactions; release waves in the target propagate inwards from the jet edge and meet on the axis causing a net tension [19]. The features of damage described in this section are dependent on the geometry of the target. For instance, a 0.5mm thick sample impacted with droplets exhibited rear surface tensile failure, though this was not seen in a sample 2 mm thick. However, the latter showed no improvement in DTV compared to the former because it is difficult to maintain the same quality of the diamond with thicker samples.

The DTV of CVD diamond is considerably lower than natural diamond. Tests on type IIa natural diamond, using 0.8mm water droplets, were conducted over a range of velocities, beginning at 260 m s^{-1} [20]. After 10 impacts, and following microscopic examination, the velocity was increased in steps of 25 m s^{-1} up to a maximum of 530 m

s^{-1}. The sample was still intact at this velocity after 10 impacts but shattered after a further 160. This figure compares favourably with the value of 525 ±25 m s^{-1} obtained on a synthetic high temperature high pressure type Ia diamond [2]. However, this figure may be artificially low due to the small specimen size, which would result in stress wave reflections off the edges and reinforcing the damage induced by the impacts.

Material	Coating Thickness (μm)	DTV (m s^{-1})
Uncoated ZnS	N/A	130 ±10
Uncoated Ge	N/A	130 ±10
Uncoated Sapphire	N/A	425 ±25
Bulk ZnS-20% wt diamond composite	N/A	165 ±5
DLC on ZnS	2.0	120 ±10
GeC on ZnS	11.0	125 ±5
GaP on Ge	14.6	250 ±10
BP on Ge	16.2	250 ±10
CVD diamond on ZnS	Not stated	212 ±12
CVD diamond on Ge	Not stated	250-300
CVD diamond on Si	Not stated	325-370
CVD diamond on sapphire	Not stated	565 ±15

Table 4.2: Typical values of Damage Threshold Velocity for I.R transparent materials and coatings impacted by a 0.8mm liquid jet.

Liquid impact studies of CVD diamond have shown a steady improvement in performance over the last few years but the DTV of CVD diamond has yet to reach that of natural diamond. The highest figure recorded to date is 475 ±25 m s^{-1} for a sample 500μm thick [18]. However, as can be seen in Table 4.2, the most recent paper from the Cavendish Laboratory [17] on this subject quote a DTV of CVD diamond on sapphire of 565 ±15 m s^{-1}.

4.3 Hardness and Elastic Modulus

Both hardness and elastic modulus values in the literature for natural and CVD diamond vary over a wide range. Field [21] quotes the hardness of natural diamond to be 90GPa, though values of between 57 and 104 GPa have been recorded. The hardness of CVD diamond also falls within this range. Measuring the hardness of diamond is

difficult: the test involves impressing a diamond indenter into a diamond surface so the assumption that the indenter does not undergo significant deformation during the test is no longer valid.

Brookes [22] has investigated the effect of different crystallographic orientation on the hardness using a Knoop indenter. It was found that the values achieved varied from 56GPa on the {111} to 108GPa on the plane with the greatest hardness, the {110}. This is thought to be due to differences in critical resolved shear stress in different crystallographic directions. However, in polycrystalline CVD diamond grains of different orientation are present. In the present study, x-ray diffraction (see Chapter 6) has indicated that the grains are orientated predominantly in the (111) and (220) directions. Therefore, this dependence of hardness on orientation is less important than for single crystal diamond.

The greatest success has been achieved by using nanoindenters on diamond films. The test, which is similar to a microhardness test, involves loading a diamond indenter at extremely low loads, typically <300mN. The indenter is usually in the form of a three-sided pyramid known as a Berkovich indenter. The output of the results is in the form of a graph of load versus displacement, a typical example of which is shown in Figure 4.1. The extent of the area bounded by the loading and unloading curves indicates the degree of non-elastic deformation. In purely elastic materials the curves will be superimposed on top of each other. The procedure used in obtaining the hardness and elastic modulus has been described by McHargue [23]. One advantage of the nano-indenter over the micro-hardness indenter is that imaging of the indent is unnecessary. This is particularly beneficial in the study of ultra-hard materials where the indent may be extremely small, leading to difficulties in the accurate measurement of its dimensions.

Extreme care is required, both in the use of nano-indenters as well as in interpreting the results. It must also be recognised that degradation of the indenter, by blunting and/or fracture, occurs over a period of time. Another point to remember is that the total depth of indentation must not exceed approximately 10% of the coating thickness for these measurements to be free of any substrate influence. This is to ensure that the stress field

beneath the indenter is contained within the coating and does not extend into the substrate.

Nano-indentation has been used to study a wide range of thin films ranging from ion implanted surfaces to diamond coatings. In studies of CVD diamond McHargue [24] compared the indentation behaviour of polished CVD Diamond coatings on silicon with that of natural (type IIa) diamond. Unfortunately, the thickness of the coatings is not given. Using loads of up to 120mN, no significant differences were found in the performance of the samples, with the elastic modulus being within the realm of statistical scatter. However, the unloading part of the load-displacement graph did not follow the same path as the loading curve, indicating the presence of some non-elastic deformation. This is in contrast to natural diamond, which gave a totally elastic response during the test. It was thought that the cause of the apparent plasticity could be attributed to grain boundary sliding. While plastic deformation of the diamond is unlikely at room temperature, grain boundary sliding is possible if the technique used to deposit the diamond film has led to the formation of graphite at the grain boundaries.

Nicholson *et al* [25] performed nano-indentations on CVD diamond films and compared the values of elastic modulae with those obtained by the bulge and vibrating reed tests. Close agreement was seen between nano-indentation and bulge test, where the average values were 1074 GPa and 1036 GPa respectively. The values obtained from the vibrating reed test resulted in consistently lower values, being typically 75% of the values from the other two methods. In the case of the indentation results, it was thought that the true value of the elastic modulus may be lower than the values obtained via this method. The most likely causes of this discrepancy were thought to be (i) errors introduced by degradation of the indenter and (ii) the presence of a hydrostatic stress in the region under the contact zone which will result in an inflated elastic modulus. Furthermore, there are differences in the stress state induced by each method. Nano-indentation produces a triaxial modulus while biaxial and uniaxial modulae are produced by the bulge and vibrating reed tests respectively. For this reason, the method by which the elastic modulus was obtained must be quoted along with the actual value.

4.4 Fracture Toughness

The use of indentation to measure the fracture toughness of brittle materials is well established. The technique consists of loading an indenter, usually a Vickers pyramid, into the surface of a brittle material. Cracks are formed by the indentation and propagate from the corners of the indenter. The lengths of these cracks are used to calculate the fracture toughness, K_{Ic}, with the longer the cracks the lower toughness of the material. A schematic diagram showing typical crack morphology is shown in Figure 4.2. The indentation method has proved a useful means of calculating the toughness of brittle materials, in particular ceramics.

A number of models have been developed to enable the fracture toughness to be calculated from indentation techniques. Ponton and Rawlings [29,30] have reviewed the most prominent ones. The difficulties outlined in the previous section in carrying out indentation studies of diamond apply equally for the determination of fracture toughness. Moreover, a large degree of scatter in the results of K_{Ic} is often seen. This is due in part to the grain size and the probability of a crack finding a favourable crystallographic direction on which to propagate.

Drory *et al* [31] have used a Vickers indentation method to obtain values of fracture toughness of free-standing CVD diamond films approximately 400μm thick. The films were polished to an average peak to valley surface roughness of 40nm. Loads between 5 and 8N were used to reduce the possibility of indenter damage. The following equation was used to calculate the fracture toughness:

$$K_c = \xi\left(\frac{E_1}{H}\right)^{1/2}\left(\frac{P_{ind}}{c_{cr}^{3/2}}\right) \tag{4.2}$$

Where ξ = 0.016 ±0.004 (empirically determined), c_{cr} is the crack length and P_{ind} the applied load. This equation has been used in all the indentation-based fracture toughness studies of diamond described in the literature. A mean fracture toughness of 5.3 MPa$\sqrt{m}$ was obtained, though the authors also noted considerable scatter, partly due to measuring the exact lengths of the cracks emanating from the corners of the indents. Fractures having greater roughness can increase the value of K_{Ic}. The K_{Ic} of 5.3 MPa$\sqrt{m}$ compares with a value of 3.4 MPa$\sqrt{m}$ for natural diamond; however, part of

this could be due to grain boundaries. This could be overcome by using large enough loads to propagate cracks longer than the average grain size. However, for diamond, the load required to do so exceeds the fracture strength of the indenter. Considerable scatter was also seen in the hardness values. The average, 80.6 GPa, compares well with other recorded values [27] though the overall range was from 57.5 to 108 GPa, in line with values obtained by other workers.

Ref.	Thickness (μm)	Substrate	Indenter	Load (N)	H (GPa)	E (GPa)	K_{1c} (MPa√m)
32	300	None	Vickers	35	100	Not recorded	6.0
31	400	None	Vickers	5-8	81 ±17	Not recorded	5.3 ±1.6
27	3	Si	Berkovich	67-100 mN	80-100	500-533	Not recorded
26	0.25-7.5	Si	Knoop	3	55-112	Not recorded	Not recorded
25	5.8-11.0	Si	Berkovich	Not recorded	52.5-83.1	830-1240	Not recorded
28	5.8-11.0	Si	Berkovich	7.5×10^{-3}	52.5-83.1	830-1240	Not recorded
34	N/A	N/A	Vickers	0.5-10	114-257	Not recorded	4.5-8.7
35	90	None	Vickers	5	75	Not recorded	Not recorded
36	100-300	None	Vickers	4-7	Not recorded	Not recorded	4.8-5.5

Table 4.3: Summary of other indentation studies of diamond to determine hardness, elastic modulus and fracture toughness. With the exception of reference [34], which was on the (001) surface of a synthetic diamond, all other studies listed were conducted on CVD diamond.

Sussmann *et al* [32] describe fracture toughness measurements of a 300μm thick diamond film using a Vickers diamond pyramid indenter. Using a load of 3.5kg they calculated the fracture toughness, also using equation (4.2), to be 6.0 MPa√m. This value is higher than natural diamond (3.4-5.0) but grain boundaries could be

responsible as they are thought to impede crack propagation. In view of the comments made by Drory *et al* regarding the effect of load on indenter degradation [31], the authors do not record any details about the condition of the indenter after the test.

An alternative method of determining fracture toughness has been described by Telling and Field [33] who developed a double torsion apparatus to produce a stable crack, which could be incrementally extended to determine the mode I stress intensity factor. The mean value of 8.7 MPa$\sqrt{m}$ is notably higher than values obtained from indentation techniques. The cause of this discrepancy was attributed to the greater "true" fracture surface area associated with this test. Grain boundaries were not seen to represent an easy path of crack propagation. It is interesting to note that a notch was ion-milled into the sample using Ga ions to initiate crack propagation; however, during the test, the crack did not initiate from this location.

4.5 Strength of CVD diamond

The determination of tensile strength of CVD diamond is beyond the scope of this project. However, it is instructive to consider the variation in tensile strength observed in various CVD diamond specimens and the factors that influence the tensile strength. This section will consider the strengths recorded on CVD diamond samples. In order to eliminate any confusion, all CVD diamond samples described in this section, unless otherwise stated, were free-standing, and not in the form of a coating.

The fracture stress of a type IIa single crystal natural diamond (thickness 0.178mm), measured by cantilever beam geometry, has been recorded at 2.4 GPa [15]. In indentation studies, using a 0.39mm diameter WC sphere, Field [21] recorded a mean value of 3.75 GPa. This figure corresponds to good quality diamonds having sharp-ended defects of approximately 0.5μm in length. However, the strength of CVD diamond is less than half this figure. Sussmann *et al* [32] conducted pressure burst tests of CVD diamond discs 14 and 24mm diameter and 179-300μm in thickness. The results showed that the fracture stress values were in the range 746-1138 MPa with a general trend of thinner samples requiring higher burst pressures. In another pressure burst study of CVD diamond, Olsen *et al* [37] recorded fracture stresses of between 230 and 410 MPa for 6.35mm diameter diamond discs 254μm in thickness. This is considerably lower than the values recorded in the previous study [32]; the lower

quality of the diamond film is thought to be the most likely explanation for the discrepancy. The multiplicity of variables involved in the growth of diamond films makes the direct comparison of CVD diamond samples grown in different laboratories problematic.

Savage *et al* [38] showed that the strength of CVD diamond, as measured in the three-point bend test was determined by two factors: grain size and thickness. In general, a straight-line relationship is observed between fracture stress and (grain size)$^{-0.5}$. However, this relationship breaks down at small grain sizes (≤8μm). The point at which this occurs is thought to be when the dominance of grain size is superseded by other factors. As an example of the influence of grain size on fracture stress, tests on samples 250μm thick recorded a fracture stress of 668MPa (grain size 200μm) and 769MPa (grain size 100μm). Table 4.4 summarises results from the most significant investigations undertaken on CVD diamond.

Ref.	Type of test	Thickness (μm)	Fracture stress (MPa)
32	Pressure burst	179-300	746-1138
36	Three point bend	400-1400	390-470*
36	Three point bend	400-1400	770-1000**
5	Indentation	15	1400^{+}
39	Ball-on-ring	174-399	650-971

Table 4.4: Summary of Strength tests of CVD diamond. Note: * = Growth surface in tension; ** = Nucleation surface in tension; + = Diamond film on Si_3N_4 substrate.

Field and Pickles [40] have pointed out the importance of quoting the test geometry along with the strength of CVD diamond. The reason for this is that much broader range of flaw sizes can be activated when large volumes are stressed, as is the case with the burst test. As a consequence, lower strengths are often recorded when using this test method compared to tests that stress smaller volumes, such as the indentation test.

It can therefore be seen that wide variations are seen in the strength of CVD diamond. Moreover, all the values recorded fall far short of those values obtained from high quality natural diamond. The main reason for this is the microstructure of CVD diamond, which contains significantly higher levels of defects, as well as those defects

being larger in size. The next section will explore the nature of those defects and the role they play in the deformation of CVD diamond.

4.6 The nature of microstructural defects

While diamond is not normally regarded as a ceramic it has many characteristics that enable it to be placed in the same category, notably its non-metallic, inorganic nature. One characteristic of ceramics is that they often have low values of fracture toughness and behave in a brittle manner. This is a consequence of the covalent / ionic bonding and when fracture occurs it is often sudden and catastrophic.

An important question that needs to be considered in this project is "What causes brittle materials to fracture?" Fracture initiates at flaws present in the material. These flaws can be in many forms. They include intrinsic microstructural defects (inclusions, porosity, weak grain boundaries) or extrinsic features generated by surface finishing or service environments (scratches, pits, cracks etc.). Whatever their origin, these flaws can act as stress concentrators. Ceramics are unable to deform plastically under most conditions and thus cannot relieve these stress concentrations. For a brittle material, the Griffith equation is applicable:

$$\sigma \propto \frac{K_{1c}}{\sqrt{a_f}} \tag{4.3}$$

The equation shows that the measured strength, σ, of a material is a function of its critical stress intensity factor, K_{Ic}, and the flaw size a_f. Larger flaws result in a lower strength. However, it is also necessary to know the flaw population and where in the material these flaws are located. Some brittle materials, for instance certain glasses, have a high density of flaws at the surface, caused by environment (for instance ageing) and scratches. The effect on the materials of their presence is to render them susceptible to surface failure from Rayleigh waves following impact from liquid or some solid particles. Of the three waves generated by the impact event Rayleigh waves have the least attenuation and the greatest energy. Moreover, they are concentrated at the specimen surface where they can exploit the largest flaws in a typical brittle target [41]. The exact depth of penetration of the Rayleigh waves is dependent on the impact duration. Bowden and Field [41] found that glass etched with a 10% HF solution exhibited a much lower density of surface cracks compared to unetched owing to the removal, by the etching process, of the largest surface flaws. Etched glass also

exhibited an order of magnitude improvement in strength compared to glass that was unetched. The purpose of this section is to consider the nature of microstructural flaws that are present in diamond and their influence on the mechanical behaviour.

In CVD diamond there are several types of flaws, which have potentially serious implications for the integrity of the material. The most prominent of these flaws are (i) crystal cleavage planes; (ii) twins; (iii) grain boundaries; (iv) micro-fractures.

In single crystal diamond the most prominent defect is the tendency for easy cleavage on the {111} crystallographic plane. This has been exploited in a positive way for centuries to create gems of great beauty, to sub-divide large diamonds into smaller pieces and to remove regions containing large flaws. In this way the aesthetic appearance of the gem can be enhanced. However, the cleavage of single crystal diamonds represents a serious weakness in mechanical applications. Although the polycrystalline nature of CVD diamond means that the importance of the cleavage planes is slightly diminished, it is still significant.

Ramaseshan [42] explained this preference for cleavage on the {111} plane by calculating the strain energy to failure in each direction by multiplying the number of bonds cut per unit area with the energy of one C-C bond. This gave a ratio of 1.73:1.22:1 for the {100}, {110} and {111} planes respectively. However, this difference is not sufficient to adequately explain the dominance of the {111} plane. Telling *et al* [43] have offered an alternative explanation. They determined the stress and energy as a function of applied strain in perfect diamond in the three low index crystallographic directions [111], [110] and [100]. The maximum strengths are 90, 130 and 225 GPa respectively. These corresponded to the point of inflexion on the respective total energy curve. By equating the cleavage surface energy with the strain energy to failure for each direction, this gave the ratio of energies for fracture as 7:2.8:1 on the {100}, {110} and {111} planes respectively. In fracture experiments using the double torsion apparatus, Kennedy *et al* [44] observed that the crystal cleavage planes were seen to noticeably change the course of the crack. The path taken by the crack was to "zig-zag" through the material.

Twinning is a common feature in the microstructure of CVD diamond, which produces crystals with apparent five-fold symmetry axes and the frequent appearance of interpenetrating crystals. TEM examination of CVD material has shown twinning to be most prevalent in the (111) growth zones, and least in the (100) zone [45]. Williams *et al* [46] also used TEM to image microstructural defects in CVD diamond films. They observed high levels of twins, stacking faults and dislocations.

Grain boundaries are also a potential source of weakness in CVD diamond. However, a fracture study by Kennedy *et al* [44] has shown no preference for either inter-granular or trans-granular crack propagation, which suggests that the influence of grain boundaries is minimal. This has been seen in other, similar, studies [5,47].

Micro-fractures are likely to represent one of the more serious threats to the integrity of the diamond. In the previous section, it was shown that the tensile strength of CVD diamond is considerably lower than that of natural diamond. The principal reason for this discrepancy is the presence and size of the flaws in the microstructure.

Using three-point bend tests of as-grown and lapped CVD diamond, Pickles *et al* [15] found little difference in fracture stress for samples of similar grain size. This is significant as it suggests that CVD diamond does not have many large surface flaws. Therefore, bulk flaws are likely to be the governing factor affecting the strength of CVD diamond. The next section will consider the nature, location and size of these flaws.

Pickles *et al* [15] also found that the bulk flaws, in the form of micro-fractures, were of similar size to individual grains; this was irrespective of the grade of CVD diamond (i.e. mechanical (black) or optical (transparent) diamond). They suggested a number of origins for these fractures: (i) non-diamond carbon; (ii) grain boundaries; (iii) defective growth. The most likely explanation was thought to be defective growth, which leads to variations in the defect density in adjacent growth sectors [33]. This creates highly localised micro-stresses leading to fracture zones of a size close to that of the grain. Large variations in stress across individual grains are often seen with one area of a grain in tension while an adjacent area is in compression. However, in some cases this

variation in residual stress can be beneficial, as cracks propagating through a tensile region will often become arrested when they reach a compressive region.

Telling and Field [33] have studied the microstructure of free-standing optical diamond in order to identify defects. They found that cracks were visible throughout the material. The cracks were comparable in size to that of the grain, though they were not always this size. They were often seen to originate within twins, which are thought to act as initiation sites for cracking, owing to mis-matches in crystal orientation.
The fracture stresses, described in the previous section, can be used to calculate the critical flaw size. This has been done using the following equation:

$$\sigma = m\left(\frac{E\gamma}{c}\right)^{1/2} \tag{4.4}$$

Where σ is the fracture stress, m is a modifying factor approximately 1, γ the fracture surface energy (5.3 J m^{-2} for diamond) and E the elastic modulus. The last parameter in the expression, c, is a measure of the perfection of the crystal: in a perfect crystal c would be the nearest neighbour distance (0.154nm for diamond) and m would be 1. However, when defects are present, this becomes the crack length. Using this expression Olsen *et al* [37] used the range of burst pressures of 230-410 MPa to obtain crack lengths of between 105 and 33μm respectively.

Most of the diamond samples described in this section have been free-standing samples rather than coatings. For coatings, it is often the interface between the coating and the substrate that is more critical to the performance of the coating. Work by the present author has shown that significant amounts of porosity are often present in the diamond at the grain boundaries close to the interface. The average size of this porosity is approximately 9μm, with pore sizes between 3 and 18μm observed. Therefore, this porosity is likely to present a much more serious threat to coating integrity than cracks present within the coating, though the latter cannot be ignored. These pores act as nucleation sites for coating debonding.

The previous section showed that thinner diamond coatings usually possess higher tensile strengths. However, we have also seen that the interface between the coating and substrate is critical and it is this that has a greater influence on the life of the

coating. From a purely intuitive standpoint, the tensile strength of the growth surface of the diamond coatings considered in this project is thought to be in the region of 800MPa. Furthermore, the presence of a compressive residual stress ~0.9GPa in coatings ≥60μm will further inhibit the formation of tensile cracks in the coating surface for well-bonded coatings.

The stresses associated with impact are more likely to exceed the fracture stress of the silica sand particles than that of the diamond. Thus the tensile stresses generated by the particle impacts are likely to be considerably lower than those predicted by Hertz. This is another reason why, as Chapter 9 will show, Hertzian ring cracks are not seen in some cases.

4.7 The statistical nature of strength

Another consequence of the brittle nature of ceramics is that the critical flaw size that causes failure is not constant over a batch of specimens or components. For this reason ceramics show a range of strengths rather than a unique strength. The statistical nature of strength in ceramics is analysed using Weibull statistics.

Weibull statistics define a probability of survival, P_s, at a given stress, σ:

$$P_s = \exp\left\{\left(\frac{\sigma}{\sigma_o}\right)^m\right\} \tag{4.5}$$

Where σ_o is the characteristic strength; when $\sigma = \sigma_o$, $P_s(V_o) = 1/e \approx 0.37$. The Weibull modulus, m, is a measure of the degree of scatter in the strength value. The higher the value of m, the narrower the distribution, i.e. the smaller the scatter in the measured fracture stress. Most metals have values in the range 50-100. In contrast, ceramics having Weibull modulae greater than 20 are rare with most having modulae considerably lower.

Strength is also volume dependent. At a constant stress, the P_s decreases as the volume increases, as the probability of a critical flaw being present increases. This is significant in erosion as brittle materials (e.g. ceramics) having larger grain sizes generally exhibit higher erosion rates.

$$\left(\frac{V_1}{V_2}\right)=\left(\frac{\sigma_2}{\sigma_1}\right)^m \tag{4.6}$$

When comparing the Weibull modulae of various hard materials it is found that CVD diamond has a Weibull modulus that is higher than most ceramics. Table 4.5 lists the values of diamond coatings along with a number of ceramics. It has also been found that the critical flaws in diamond lie in the bulk of the material rather than at the surface [15]. The benefit of this is that diamond is less vulnerable to surface flaws being opened up by Rayleigh surface waves generated by impacts.

Material	Weibull Modulus (Dimensionless)	Fracture Toughness (MPa√m)
CVD Diamond Growth surface (tension)	15.6 ±1.8 [48]	6.0 [32]
CVD Diamond Nucleation surface	17.5 ±2.5 [48]	6.0 [32]
Natural Type IIa Diamond	2 [51]	3.4-5.0 [21]
Sapphire	5 [51]	2.0 [49]
CVD SiC	11.5 [51]	3.3 [51]
Sintered α-SiC	10 [50]	4.6 [50]
Sintered B_4C	5 [50]	2.5 [50]
Sialon	15 [50]	6.0–8.0 [50]
Alumina	10.4 [50]	3.8 [50]
ZTA (Zirconia toughened Alumina)	9.0 [50]	6.5 [50]

Table 4.5: Typical Weibull modulae of CVD diamond and other ceramics.

4.8 Conclusions

This chapter has examined the erosion studies reported in the literature to date in order to provide a context for the work described in this thesis. It has been shown that the mechanical properties of CVD diamond (hardness, strength etc) enable it to exhibit much greater erosion resistance than other hard materials, for instance tungsten carbide. The chapter has also examined the nature of the microstructural defects in present in CVD diamond. Of particular interest is the influence they have on both the mechanical and erosion behaviour.

To date, apart from studies of free-standing diamond films >500μm thick [10,11], no erosion studies of diamond coatings greater than approximately 20μm have been

reported in the literature. However, in some applications, thicker coatings are required in order to contain the applied stresses from erosion and protect the interface. Therefore, it is necessary to determine the erosion behaviour of CVD diamond coatings, >20μm in thickness, as well as the degradation mechanisms they exhibit when subject to various mechanisms of wear.

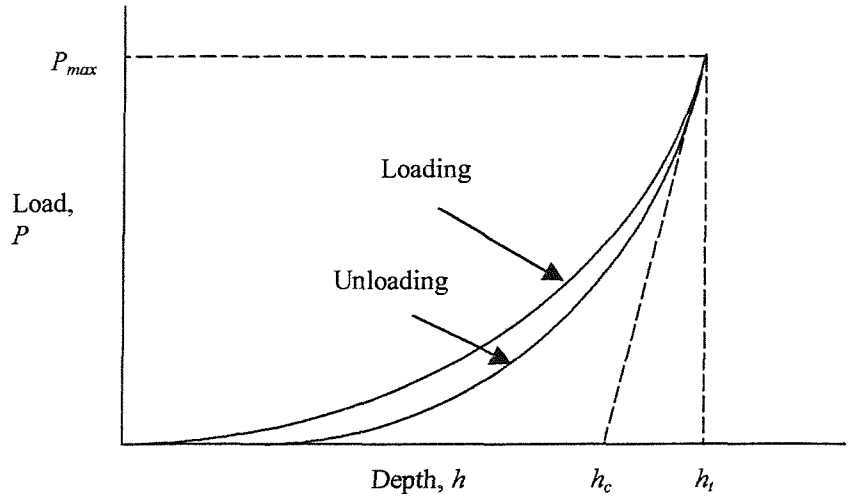

Fig. 4.1: Typical curve of load as a function of indenter penetration depth.
Key: P_{max} = maximum load; h_c = Indentation contact depth; h_t = Indentation depth at maximum load

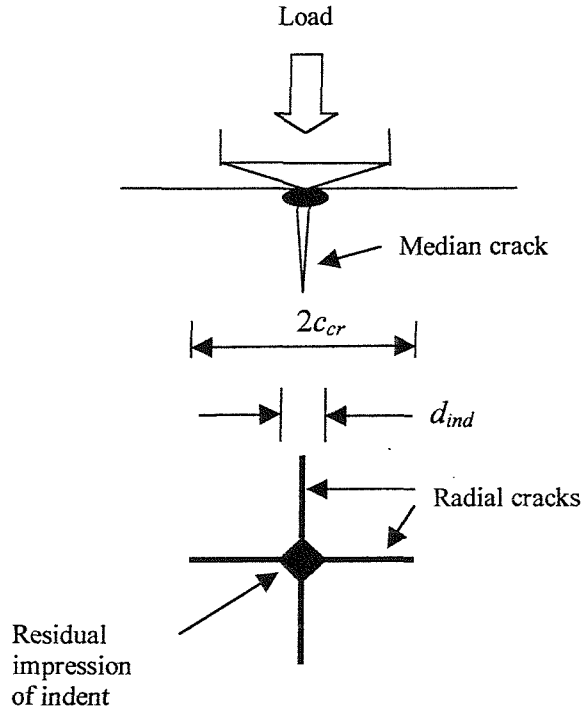

Fig. 4.2: Typical damage features caused by indentation of a brittle material with a Vickers pyramid indenter. The average length of the cracks propagating from the corners of the indentation impression, c_{cr}, is used to calculate the fracture toughness of the material.

5

EXPERIMENTAL DETAILS

5.1 Materials Tested

The coatings used in the present study were supplied by De Beers Industrial Diamonds (UK) Ltd. It is thought that they were produced by microwave plasma CVD; however, as the details of the deposition process are not available in the public domain, they were not disclosed to the author. The diamond was mechanical grade "black" diamond, and was, therefore, not transparent. All coatings were deposited on tungsten and tungsten carbide-6 wt % cobalt substrates. The coatings were supplied in both the "as-grown" condition and lapped, to a surface roughness (R_a) of 0.2μm. The thickness range of the diamond films were between 10 μm and 250μm. The coating samples were 50mm diameter and 6mm thick and were tested in the as-received condition.

In addition to this, a number of other materials were also tested under the same conditions for the purposes of comparison. Both the diamond coatings and the reference materials are listed in Table 5.1.

Material	Hardness (H_v)	Surface R_a (μm)	Mean grain size (μm)	Thickness (μm)
CVDD on W	8000	0.2-4.3	10-120	10-200
CVDD on WC-6Co	8000	5.2-6.9	60-80	87-195
Stainless Steel 316	220	0.05	Not known	6000*
WC-7 wt %Ni	1600	0.20	1.5	6000*
WC-6 wt %Co	1540	0.20	1.3	6000*
PCD on WC	5000	0.05	10	1000

Table 5.1: Materials tested as part of the study. Key: * = Bulk material.

5.2 Surface Microstructure

The surface roughness is known to affect the erosion resistance of a coating. For this reason, the R_a of all coatings was measured prior to testing. The measurements were

made using a Rank Taylor Hobson Form Talysurf profilometer. This instrument features a diamond stylus, with 2μm tip radius, which is drawn across the surface of the sample. The profilometer is highly accurate, having a vertical resolution of 10nm. All the major parameters, which are used to quantify the surface roughness (R_a, R_p, R_q, R_{sk}, R_{ku}, S etc.), can be calculated and the whole process is controlled from a PC.

5.3 Raman Spectroscopy

The use of Raman spectroscopy in determining the nature of the diamond coating, for instance differentiating between diamond, graphite and amorphous carbon, has already been introduced in Chapter 3. Raman spectroscopy was performed on the diamond films using a Renishaw Raman microscope equipped with a 100 mW Ar ion laser with a slit width of 50μm ≡ 4cm^{-1} resolution. This enables characterisation of the coatings to be undertaken, while minimising the influence on the spectra of the substrate. The depth of analysis is approximately 10μm, so the sampling volume is contained within the coating for all but the very thinnest coatings.

5.4 X-Ray Diffraction

X-Ray Diffraction was conducted on a small number of samples to identify the predominant crystallographic orientations in the film. A Phillips diffractometer was used in this work and the incident angle of the x-rays was 3° to minimise the influence of the substrate on the spectra. CuKα was used as the source and the voltage and current selected were 40 kV and 50 mA respectively.

5.5 Indentation Studies

A CSEM NHT nano indenter was used to obtain values of the hardness and elastic modulus. The indenter was of the Berkovich design and the maximum load was 300 mN; the resolution of the force was 10 μN. The apparatus was also equipped with depth-sensing capability, which could measure the depth of indentation to a resolution of 1 nm. The indentations were made on the sample and loading-unloading curves produced for each, which were used to calculate the hardness and elastic modulus.

5.6 Microscopy

The coatings were examined both pre- and post-test using a Jeol JFM6400 scanning electron microscope (SEM). They were also examined using an Olympus optical microscope. This enable the grain size to be measured for the different thickness of coating as this was thought to influence the erosion behaviour of the coatings. For SEM examination the dielectric character of the diamond necessitated the coating of the samples with a thin (20 nm) layer of gold in order to make it electrically conducting. The gold coating was deposited using an Anatech sputter coater.

5.7 Air-Sand Erosion Tests

The erosion testing was performed using an air-sand erosion rig. Full details of this equipment can be found in [1]. Nevertheless, it is instructive to summarise the main features of this rig in the present document.

A schematic diagram of the main constituents of the rig can be seen in Figure 5.1 and a photograph is shown in Figure 5.2. The rig specification is also listed in Table 5.2. The air is supplied by a 30 kW rotary screw compressor, capable of a maximum output of 380 m^3 hr^{-1} at a pressure of 7 bar g, and then fed through a two-column desiccant dryer. This lowers the dew point to –70 °C. After passing through a receiver, a flow regulator and a flow meter, sand is injected into the air-stream in a sand injection chamber. The sand injector is fed by means of a vibratory feeder and hopper arrangement. The vibratory feeder supplies the sand into a split funnel, the position of which can be altered relative to the position of the feeder, to control the amount of injected sand. This air-sand mixture is subsequently accelerated down a type 316 stainless steel tube, 16mm diameter and 1 metre in length, before entering an enclosed erosion chamber where it strikes the test specimen before leaving the chamber. The rig was designed with aid of Computational Fluid Dynamics (CFD), which provided information on the optimum nozzle / bore diameters and particle acceleration length required. Within the erosion chamber, the impact angle between the particles and the sample can be varied from 90° to 20°. The nozzle to sample stand-off distance can also be varied, the range being between 20 and 100 mm. The test sample is held in place by means of a vacuum pump. The sand is not recycled and large particles collect in the base of the erosion

chamber whilst smaller particles are collected in a baffled chamber further downstream.

The air flow rate can be varied between 40 and 380 m^3 hr^{-1} whilst the sand injection system has a turn down ratio of 100:1 enabling feed rates of between 1 and 100 g min^{-1} to be selected. This corresponds to flux rates of 0.05 and 8.0 kg m^{-2} s^{-1} respectively. In the present tests, a blend of 3 commercially available grades of quartz silica sands supplied by Hepworth Minerals and Chemicals Ltd., Redhill, was used. The blend, a mixture of Redhill 50, 65 and 110 grades, was used to reproduce the size distribution found in the North Sea Forties oil field. The morphology of the sand varied from angular to sub-angular and the broad size distribution was in the range of 90 to 355μm; the average diameter was 194μm. The size distribution of the sand blend was obtained by sieving a sample in accordance with BS410. The resultant distribution is shown in Figure 5.3; more details of the sand used can be found in Chapter 9.

Particle size	Up to 1 mm
Particle type	Sand, SiC, Al_2O_3, and diamond grit
Impact Angles	20-90°
Particle speed (m s^{-1})	10 – 400
Particle flux (kg m^{-2} s^{-1})	0.05-8.0
Test duration	1s upwards
Maximum dose (kg)	225
Specimen size (mm)	50-200mm diameter or square 5-15mm thick, <200g in weight
Acceleration tube bore (mm)	16
Acceleration tube length (m)	1.0
Acceleration tube internal roughness (R_a) (μm)	1-2
Aspect ratio	62.5
Test temperature (°C)	10-20
Noise levels (dBA)	<70
Propelling gas	Dry compressed air (dew point –70°C) from continuous supply from compressor
Specimen mass measurement	Weighing on precision balance (±0.02mg) pre- and post-test

Table 5.2: Specification for the air-sand erosion rig

The rig was calibrated using a high-speed Imacon 790 image converter camera, which is capable of operating between 1 x 10^4 and 2 x 10^6 frames s^{-1}. At a range of flow rates from 0 to 380 $m^3 hr^{-1}$ the camera was triggered with the aim of capturing sand grains in flight. Photographs of captured particles were scanned into a Hamamatsu Argus-20 image analyser and enhanced to obtain particle velocities. The particles were tracked from frame to frame and the distance travelled measured in order to calculate the particle velocities. The particle size was also measured and the velocities were grouped according to size. This is because, owing to the large size distribution in the sand used, the smaller particles will be travelling faster than the larger particles. Using these data a graph of particle velocity against air mass flow rate was produced, an example of which is shown in Figure 5.4.

In the erosion tests described in Chapter 8, four particle velocities were employed: 33, 63, 148 and 268 m s^{-1} with a sand flux of 0.5 kg m^{-2} s^{-1}, corresponding to a feed rate of 6 g min^{-1}. This flux rate is below the level at which particle-particle interactions begin to significantly reduce the erosion rate [2]. The stand-off distance, from the end of the nozzle to the surface of the sample, was 30mm ±1mm. The angle of incidence of the particles with the surface was 90° ±2° as the maximum erosion rate of brittle materials occurs at this angle. The tests were periodically interrupted in order to weigh the samples to evaluate the cumulative mass loss against time. This information assists the determination of the time required for steady state erosion conditions to be determined. Coatings up to and including 120μm were tested to failure at 268 m s^{-1}. The steady state erosion rates were also calculated; their values are independent of any incubation effects associated with the initial stages of the erosion process.

The samples were weighed using a Mettler AT201 precision balance with an accuracy of ±0.01mg. In order to reduce errors in measuring the mass, all samples were cleaned in an ultrasonic bath and dried in air before and after the tests. The erosion rate, V_u, was calculated in terms of volume loss (μm^3) per particle impact and compared with those of the reference materials. By calculating V_u in this way it is possible to determine erosion performance and compare materials at a wide range of impact energies independent of particle size. The eroded samples were also examined using Talysurf

profilometry, which had a vertical resolution of 10nm, and scanning electron microscopy (SEM).

A set of lapped and as-grown coatings ranging from 10-200μm thick were tested at 268 m s^{-1} in order to investigate the effect of coating thickness and surface condition on erosion performance. In addition, four coatings with an average thickness of approximately 40 μm were tested at four separate velocities: 33, 63, 148 and 268 m s^{-1}, so that information on the velocity exponent could be obtained.

The influence of particle impact angle on the erosion behaviour of CVD diamond was also investigated. Two batches of coating of two different thicknesses (37 - 43μm and 60μm) were used and the impact angles employed were 30°, 45°, 60° and 90°. The coatings were also weighed at regular intervals throughout the tests in order to plot steady state erosion against impact angle.

The most widely used grade of cemented tungsten carbide currently used in offshore choke valves is the WC-6Co grade. A comparison of this material with another WC grade, WC-7Ni, found that the latter exhibited greater erosion resistance. For this reason, the latter grade was used as the reference material, with which diamond was compared.

5.8 Water-Sand Slurry Erosion Tests

Initial tests were carried out on the slurry jet erosion rig. This rig enables tests to be carried out under less energetic conditions: the particle velocities do not generally exceed 30 m s^{-1}. However, as will be seen in subsequent chapters, the test conditions obtainable with this rig are insufficiently vigorous to generate significant damage in all but the thinnest diamond coatings. Nevertheless, it is instructive to consider the features of this apparatus before discussing the experimental work.

Figures 5.5 and 5.6 show the arrangement of the rig in schematic form. The main constituents are a 9 litre tank (the erosion chamber) and a loop of pipework, through which the water-sand slurry is recirculated throughout the test by a variable speed mono pump. The water-sand slurry enters the erosion chamber through a hardened

steel nozzle, forming a jet. This jet impinges on the test sample, which is held directly beneath the nozzle. The nozzle to sample stand-off distance can be varied from 10mm to 90mm, while the impact angle can be varied from 20° to 90°. The flow rate is monitored by a Heinrichs type 567 electromagnetic flow meter and is recorded by a J.J. Lloyd JJ4 chart recorder. The erosion chamber remains at atmospheric pressure during the tests. During long tests, the temperature gradually increases (up to approximately 50°C for a 5 hour test); this can also be monitored and logged if required.

Two test conditions were employed on the slurry rig. They were angular 135μm sand (Redhill 110) at a slurry jet velocity of 16 m s^{-1} and sub-angular 235μm sand (Redhill 50) at 28 m s^{-1}, both for 5 hours, and will be referred to as Low Energy and High Energy respectively. In both tests the nominal impingement angle was 90°and the nozzle to sample stand-off distance was 37mm. The slurry jet nozzle was 5.9mm diameter and the concentration of sand in water was 2.1% by weight. The volume loss of the samples was determined the same way as those tests done using the air-sand rig.

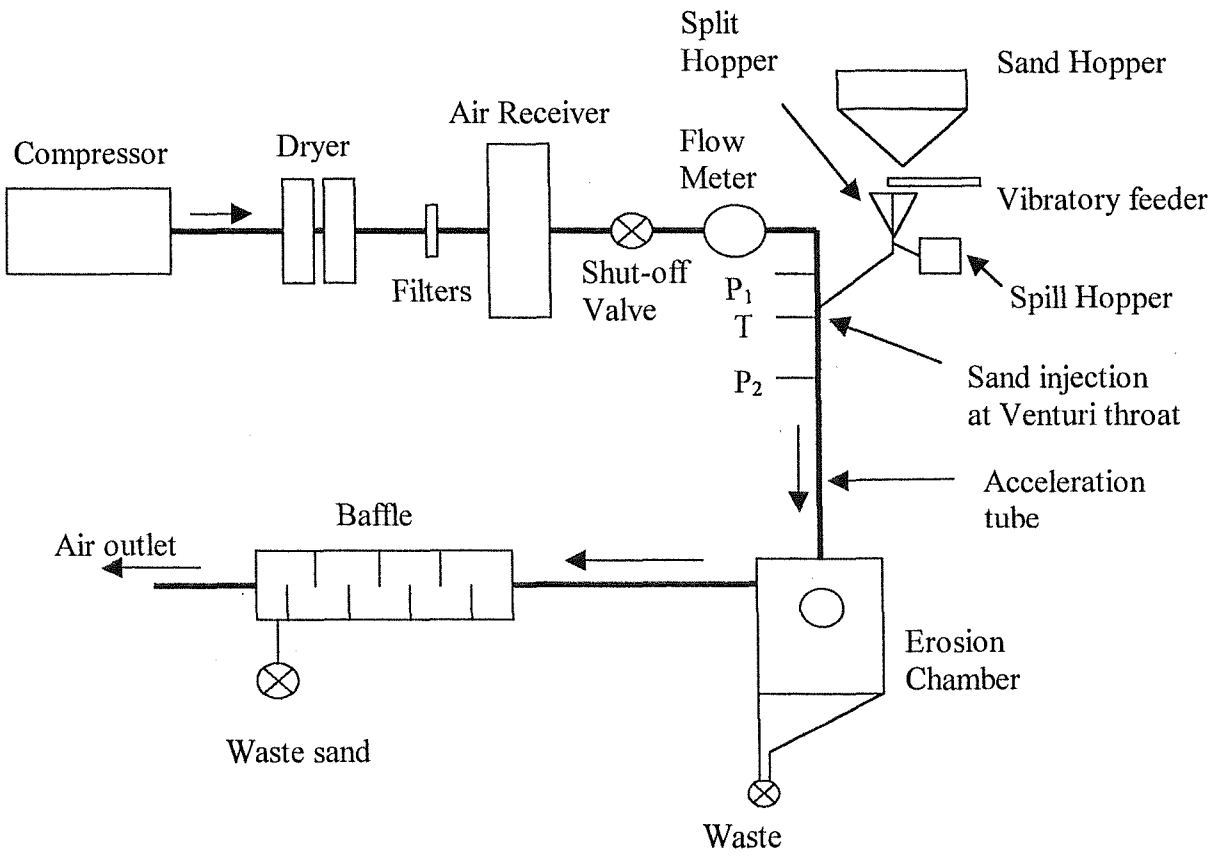

Fig. 5.1: Schematic diagram of the air-sand erosion rig used in the current work. Key: P_1, P_2: upstream and downstream pressure tappings respectively; T: temperature at throat.

Fig. 5.2: Photograph of the air-sand erosion rig, showing the erosion chamber (bottom, centre), the sand injection nozzle (centre), the sand hopper (top, left) and the air reservoir (extreme right).

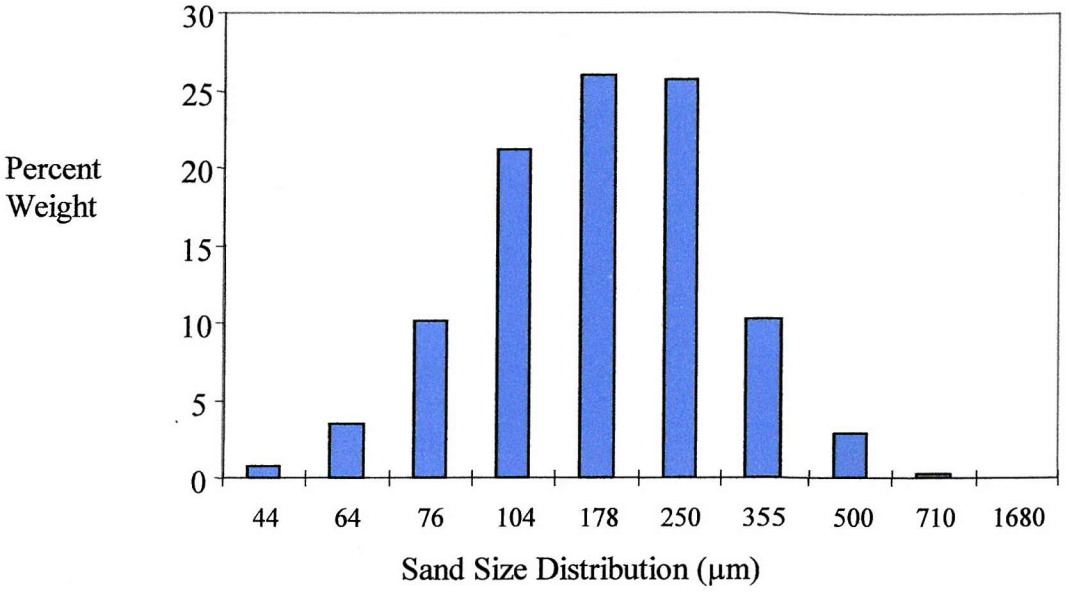

Fig. 5.3: Size distribution of the Redhill Mix sand blend

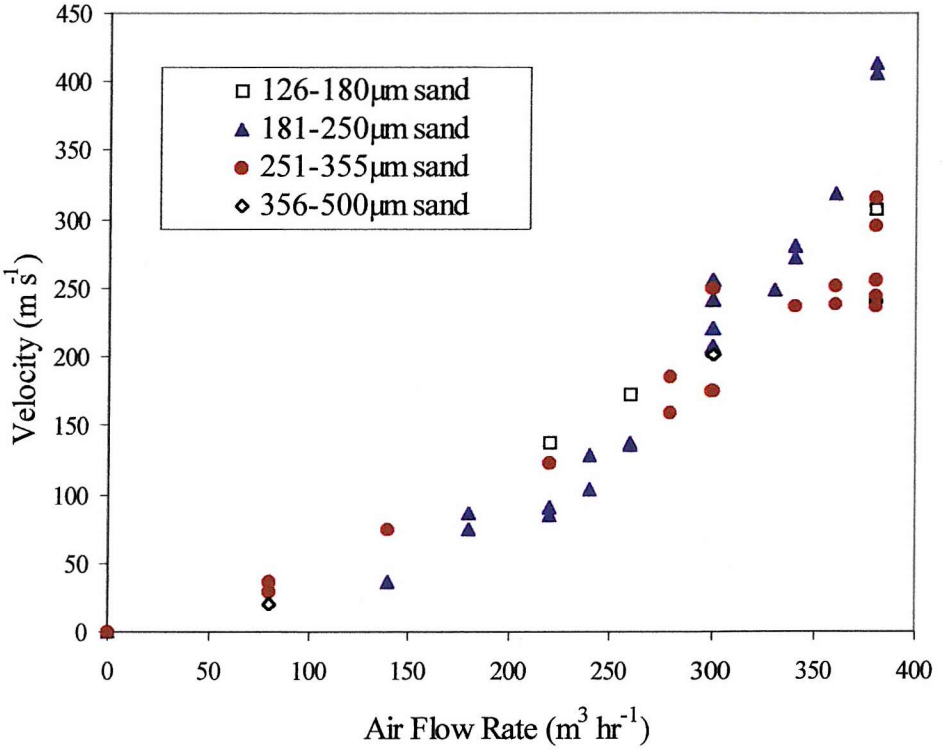

Fig. 5.4: Sand velocity calibration for 16mm bore acceleration tube against air flow rate.

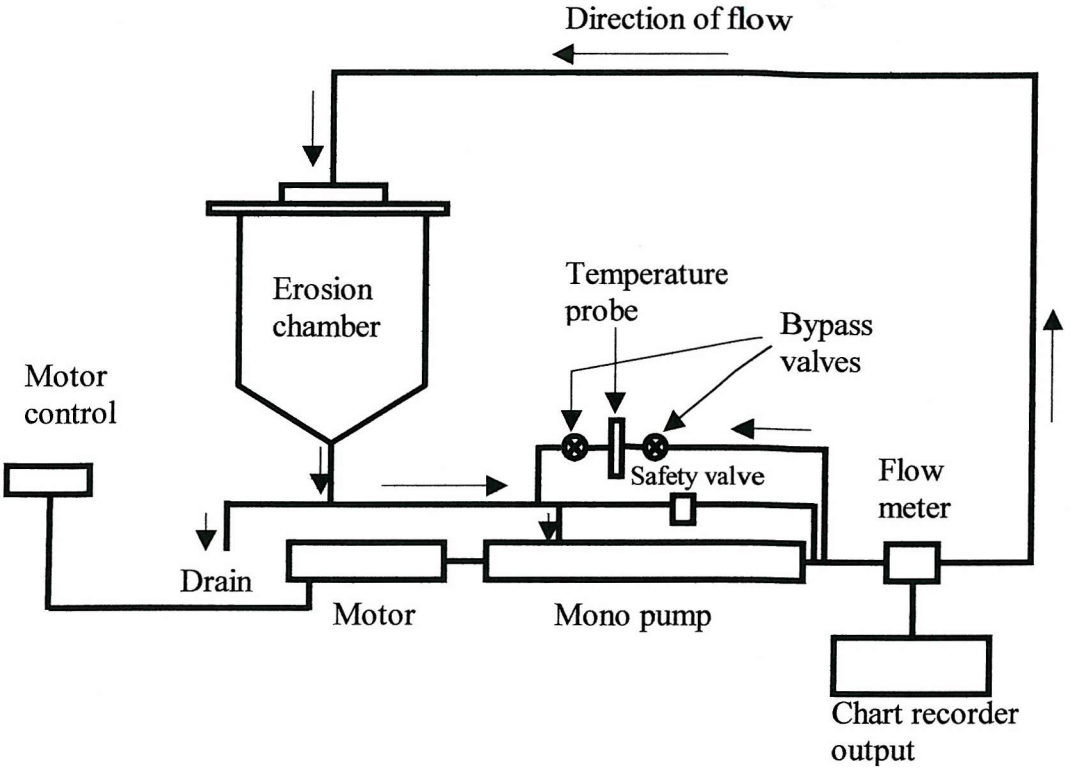

Fig. 5.5: Schematic diagram of the slurry erosion apparatus

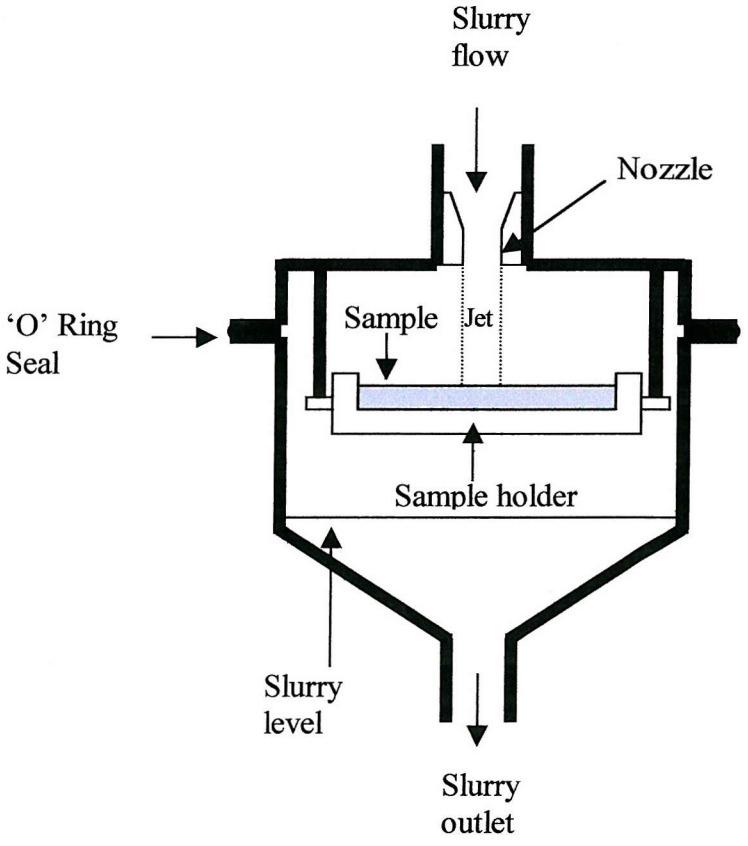

Fig. 5.6: Schematic diagram of the erosion chamber in the water-sand slurry erosion rig.

6

MATERIALS CHARACTERISATION

6.1 Coating Microstructure

Figures 6.1 and 6.2 show the change in surface roughness and grain size of the as-grown coatings with thickness. They show that both parameters increased with increasing thickness, though the profiles of the two trends differed. In Figure 6.2 a general increase in the average grain size with coating thickness can be seen, although the error bars show that there is often a large variation in grain sizes for a given coating sample. The reason for this is that as growth occurs, grain sizes increase but the average grain size is limited because new nucleation occurs on the growth surface, and these smaller grains reduce the overall grain size. On the lapped coatings, the grain boundaries were not sufficiently prominent to enable the grain sizes to be measured; however, it is not thought the grain sizes deviate significantly from those of the as-grown coatings of corresponding thickness. The micrographs in Figures 6.3 to 6.8 show the as-grown surfaces of CVD diamond coatings of various thicknesses.

The values of surface roughness R_a, also increased with increasing coating thickness. This is related to the increasing grain size with thickness discussed above. Table 6.1 lists the average values, which were the mean of at least five separate measurements. The R_a of the lapped coatings was also measured but the values are not listed in the table. All roughness values recorded were 0.20μm ±0.03μm. The greater R_a values for coatings deposited on WC-6Co is related to the larger grain size, thought to be a product of lower nucleation density.

6.2 Raman Spectroscopy

Figure 6.9 shows a typical spectrum of the growth surface of a 60μm lapped coating on tungsten. It can be seen that the only peak is diamond and the graphite peak, which is located at ~1580 cm^{-1}, is barely distinguishable from the background, indicating that the graphite content is negligible. The relative heights of the diamond and graphite

peaks cannot be used to calculate their relative proportions owing to differences in the scattering efficiency of the two species. The scattering efficiency of graphite is approximately 50 times greater than that of diamond. Therefore, the actual graphite content in the coating is likely to be even lower than the spectrum in Figure 6.9 suggests.

Substrate	Thickness (μm)	Surface Condition	Surface Roughness R_a (μm)
Tungsten	11	As-grown	1.36
Tungsten	18	As-grown	2.46
Tungsten	28	As-grown	1.56
Tungsten	43	As-grown	2.21
Tungsten	60	As-grown	2.08
Tungsten	90	As-grown	2.21
Tungsten	120	As-grown	3.07
Tungsten	150	As-grown	4.29
Tungsten	200	As-grown	4.06
Tungsten Carbide-6 wt %Co	60	As-grown	3.23
Tungsten Carbide-6 wt %Co	87	As-grown	5.16
Tungsten Carbide-6 wt %Co	165	As-grown	6.21
Tungsten Carbide-6 wt % Co	195	As-grown	6.86
Tungsten Carbide-6 wt % Co	250	As-grown	7.34

Table 6.1: Surface roughness values of as-grown diamond coatings of various thicknesses on both tungsten and tungsten carbide substrates.

The position of the main diamond peak (1335 cm^{-1}) is close to the reference position (1332.5 cm^{-1}), the shift generally being approximately +3 cm^{-1}, indicating the presence of a slight compressive residual stress. Multiple analyses of the same sample indicated that this was not an untypical spectrum. On a purely qualitative basis this suggests that the level of residual stress is slightly compressive. However, this is for only one isolated location in the coating and further work is necessary in order to determine if this is a representative spectrum. To improve the statistical basis of the results the samples need to be mapped; this is described in Chapter 7. Due to the difficulties in calculating the value of residual stress of CVD diamond, already alluded to in Chapter

2, it is not possible to use this spectrum to arrive at a quantitative figure of residual stress for this coating.

6.3 X-Ray Diffraction

Recent work by Telling and Field [1] has highlighted the influence of crystallographic orientation on erosion rate. Their results showed that the erosion rate of free-standing CVD diamond can vary by as much as an order of magnitude, depending on the crystallographic orientation. The <110> direction exhibits a greater erosion resistance than the <111> for the same grain size. For this reason, it is important to record the identity and direction of any preferred orientation present within the coatings, as well as any changes with coating thickness. Figure 6.10 shows a typical spectrum taken from a 60μm lapped coating on tungsten. The predominant peaks are those of diamond (111) and (220) directions. No significant difference in crystallographic orientation was seen in the X-ray spectra of the different coating thicknesses. It is also interesting to note that several small WC peaks are also present, thought to be cause by the presence of a carburised layer at the coating-substrate interface.

6.4 Hardness and Elastic Modulus

The results are listed in Table 6.2. It can be seen that wide discrepancies in the individual values of both parameters have been recorded. This has been reported in other publications [2] and was attributed to factors such as microstructural defects (twins, stacking faults etc) and dependence of hardness on crystallographic direction. Moreover, these variations may be exacerbated by the small indentation volume, within which the effect of microstructural variations (grain size, defects, surface roughness, dislocation density etc.) will be increased. As a consequence, the effect on individual mechanical properties recorded at those locations may be magnified.

No significant degradation of the indenter was seen. The average values of hardness and elastic modulus were 80 GPa and 1157 GPa respectively. Both figures agree well with values published by other workers. However the hardness ranged from 66 to 95 GPa while in the case of the elastic modulus the variation was even greater, from 711 to 1848 GPa. There was no correlation between the two values, i.e. the highest hardness value did not coincide with the highest modulus. In all measurements the maximum

depth of indentation did not exceed 600nm. As this depth is less than 10% of the total coating thickness, the hardness and elastic modulus values recorded can be considered to be genuinely independent of the substrate.

The wide variations in both the hardness and elastic modulus of diamond, shown in Table 6.2, have important implications for the calculation of parameters that use hardness and elastic modulus in the equations, for example fracture toughness and Hertzian contact diameter. In particular it prompts the question of which value should be used in those equations. One option is to use the average value; however, materials do not often fail in regions having "average" physical properties, they fail at areas of weakness. Therefore, it is important to evaluate the effect of variations in elastic modulus on the relevant parameters. This question will be addressed in later chapters, where relevant.

Figure 6.11 shows a typical load-displacement curve of the indentation tests of CVD diamond. It can be seen that the loading and unloading curves are not superimposed indicating some degree of non-elastic behaviour. This has been attributed in other publications to phenomena such as grain boundary sliding [3]. However, it should be noted that no residual impressions of any of the indentations were observed upon unloading.

Measurement	Hardness (GPa)	Elastic Modulus (GPa)
1	71.9	802
2	89.3	1848
3	79.1	711
4	94.6	1478
5	65.8	944
Average Value	80.1	1157
Standard Deviation	10.6	436
% of Average	13.3	37.7

Table 6.2: Hardness and elastic modulus data obtained from a 120μm lapped CVD diamond coating on tungsten.

6.5 Fracture Toughness

The surface of the lapped diamond coatings (R_a = 0.2μm) was too rough to permit measurement of the fracture toughness and no residual indents were observed following removal of the 500g load. In the same way, no indents were seen on a transverse section of 90μm thick coating when it was indented.

Three indents were made on a 600μm thick polished diamond film (R_a 0.008μm), which had been brazed to a tungsten carbide substrate. Residual indents were observed, together with radial cracks propagating from the corners of the indentation. The crack lengths were measured using optical microscopy and the fracture toughness, K_{Ic}, calculated using the following formula:

$$K_{1c} = 0.016\left(\frac{E}{H}\right)^{0.5}\left(\frac{P}{a^{1.5}}\right) \tag{6.1}$$

Where E is the elastic modulus, H the hardness, P the load and a average crack length. The values of hardness and elastic modulus used in the calculation were 80 GPa and 1063 GPa respectively. The three values of K_{Ic} obtained were 8.41, 10.15 and 11.27 MPa√m, giving a mean value of 9.94 MPa√m. This figure is almost twice the mean value given by Drory *et al* [4], using the same procedure and formula, and who quote 5.3 ±1.6 MPa√m. However, there are factors that could explain this discrepancy.

1. The small size of the indent could lead to errors in measuring the crack lengths. When measurement was repeated using the scanning electron microscope, the indents could not be located.
2. Compressive residual stresses, which are known to be compressive (overall), could inhibit crack growth, leading to a higher apparent fracture toughness. It is significant that the other fracture toughness studies quoted in the literature were conducted on free-standing diamond. Therefore, in those cases the thermal stress, which is thought to account for the largest proportion of the overall residual stress, was absent.
3. The small number of indents, necessary to minimise the influence of indenter degradation, complicates the task of comparing this study with other, similar,

studies. Nevertheless, the values obtained here are within the range of values quoted in other sources [5-8].

6.6 Conclusions

This section has focused on aspects of the characterisation of the diamond coatings. Both Raman and XRD analysis has shown that the coatings are almost entirely diamond with negligible graphitic content. Moreover, XRD has revealed no significant changes in crystallographic orientation of the coating as the thickness increases. Both the grain size and surface roughness (in the case of the as-grown coatings) increase with coating thickness; this may be significant in considering the effect of coating thickness on erosion behaviour. The hardness and elastic modulus values obtained from the coatings show that the values of both parameters are within the range reported by other workers. The fracture toughness values obtained are up to double the values reported by other workers; it is thought that this is due to the influence of a compressive residual stress present in the diamond. However, the values obtained are still within the overall range reported in the literature. The large variation in the values of the hardness, elastic modulus and fracture toughness also highlights the difficulty of selecting appropriate values for insertion into erosion models to predict the erosion rate.

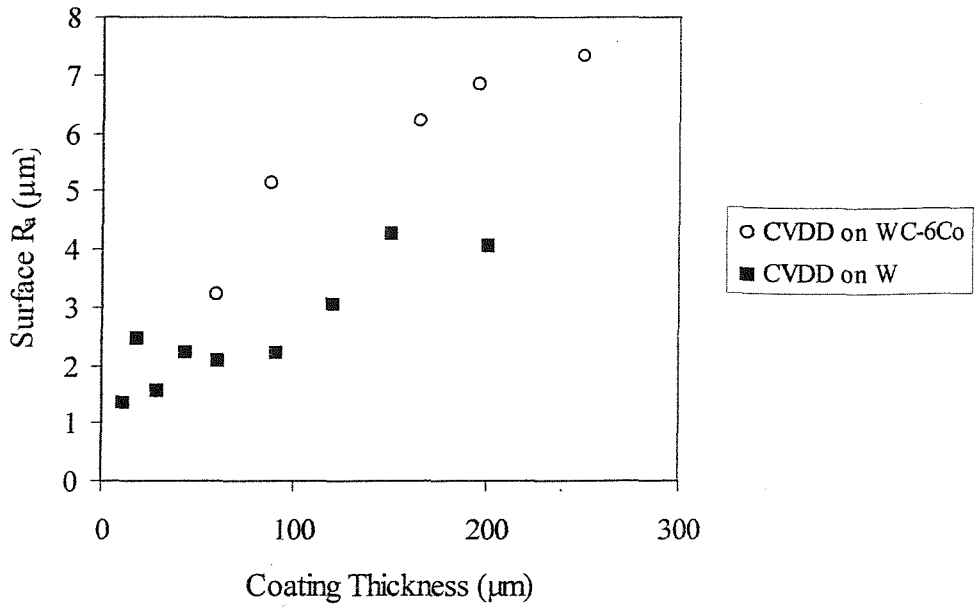

Fig. 6.1: Graph showing the relationship between Surface R_a and Coating Thickness for as-grown CVD diamond coatings on both W and WC-6Co substrates.

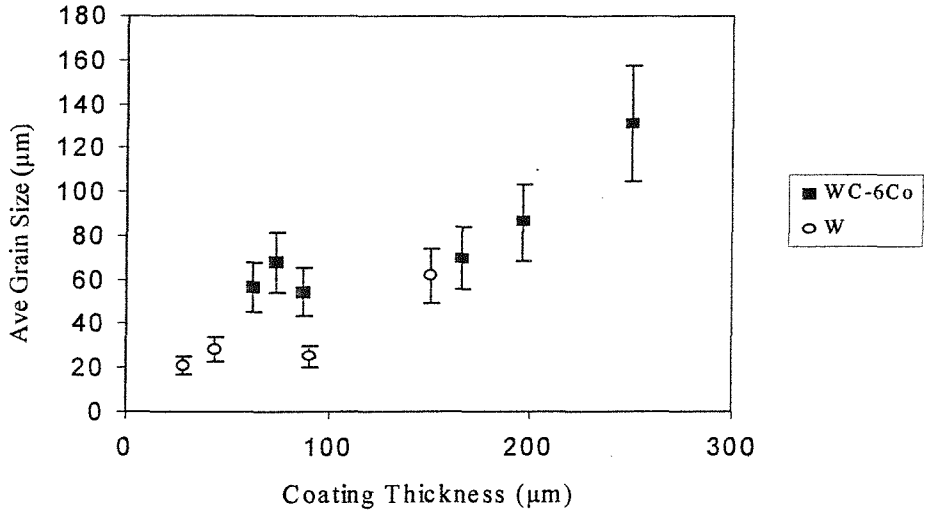

Fig. 6.2: Graph showing the relationship between Average Grain Size and Coating Thickness for as-grown CVD diamond coatings on both W and WC-6Co substrates. The error bars denote the spread of measured grain sizes.

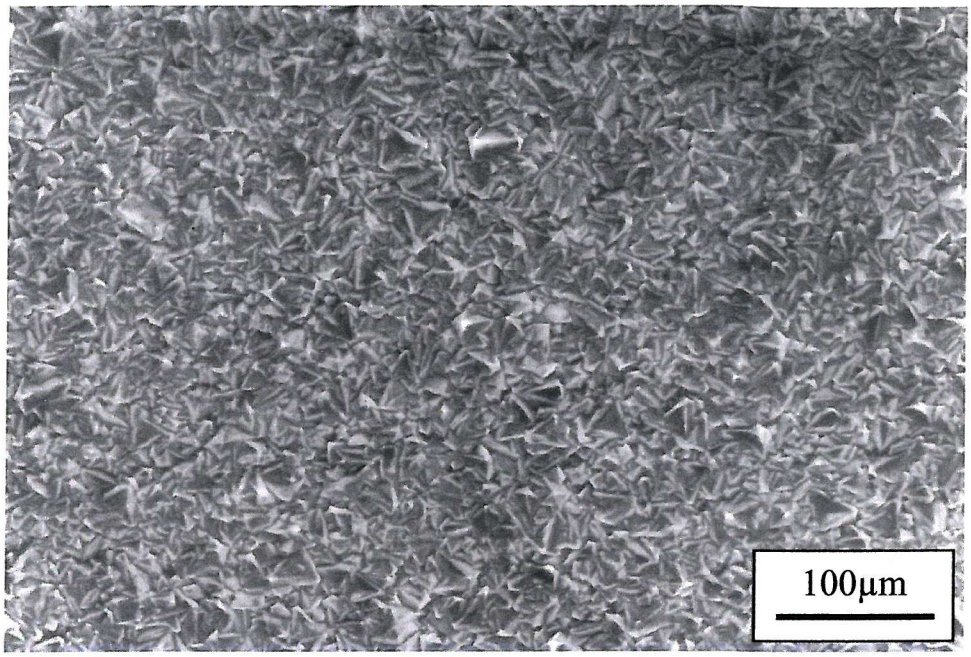

Fig. 6.3: Micrograph showing the untested as-grown surface of a 28μm CVD diamond coating on tungsten.

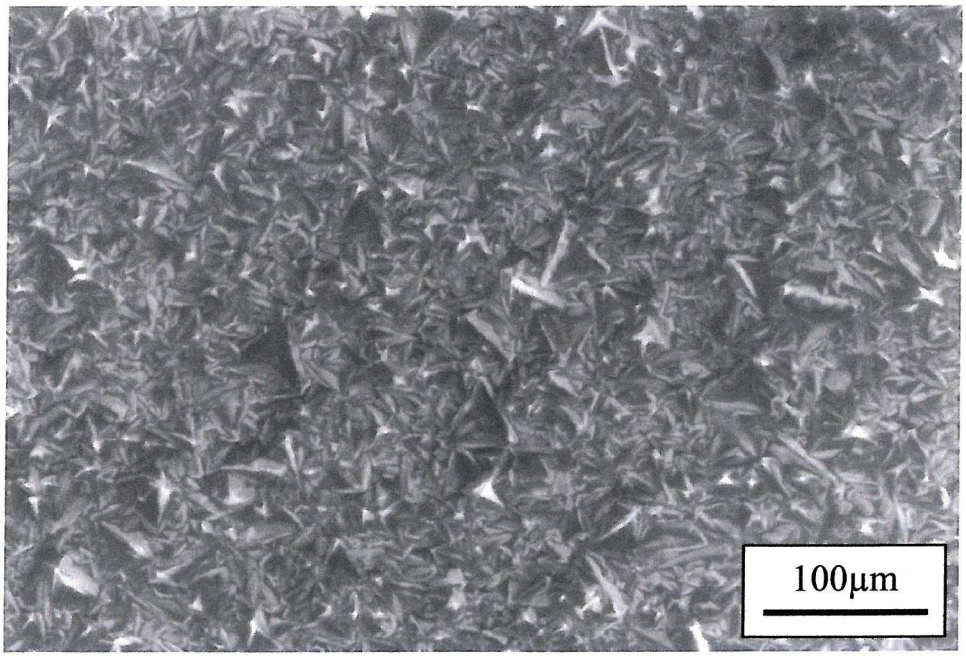

Fig. 6.4: Micrograph showing the untested as-grown surface of a 43μm CVD diamond coating on tungsten.

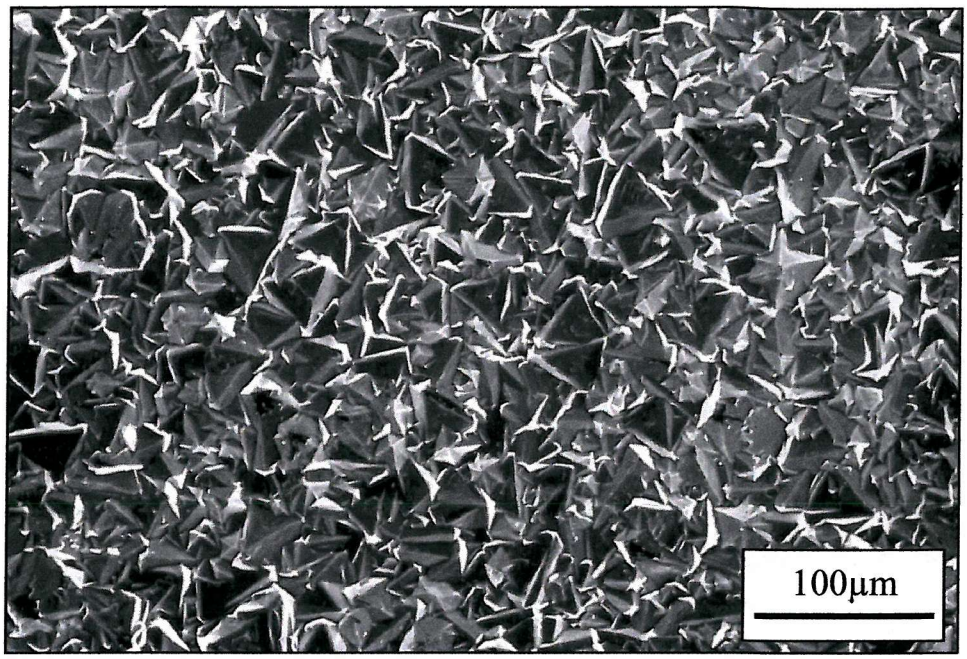

Fig. 6.5: Micrograph showing the untested as-grown surface of a 60µm CVD diamond coating on tungsten.

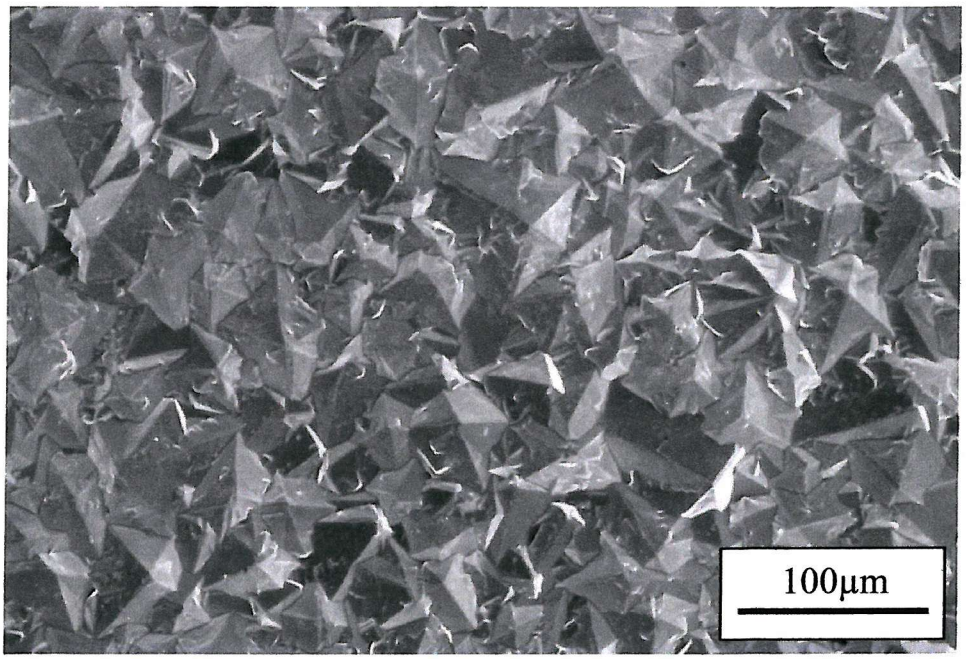

Fig. 6.6: Micrograph showing the untested as-grown surface of a 150µm CVD diamond coating on tungsten.

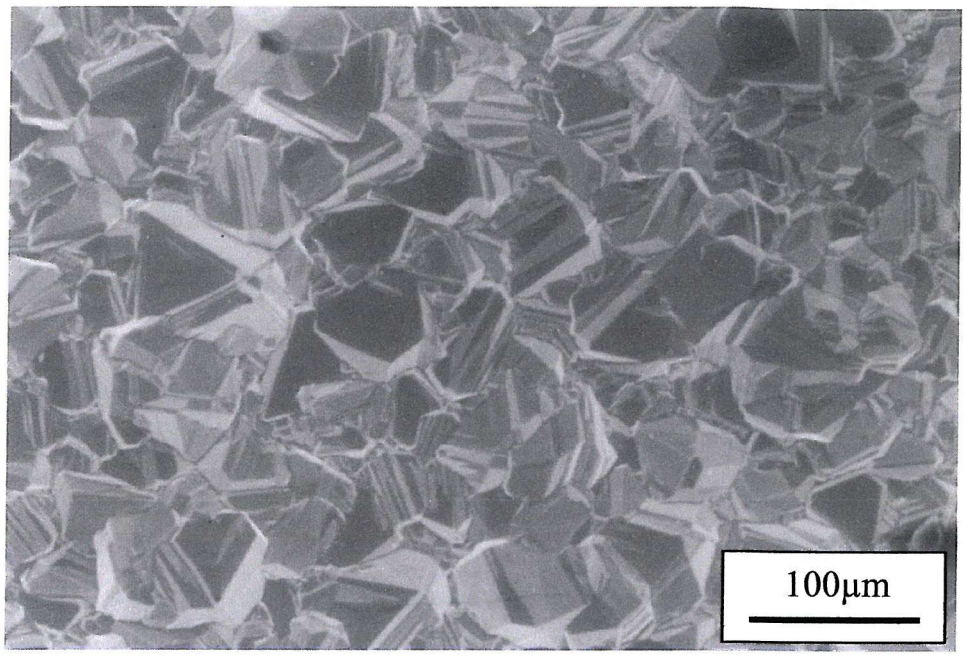

Fig. 6.7: Micrograph showing the untested as-grown surface of an 87μm CVD diamond coating on tungsten carbide-cobalt.

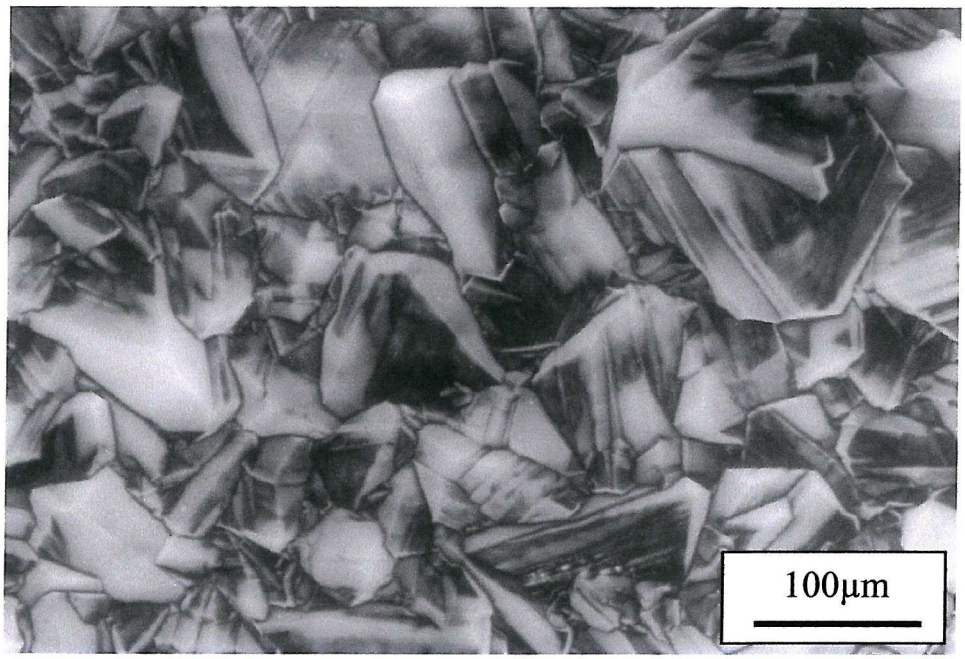

Fig. 6.8: Micrograph showing the untested as-grown surface of a 195μm CVD diamond coating on tungsten carbide-cobalt.

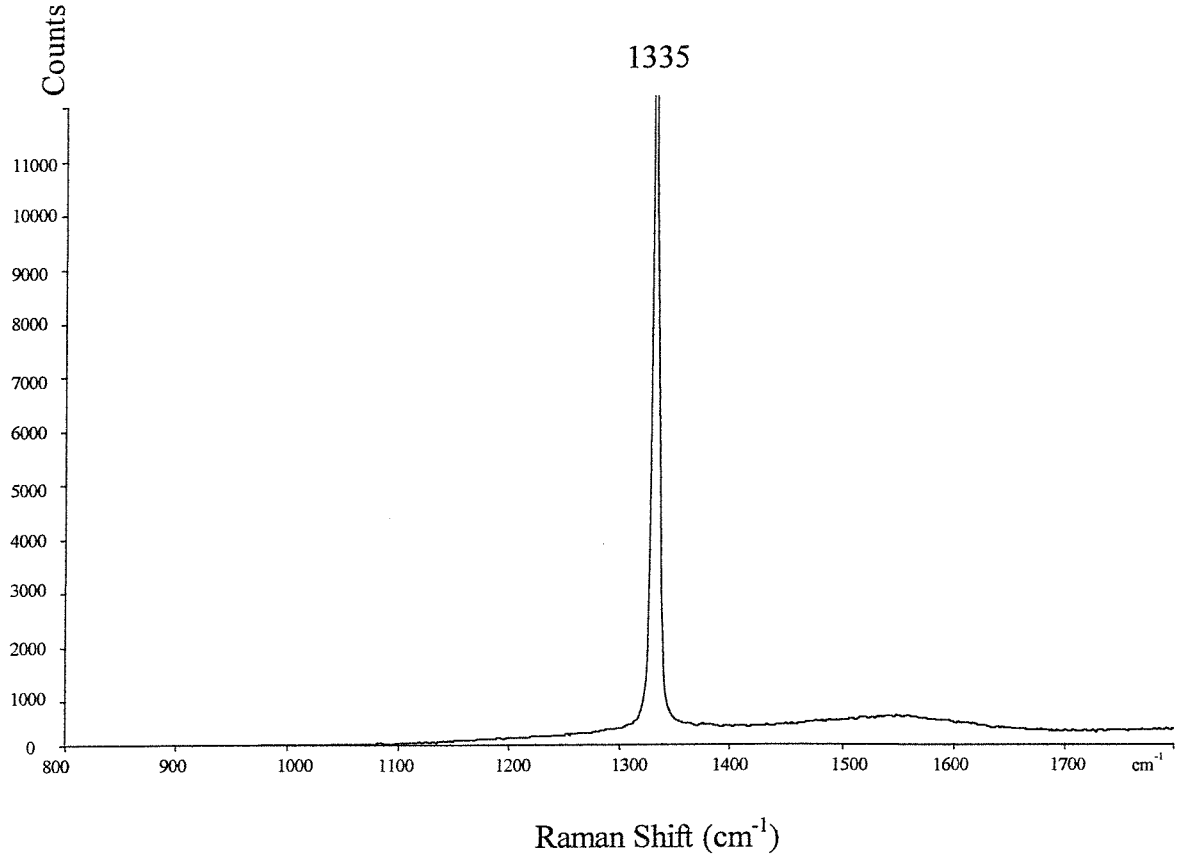

Fig. 6.9: Typical Raman spectrum from the growth surface of an untested lapped 60μm diamond coating on tungsten.

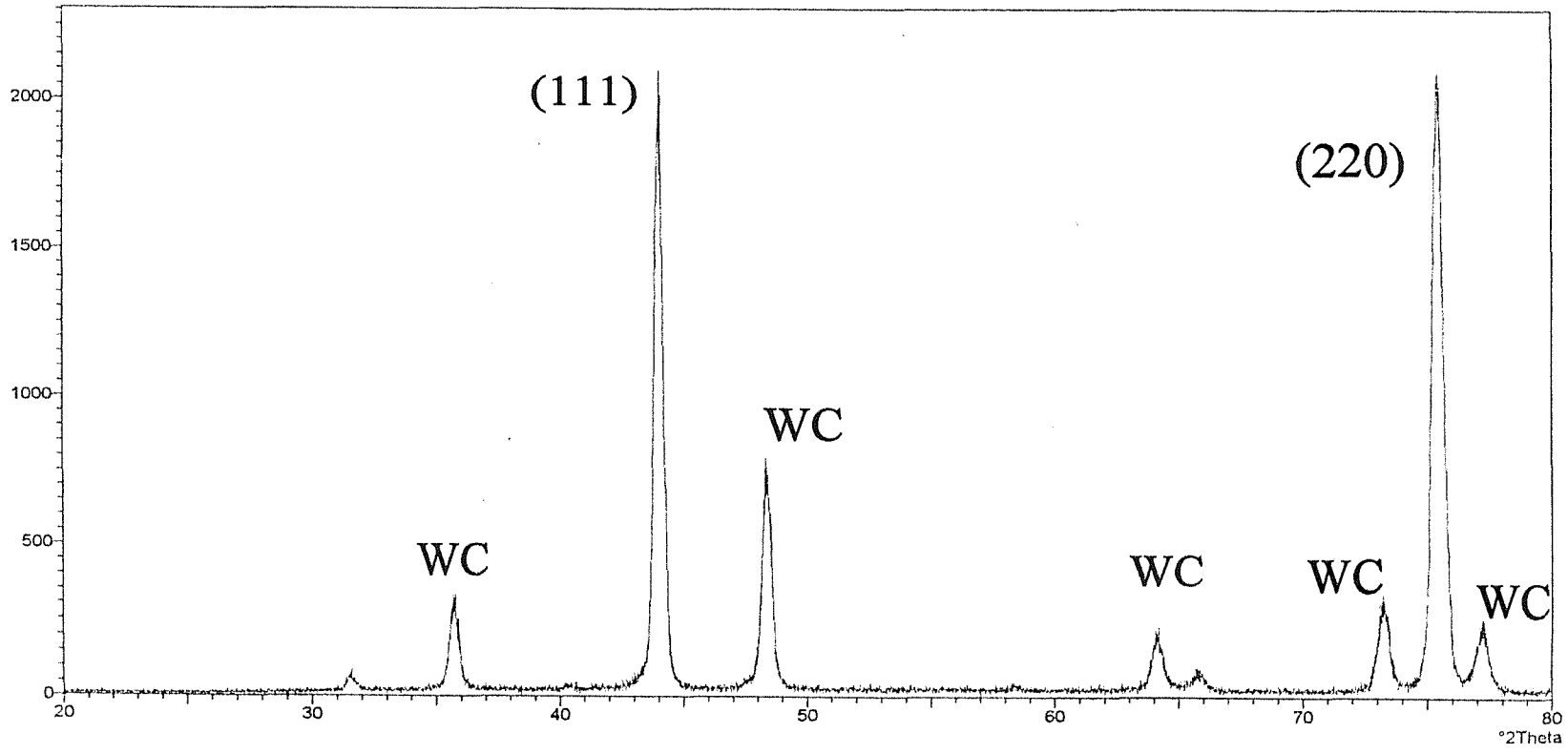

Fig. 6.10: X-ray diffraction spectrum of an untested 120μm lapped diamond coating on tungsten showing the crystallographic orientation of the film.

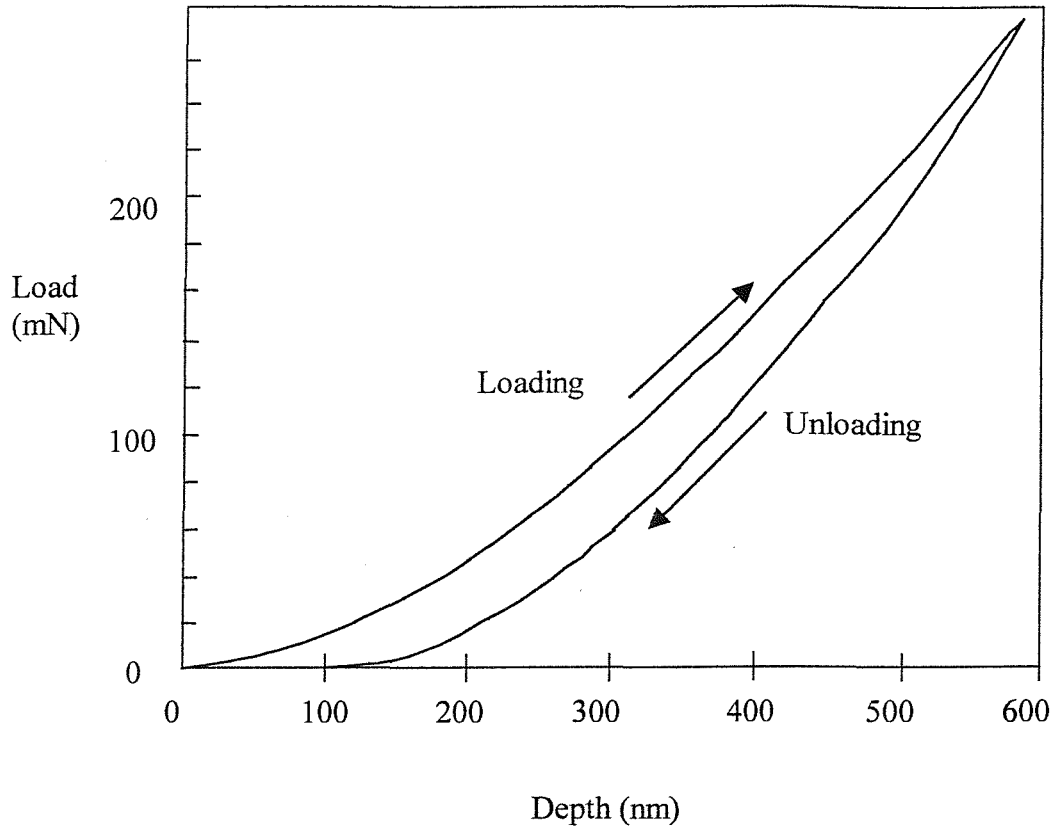

Fig. 6.11: Typical Load-Displacement from a nanoindentation test, using a Berkovich indenter, on a lapped 120μm diamond coating on tungsten. Equipment used: CSEM NHT nano indenter; Maximum load 300 mN; Hardness = 71.9 GPa; E = 802 GPa.

7

RESIDUAL STRESS

7.1 Introduction

Chapter 2 has already shown that residual stress can often influence coating behaviour. This chapter describes the use of Raman spectroscopy to evaluate the residual stress in the CVD diamond coatings on tungsten that are used in the present work. While it is difficult to obtain quantitative values of residual stress of diamond coatings using Raman spectroscopy it can indicate the variation with thickness. From a small change in mean Raman peak position with thickness it may be inferred that its influence on the erosion behaviour of CVD diamond coatings would be minimal. The object of the present work was to determine the extent of this variation with thickness.

7.2 Experimental

Lapped diamond coatings (R_a 0.2 ±0.03μm) on tungsten, ranging in thickness from 11 to 120μm were examined using Raman spectroscopy. The shift in the main (1332.5 cm^{-1}) Raman peak was used as an indication of the level of residual stress. In the present case, in order to improve the statistical basis of the present results, an area of each sample was scanned. The sampling areas were of two sizes: 2mm x 2mm and 50μm x 50μm. In each case, the number of points where the measurements were 10 x 10, i.e. each sampling location was 200μm and 5μm apart respectively.

A Renishaw Raman microscope was used and the samples were mounted on a computer-controlled x-y table. A 3 mW Ar ion laser (having an excitation wavelength of 488nm) was used at an objective of x50. The diameter of the laser beam was approximately 4μm while the sampling depth of the laser beam was estimated to be approximately 10μm. The sample was scanned in a raster pattern and the acquisition time was 5 seconds per point. On

completion, background subtraction was performed on each spectrum followed by Lorentzian curve fitting routines, though for spectra with a high background, a mixed Lorentzian-Gaussian function was used instead. The value of the main Raman peak at each point was plotted in a map in order to observe the variation across the area analysed. The same procedure was performed in order to see the variation in the peak width (FWHM) over the same area.

7.3 Results and Discussion

7.3.1 Effect of coating thickness on Raman peak position

The results of the Raman mapping are summarised in Tables 7.1 and 7.2. They show that all values of the main Raman peak lie within the region of 1332.8 - 1337.6 cm^{-1}. Figure 7.1 shows a typical distribution of the main peak position for the 120μm coating. No significant difference was observed between the mapping carried out over the 2mm x 2mm area and the smaller 50μm x 50μm area. All maps indicate the presence of an overall compressive stress.

Coating Thickness (μm)	Average peak position (cm^{-1})	Range of peak positions (cm^{-1})	Standard deviation (cm^{-1})	Area analysed (μm)
11	1336.2	1335.1 -1337.6	0.43	2000 x 2000
60	1335.1 1335.0	1333.9 - 1337.0 1333.6 - 1336.8	0.48 0.49	2000 x 2000
103	1335.2	1333.6 - 1337.2	0.58	2000 x 2000
120	1334.9 1334.9	1332.8 - 1336.4 1333.7 - 1336.4	0.62 0.49	2000 x 2000
60	1334.9	1332.8 - 1336.4	0.59	50 x 50
120	1334.9	1333.5 - 1336.4	0.57	50 x 50
120*	1333.0	1332.1 - 1333.9	0.47	1000 x 1000
120*	1333.0	1331.2 - 1334.0	0.56	1000 x 1000

Table 7.1: Summary of peak position data taken from the Raman mapping. Key: * = free-standing diamond.

UNIVERSITY OF SOUTHAMPTON LIBRARY

Figure 7.2 plots the average Raman peak position against coating thickness. It is significant that the average peak positions of the coatings all lie within 0.3 cm^{-1} of each other with the exception of the 11μm coating, which is approximately 1 cm^{-1} greater than the thicker coatings. There is also a small (~2cm^{-1}) positive shift in the range within which all the values fall for this coating. This suggests that the 11μm coating is under a greater compressive stress. This agrees with another Raman study of CVD diamond coatings on silicon by von Kaenel *et al* [1], who found that the coating was under compressive stress, which rapidly decreased and then stabilised, though remained compressive. It is thought that the apparent reduction in residual stress as the coating thickness increases is due to the increase in microstructural flaws, which contribute to the intrinsic stress, itself largely tensile in nature. Thus, it is possible that the tensile intrinsic stress has cancelled out part of the compressive thermal stress in the thicker coatings.

Coating Thickness (μm)	Average peak width (cm^{-1})	Range of peak widths (cm^{-1})	Standard deviation (cm^{-1})	Area analysed (μm)
11	9.19	6.6 - 13.6	1.01	2000 x 2000
60	8.66	4.9 - 13.4	2.14	2000 x 2000
103	9.85	5.4 - 17.3	2.43	2000 x 2000
120	8.22	4.3 - 14.7	3.79	2000 x 2000
60	9.03	4.5 - 14.3	2.05	50 x 50
120	7.78	4.6 - 12.5	1.74	50 x 50
120*	7.95	4.8 - 15.1	1.96	1000 x 1000
120*	6.98	5.0 - 7.6	0.93	1000 x 1000

Table 7.2: Summary of peak position data taken from the Raman mapping. Key: * = free-standing diamond.

7.3.2 Effect of coating thickness on Raman peak width

Peak width, in the form of the Full Width at Half Maximum (FWHM), is an indication of intrinsic intergranular stress, which is proportional to width [2]. The average peak widths were found to be in the range 7.0 - 9.9 cm^{-1}. All samples displayed FWHM values within this range. This compares with typical values of between 2.8 cm^{-1} and 3.1 cm^{-1}, which are

observed in both high quality stress-free single crystal type IIa natural diamond and optical quality CVD diamond [3]. However, it is close to the value (9.0 cm^{-1}) quoted from other sources for "dark" CVD diamond [4]. It is thought that the difference between this value and those quoted above is due to microstructural features such as grain boundary structure and grain size, the same factors that render the material opaque. In contrast to the Raman peak position data, the average FWHM of the 11μm coating was not markedly different to the other coatings. Figure 7.3 shows a typical distribution of the peak width for the different coatings. Figure 7.4 shows the variation of FWHM with coating thickness.

In studying the residual stress in diamond coatings, it is desirable to evaluate the contribution of the substrate to its overall magnitude. For this reason, a free-standing diamond coating 120μm in thickness, which had been removed from its substrate was examined under the same conditions as the coatings. The size of the diamond sample, however, limited the scanning area to 1mm x 1mm. The results, also listed in Tables 7.1 and 7.2, show a significant reduction in the position of the Raman peak, the average position, 1333.0 cm^{-1}, being closer to the unstressed value. The spread of values, which are plotted in Figures 7.5 and 7.6, is reduced on the free-standing diamond. These results indicate that the largest contribution to the residual stress is from the thermal stress. This agrees with residual stress studies made by Rats *et al* [5] on diamond coatings deposited on SiO_2, Si_3N_4, Si, SiC, WC-Co, Mo and Ti-6Al-4V substrates, which found that the thermal stress was the dominant contributor to the overall residual stress. The average peak positions on the nucleation and growth surfaces of the coating were virtually identical, though the spectra taken from the nucleation surface also revealed large additional peaks at 1350 cm^{-1} and 1580 cm^{-1}, indicative of the presence of amorphous carbon and graphite respectively. The distribution in peak widths for both the nucleation and growth surfaces can be seen in Figures 7.7 and 7.8. No reduction was seen in the average FWHM of the growth surface of the free-standing diamond compared to that of the coating of the same thickness.

The results therefore suggest that, on a purely qualitative basis, the variation in the Raman spectra, and hence the residual stress, over the thickness range is small. As a result, its

influence on erosion behaviour is likely to be minimal. However, it is necessary to remember that there are many factors affecting the magnitude of residual stress in diamond coatings. The deposition conditions, notably temperature and methane content, are a major factor as they can alter the microstructure (grain size, impurity levels, structural defects etc.) and, hence, the intrinsic stress. It is, therefore, unwise to assume that the same will be true for diamond coatings produced by other sources.

Thickness (μm)	Mean Peak Position (cm^{-1})	Deviation from 1332.5 cm^{-1}	Ave residual stress (GPa)	Peak position S.D. (cm^{-1})	Residual stress S.D. (GPa)
11	1336.2	+3.7	-1.295	0.43	0.15
60	1335.1	+2.6	-0.91	0.48	0.17
60	1335.0	+2.5	-0.875	0.49	0.17
103	1335.2	+2.7	-0.945	0.58	0.20
120	1334.9	+2.4	-0.84	0.362	0.22
120	1334.9	+2.4	-0.84	0.49	0.17
120*	1333.0	+0.5	-0.175	0.47	0.16
120*	1333.0	+0.5	-0.175	0.56	0.20

Table 7.3: Summary of residual stresses. Note minus sign in "Residual stress" column denotes compressive stress. Key: * = free-standing diamond; S.D. = standard deviation.

Using the relationship between Raman peak shift and residual stress suggested by Boppert *et al* [6], the mean peak shifts were used to calculate an approximate value of the residual stress of the coatings. The results are listed in Table 7.3. They show that over the range 60 – 120μm the mean residual stress is 0.87 ±0.19 GPa. These residual stress values are all compressive. It should be remembered, however, that they are only average values and large variations can often be seen across the area analysed. Nevertheless, the residual stresses of these coatings are in close agreement with those of Harker *et al* [7] who used x-ray diffraction ($\sin^2$ method). They found variations in residual stress of ±0.3 GPa for 100μm CVD diamond on Si substrates generated by thermal expansion mis-match. They also found that the average residual stress in free-standing films 0.5 – 2mm thick was

negligible. Within individual grains, localised stress variations of the order of 0.5 to 0.8 GPa could be distinguished.

7.3.3 Effect of thermal expansion mismatch between coating and substrate on residual stress

It has been seen that one of the factors that have the greatest influence on the magnitude of the residual stress in the diamond coatings is the mismatch in thermal expansion coefficient between the coating and the substrate. It is possible to calculate this stress, σ'_{th}, using the following expression [8]:

$$\sigma'_{th} = E_f(\alpha_f - \alpha_s)\Delta T \tag{7.1}$$

E_f is the biaxial elastic modulus of the coating, α_f and α_s the thermal expansion coefficient of the coating and substrate respectively, and ΔT the difference between the deposition temperature and room temperature. For this calculation the following values have been assumed: $E_f = 1157$ GPa; $\alpha_f = 0.9 \times 10^{-6}$ K^{-1}; $\alpha_s = 4.5 \times 10^{-6}$ K^{-1} and $\Delta T = 875$ K. It should be stressed that the deposition conditions (which include the deposition temperature) are not known to the author. For this calculation the deposition temperature has been *assumed* to be 900°C. Using these figures a value for σ'_{th} of –3.64GPa has been obtained. The minus sign indicates that the stress is compressive, in line with the Raman measurements.

In calculating the thermal residual stress for diamond a further calculation is required owing to the high elastic modulus of the diamond and, in the case of wafer fabrication, the film is no longer thin. Equation (7.1) assumes that there are no bending moments and that the stiffness can be ignored. For this reason, it is necessary to apply corrections for stiffness and bending moment (thickness) to it; the modified equation is listed below:

$$\sigma_{th} = \sigma'_{th}\left[1 - 3\left(\frac{E_f C_T^{\,2}}{E_s S_T^{\,2}}\right)\right]\left[1 + \frac{E_f C_T}{E_s S_T}\right] \tag{7.2}$$

Where C_T and S_T represent the thickness of the coating and substrate respectively and E_f and E_s are the elastic modulae of the coating and substrate respectively. The stress σ'_{th} was calculated in equation (7.1). For this calculation the following values were used: C_T = 60μm; S_T = 6mm; E_f = 1157 GPa and E_s = 411 GPa. Using this expression, the thermal residual stress is modified slightly to –3.70 GPa.

Equation (7.2) was also used to calculate the variation in σ_{th} with coating thickness. The results are shown in graphical form in Figure 7.9. Once again, the results mirror the Raman measurements in that the variation in σ_{th} with thickness is small. The figures are considerably higher than the figures suggested by the Raman measurements. It should be remembered, though, that this is only the thermal component of the residual stress and this figure does not take into account the intrinsic stress, which is usually tensile. Nevertheless, it is not known whether the combined influence of the intrinsic defects present can account for this difference, which is approximately 2.9 GPa. For this reason it is likely that the overall value of the residual stress will be lower than the figure calculated here. Whatever the overall magnitude of the residual stress in the coatings, it is clear that its variation with coating thickness is small.

7.3.4 Effect of residual stress on indentation behaviour

The depth of analysis of these tests is approximately 10μm. Because the same analytical conditions were employed throughout the tests the depth as a percentage of coating thickness is not constant. For this reason it is necessary to consider supporting evidence before it is possible to state with confidence that the residual stress does not vary significantly with coating thickness.

Another method of assessing the effect of residual stress is to carry out indentation studies of the coatings. Several workers have used adhesion tests to determine coating adhesion. As residual stress can often promote coating debonding, the critical load that was required to cause delamination could be used to observe the effect of residual stress with coating thickness. In an indentation study of CVD TiC coatings on WC-Co substrates Mehrota and

Quinto [9] found that as the coating thickness increased from 6 to 19μm the critical load to cause delamination decreased. This was attributed to increased interfacial residual stresses generated by thermal expansion mismatch between coating and substrate.

In the present study, diamond coatings of three different thicknesses (10, 30 and 60μm) were subjected to a Rockwell hardness test using a conical diamond indenter of 200μm tip radius. Three loads were used (588, 981 and 1471 N) with three indentations made at each load. The indents were examined under both optical and scanning electron microscopy. In contrast to the findings of Mehrota and Quinto [9] the results showed that as the coating thickness was increased the load required to cause coating delamination increased. For the 10μm coating, delamination was observed at all loads, though its extent was greater at higher loads. For the 30μm coating delamination was only seen at the highest load. The thickest coating tested (60μm) exhibited no delamination at any load. Figures 7.10 to 7.12 show electron micrographs of the indents made at 1471 N for all three coatings.

7.4 Conclusions

Raman spectroscopy has been used to map the surface of CVD diamond coatings on tungsten of thickness between 11 and 120μm. The variation in these maps with thickness has been studied to provide an indication of residual stress variation with coating thickness.

The results show that, with the exception of the thinnest coating (11μm) the average position of the Raman peak is essentially independent of thickness over the range studied. From these results, it may be inferred that residual stress does not vary significantly with coating thickness in the present study. However, as the nature of residual stress in diamond coatings is highly dependent on deposition conditions and choice of substrate, the conclusions of the current study must not be applied to other diamond coatings produced elsewhere.

The variation in average peak width of the main Raman diamond peak in all coatings is small, being within the range 7.0 to 9.9 cm^{-1}. However, these values are considerably higher

than those for stress-free single crystal type IIa diamond, though are close to previously reported data for "black" diamond. No significant difference was observed in the average FWHM between the growth surface of a free-standing 120μm diamond film and a backed film of the same thickness. This suggests that intrinsic features, such as microstructural defects are exercising a minimal influence on the value of this parameter, and hence the residual stress.

Raman spectra of free-standing diamond films has shown a marked reduction in the average peak position and is close to that for a stress-free diamond. This demonstrates that a significant contribution to the residual stress, as measured by peak position, comes from the mis-match in properties, for example thermal expansion coefficient, between coating and substrate.

The average residual stress appears to be approximately 0.87 ±0.19 GPa, and is compressive in nature. It is thought that this stress, while not being deleterious to coating adhesion or erosion resistance, may actually be beneficial in preventing the nucleation of cracking at the surface. The exact orientation of the stress is not known; therefore, the data presented here represents an aggregate value.

The indentation study shows that as the coating thickness is increased from 10 to 60μm the critical load to cause delamination increases significantly. This demonstrates that the influence of residual stress on coating integrity is negligible.

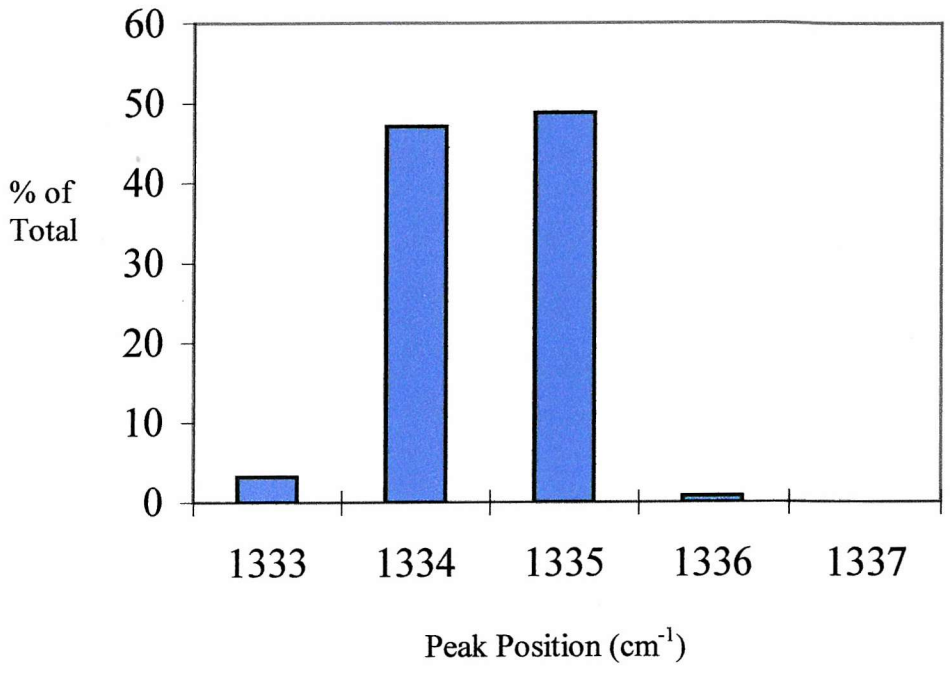

Fig. 7.1: Histogram showing the distribution in Raman peak position for a lapped 120μm diamond coating on tungsten.

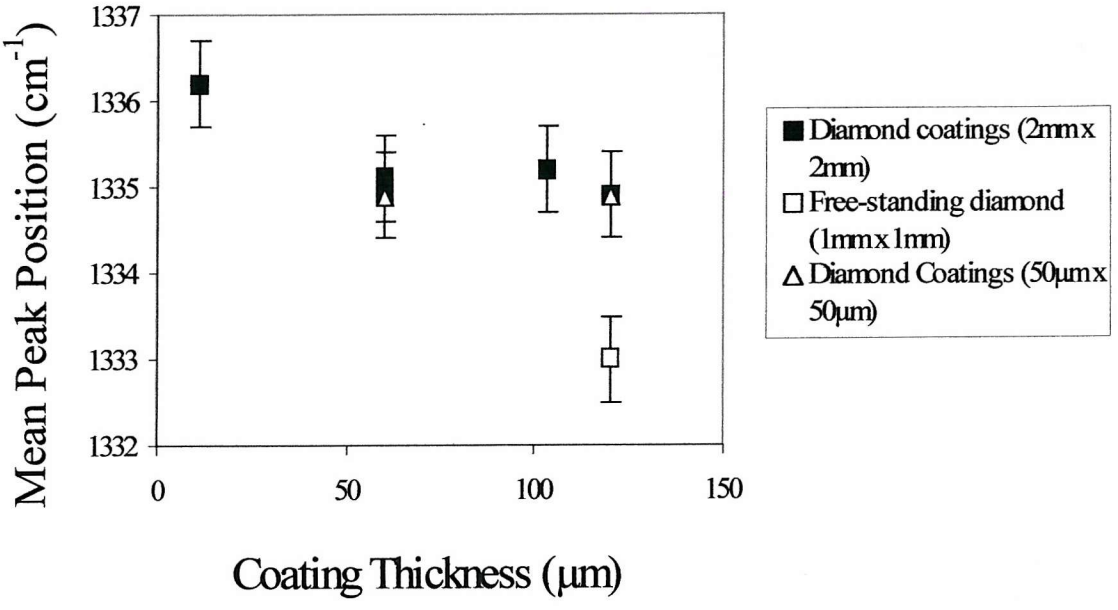

Fig. 7.2: Graph showing the relationship between Mean Raman Peak Position and Coating Thickness. The error bars denote 1 standard deviation.

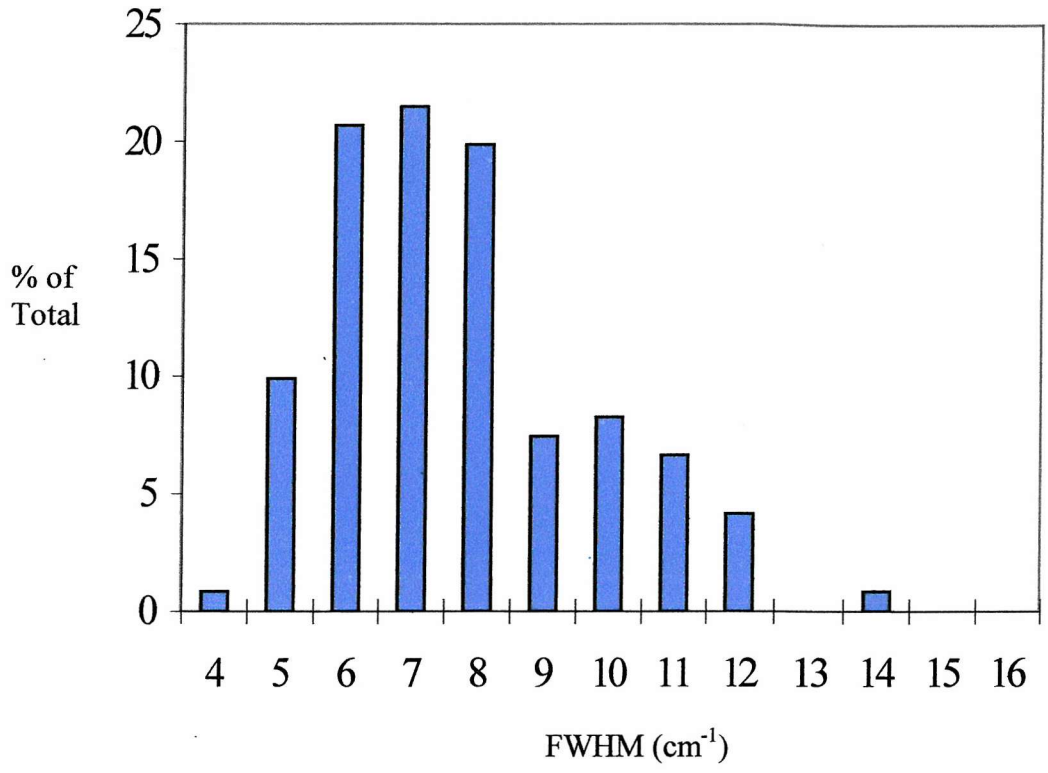

Fig. 7.3: Histogram showing distribution in peak widths for a 120μm diamond coating on tungsten.

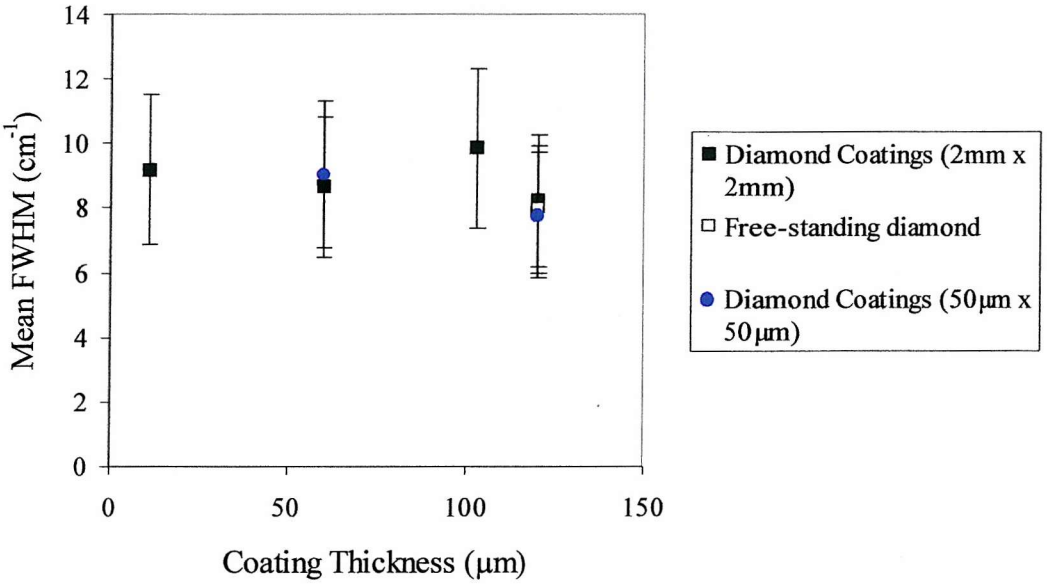

Fig. 7.4: Graph showing the relationship between Mean peak width (FWHM) and Coating Thickness. The error bars denote 1 standard deviation.

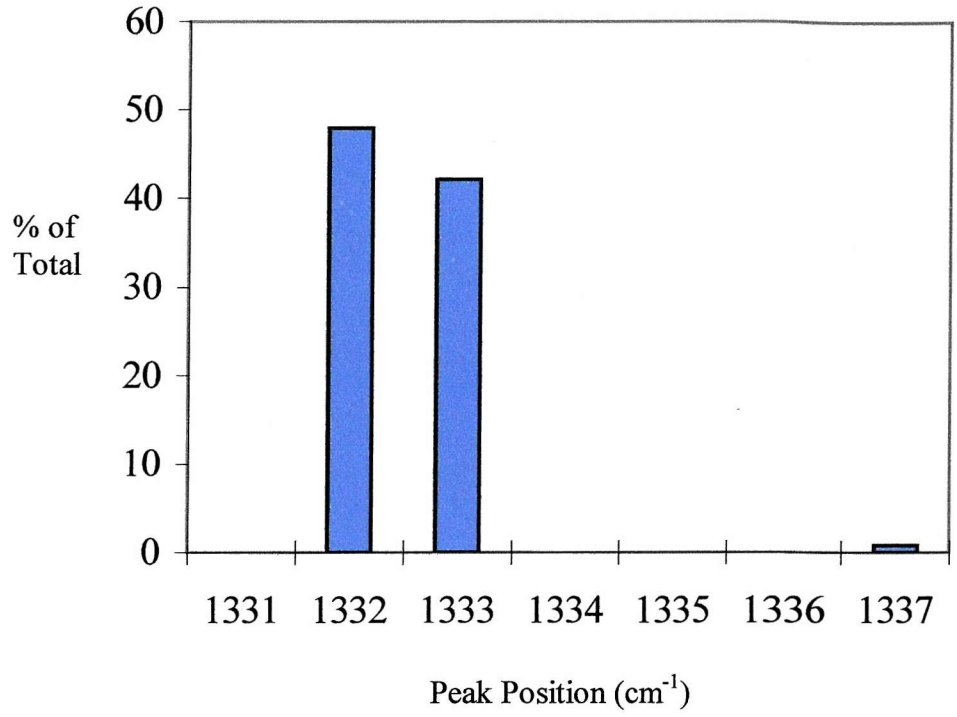

Fig. 7.5: Histogram showing the distribution in Raman peak positions for 120μm free-standing diamond film (growth surface).

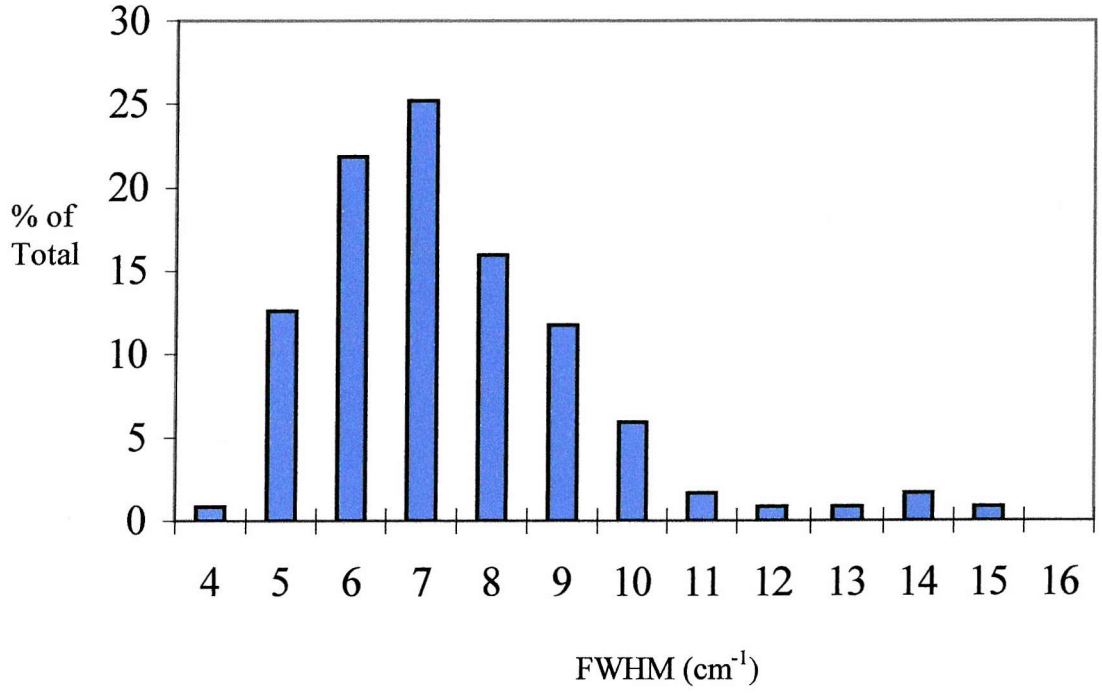

Fig. 7.6: Histogram showing distribution of peak widths for a free-standing 120μm diamond film (growth surface).

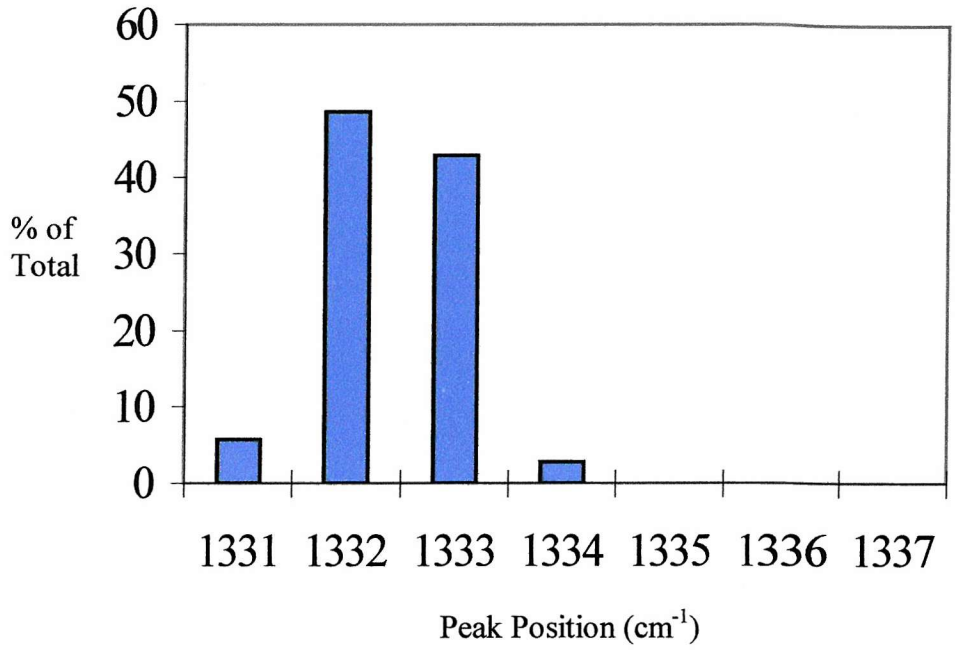

Fig. 7.7: Histogram showing distribution in Raman peak position for 120μm free-standing diamond film (nucleation surface).

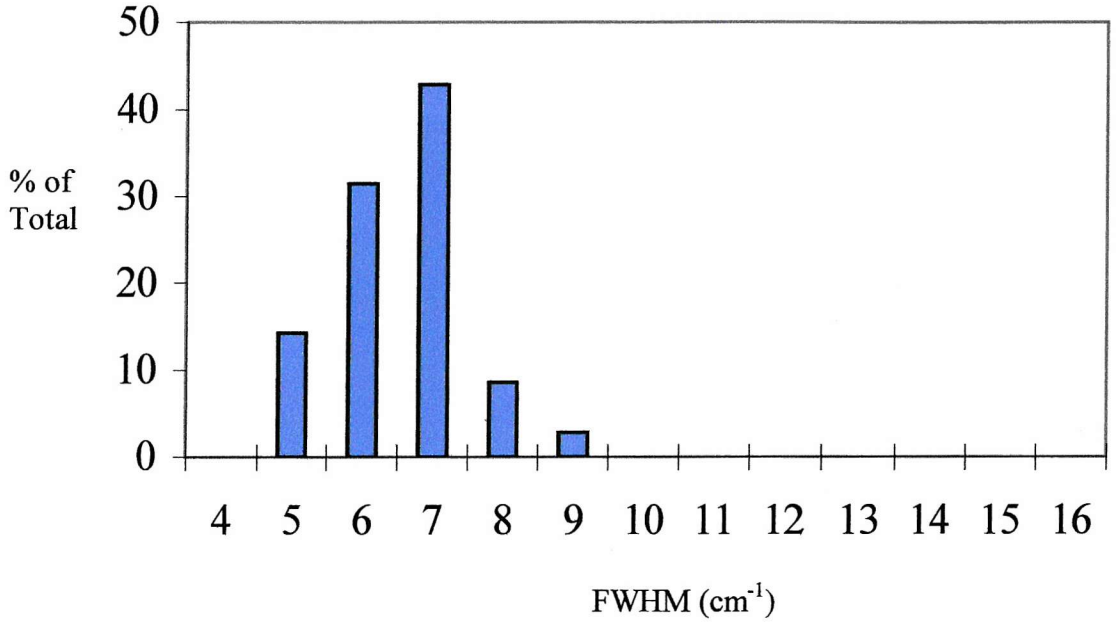

Fig. 7.8: Histogram showing distribution in peak widths for a 120μm free-standing diamond film (nucleation surface).

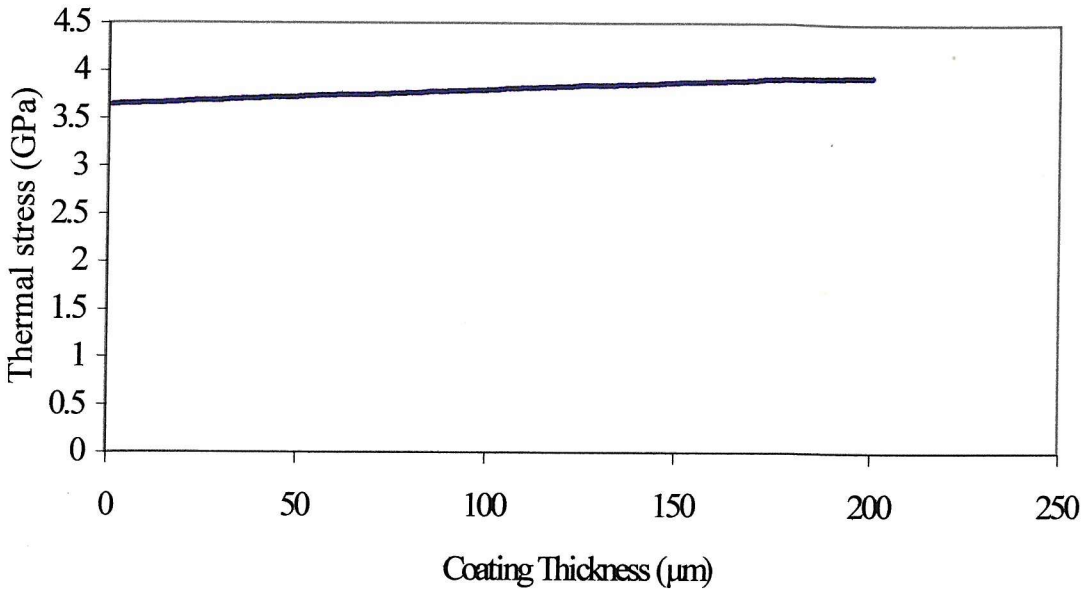

Fig. 7.9: Graph showing the variation of thermal residual stress, calculated using equation 7.2, with coating thickness for diamond coatings on 6mm thick tungsten substrates.

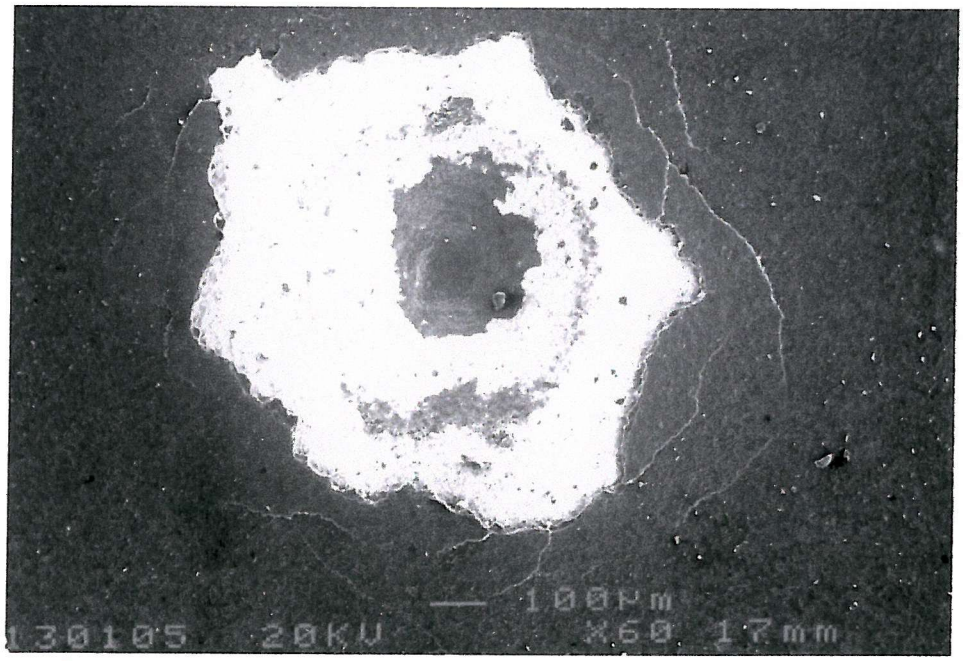

Fig. 7.10: Micrograph of Rockwell indent made in a 10μm diamond coating on tungsten at a load of 1471N.

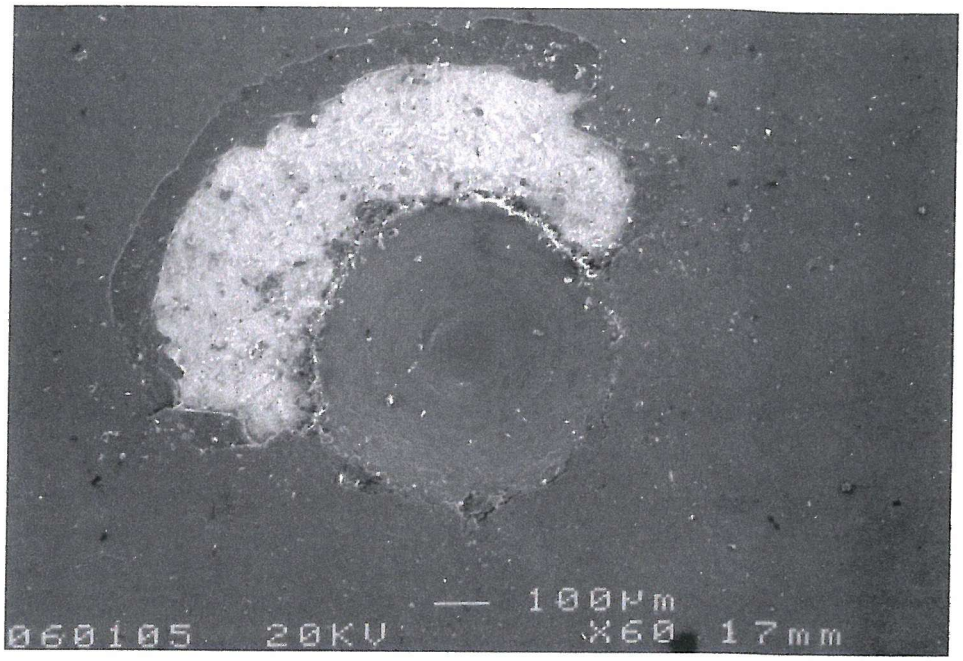

Fig. 7.11: Micrograph of Rockwell indent made in a 30µm diamond coating on tungsten at a load of 1471N.

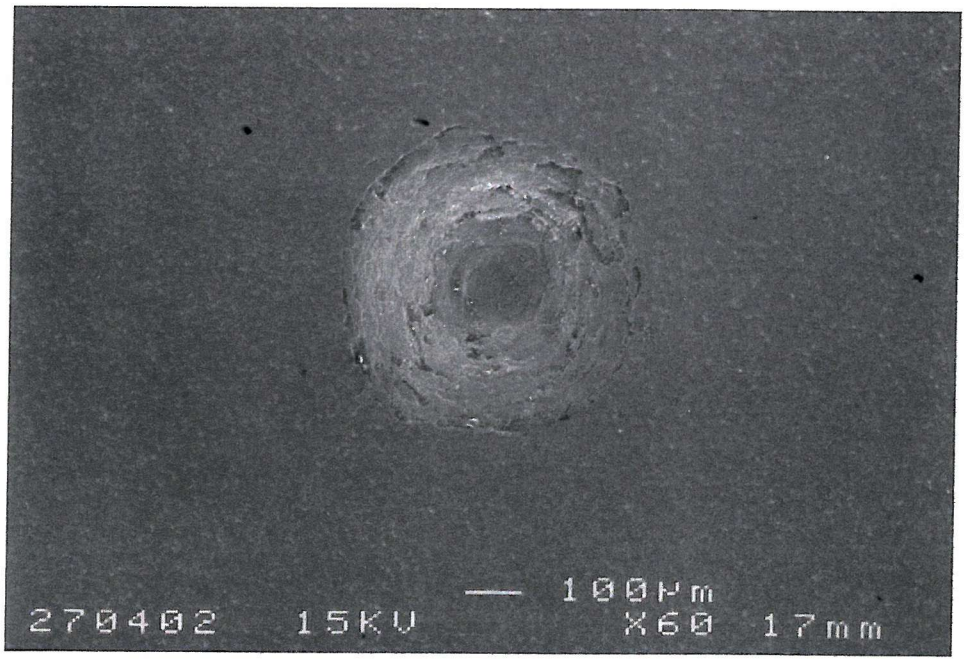

Fig. 7.12: Micrograph of Rockwell indent made in a 60µm diamond coating on tungsten at a load of 1471N.

8

EROSION PERFORMANCE OF CVD DIAMOND

8.1 Erosion Rates

The results of the tests comparing CVD diamond with the other materials are listed in Table 8.1. They show that, at 268 m s^{-1}, the erosion rate of 39-47 μm CVD diamond was still approximately 6 times lower than WC-7Ni, the most erosion-resistant grade of sintered tungsten carbide that was tested. When compared with the more common WC-6Co, the margin of superiority of CVD diamond is even greater, being approximately an order of magnitude. Diamond coatings ≤ 33μm in thickness were insufficient to resist particle impacts at the highest velocity (268 m s^{-1}), and failure began to occur before steady-state erosion conditions had become established.

Velocity (m s^{-1})	Kinetic Energy, E_k (μJ)	V_u (μm^3 $impact^{-1}$) 45μm CVDD on W	V_u (μm^3 $impact^{-1}$) WC-7Ni	V_u (μm^3 $impact^{-1}$) SS Type 316
16*	0.49	Not tested	0.013	0.55
28*	7.5	0.09	0.52	18
63	20	0.2	7.03	70.4
148	110	1.0	20.1	470
268	360	4.1	25.6	1968
Energy Exponent, m, (Dimensionless)	N/A	0.98	1.21	1.24

Table 8.1: Erosion rates versus particle velocities. Key: * = Tests conducted in the water-sand slurry rig.

The results of the erosion tests have been plotted against particle kinetic energy, E_k in Figure 8.1. They allow the performance of different materials to be compared over a wide range of test conditions, independent of particle size or velocity. Some materials have different relative performances as the test severity varies. Figure 8.1 shows such a

plot containing the data from Table 8.1 in graphical form. It shows that the steady state erosion rate of diamond appears to be dependent on E_k.

Diamond Coated Sample	Thickness (μm)	Surface Condition	Erosion Rate (μm^3 $impact^{-1}$)
A	60	As-grown	7.82
B	90	As-grown	6.96
C	120	As-grown	10.14
D	150	As-grown	10.43
E	200	As-grown	10.72
F	46	Lapped	4.10
G	60	Lapped	4.06
H	90	Lapped	3.77
I	120	Lapped	1.31
J	160	Lapped	2.89
K	87	As-grown	8.98
L	195	As-grown	11.59

Table 8.2: Results of the erosion tests of CVD diamond coatings

The energy exponents are also listed in Table 8.1. The equivalent velocity exponents ($2m$) of the diamond, tungsten carbide and stainless steel correspond to 1.96, 2.42 and 2.48 respectively. The value for stainless steel is in line with that predicted by Hashish (2.5) for ductile materials [1] while brittle materials are predicted to have exponents closer to 2.0. However, as more than one size of sand was used in the tests these figures must be regarded as approximate figures. Nevertheless, the velocity exponent for diamond is within the range reported in other studies of brittle materials, for example by Feng and Ball [2]. In that study the velocity exponent of Al_2O_3 was dependent on the properties of the erodent, varying from 1.5 for more friable particles such as SiO_2 to 2.2 for harder and tougher particles, for instance SiC. However, another erosion study of 2mm free-standing CVD diamond by Davies *et al* [3] reported a velocity exponent of 3.4; the reasons for this are not known, though microstructural defects present in such thick samples may be partly responsible.

8.2 Effect of coating thickness on erosion performance

Table 8.2 lists the results of erosion rate, V_u, as a function of coating thickness for all diamond coatings tested at 268 m s^{-1} where steady state erosion conditions were established. They are shown in graphical form, for both the as-grown and lapped coatings in Figure 8.2. It can be seen that the as-grown coatings show a general increase in erosion rate with thickness. In contrast, the lapped coatings show little variation in V_u. A slight decline is observed as the thickness is increased from 60μm, reaching a minimum value for the 120μm coating before increasing again for thicker coatings (160μm). The lapped coatings also display significantly lower erosion rates than as-grown coatings of the same thickness. In order to assess reproducibility of the erosion rates, the erosion tests of lapped 60μm and 120μm coatings were repeated. They show that a high level of reproducibility is possible (±15%), as can be seen in Figure 8.3. The reason for the minima in erosion rate at a thickness of 120μm is, at present, unclear. Overall, the range of erosion rates for the lapped coatings (1.3 to 4.1 μm^3 $impact^{-1}$) is small and, at 268 m s^{-1}, represents an improvement in erosion resistance of at least six times that of cemented tungsten carbide. Table 8.3 lists a more comprehensive comparison of CVD diamond with more reference materials at the highest velocity, 268 m s^{-1}. The figures for CVD diamond represent the best figures for those groups. The bar chart in Figure 8.4 shows the comparative performances of these materials in graphical form. Although these materials do not have the same surface roughness the overall range of R_a values is small. Previous work by Wheeler and Wood [4] on WC-Co-Cr coatings showed that over the R_a range 0.01 to 0.2 the influence of surface roughness on erosion rate was minimal.

For both lapped and as-grown coatings the range of erosion rates, as a function of coating thickness (and thus grain size), is small. However, the lapped samples display significantly lower values as well as different trends with increasing coating thickness. There are two reasons for the poorer performance of the as-grown CVD diamond coatings. The first is that the contact pressures generated by the sand impacts on the as-grown surface will be greater than the lapped surfaces due to the lower actual contact area. The differences in the impact situation between as-grown and lapped coatings are shown in schematic form in Figure 8.5. Secondly, the surface roughness values of the as-grown coatings are greater: therefore the critical crack length for material removal from asperities is reduced, thus making it easier for pieces of the coating to be removed

by chipping. Moreover, as seen in Figure 8.2, the as-grown CVD diamond coatings show an increase in erosion rate with thickness. This is due to the increasing grain size: the tensile strength generally increases with $d_g^{-1/2}$, where d_g is the grain size [5]. The size of the intrinsic flaws is greater in larger grains and, therefore, the probability that a critical flaw is present is also increased. For the lapped coatings, the graph of V_u against coating thickness indicates that the optimum thickness is in the region of 120μm, where the erosion rate is 1.31 ±0.15 μm^3 $impact^{-1}$.

Material	Erosion Rate (μm^3 $impact^{-1}$)
CVD Diamond on W (lapped) (120μm)	1.31
CVD Diamond on W (as-grown) (60μm)	6.96
PCD (1mm layer on WC)	16.2
WC-7Ni	25.6
WC-6Co	39.2
Stainless Steel Type 316	1,370

Table 8.3: Table of comparative erosion rates for diamond and other materials tested at 268 m s^{-1}.

Parameter	Tungsten	Tungsten carbide-6% Co
Hardness (H_v)	400	1540
Elastic Modulus (GPa)	411	624
Yield strength (MPa)	725	-
UTS (MPa)	900	3000*
Fracture Toughness (MPa$\sqrt{m}$)	50	9.8
Poisson's ratio	0.28	0.22
Density (kg m^{-3})	19320	14970

Table 8.4: Comparison of the mechanical properties of tungsten and cemented tungsten carbide. N.B. * = 3 point bend flexural strength.

8.3 Effect of substrate material on erosion rate

The majority of the coatings described in this study have been deposited on tungsten substrates. However, for choke valves, cemented tungsten carbide is the most widely used trim material and is a more suitable substrate due to its superior mechanical properties. For the purposes of comparison Table 8.4 lists some relevant mechanical

properties of the two materials. The deposition of diamond on tungsten carbide can present other challenges, the most prominent being the presence of Co or Ni as binders in cemented WC as they can catalyse the formation of graphite. The effect of the substrate on erosion performance was investigated by comparing as-grown coatings of comparable thickness: 90μm and 200μm coatings on W and 87μm and 195μm coatings on WC-6Co. As shown in Figure 8.2 the results show a higher erosion rate for the diamond films deposited on WC than on W. The principal reason for this is thought to be its higher surface roughness, indicating the presence of larger grains of reduced strength. In order to assess the adhesion strength of the coatings, it will be necessary to continue the tests and determine the time to failure.

8.4 Coating behaviour during the test

The graph showing the relationship between cumulative mass loss against time of a 46μm coating tested in the air-sand rig can be seen in Figure 8.6. This graph consists of three distinct stages, which are shown in schematic form in Figure 8.7. They can be used to describe the erosion process of the diamond. Stage 1, the initial non-steady state region; Stage 2: the steady state region and Stage 3: coating failure.

During Stage 1, the most prominent areas of the coating surface are removed by a micro-chipping action. This occurs both on lapped, as well as as-grown, coatings, though in the former case it is on a much smaller scale. In general, this stage does not account for a significant percentage of the overall coating life. An example of the chipping features can be seen in Figure 8.8, which shows the lapped surface of a 120μm coating after four hours at 268 m s^{-1}. The untested surface is also included for comparison. Figure 8.9 shows the equivalent micrographs for an as-grown 90μm coating.

The process of micro-chipping continues in stage 2, the steady state region, though the erosion rate in stage one has reduced to a steady state value of 4.1 μm^3 $impact^{-1}$. In this stage, which forms the majority of the coating life, the chipping process is the main contributor to the value of the erosion rate. The gradient of the line in Stage 2 corresponds to the steady state erosion rate of the coating. However, a more significant feature of this stage is the formation in the coating of circumferential cracks and pin-holes within the area of particle impact. An example of a circumferential crack is

shown in Figure 8.10, while pin-holes are shown in Figures 8.11 and 8.12. In most erosion tests, pin-holes are generally first observed by the time one-third of the coating life has elapsed (i.e. $t_f \approx 0.3$, where t_f is time to failure). They do not form all at once but steadily increase as the particle impacts continue. Circumferential cracks and pin-holes were seen on coatings tested at all angles.

As the particle impacts continue, the pin-holes increased in both number and depth; in some cases complete penetration of the coating has been observed, as in Figure 8.13. Pin-holes have not been reported in any other erosion studies of CVD diamond coatings. In the test of the 46μm coating, macroscopic evidence for their formation was first seen after 1 hour. No acceleration in the erosion rate was associated with the appearance of this feature. Pin-holes were also seen in as-grown coatings, examples of which can be seen in Figures 8.14 to 8.16. It is interesting to note that the size of the pin-hole is considerably greater than the grain size of the coating and that grain boundaries appear to have little effect on the shape of these holes. Cracking appears to be trans-granular.

Figure 8.17 shows the cumulative mass loss of a 60μm coating together with the number of observed pin-holes against time. It is instructive to ascertain the influence of pin-hole nucleation and growth on the value of the steady state erosion rate, V_u. Figure 8.18 shows a typical pin-hole on the surface of this coating. The diameter of the region where material has been removed is approximately 150 μm. For simplicity, the volume lost in the centre of this pin-hole was treated as a hemisphere. The volume of a hemisphere of these dimensions was calculated to be 8.84×10^{-13} m^3, which corresponds to a mass of 0.003 mg. The smallest mass loss detectable by the precision balance is 0.01mg. Therefore, 4 pin-holes of this size are required to form before the mass loss can be detected. After erosion testing at 268 m s^{-1} for 5 hours, the number of pin-holes observed in the coating, by optical microscopy, was 19. Therefore, assuming the mass of each pin-hole to be 0.003 mg, this gives a total of 0.057 mg. As the total mass loss of the coating over the five hour test was 1.28 mg, the total mass loss attributable to the pin-holes corresponds to 4.4% of the total mass loss of the coating. Therefore, the nucleation and growth of pin-holes is not a significant contributor to the mass loss, and hence the steady state erosion rate.

The third and final stage of the erosion process is failure of the coating, which occurs catastrophically by spalling at the coating-substrate interface. An examination of the failed region indicated that the coating was removed in stages. The coating initially fails in the centre of the erosion scar, leading to the surrounding coating becoming undermined. This caused the delaminated region to spread progressively away from the centre until the entire coating was removed. As will be seen in Chapter 10, the coatings become more delaminated throughout the test prior to failure. An increase in the area of delamination results in a reduction in the interfacial fracture toughness and, hence, the stress required for further delamination is also reduced.

Close inspection of the failed coating samples suggests that the "weakest link" in the system is not the coating itself but the bond between the coating and the substrate. Surface profilometry of the edge of a spalled region on a coating revealed the step at the edge was 46μm: the thickness of the coating. Moreover, examination of the area where the coating had been removed revealed that scratches were visible. These scratches were thought to have been generated in the substrate by the pre-deposition treatment. These two findings, coupled with the fact that no traces of the coating were found on substrates where the coating had been removed, indicate that failure of the diamond film occurred directly at the coating-substrate interface.

8.5 Effect of thickness on coating life

It has already been seen in a previous section that coatings of ~40μm in thickness have an erosion rate of approximately an order of magnitude lower than sintered tungsten carbide at the highest velocity. However, a characteristic of hard coatings is that they often fail suddenly and catastrophically under erosive conditions. Prior to this they may not exhibit any indications of imminent failure. Therefore, although the steady state erosion rates of the diamond coatings are more than 10 times lower than the various WC grades, this does not provide any indication as to the life of the coating. For real components, for instance choke valves, time to failure (t_f) may be a more useful parameter with which to assess and compare coatings. The "weakest link" in the coating system is often the coating-substrate interface, rather than the coating itself. Therefore, t_f could also provide a measure of coating adhesion. Indeed, erosion has already been used to assess the adhesion of diamond coatings to WC-Co substrates. Schneider *et al* [6] used a commercial sandblast unit to subject the coatings to 90-

125μm diameter Al_2O_3 particles (the velocity was not specified) at an impact angle of 90°. The minimum time to detach the diamond coating from the substrate, termed the "critical blasting time", was used to compare the different coating samples.

The results are listed in Table 8.5 and plotted in graphical form in Figure 8.19. They show that the time to failure of the diamond coatings increased with thickness from 5 minutes (10μm) to 31 hours (120μm). A considerable increase in time to failure as the coating thickness was increased from 33μm to 46μm. For instance, the life of the 46μm coating is more than double that of the 33μm coating. The 120μm coating did not fail until 31 hours had elapsed, i.e. more than 10 times that of the 46μm coating. The results indicate an approximately exponential relationship between coating thickness and time to failure. The reasons for the increased life with thickness will be explored in Chapter 11.

Coating thickness (μm)	Time to failure (mins)
10	5
17	8
33	80
46	185
120	1860

Table 8.5: Results from the erosion tests conducted on lapped diamond coatings on tungsten at 268 m s^{-1}, showing the effect of coating thickness on time to failure of the coating.

The results above appear to support the conclusions made in Chapter 7 that residual stress does not significantly affect the erosion performance. If a large increase in residual stress with increasing coating thickness was seen it is unlikely that the time to failure of the thicker coatings would continue to increase in the manner that has been observed. It is instructive to compare these results with those of Brookes *et al* [7], which were described in Chapter 2. In that case, residual stress was attributed to be the cause of the poor performance of the coatings greater than 48μm in thickness.

8.6 Comparison of different types of CVD diamond

For tribological applications, an alternative to depositing a diamond coating onto a component is to bond free-standing diamond to components by brazing or gluing. This approach can often be easier, for instance where the substrate composition presents difficulties in the deposition of adherent diamond films. In erosion tests of choke valves, described by Wheeler *et al* [8], free-standing diamond 600μm thick was bonded to the tungsten carbide valve trim using a high temperature adhesive. The complex geometry prevented deposition of diamond films onto the trim components. Therefore, it is useful to compare the erosion behaviour and damage mechanisms observed in a bonded free-standing diamond and a diamond coating deposited directly onto a substrate.

Free-standing diamond, 600μm in thickness, which had been brazed to a tungsten carbide substrate, was compared with a 60μm coating, deposited directly onto a tungsten substrate. Both samples were lapped to a surface roughness (R_a) of 0.2μm. The samples were tested at the highest velocity, 268 m s^{-1}, for 5 hours. All other test conditions are identical to those described for the samples above.

The results, listed in Table 8.6, show that both types of diamond have considerably greater erosion resistance compared with the cemented tungsten carbide. The steady state erosion rates of the diamond samples were between 12 and 30 times lower than tungsten carbide. What is also notable is that the CVD diamond coating has an erosion rate approximately 2.4 times lower than the brazed free-standing diamond. However, as will be demonstrated in Chapter 10, steady state erosion rate is not the most useful guide to comparing the performance of coatings.

On the 60μm coating, in addition to micro-chipping, pin-holes were observed, an example of which has already been seen Figure 8.18. In the present case, the first pin-holes were observed after 1 hour and were seen to steadily increase in number throughout the remainder of the test. No pin-holes were seen on the brazed diamond and the erosion damage was restricted to micro-chipping. As will be seen in Chapter 10 the appearance of pin-holes is related to the development of sub-surface debonding at the coating-substrate interface. The greater thickness and adhesion of the brazed diamond sample has prevented debonding, and thus no pin-holes are observed on this

sample. Figure 8.20 shows the eroded surface of this sample. It shows regions where material has been removed from the specimen. These pieces appear to be approximately about 20μm. This is in contrast to the CVD diamond coating where, apart from the pin-holes, the incidence of chipping was considerably smaller.

The difference in erosion rate between the two samples is thought to be principally due to the difference in grain size, and hence intrinsic flaw size. The grain size of the 60μm coating is between 20 and 40μm. In contrast the grain size of the 600μm free-standing diamond is approximately 200μm. Therefore, the intrinsic flaw size of the brazed diamond will be greater than that in the coating. Previous studies have indicated that strength-controlling flaws of similar size to the crystal grains are present in CVD diamond [9]. Therefore, it is likely that the greater intrinsic flaw size of the brazed diamond may render it more susceptible to erosion from micro-chipping. However, the difference in erosion rates is still small when compared with the values of other materials, for instance sintered tungsten carbide.

Material	Erosion Rate, V_u (μm^3 $impact^{-1}$)
Brazed 600 μm CVD Diamond	2.95
60 μm CVD Diamond Coating on Tungsten	1.22
WC-5.67 Ni-0.33Cr	37.2
WC-4Ni-3.2Co-0.8Cr	37.2

Table 8.6: Steady state erosion rates of the materials tested at 268 m s^{-1}.

8.7 Conclusions

1. The erosion performance and behaviour of 10-200μm CVD diamond films have been investigated and compared with other hard materials that are currently used in choke valve trims.
2. The results show that, at 28 m s^{-1}, diamond films of thickness less than 15-20 μm are insufficient to withstand the stresses generated by sand particle impact at all velocities and fail rapidly and catastrophically.
3. As the velocity is increased, thicker coatings are required in order to confer enhanced resistance to particle impact. At 268 m s^{-1}, coatings ≤ 33μm began to fail before steady state erosion conditions were established.

4. The results of the tests show that at 268 m s^{-1} the erosion rate of 39-47μm CVD diamond on tungsten was still 6 times lower than cemented WC-7Ni. However, the coating had a tendency to fail catastrophically when large pieces became detached at the coating-substrate interface.
5. The erosion rates of thick CVD diamond coatings having a lapped surface are more than an order of magnitude lower than cemented tungsten carbide at a particle velocity of 268 m s^{-1}. They therefore represent a significant improvement in erosion resistance. The test results also show that a coating with a lapped surface has an erosion performance approximately three to four times better than an as-grown surface of comparable coating thickness.
6. For lapped coatings between 60μm and 160μm the erosion rate is essentially independent of thickness. The optimum coating thickness at 268 m s^{-1}, using 194μm diameter sand, appears to be in the region of 120μm.
7. During the erosion tests of the coatings the damage accumulation process can be divided into three stages. They are: (i) Initial period prior to steady state erosion where micro-chipping takes place; (ii) Steady state period where the micro-chipping is augmented by the nucleation of circumferential cracks and pin-holes and development of debonded areas at the coating-substrate interface; (iii) Failure of the coating.
8. The mass loss associated with the formation of pin-holes has been estimated to account for less than 5% of the total mass loss. Therefore, the value of the steady state erosion rate is primarily a product of surface micro-chipping.

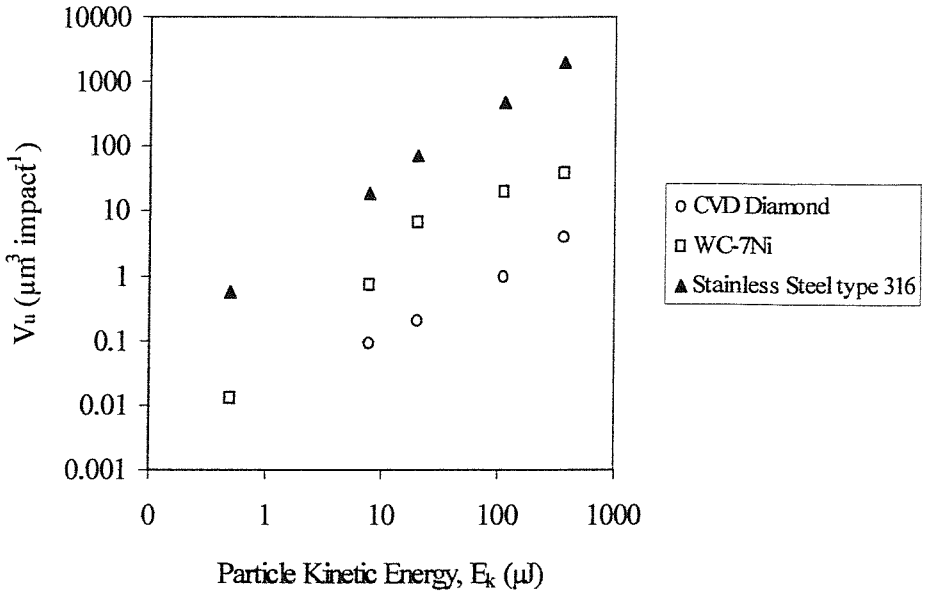

Fig. 8.1: Graph showing the relationship between Erosion Rate, V_u, and Particle Kinetic Energy, E_k, for lapped CVD diamond coatings (39-47μm in thickness) on tungsten, sintered tungsten carbide and stainless steel type 316. The range of kinetic energy values corresponds to a velocity range from 16 – 268 m s^{-1}.

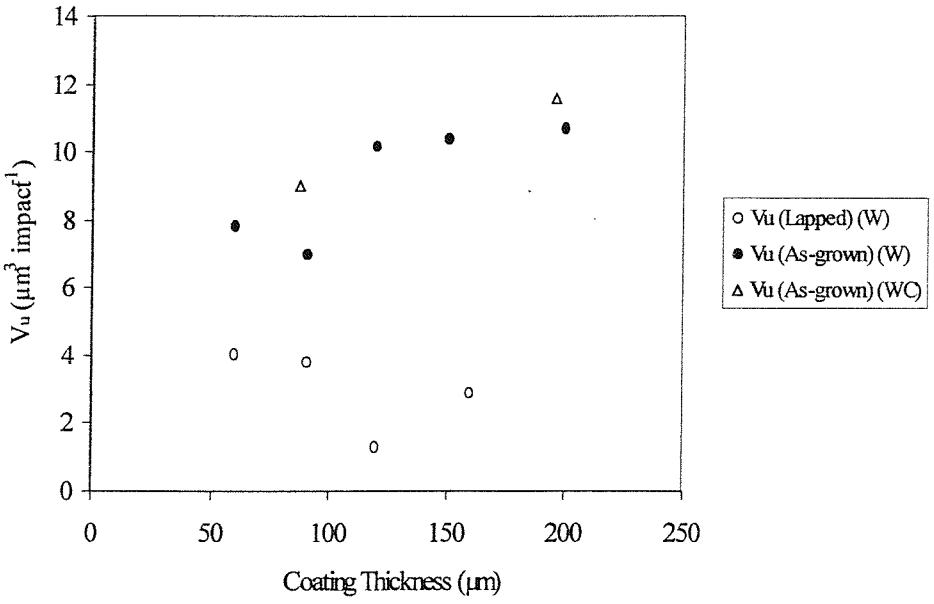

Fig. 8.2: Graph of erosion rate, V_u, vs. coating thickness for as-grown and lapped CVD diamond coatings on tungsten and two as-grown CVD diamond coatings on WC-6Co, erosion tested at a velocity of 268 m s^{-1}.

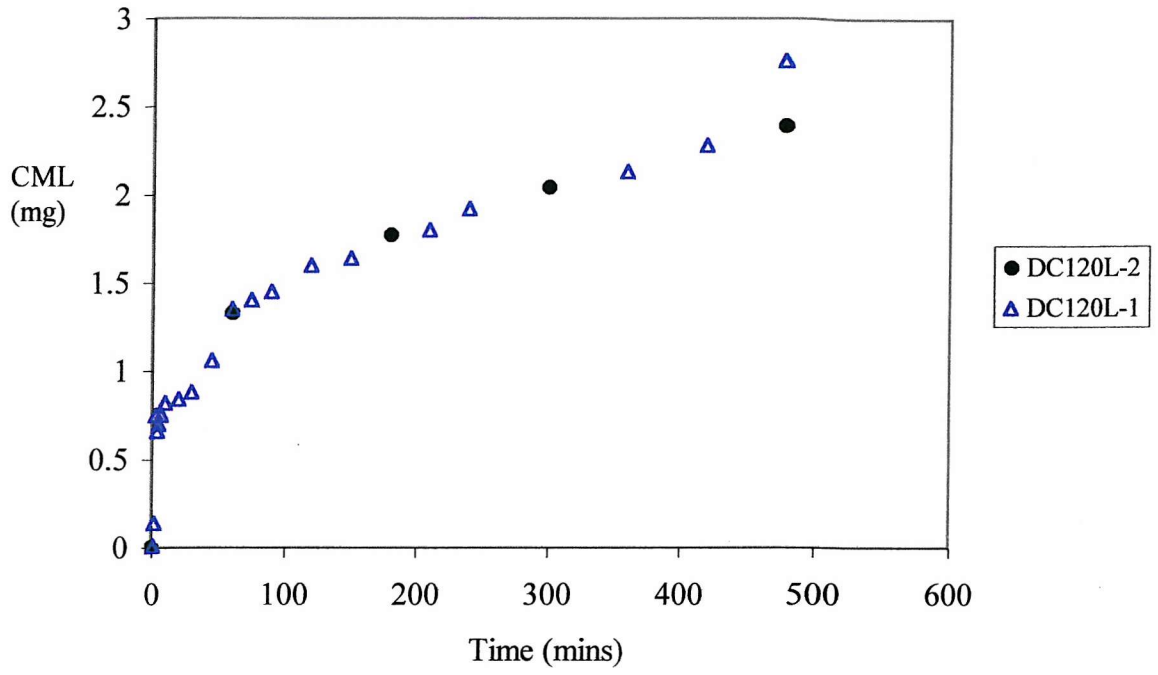

Fig. 8.3: Graph of Cumulative Mass Loss (CML) vs. Time for two 120μm lapped CVD diamond coatings on tungsten, erosion tested at 268 m s^{-1}.

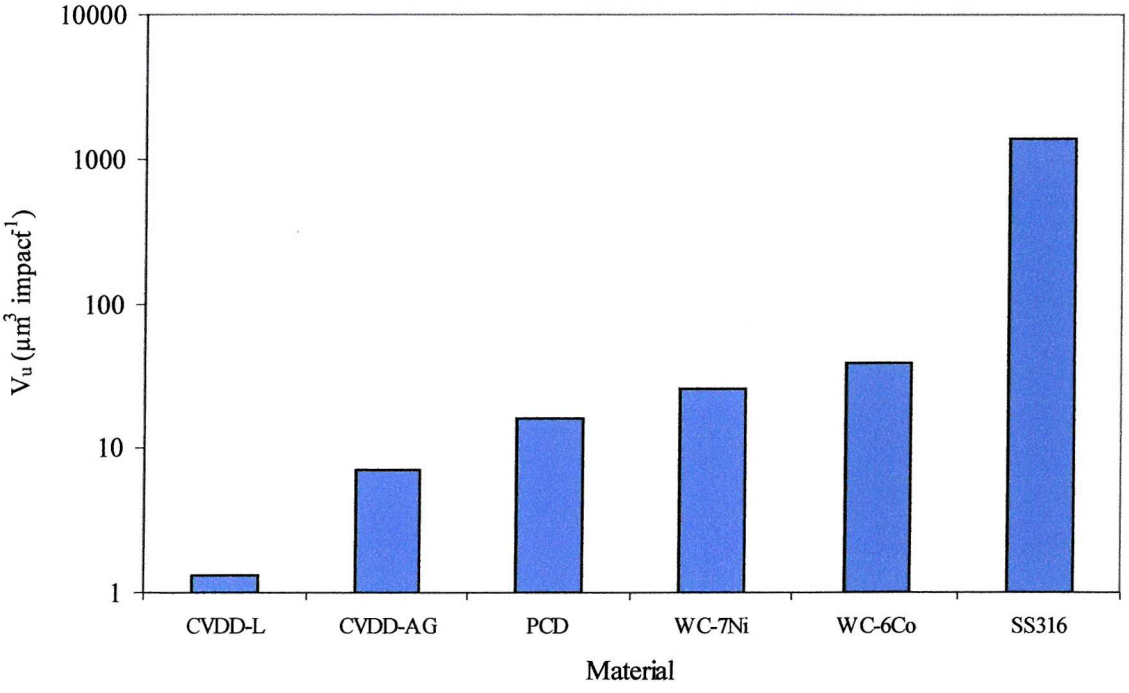

Fig. 8.4: Bar chart showing the comparative erosion performance at 268 m s^{-1} of CVD diamond, together with the reference materials.

a

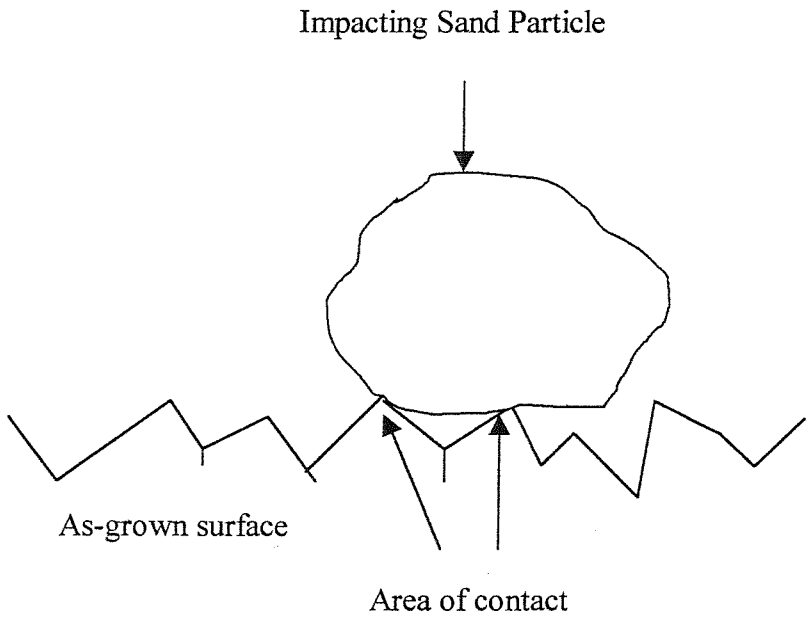

b

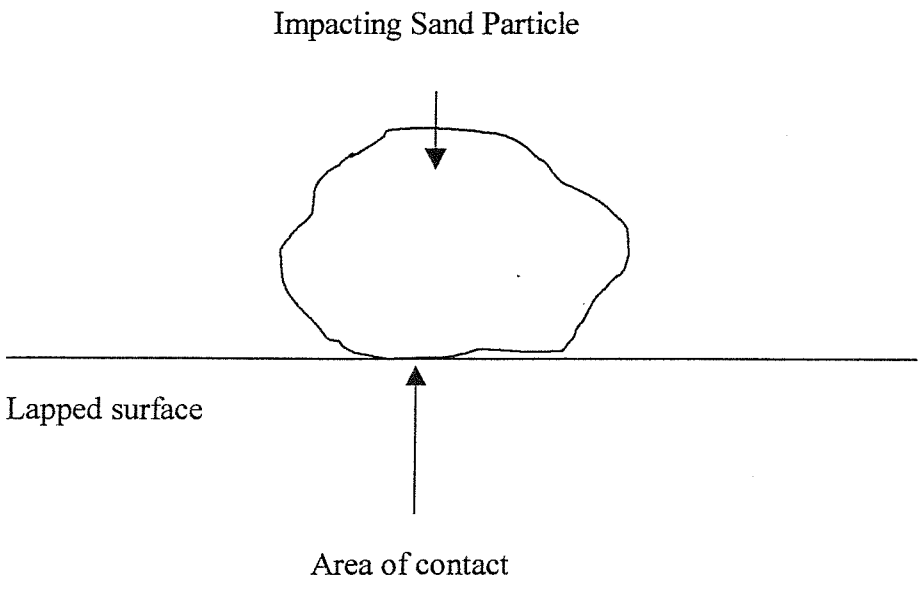

Fig. 8.5: Schematic diagram showing the differences in contact area during the impact of a sand particle with (a) an as-grown surface; and (b) a lapped surface, of a CVD diamond coating. Drawing not to scale.

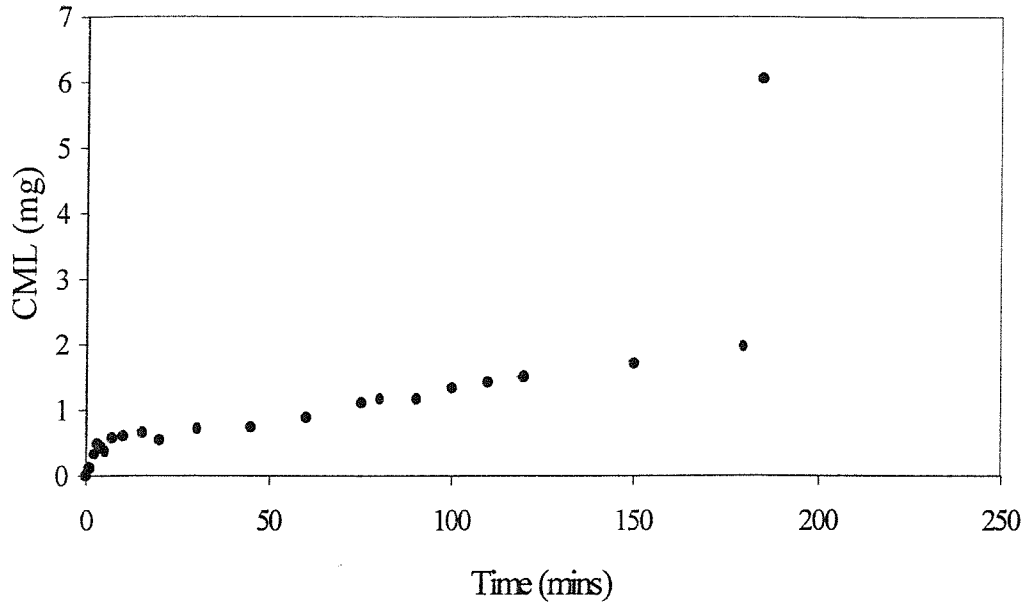

Fig. 8.6: Graph of Cumulative Mass Loss vs Time for a lapped 46μm CVD diamond coating on tungsten tested at 268 m s^{-1}.

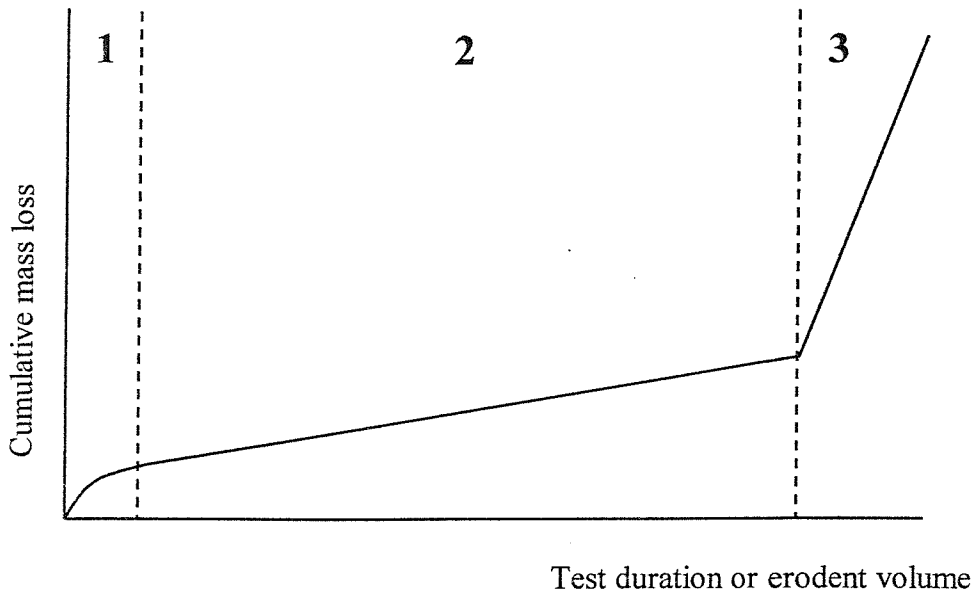

Fig. 8.7: Schematic diagram of the erosion history of a CVD diamond coating, showing the three distinct stages of the erosion process.

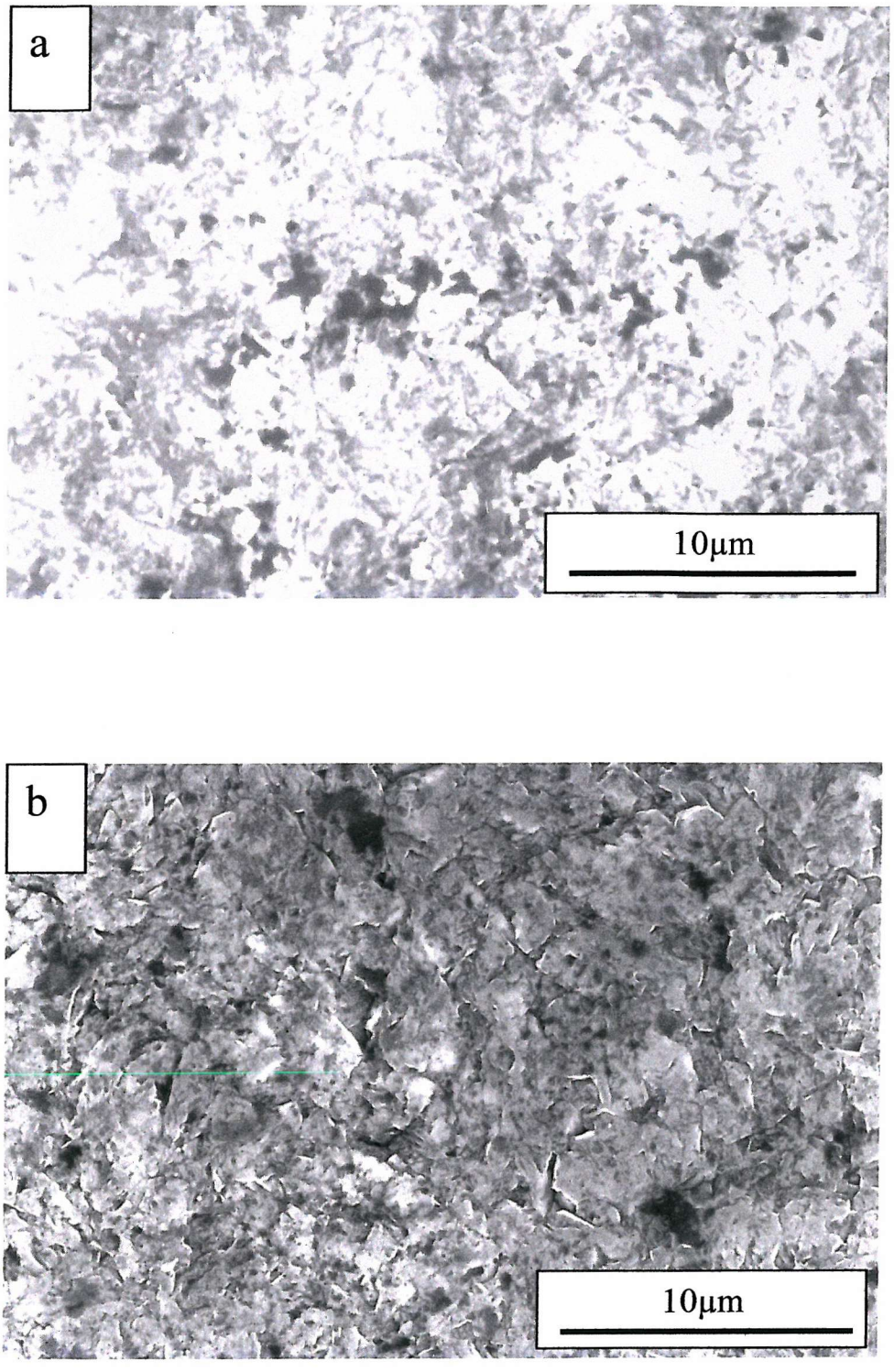

Fig. 8.8: SEM micrographs of a lapped 120μm CVD diamond coating on tungsten showing (a) the untested surface and (b) the eroded surface after 4 hours at 268 m s^{-1}.

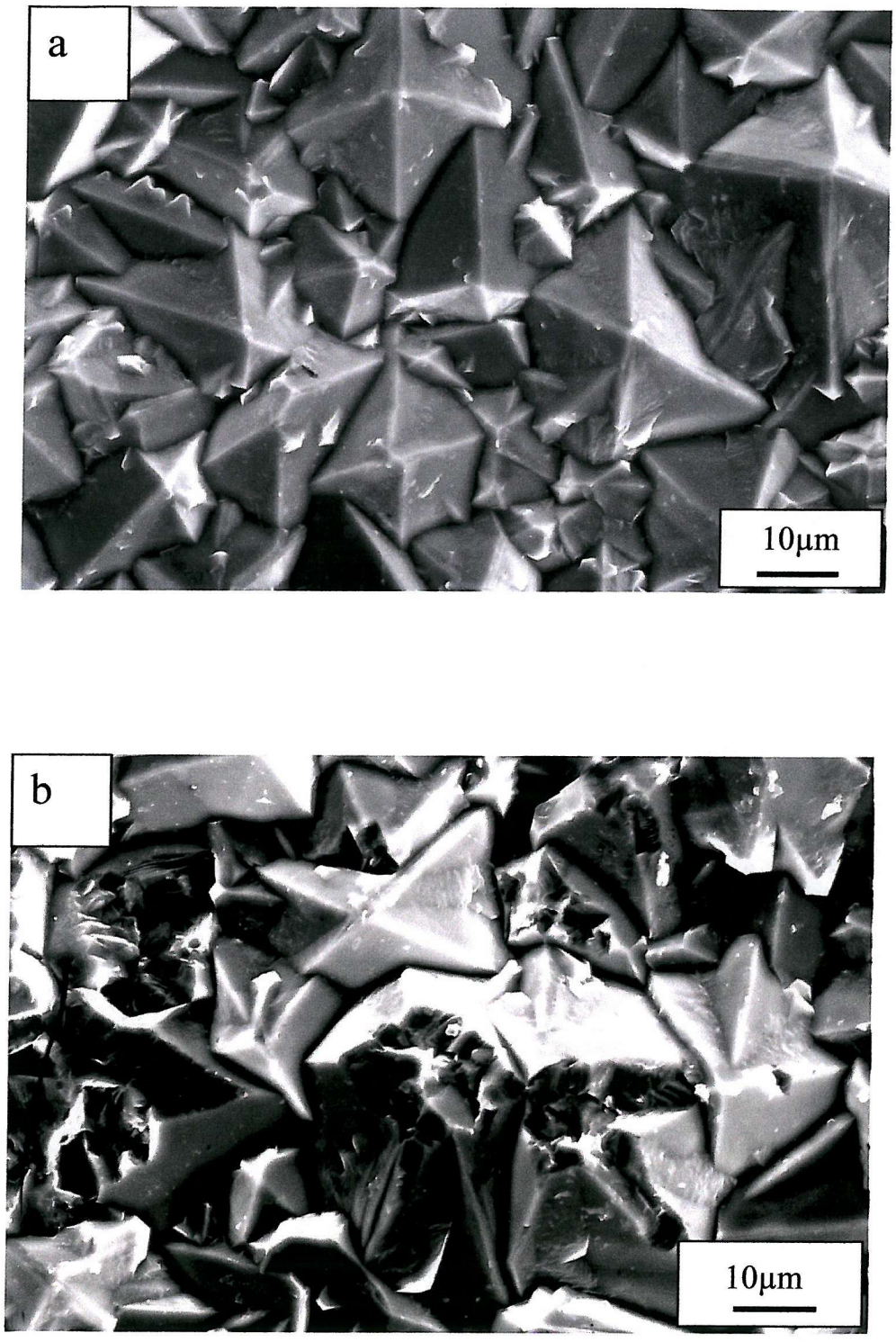

Fig. 8.9: Micrographs of an as-grown 90μm CVD diamond coating on tungsten showing (a) the untested surface and (b) the eroded surface after 1 hour at 268 m s^{-1}.

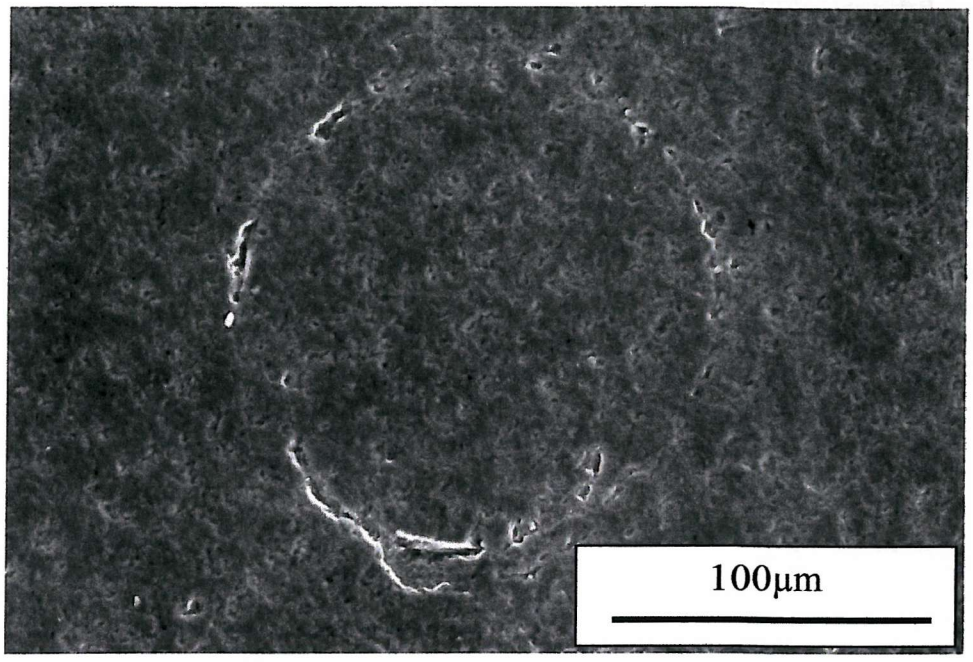

Fig. 8.10: Micrograph from a lapped 46μm diamond coating on tungsten, erosion tested at 268 m s^{-1} for 3 hours, showing a circumferential crack, which is a precursor to a pin-hole.

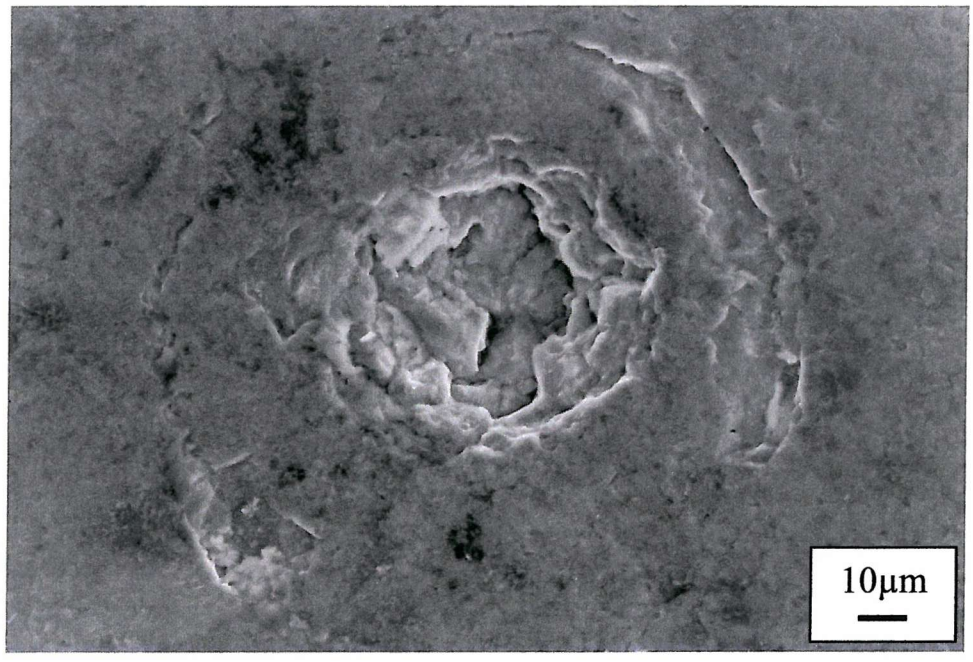

Fig. 8.11: Micrograph from a lapped 33μm diamond coating on tungsten, erosion tested at 268 m s^{-1} for 80 minutes, showing a circumferential crack, within which is a pin-hole in its early stages.

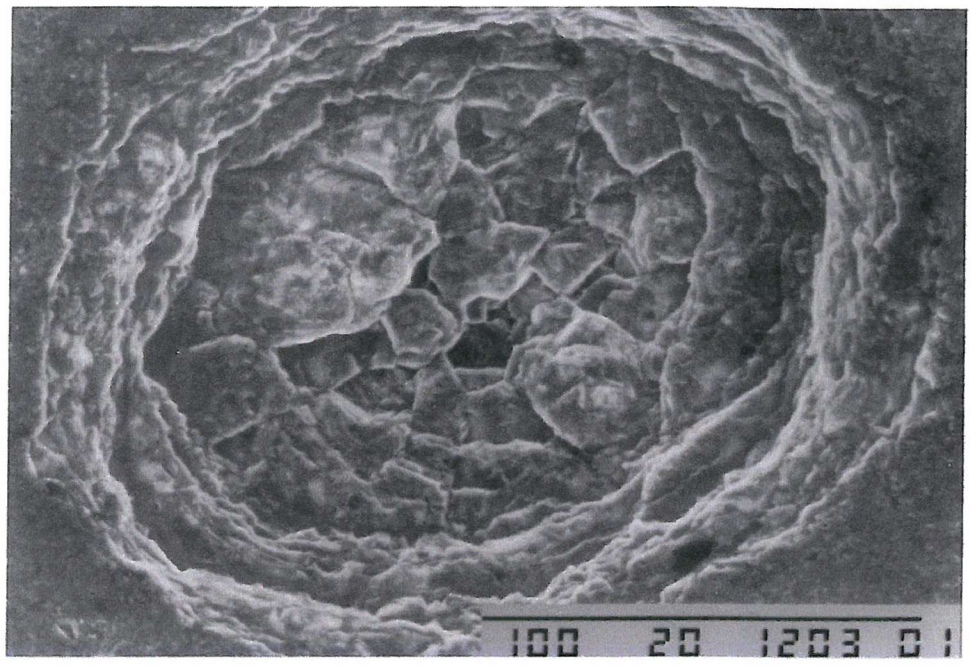

Fig. 8.12: Micrograph from the same sample as Fig. 8.10, showing a pin-hole which has partially penetrated the coating.

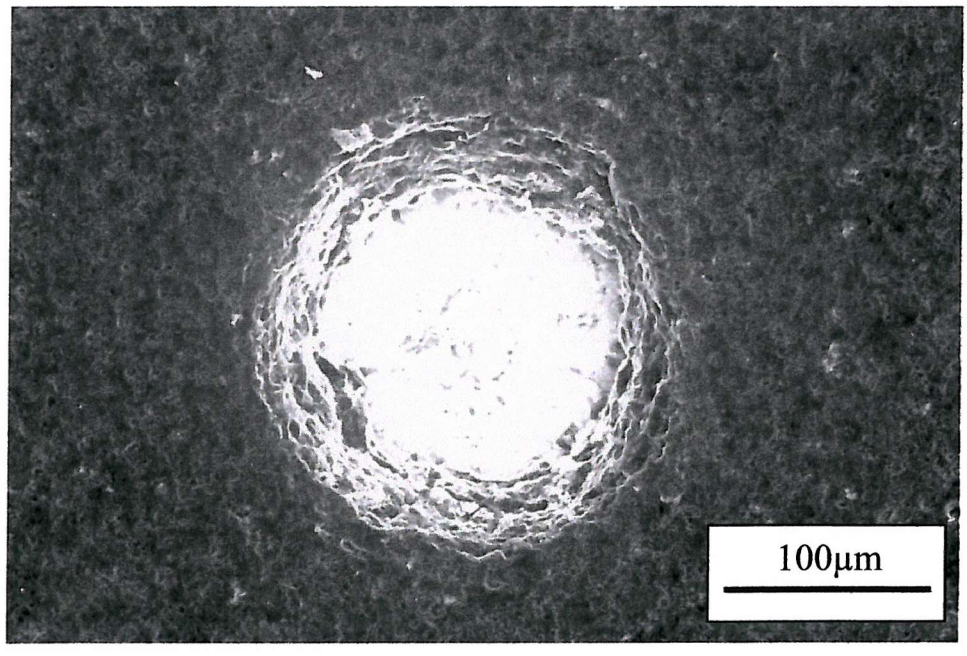

Fig. 8.13: Micrograph from a lapped 43μm diamond coating, tested at 268 m s^{-1}, showing a pin-hole which has completely penetrated the coating.

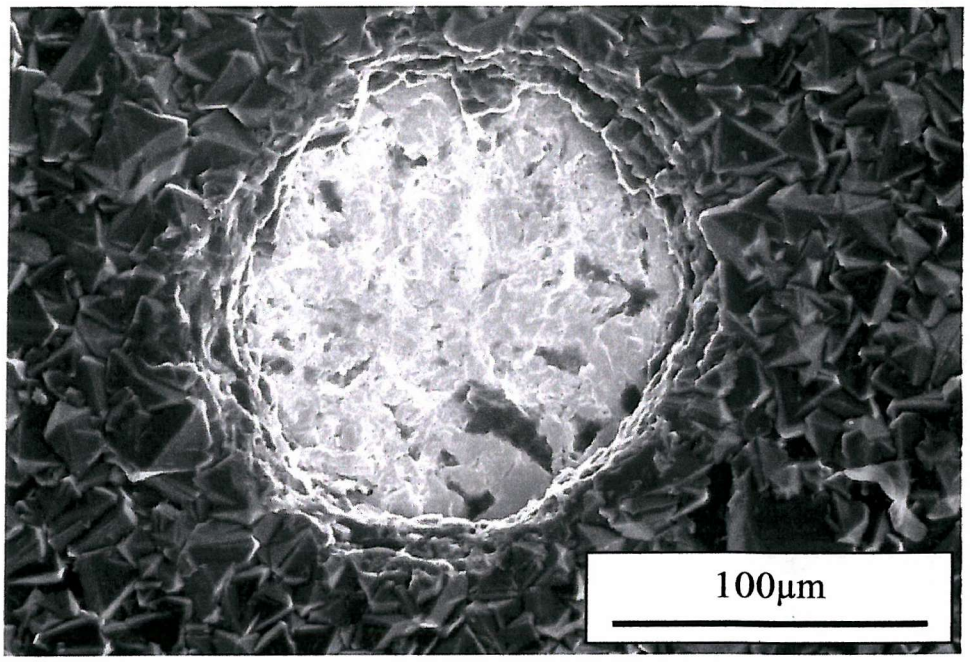

Fig. 8.14: Micrograph from a 30μm as-grown CVD diamond coating on tungsten, tested at 268 m s^{-1} for 30 minutes, showing a pin-hole which has penetrated the coating.

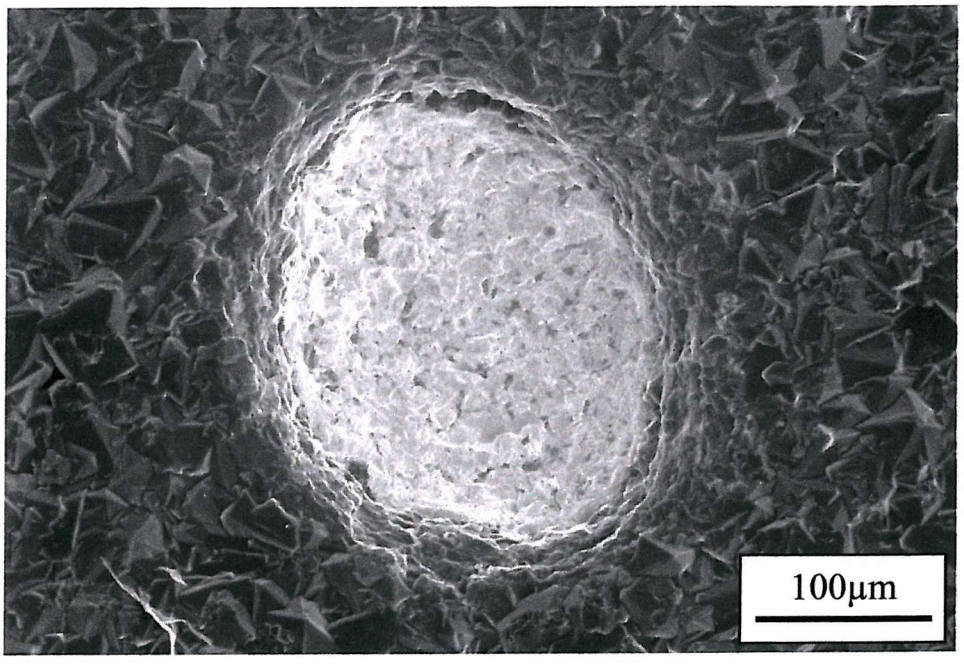

Fig. 8.15: Micrograph from a 60μm as-grown CVD diamond coating on tungsten, tested at 268 m s^{-1} for 1 hour, showing a pin-hole which has completely penetrated the coating.

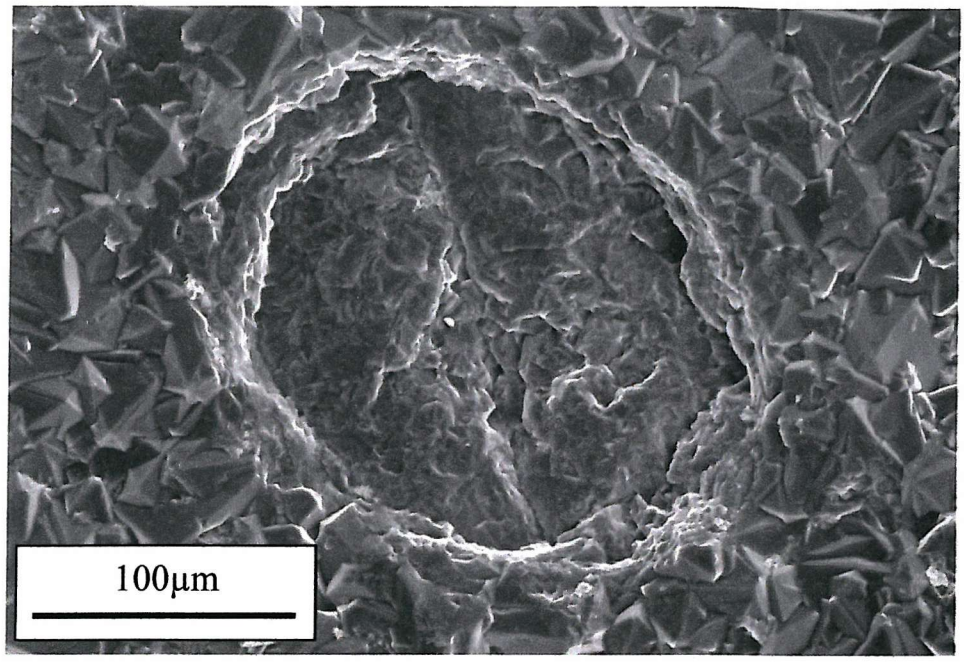

Fig. 8.16: Micrograph from a 60µm as-grown CVD diamond coating on tungsten, tested at 268 m s^{-1} for 1 hour, showing a pin-hole which has partially penetrated the coating.

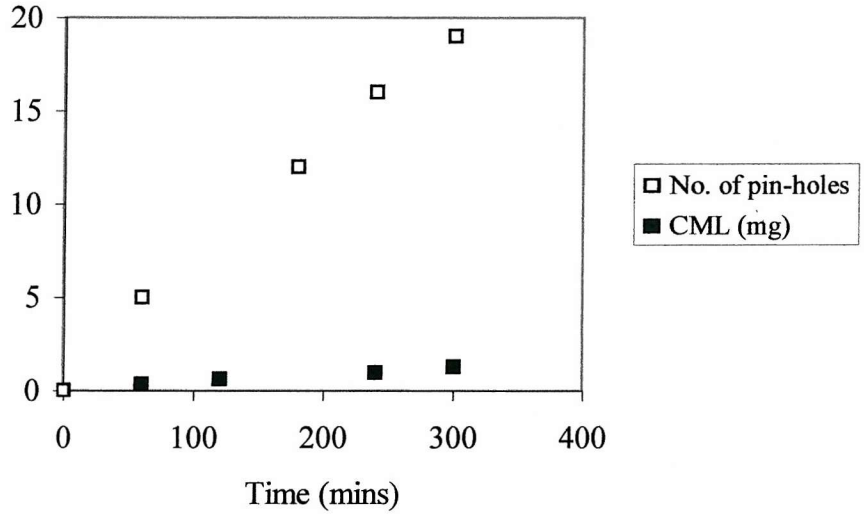

Fig. 8.17: Graph showing cumulative mass loss and number of pin-holes against time from a lapped 60µm diamond coating on tungsten tested at 268 m s^{-1} for 5 hours.

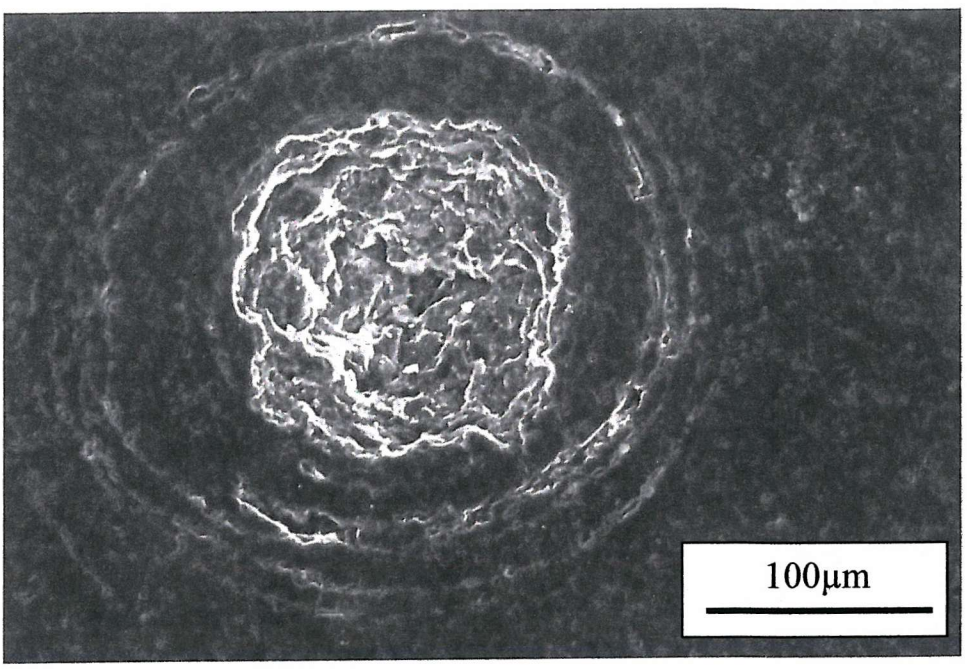

Fig. 8.18: Micrograph of a pin-hole on the surface of a lapped 60μm diamond coating on tungsten tested at 268m s^{-1} for 5 hours.

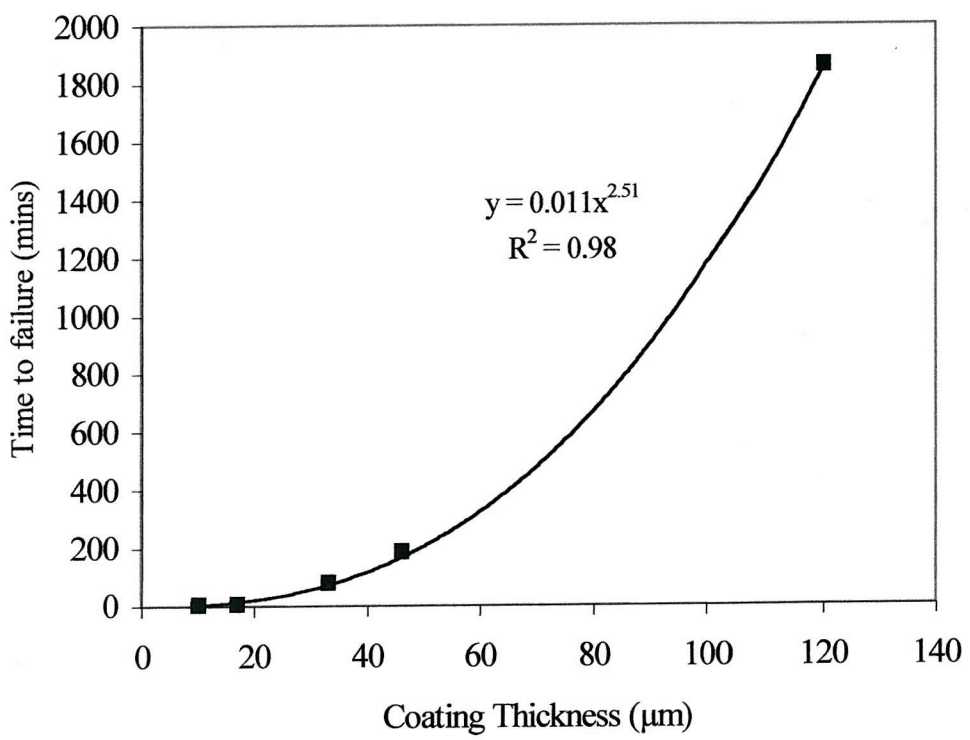

Fig. 8.19: Graph of Time to Failure (t_f) against Coating Thickness (C_T) for lapped diamond coatings.

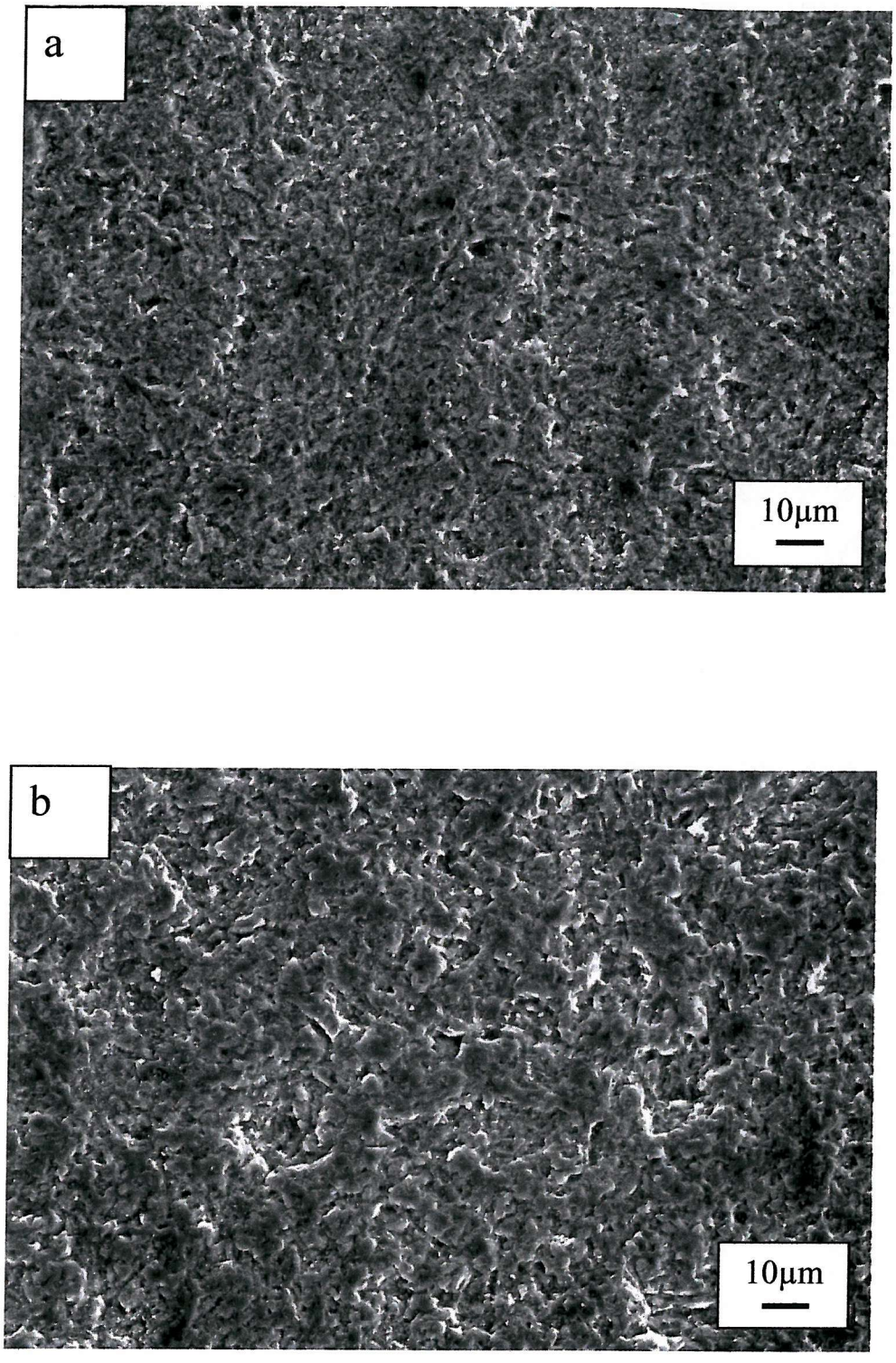

Fig. 8.20: Micrographs of a lapped 600μm free-standing diamond in (a) the untested condition; and (b) erosion at 268 m s^{-1} for 5 hours.

9

SURFACE EROSION DAMAGE

9.1 Introduction

In examining the erosion of CVD diamond it is important to understand the damage features observed and the mechanisms by which they are formed. It has already been seen that there are two surface damage features caused by the high velocity impact of sand particles on CVD diamond. They are (i) surface micro chipping; and (ii) circumferential cracks and pin-holes. This chapter considers these features and will attempt to explain the mechanisms by which they are formed. It will concentrate on the mechanism behind circumferential crack and pin-hole formation and the stages of growth following initiation. However, as surface micro chipping is the first feature seen during the erosion process, this will be considered first.

9.2 Surface micro chipping

Surface micro chipping is the main contributor to the steady state erosion rate of the coatings; examples of this type of damage have already been shown in Figures 8.8 and 8.9. It is the only feature of note on the surface of the diamond prior to the advent of the circumferential cracks and pin-holes. Erosion studies of other brittle materials have often reported radial and lateral cracks, which have not been seen in the present case. In order to understand the reasons for this it is necessary to consider the nature of the erodent and the target materials.

Diamond has the highest resistance to plastic deformation of any material, having an elastic modulus approximately five times that of stainless steel. Taken together with its high hardness it is probable that most erodents will suffer greater damage than the target material. This is particularly true in the case of silica sand (SiO_2). Table 9.1 shows that the average hardness and fracture toughness values of SiO_2 are considerably inferior to those of diamond. In contrast, the degradation of the diamond is likely to be limited, primarily in the form of micro chipping.

Property	CVD Diamond [1]	Silica sand (SiO_2) [2,3]
Elastic modulus (GPa)	1157	87
Poisson's ratio	0.07	0.21
Density (kg m^{-3})	3520	2650
Hardness (GPa)	80	13.1
Fracture Toughness (MPa$\sqrt{m}$)	6.0	1.4

Table 9.1: Physical properties of diamond and sand.

Elastic-plastic damage is often observed on brittle materials subjected to impact from angular particles. However, this damage is only generally seen when the hardness of the particle exceeds that of the target [4]. Indeed, many erosion models based on this approach assume that the particles remain undamaged by the impact process [5]. In erosion studies of a range of ceramics by both quartz silica and SiC erodents [4], it was found that while all targets eroded by SiC exhibited elastic-plastic damage, this was largely absent when silica was the erodent; the most severe features being in the form of shallow chipping. In contrast, Srinivasan and Scattergood [6] studied the erosion of Al_2O_3 using different particles and found that erodents softer than the target could still generate radial and lateral cracks but that the number of impacts required was greatly increased. Shipway and Hutchings [2] found that for particles of lower hardness than the target material some impacts fail to cause immediate damage; instead, damage is accumulated before material can be detached. It is thought that this may be occurring in the erosion of the diamond coatings as the mass loss curves were often seen to develop in a stepwise fashion.

Surface profilometry of the eroded 60μm and 120μm lapped coatings showed that the reduction in film thickness was largely below the detectable limit of the equipment (10 nm), as was any change in surface roughness of the erosion scar. Examination of the eroded surface of the diamond coatings revealed no evidence of any plastic deformation generated by the erosion process. No "elastic-plastic" radial and lateral cracks were seen on the eroded surfaces. On the thicker coatings, where no pin-holes had formed, the only features of note were the presence of small amounts of micro-chipping in the area of the coating immediately beneath the nozzle.

9.3 Erodent behaviour during impact

9.3.1 Particle fragmentation on impact

Samples of sand used in the erosion tests were collected for examination in the electron microscope. As Figure 9.1 shows, the sand has undergone a considerable reduction in size following impact with a diamond surface at 268 m s^{-1}. It should be remembered that the sand is not recirculated in the erosion rig and therefore has only impacted the surface once. Sieving of the used sand revealed that the average size of the sand had decreased from 194μm to 87μm; Figures 9.2 and 9.3 show the size distributions before and after the test. The sand collected for this analysis was from the erosion chamber. It is known that smaller sand particles are carried further downstream: if such particles are also included in the sieved sample then the recorded drop in average particle size will be even greater. Evidence of the plastic deformation of the sand was also seen, examples of which are seen in Figure 9.4. They show particles that have become smeared across the surface of lapped 60μm coatings. This smearing is a result of the high strain rates generated on impact.

9.3.2 High-speed photography

In addition to sand sieving and microscopy, sand degradation was also studied using high-speed photography. High-speed photography also enables information on particle fragmentation and trajectory as well as any possible interactions within the erodent plume. At present it is assumed that all particles impact the surface once. It was not known whether the rebounding particles affect the path taken by the incoming ones and whether some particles impact the surface more than once.

A Kodak 4540 high-speed camera was used in conjunction with a Kodak Ektapro HS motion analyser to capture the impact of the sand on the diamond coatings. This camera is capable of operating at framing speeds of up to 4,500 fr sec^{-1} (full screen), and up to 40,500 fr sec^{-1} (reduced screen size) and the output is displayed on a monitor. The photography was illuminated using two halogen spot lamps located 90° from the camera in each direction. The moving sand particles captured by the camera appear as streaks on a single frame. The velocity of the sand particles can be obtained by dividing the streak length by the duration of the frame.

The sand used in the high-speed photographic work was sieved so that all particles were 500-710μm in size. This is approximately three times greater than the average diameter of the Redhill Mix; however, smaller particles were less distinct on the monitor, and this made measurement more difficult. Smaller particles were used in some experiments and were observed to behave in a similar manner, though they suffered less fragmentation owing to the smaller flaw size in those particles.

The sequence of images in Figure 9.5 show the impact of a 500-710μm sand particle impacting on the surface of a 160μm lapped diamond coating at a velocity of 49 m s^{-1}. The framing speed employed was 4500 fr sec^{-1} and the particle of interest is marked with an arrow. The particle can be clearly seen fracturing into approximately six fragments following impact. Particle fragmentation was more extensive at higher impact velocities owing to the greater forces associated with impact. However, even at low velocities (25 m s^{-1}) the amount of degradation on impact was still significant, as approximately 75% of particles fractured into two or more pieces. At higher velocities, the particles were observed to shatter into six or more fragments.

The high-speed photography also provides information on the particle trajectories. A consequence of the low particle flux rates is that the rebounding particles do not appear to interfere with the path taken by other incoming particles. Furthermore, no cases of particles impacting the target more than once were observed. Rebounding particles did not remain in the impact zone but were instead displaced to the periphery of the erosion chamber and did not influence succeeding impacts. This is because, as Section 9.3.3 will show, the coefficient of restitution is considerably less than 1, particularly at the higher velocities. Therefore, the kinetic energy, and hence the velocity, of the rebounding particles is only a fraction of the incoming particles. Moreover, very few particles remain in the erosion chamber following impact, with the majority being removed in the exhaust air.

The rebound angle of the particles was measured and the results are listed in Table 9.2 and plotted in Figure 9.6. It can be seen that a significant reduction is seen. This is a consequence of the flow characteristics of the air jet carrying the erodent.

Air Flow Rate (m^3 hr^{-1})	Particle rebound angle (°)	Standard deviation (°)
100	70	9.9
150	56	9.3
200	51	18.5
250	31	11.6

Table 9.2: Particle rebound angle as a function of air flow rate.

9.3.3 Coefficient of restitution

In addition to studying particle fragmentation high-speed photography can also be used to estimate the amount of energy transfer that takes place during impact, in particular the coefficient of restitution. It is a measure of the elasticity of a collision and, hence, can provide information about the amount of energy transfer from particle to target during impact. For a collision between the two bodies, it is defined as:

$$e = \frac{V_2 - V_1}{U_2 - U_1} \tag{9.1}$$

Where U_1 and U_2 are the velocities of the two bodies prior to collision and V_1 and V_2 are their velocities following the collision. In a purely elastic collision e = 1 while a value of e = 0 signifies a purely plastic collision where all the energy is lost in the collision process. In the case of a particle impacting onto a stationary target, the above equation reduced to:

$$e = \frac{V'}{V_o} \tag{9.2}$$

Where V_o is the incoming velocity perpendicular to the target and V' the rebound velocity. The energy of the incoming particle can be lost on impact to many different effects. These are due to the excitation of elastic vibrations in the target material [7]. Kinetic energy can also be dissipated in the form of heat and friction between particle and target. The coefficient of restitution can be further reduced as a result of deformation of the erodent and/or the target material.

Tsai and Kolsky [8] used 12.5 mm diameter steel balls to impact glass targets to examine the change in coefficient of restitution with impact velocity. At velocities up to ~15 m s^{-1}, e was largely unaffected, all values lying in the region 0.9-1.0. At higher

velocities, however, *e* undergoes an abrupt reduction, thought to be associated with the onset of radial cracking and crushing of the target. At velocities of approximately 30 m s^{-1}, it had decreased to about 0.5. Knight *et al* [9] reported similar findings: they impacted targets made from the same material with 0.8 and 1.0mm diameter steel balls. In this case, the velocity at which the abrupt reduction occurred was considerably higher, being above 100 m s^{-1}.

The technical limitations of the camera prevented any tests from being conducted at particle velocities greater than 133 m s^{-1}. The higher velocities necessitated framing speeds of more than 4,500 fr sec^{-1}; at higher speeds the screen size is reduced, preventing the sand particles from being viewed both before and after impact. The target material was a CVD diamond coating on tungsten 160μm in thickness, which was located directly beneath the nozzle and the particles impacted the target at an angle of 90° to its surface. The particle flux rate was 0.5 kg m^{-2} s^{-1}: identical to the erosion tests described in previous chapters. It is necessary to note the way in which the coefficient of restitution was measured. The velocities measured were the actual velocities and not the normal components. A survey of the literature has shown that both parameters have been used. Sheldon *et al* [10] used the terms V_o and V' in calculating the coefficient of restitution though other workers, for instance Salman *et al* [11] have used NV_o and NV'. Figure 9.7 explains the terms in schematic form. As shown in Table 9.2, the rebound angle is dependent on the air flow rate, and hence velocity. For this reason, it was decided to use the actual velocity to eliminate this complication.

The results are shown in graphical form in Figure 9.8. Despite the scatter in the results, there is a clear trend of decreasing coefficient of restitution with increasing impact velocity. This is in line with previous studies [8,9]. The cause of this reduction is thought to be a consequence of particle fragmentation. In purely elastic contact, the coefficient of restitution is unity [12]. In practice there will always be some losses associated with elastic wave dispersion, internal friction and hysteresis of the materials [7]. Much larger reductions in the coefficient of restitution are observed when the target undergoes plastic deformation on impact. As the amount of plastic deformation is increased this is accompanied by a further decline in the coefficient of restitution [13,14]. However, in the present case, there is no plastic deformation of the diamond

and the energy of impact is transferred to the diamond and to the sand erodent. It is this deformation of the erodent that causes the reduction in the coefficient of restitution. Although it was not possible to measure the coefficient of restitution at the highest velocities employed in the erosion tests (268 m s^{-1}), the graph suggests that it may be as low as 0.1.

9.4 Circumferential crack and pin-hole formation

9.4.1 Appearance of the circumferential cracks and pin-holes

The direction of propagation is initially perpendicular to the direction of maximum tensile stress. For those pin-holes that have completely penetrated the coating the sides are convergent, the diameter being smaller at the interface than at the growth surface of the coating. This contrasts with the Hertzian case, where the crack extends in depth in a diverging conical shape (see Figure 2.9). The appearance of the pin-hole resembles the profile of the columnar grains in diamond coatings, which increase in diameter with distance away from the nucleation surface. A transverse section of the pin-hole in Figure 9.9 is shown in schematic form in Figure 9.10. It shows that the angle the sides make with the interface is 42°. This can be compared with Figure 9.11, which shows a columnar grain from a 60μm as-grown coating on WC-6Co substrate. The angle of the grain boundaries has been calculated to be 63° and 74°. However, this is not a common occurrence, as most columnar grains tend to be more parallel-sided, making the angles considerably higher (>80°). Therefore, the angle of the pin-hole is considerably lower than the angle most columnar grain boundaries make. Moreover, as can be seen in Figure 6.2, the diameter of the pin-hole (featured in Figure 9.9) at the growth surface is approximately 10 times greater than the grain size for a coating of this thickness. The average grain size of diamond coatings 40-50μm thick has been measured as 27μm, though the overall range of grain sizes is approximately 20-40μm. Therefore, the diameters of the pin-holes are considerably larger than the sizes of the individual grains: the pin-holes are formed by the removal of several grains rather than by the ejection of individual grains.

In many micrographs the sides of the pin-holes have a layered appearance. It is not clear what has caused this, though one possibility could be that they represent the successive position of an advancing crack front. The side of a pin-hole can be seen in

more detail in Figure 9.12. These features were absent from the side of the coating at the edge of the spalled region where a cleaner appearance was apparent. This is to be expected, as the spalling process was sudden and catastrophic. Study of the coating at the edge of the spalled region showed delamination of the coating from the substrate. This can be seen in Figure 9.13. On the basis of these observations it seems likely that the coating delamination is taking place either prior to, or in parallel with, the nucleation and growth of the pin-holes. Once local debonding has occurred, further impacts will accelerate damage. The cause of the pin-holes will be discussed in detail later in this Chapter.

At lower velocities the time (or number of particle impacts) required before circumferential cracks and pin-holes are observed is greatly increased. The influence of velocity on pin-hole formation was investigated on a number of coatings 39-47μm in thickness. At 268 m s^{-1}, the first pin-hole was observed after 1 hour. This increased to 3 hours at 148 m s^{-1} and 12 hours at 63 m s^{-1}. At 33m s^{-1} the coatings was tested for 25 hours, but no pin-holes were observed. The test was not continued, as it was felt that the velocity of impact was below the critical velocity required for pin-hole formation.

9.4.2 Evolution of circumferential cracks and pin-holes under repeated particle impacts

In order to understand the evolution of circumferential cracks and pin-hole development further, a lapped 60μm coating was tested at 268 m s^{-1} and examined at regular intervals to record the progression of any damage features observed.

Figures 9.14 to 9.17 show the changes in one circumferential crack, which was the first to be seen on the eroded coating. In Figure 9.14, it is indistinct and the circumferential crack does not form a complete ring. On the left hand side of the ring, indications of a secondary ring outside the main circumferential crack can also be seen. As the test continues, the main circumferential crack becomes more distinct and more continuous, though still not complete. The secondary crack is also more prominent. It is interesting to note that in Figure 9.17, taken after 11 hours of testing, intersection of the main circumferential crack and the secondary crack has occurred, resulting in the ejection of surface material. However, it is not until 17 hours have elapsed that material is lost from the central region within the circumferential crack to become a pin-hole.

Figures 9.18 to 9.20 show another feature on the same sample that has become a pin-hole in a shorter period of time. Figure 9.18 shows the pin-hole after the central damage has begun and it can be seen in Figures 9.19 and 9.20 that this central damaged region increases in size until it reaches the circumferential crack and the coating-substrate interface. Figure 9.20 shows that the coating has been completely penetrated.

Figures 9.21 to 9.24 show another site on the same sample where three circumferential cracks have formed in close proximity to each other. Figure 9.21 shows a general micrograph showing the situation with regard to one another. It can be seen that the two lower circumferential cracks overlap and some of the coating has been removed at this point. Of these two cracks the one on the right also exhibits some secondary cracking outside the main circumferential crack in a similar manner to the crack in Figures 9.15 to 9.17.

Prior to the formation of the pin-hole, the circumferential cracks resemble liquid impact damage where a central undamaged area is surrounded by short circumferential cracks. As the erosion process continues, repeated particle impacts cause incremental growth of these circumferential cracks, often leading to complete rings [15].

9.5 Comparison of crack diameters with Hertz theory

The usual damage features in the solid particle erosion of diamond by spherical particles are Hertzian ring cracks. This has been found in other erosion studies [3,16]. For this reason, the sizes of the pin-holes were compared with those predicted by Hertz impact theory. The procedure is listed below and the results can be found in Table 9.3. The values used in these calculations can be found in Table 9.1. Figure 9.25 shows a schematic diagram of the parameters in the Hertzian contact of a spherical particle contacting a coated material.

Hertz theory can be used to calculate the contact conditions for the case of a particle impacting the surface of a target [17]. The maximum load, F_m, is calculated using:

$$F_m = \left(\frac{5\pi\rho_e}{3}\right)^{3/5}\left(\frac{4k}{3E_1}\right)^{-2/5} R^2 V^{6/5} \qquad (9.3)$$

The mean contact pressure, P_m, is:

$$P_m = \frac{1}{\pi}\left(\frac{5\pi\rho_e}{3}\right)^{1/5}\left(\frac{4k}{3E_1}\right)^{-4/5} V^{2/5} \tag{9.4}$$

where ρ_e is the density of the impacting particle, E_1 the elastic modulus of the diamond, R the particle radius and V the particle velocity. The value of k is obtained using the following equation:

$$k = \frac{9}{16}\left[\left(1-\nu_1^2\right)+\left\{\left(1-\nu_2^2\right)\left(\frac{E_1}{E_2}\right)\right\}\right] \tag{9.5}$$

where E_1, ν_1 and E_2, ν_2 are the elastic modulae and Poisson's ratios of the target material and erodent respectively. The values of F_m and P_m, from Equations (9.3) to (9.5), can be used to calculate the maximum contact radius, a_m:

$$a_m = \sqrt{\frac{F_m}{\pi P_m}} \tag{9.6}$$

The maximum tensile stress at the contact circle, σ_m, can also be calculated, using the following formula:

$$\sigma_m = \frac{1}{2}(1-2\nu_1)P_m \tag{9.7}$$

The expression used to calculate the duration of elastic impact, t_e, can be calculated using the following formula:

$$t_e = 2.94\left[\frac{5\pi\rho}{4}\left(\frac{1-\nu_1^2}{E_1}+\frac{1-\nu_2^2}{E_2}\right)\right]^{2/5} V^{-1/5} R \tag{9.8}$$

For a circular point contact, a shear stress is generated in the region beneath the contact zone. The maximum value of this shear stress, τ_m, can be calculated, assuming no relative motion at the interface, using:

$$\tau_m = 0.31\left(\frac{3P_m}{2}\right) \tag{9.9}$$

The depth, z_τ, at which this occurs, is:

$$z_\tau = 0.32a_m \tag{9.10}$$

The depth given in the equation above, $z_\tau = 0.32a_m$ is lower than the usually quoted figure of 0.48 a_m. However, this latter figure is for materials having a Poisson's ratio of 0.3. The considerably lower Poisson's ratio of diamond (0.07) [28] has necessitated recalculation, hence the revised figure. Further details of this have been given in Chapter 11.

The vertical displacement, w, of the coating in the centre of the impact site is given by:

$$w = \frac{3(1-\nu_1)F_m}{16G_1a_m}(2 - R^2/a_m{}^2) \tag{9.11}$$

where G_1 is the shear modulus of the target material. At a velocity of 268 m s^{-1} a 194μm diameter sand particle impinging on the surface will displace the surface by 0.9μm. This dimension corresponds to 2% of the overall thickness of a 46μm coating.

The mean Hertzian contact diameter for impacts of a 194μm diameter sand particle (the average diameter of the sand used in the Redhill Mix blend) at 268 m s^{-1} has been calculated to be 76μm. However, this does not agree with measured values taken from eroded samples. One possible explanation for this lack of agreement is that friction between the sand particle and the diamond surface (arising from differences in elastic properties between indenter and target) has increased the diameter at which the maximum tensile stress is located. Johnson *et al* [18] have shown that this phenomenon

can increase the measured ring crack diameter by up to 30% greater than the predicted value. However, as can be seen in Figure 8.10 for example, the circumferential crack diameter is more than twice this predicted figure.

Velocity V (m s^{-1})	33	63	148	268
Mean Particle Radius R (μm)	97	97	97	97
Range of Particle Radii (μm)	30-250	30-250	30-250	30-250
Mean E_k (μJ)	5.6	20	110	366
Coating Thickness, C_T (μm)	40	39	47	46
Maximum contact load F_m (N)	4.4	10	27	54
Max Contact Pressure P_o (GPa)	6.9	8.9	12.5	15.9
Mean contact pressure P_m (GPa)	4.6	5.9	8.3	10.6
Mean contact radius a_m (μm)	17	23	32	38
Mean contact diameter d_m (μm)	34	46	64	76
Mean measured pin-hole diameter (μm)	-	170	182	193
Range of contact diameters d_m (μm)	-	130-200	150-250	150-245
Tensile stress σ_m (GPa)	2.0	2.5	3.6	4.6
Time of impact, t_e (μs)	0.28	0.25	0.21	0.19
Maximum shear stress τ_m (GPa)	2.1	2.7	3.9	4.9
Depth of τ_m, z_τ (μm)	5.4	7.4	10.2	12.2
z_τ/C_T	0.14	0.19	0.22	0.27
C_T/a_m	2.36	1.7	1.46	1.12
Vertical Displacement w (μm)	0.18	0.31	0.59	0.92
Number of impacts on area A (hr^{-1})	653	1196	2316	3802
Time required to form 1st pin-hole (hrs)	-	12.0	3.0	1.0
No. of impacts to form 1st pin-hole *N (Hertz)*	-	14362	6948	3802
E_{kt} (J) (Hertz)	-	0.287	0.764	1.392
No. of impacts on SW area A_{SW} (hr^{-1})	18321	17516	24938	23997
No. of impacts to form 1st pin-hole *N (SW)*	-	210192	74814	23997
E_{kt} (J) (SW)	-	3.78	7.54	8.03

Table 9.3. Calculated values from Hertzian impact theory. Key: SW = stress wave.

It has already been noted that the sand particles used in the erosion tests are of a predominantly angular morphology. As a result, the contact radius of an angular particle on the coating will be smaller than that of a spherical particle. Therefore the radius at which the maximum tensile stress occurs will also be smaller, which leaves

the investigator no nearer to explaining the origin of the pin-hole and the relationship between their diameter and the impact condition.

Parameter	Hertzian	Modified Hertzian
w (μm)	0.9	1.0
P_o (GPa)	15.9	19.7
R_p (mm)	1.89	1.11
σ_m (GPa)	4.5	4.4

Table 9.4: Comparison of certain parameters calculated using Hertzian theory and modified Hertzian theory.

In Chapter 6 it was shown that wide variations in elastic modulus of the diamond coatings were recorded using nanoindentation. The average value (1157 GPa) was used to calculate the Hertzian contact diameter; however, it is important to quantify the effect of the variation in elastic modulus on the contact diameter. Recalculating the contact diameter revealed its effect on d_m is minimal: this is thought to be due to the large discrepancy between the elastic modulus of diamond and that of silica sand. When the elastic modulus is increased from 711 GPa to 1848 GPa the contact diameter varies by only 1.1μm. Therefore, this cannot account for the difference between contact diameter and circumferential crack diameter.

Another influence that could be modifying the stress field to give larger contact diameters than in theory is the tungsten substrate. However, both theory and experiment have shown that for a hard coating of thickness $C_T / a_m = 0.5$ and where the elastic modulus of the coating is approximately 3 times that of the substrate the measured contact size is almost the same as that for a half space of the coating material [19]. In the tests described in Table 9.3 the C_T / a_m ratio is between 1.1 and 2.4. Therefore, effect of the substrate can be ignored in the present case.

One of the limitations of the Hertzian approach is that it is only strictly applicable in cases where $a_m / R < 0.1$, where a_m is the contact radius and R the radius of the spherical indenter. Use of the theory outside this range can give rise to errors. These errors increase with increasing a_m / R ratio and are particularly marked in materials of low

Poisson's ratio. Yoffe [20] has analysed the case where $a_m / R > 0.1$ and subsequently derived modified expressions for such situations. The vertical displacement becomes:

$$w = \frac{4(1-\nu_1)F_m}{3\pi G_1 a_m} \tag{9.12}$$

The radius of curvature of the displaced surface, R_p, at the axis is now given by:

$$\frac{1}{R_p} = \frac{2(1-\nu_1)F_m}{\pi G a_m^3} \tag{9.13}$$

Table 9.4 shows that the differences between the two approaches are minimal. Therefore, the fact that the present case is outside the range of applicability for Hertz theory does not alter the basic conclusions.

From a mechanistic standpoint in comparing the time elapsed before pin-holes are observed for the different velocities it is more instructive to compare the tests in terms of number of particle impacts. The number of particle impacts per Hertzian zone *N(Hertz)* is calculated using the following expression:

$$N(Hertz) = \frac{AFt}{m_s} \tag{9.14}$$

Where F is the flux rate in kg $m^{-2}s^{-1}$, t is the test duration and m_e is the mass of the erodent particle, given by $(4\rho_e \pi R^3)/3$. A is the size of the Hertzian zone, which is defined as:

$$A = \pi(2a_m)^2 \tag{9.15}$$

This calculation that any impact having its centre within $2a_m$ will overlap the previous one. The number of impacts, *N(SW)*, can also be calculated by replacing $2a_m$ with d', the diameter at which the stress wave reinforcement occurs. The concept of stress wave reinforcement will be explained in the Section 9.6.

Table 9.3 also lists the tensile stresses generated at the contact edge for the different velocities. They range from 2.0 GPa at 33 m s^{-1} to 4.6 GPa at 268 m s^{-1}. The values of tensile stresses generated by the particle impacts, σ_m, all exceed the critical value of

tensile strength, obtained by static indentation tests, for 15μm diamond coatings given by Feng *et al* [16]. This value of 1.4 GPa is the revised figure as a factor 2 was omitted from the original calculation, which gave the tensile strength twice as high as this [21]. The tensile strength of CVD diamond has been observed to decease with increasing thickness [22] owing to the greater size of microstructural defects: therefore, it is likely that the tensile strengths of the 39-47μm coatings used in this study will be less than 1.4 GPa. However, particle fragmentation on impact means that the real value of σ_m is likely to be significantly lower than the calculated value.

A further impediment to ring crack formation is the compressive residual stress present in the coating, which will affect the stress field as well as the contact conditions. The presence of a compressive stress increases the critical contact pressure (and, therefore, tensile stress) required to initiate ring cracks at the contact edge. Before this higher load is reached the fracture of the sand particles may occur, thereby preventing that load from being attained. Roberts *et al* [23,24] have investigated the effect of compressive residual stress on the fracture load in a Hertz indentation test indenting glass with a 10mm diameter glass ball. They found that as the surface compressive stress increased from 0 (nominally "stress free") to 500MPa the minimum fracture load increased by more than an order of magnitude. The average residual stress in the diamond coatings has been estimated to be approximately 800MPa. Therefore, the increase in load required to initiate Hertzian ring cracking compared with the "stress free" case will be even greater, even without taking into account the increased chance of particle fracture.

There are a number of difficulties which are encountered in attempting to use Hertz theory to explain the formation of the pin-holes. Among the assumptions made in the Hertzian calculations are that the contact is elastic and that both erodent and target remain undeformed during the impact process. However, as shown in Section 9.3, the high degree of sand degradation, together with the fact that the coefficient of restitution is so far from unity demonstrates that these assumptions are not valid in the present case. Furthermore, the theory is only applicable to a sphere on flat geometry. It has already been noted that the morphology of the sand particles used in the current tests are predominantly angular. This, therefore, represents a further departure from the strict Hertzian approach. In conclusion, the evidence suggests that Hertz theory is not

applicable for explaining circumferential crack formation and that other approaches need to be considered in order to explain the formation of the circumferential cracks.

Range of particle diameters (μm)	90-500	355-500
Mean Particle Diameter (μm)	194	428
Coating Thickness, C_T (μm)	46	40
Particle Velocity, V (m s^{-1})	268	250
Maximum Contact load F_m (N)	62	276
Mean Contact Pressure P_m (GPa)	13.8	13.4
Mean Contact radius, a_m (μm)	38	81
Mean Contact diameter d_m (μm)	76	162
Mean measured circumferential crack diameter (μm)	193	178
Range of circumferential crack diameters (μm)	150-245	130-220
Tensile stress σ_m(GPa)	5.9	5.8
Time of impact t_e (μsec)	0.16	0.36
Maximum shear stress, τ_m (GPa)	6.4	6.2
Mean E_k (μJ)	366	3406
Mean C_T/a_m	1.21	0.49
Mean Depth of Maximum Shear z_τ (μm)	12	26
Mean z_τ/C_T	0.26	0.65
Mean Vertical Displacement, w (μm)	0.92	2.7

Table 9.5: Comparison of two erosion tests using sand of different size distributions

One of the complications in the present case is the wide size distribution of the Redhill Mix. The majority of the sand grains have a diameter in the range 90-355μm. While this blend provides a realistic reproduction of the sand used in the North Sea reservoirs (and thus realistic choice of erodent for evaluating candidate choke valve trim materials) the wide range of particle sizes complicates the task of determining the contact conditions and hence the damage mechanism. Using the average diameter, 194μm, in the Hertzian calculations, means that at 268 m s^{-1}, the predicted ring crack diameter is 76μm, irrespective of the coating thickness. However, if we consider, for example, a 400μm diameter particle, the predicted diameter becomes 167μm. This is closer to the average pin-hole diameters measured in the tested samples and is especially true considering that the actual diameter is often up to 30% greater, as discussed earlier. Therefore, it is possible that the contribution to the formation of these pin-holes could be from sand greater than a particular size. The sieve size range 355-

500μm (into which the 400μm particle would fall) accounts for 10.2% of the overall range of sand sizes in the Redhill Mix.

In order to find out more about the effect of a narrower particle distribution, a 40μm lapped coating was tested at 250 m s^{-1} using sand that had been sieved to ensure all particles had diameters within the range 355-500μm. The velocity of 268 m s^{-1} using 355-500μm sand was beyond the capability of the erosion rig. Nevertheless, the conditions are sufficiently close that it is possible to compare the two cases; they are listed in Table 9.5. While the average crack diameter in this case is close to the Hertzian contact diameter there are many reasons why Hertz is not applicable for explaining the circumferential crack diameters; these are explained in more detail in the following sections. Therefore, while the crack diameters in the present case are close to those predicted by Hertz, this is thought to be coincidental.

9.6 Use of stress wave theory to explain circumferential crack formation

In the measurement of the circumferential crack diameters, it was noted that the diameter increased considerably with increasing coating thickness. This trend contrasts with Hertzian theory, which has no such dependency. In the absence of agreement between Hertz theory and the experimental results, it is necessary to consider alternative approaches. One alternative cause for the formation of circumferential cracks could be by stress waves generated by particle impact. Based on liquid impact studies of brittle materials, Bowden and Field [25] suggested that for thin targets, stress wave reflection from the rear surface could cause fracture. Coad and Field [26] found a trend of crack diameter vs. sample thickness over the range 0.5–2.5mm in liquid impact of free-standing CVD diamond. The trend of increasing circumferential crack diameter with coating thickness suggests that the cracks may be formed by stress wave reflections at locally delaminated regions of the coating. Although the stress wave theory proposed by Bowden and Field was for liquid impact, the variation in circumferential crack diameter with coating thickness, which is not predicted by Hertz, means that it merits further investigation.

9.6.1 Theory of stress wave reflection and reinforcement

There are two possible ways in which reflected bulk waves can reinforce Rayleigh surface waves; these are shown in Figure 9.26. The first is when a compression wave is

reflected and returns as a tensile wave. Alternatively, a compression wave can undergo mode conversion to a shear wave, or vice versa, before returning to the front surface. When the tensile Rayleigh wave is augmented at the surface by a returning tensile wave the resultant stress may be sufficient to generate cracking in the front surface of the material. The high stress wave velocity and low attenuation in diamond means that, in the present case, this may be significant in the generation of pin-holes.

Coad and Field [26] found good agreement between measured circumferential crack radius and the theoretical radius calculated using this approach. However, it was not known whether this theory would be applicable in the case of thinner coatings on substrates, under impact by solid particles.

On the basis of the two stress wave reflection scenarios, the radii of the circumferential cracks were predicted by Bowden and Field [25] and later extended by Seward *et al* [27]. The ratios of the compression and shear wave velocities are given by:

$$\frac{c_1}{c_2} = \left\{\frac{2(1-\nu)}{(1-2\nu)}\right\}^{1/2} = 1.47 \tag{9.16}$$

The velocities of the three wave types in diamond used in the calculations were c_1 = 17,470 m s^{-1}; c_2 = 11,876 m s^{-1}; and c_R = 10,688 m s^{-1}. A Poisson's ratio, ν, of 0.07 was used in the velocity calculations. Using this information, it is possible to predict the radii of these two reinforcements, y_1 and y', as a function of thickness, x_{th}. The calculated radii are:

$$\frac{y_1}{x_{th}} = 1.52 \tag{9.17}$$

and

$$\frac{y^1}{x_{th}} = 2.14 \tag{9.18}$$

This gives the diameters of the circumferential cracks as:

$$d_1 = 2y_1 + \Delta y \tag{9.19}$$

and

$$d^1 = 2y^1 + \Delta y \tag{9.20}$$

Δy is the diameter over which the high pressure phase exists and = $2RV/C$ (in the case of liquid impact). For a 194μm diameter sand particle impacting on diamond at 268 m s^{-1} Δy is 9μm. According to Seward *et al* [27] the dominant reinforcement for materials with low Poisson's ratios should be y'. Therefore, the pin-hole diameters were compared with the diameter at which this reinforcement occurs. In the present work, the coating thickness, C_T, has been substituted for x_{th}.

9.6.2 Effect of coating thickness on circumferential crack diameter

The average measured circumferential crack diameters were plotted against coating thickness in Figure 9.27; the predicted diameters according to the theory described above are also included for comparison. It can be seen that the two sets of data agree well, though it should be remembered that the circumferential crack diameters form a range of values. This is thought to be due to the wide range of sand diameters. The influence of sand diameter on the diameter of stress wave reinforcement is, at present, unclear. However, the test of the 40μm coating with sieved 355-500μm sand showed that the range of circumferential crack diameters was the same (see Table 9.5). Other factors could include scattering of bulk waves at the coating-substrate interface by grain-boundary porosity; the calculation ignores such effects and assumes a perfect interface. The columnar grains and grain boundaries could also scatter the waves, as may the presence of residual stresses and variations in Poisson's ratio within the coating. In the case of the latter parameter, the calculations employed an aggregate value of 0.07, though it is known to vary with crystallographic orientation from 0.01 to greater than 0.2 [28]. Moreover, the increasing grain size with thickness increases the possibility of large grains behaving as single crystals.

It is also interesting to note that deviations between measured and calculated diameters increase as the coating thickness reduced. In the case of a 17μm coating the measured diameter is 28% greater than the predicted value. It is not certain that this approach is valid at this thickness as other factors may be in operation here. According to Bowden and Field, many analyses of wave motion become less applicable as the origin is approached. Furthermore, C_T / a_m ratio is 0.41, which means that the influence of the substrate cannot be disregarded. On this coating, the features resembling pin-holes may instead be sections of the coating that have been removed and may be unrelated to stress wave reflection. Nevertheless, for the thicker coatings, the dimensions predicted

by this theory are closer to the dimensions of the circumferential cracks than the predictions of Hertz theory.

C_T (μm)	Mean Crack Diameter (μm)	SW reinforcement diameter (d_1) (μm)	SW reinforcement diameter (d') (μm)	Circumferential Crack Diameter Standard Deviation (μm)
17	105	61	82	31
33	163	109	150	26
46	193	149	206	30
60	281	191	266	20
90	387	283	394	-*
120	344	374	523	-*

Table 9.6: Measured circumferential crack diameters as a function of coating thickness for lapped diamond coatings tested at 268 m s^{-1} and compared with the predicted stress wave (SW) reinforcement diameter. Key: * = Not applicable as only one pin-hole was seen in that coating.

In the case of the 120μm coating there was only one circumferential crack observed, which was seen after 10 hours at 268 m s^{-1}. However, in contrast with the other coatings up to 90μm, the diameter did not agree with the theory of stress wave reinforcement (compression wave reflected as shear wave). The diameter is 344μm, is approximately 35% less than the diameter at which stress wave reinforcement occurs (523μm). However, it is closer to the reflection of compression waves (374μm). Although, as has already been mentioned, the dominant reinforcement mechanism in low Poisson's ratio materials is by the interaction between surface waves and reflected compression-shear waves this does not preclude interaction between surface waves and reflected compression-compression waves. Indeed the dependence of Poisson's ratio on crystallographic direction in diamond, together with the polycrystalline nature of CVD diamond, means that on grains of some orientation compression-compression reflection can occur and this could partially explain the variation in circumferential crack diameter.

Pin-holes were also observed on as-grown coatings; the mean diameters are listed in Table 9.7. As with the lapped coatings, they show reasonable agreement with stress

wave reinforcement diameter. The greater roughness of the coatings (see Chapter 6) prevented any circumferential cracks from being seen prior to the advent of pin-holes.

C_T (μm)	Mean Crack Diameter (μm)	SW reinforcement diameter (d') (μm)	SW reinforcement diameter (d') (μm)	Circumferential Crack Diameter Standard Deviation (μm)
30	161	100	137	24
40	185	131	180	43
60	229	191	257	29

Table 9.7: Measured circumferential crack diameters as a function of coating thickness for as-grown diamond coatings tested at 268 m s^{-1} and compared with the predicted stress wave (SW) reinforcement diameter.

9.6.3 Effect of impact velocity on circumferential crack diameter

It can be seen from the Hertz equations that the contact diameter is dependent on the impact velocity. In a further assessment of the stress wave theory, the influence of impact velocity was evaluated using two sets of coatings of different thickness (39-47μm and 60μm) and tested at different velocities between 63 and 268 m s^{-1}. The circumferential crack diameters were measured and the mean values are listed in Table 9.8 and plotted in Figure 9.28. The graph shows that the variation in pin-hole diameter with velocity is small. The average diameter increases by between 20 and 60μm over the velocity range. Another significant point to note is that the rate of increase of circumferential crack diameter with velocity is approximately the same as the predicted Hertzian diameter though the circumferential crack diameters are between two and four times the Hertzian contact diameter. Furthermore, it can be seen that, in line with the previous findings, the crack diameter is once again dependent on coating thickness. It is also worth noting that for a given thickness of coating, the time required to generate a pin-hole increased dramatically at lower velocities. Moreover, the number of pin-holes were greater on the samples tested at higher velocities. It is thought that if pin-holes only form at debonded regions then at lower velocities the debonding process takes longer. This will be examined in more detail in Chapter 11. The dependence of crack diameter on impact velocity has been seen in liquid impact studies of PMMA [29] and ZnS [30].

9.6.4 Effect of impact angle on circumferential crack diameter

Examples of pin-holes from the different impact angles are shown in Figures 9.29 and 9.30. A notable finding in this work was that the number of circumferential cracks and pin-holes at the more oblique angles (30° and 45°) was significantly lower compared with the samples tested at 60° and 90°. Furthermore, the time, or number of impacts, required to generate the pin-holes was also significantly increased. Figure 9.31 shows a graph of the time required to generate the first pin-hole on the 60μm coatings, as a function of impact angle.

The mean diameters of the circumferential cracks are listed in Table 9.9, while the variation of circumferential crack diameter with impact angle is shown in Figure 9.32. They show that, with the exception of the 43μm coating tested at 90°, there is essentially no variation in mean crack diameter with angle for both sets of coatings. Though the overall numbers of circumferential cracks on some of the 60μm coatings are low, the basic trend is observed for both sets of coatings.

Particle Velocity ($m\ s^{-1}$)	Coating Thickness (μm)	Average Measured Diameter (μm)	SW reinforcement diameter (d') (μm)	Standard Deviation
63	39	170	169	19.8
148	47	182	206	27.1
268	46	193	206	30.0
148	60	244	266	47.6
189	60	234	266	39.2
232	60	300	266	38.7
268	60	281	266	62.6

Table 9.8: Measured circumferential crack diameter as a function of velocity for lapped CVD diamond coatings of two thicknesses.

Many of the circumferential cracks, especially those observed from tests conducted at non-normal impact angles were not circular, having a slightly elliptical shape. In order to quantify the shape the aspect ratios were measured; the term "aspect ratio" is defined schematically in Figure 9.33. An aspect ratio of 1 signifies a completely circular circumferential crack. As can be seen in Table 9.9 the aspect ratio of the circumferential cracks does not appear to be dependent on impact angle.

The crack diameters were compared with the stress wave reinforcement diameters predicted by theory, and close agreement was found between them. Using the approach of Seward *et al* [27], and assuming that the stress waves are reflected at the coating-substrate interface at delaminated regions of the sample, the results from the present study were compared with the theory. The results, which are shown in Table 9.8, demonstrate good agreement between the experimental results and those predicted by theory. While there are differences between solid particle impact and liquid impact, the stress wave reinforcement theory provides a more convincing explanation for the circumferential cracks than does Hertz theory.

C_T (μm)	Impact Angle (°)	Calculated Diameter (d') (μm)	Mean crack diameter (μm)	Range of crack diameters (μm)	Mean Crack Aspect Ratio
37	30	167	162	136-210	1.12
39	45	176	165	120-230	1.15
42	60	189	162	132-238	1.16
43	90	193	196	132-250	1.05
60	30	266	300	300*	1.07
60	45	266	290	280-300	1.28
60	60	266	293	260-325	1.23
60	90	266	292	268-358	1.14

Table 9.9: Comparison of mean measured circumferential crack diameter with the calculated stress wave reinforcement diameter, d'. Key: * = Only one circumferential crack observed on this sample.

Figure 9.31 showed that the time (or number of particle impacts) required to generate pin-holes increases as the impact angle is reduced. Therefore, impact at more oblique angles does not generate as much coating debonding over a given period of time. One reason for this is that as the impact angle is reduced the impact area increases, as does the path length through the sample. F_θ, the particle flux at an angle θ is related to the flux at 90° impact, F, by the following relationship:

$$F_\theta = F \sin\theta \tag{9.21}$$

The Flux rate at an impact angle of 30° is 0.25 kg m^{-2} s^{-1}, which is half the value at 90°. Therefore, more impacts per unit are required before debonding is effected. Another

explanation for the increase in the number of impacts to generate circumferential cracks at lower angles is that as the impact angle, θ, is reduced the normal component of the impact velocity, will reduce with $\sin \theta$. This reduction will have the effect of reducing the impact load, the kinetic energy of impact and the depth at which the maximum shear stress occurs. Therefore, if the number of impacts to cause coating debonding is increased then it can be expected that the number of impacts to cause pin-hole formation will also be increased.

It is instructive to compare the findings of the present study with liquid impact studies. In the work by Gorham and Field [31], it was found that the region of sub-surface shear is displaced in the direction of the lateral impact velocity. As the impact angle is reduced, the zone of maximum shear stress is shifted progressively away from the interface and towards the surface. It is thought that this is taking place in the present case and could explain the trend in Figure 9.31.

However, while there are similarities between the damage features seen in the liquid impact studies and the present one, there are also differences. The similarity is that the extent of the impact damage is proportional to $\sin \theta$ [32]. The most significant difference is that in liquid impact reduction of the impact angle causes the circumferential crack to become more asymmetrical [32]. The circumferential cracks are no longer complete on the "upstream" side of the sample. This is due to the fact that the flow of liquid, which is responsible for much of the surface cracking, is asymmetric [33]. This is in contrast with the present work, where the circumferential cracks at the more oblique angles, though fewer in number still strongly resemble those seen at the higher angles.

9.7 Appearance of circumferential cracks

The appearance of a newly formed circumferential crack can also provide clues in determining the nature of the event that precipitated its formation. As can be seen in Figure 8.9, the newly formed circumferential cracks are often discontinuous, rather than a complete ring, or even a complete partial ring. This is significant because it supports the argument that stress waves are responsible. These types of features produced by liquid impact tend to be short and discontinuous owing to the short

duration of the stress pulses produced during impact [34]. In contrast, Hertzian ring cracks nucleate from a favourably orientated surface flaw just outside the contact circle and then propagates around the contact circle to form a surface ring crack [35]. In some erosion studies the cracks did not fully encircle the contact area because of the short duration of impact [16]. The duration of impact will be further reduced if the particle fragments on impact.

It is possible that the circumferential cracks are caused by the same mechanisms as those that operate in liquid impact conditions rather than solid impact. Impact experiments using soft particles on brittle materials have generated damage features of similar appearance to those from liquid impact [36]. The particle degradation (both plastic flow and fragmentation), already described in Section 9.2, suggests that the impact conditions may not be wholly unrelated to impact either from soft particles or liquid droplets. These similarities provide further evidence for the proposition that the circumferential cracks were generated by stress wave reflection.

The circumferential cracks in Figure 9.34 show secondary banding outside the main crack. However, it is not easily distinguished from the surrounding area. This lack of secondary banding could be due to the low population of surface flaws in CVD diamond. Pickles *et al* [22] suggested that the majority of the fracture-controlling flaws resided in the bulk of the material rather than at the surface.

If the circumferential cracks are generated by stress wave reflection and interaction at locally debonded regions this could answer the question of why they form at discrete certain locations rather than being evenly distributed on the surface of the coating as is the case in other studies [16]. Furthermore, the time required before a visible pin-hole, which is seen to increase with coating thickness, could be explained by the increased time required to induce debonding in thicker coatings compared with thinner ones.

Figures 9.14 to 9.24 showed that the circumferential crack forms first. As the erosion time increases the circumferential crack(s) become(s) more distinct. It is thought that the crack is deepening caused by repeated particle impacts. The driving force for this process is thought to be the Rayleigh surface waves, which account for the bulk (67%) of the energy associated with impact with the remainder made up by shear waves

(26%) and compression waves (7%) [37]. The Rayleigh waves are tensile in nature and so will open up these cracks causing them to propagate away from the growth surface towards the coating-substrate interface. Rayleigh waves have been shown to increase the size of surface cracks / flaws artificially introduced by Vickers indentation into soda-lime glass following liquid impact adjacent to these flaws [38]. They are confined to the surface of materials to a depth of approximately 1 wavelength. The high Rayleigh wave velocity in diamond (10,688 m s^{-1}) means that a depth of one wavelength is likely to be as much as 2mm, i.e. greater than the thickness of many of the coatings described in this thesis. The figure of 2mm was calculated on the basis of a frequency being 5 MHz - the inverse of the contact duration - which has been calculated to be approximately 0.2μsec using Hertz theory. This depth is reduced when particle fragmentation occurs, as this reduces the impact duration resulting in a decreased wavelength of the Rayleigh wave.

In an investigation of the effect of repeated impact of liquid droplets on a brittle material (PMMA), Bowden and Brunton [39] used surface profilometry of the impact site after each successive impact to show a widening and deepening of the circumferential crack. After 5 impacts, the various fracture surfaces join up, and a large piece of material is removed from the surface.

In a similar study, van der Zwaag and Field [40] subjected soda lime glass to repeated impacts of 0.8mm diameter liquid droplets at 250 m s^{-1}. As the number of impacts increased crack growth occurred and new cracks also became visible. After 23 impacts the cracking had intersected the rear surface creating a hole in the specimen. This partially resembles the present case when the coating is completely penetrated through to the coating-substrate interface.

It has already been shown that shear stresses are generated sub-surface by both solid particle and liquid impacts [41]. Close study of a pin-hole where the central damage has initiated reveals the presence of an array of small cracks within the grains. These have also been seen in sections of CVD diamond. It is thought that these intrinsic flaws are activated by shear stresses to result in a pin-hole being formed within the circumferential cracks. This is supported by work by Guiberteau *et al* [42] who looked at the cyclic Hertzian test to look at the damage accumulation in polycrystalline

ceramics. In coarse-grained alumina, damage within the contact area in a zone of high shear stress and hydrostatic compression beneath the contact circle. This is a useful parallel with the present case and the two could be related.

9.8 The nature of the erodent-target combination

To investigate this further, it is necessary to consider the differences in elastic properties between particle and target. Dundurs has shown that the difference in elastic constants between indenter and half space can be quantified by the use of two independent variables, α and β, [43]. They can be calculated using the following expressions:

$$\alpha = \frac{\{(1-\nu_1)/G_1\} - \{(1-\nu_2)/G_2\}}{\{(1-\nu_1)/G_1\} + \{(1-\nu_2)/G_2\}} \tag{9.22}$$

$$\beta = \frac{1}{2}\left[\frac{\{(1-2\nu_1)/G_1\} - \{(1-2\nu_2)/G_2\}}{\{(1-\nu_1)/G_1\} + \{(1-\nu_2)/G_2\}}\right] \tag{9.23}$$

α is a measure of the difference in plain strain modulus $\{(1-\nu^2)/E\}$ and varies from –1.0, when the target is rigid, to +1.0, when the indenter is rigid. β has extreme values of –0.5 and +0.5, when one body is rigid and the other has zero Poisson's ratio. If both bodies are incompressible $\beta = 0$. The values of α and β were calculated for the case of a silica sand particle indenting a diamond surface. The results are listed in Table 9.10, together with three other combinations of indenter and half space. It can be seen that for both α and β parameters, the combination of SiO_2 and CVD diamond are close to the extreme values where the target is rigid and the particle highly deformable. It is interesting to compare the α and β values for SiO_2 and diamond with those for nylon and PMMA. Impact studies using nylon spheres on PMMA targets showed circumferential cracking around the impact zone. The values in Table 9.10 indicate that silica will show a greater propensity to deform when impacting on diamond than nylon does on PMMA. Therefore if stress wave induced damage can be generated on PMMA, on this basis it seems likely that the same may happen with SiO_2 on diamond.

Body 1 (Half-space)	Body 2 (Indenter)	G_1 (GPa)	ν_1	G_2 (GPa)	ν_2	α	β
CVDD	SiO_2	497	0.07	24	0.227	-0.89	-0.31
PMMA	Nylon	1.40	0.38	0.25	0.38	-0.62	-0.21
Glass	Steel	22	0.25	80	0.31	0.57	0.21
WC	Steel	300	0.22	80	0.30	-0.54	-0.24

Table 9.10: Values of α and β parameters for a number of indenter and half space combinations.

9.9 Erosion of CVD diamond using diamond erodent

The previous sections of this chapter have described the damage features that are observed on diamond coatings following high velocity sand particle impact. It has been shown that Hertz theory does not explain the formation of the circumferential cracks and pin-holes. One of the reasons for this was that the sand particles fragmented on impact and could not generate high enough stresses to initiate Hertzian cracks. An assumption in the Hertzian approach is that both target and erodent remain undeformed and that the damage is purely elastic. In order to see if Hertzian damage features were seen when the erodent underwent less degradation on impact erosion experiments were conducted using diamond particles. While the use of diamond erodent does not preclude particle fragmentation on impact it is likely that the incidence of fragmentation will be considerably lower than sand, thus increasing the likelihood of Hertzian ring cracking being observed.

9.9.1 Experimental Details

Free-standing CVD diamond, 50mm in diameter and 500-700μm in thickness was brazed onto tungsten carbide substrates. The diamond was polished to a surface roughness (R_a) of approximately 8nm. The relevant mechanical properties of the materials have already been listed previously. The mechanical properties of both erodent and targets were assumed to be identical. The relevant properties have already been listed in Table 9.1.

The tests were conducted using the erosion rig under similar conditions to those previously described. The erodents used were two types of diamond grit, which were supplied by De Beers: EMB, which is natural diamond, and PDA999, which is

synthetic. Both grades were 70/80 mesh in size: approximately 200μm in diameter. The principal difference between them is the morphology: EMB is highly angular, while PDA999 is blocky in shape. They are shown in Figures 9.35 and 9.36.

The particle velocity was 268 m s^{-1}, the flux 0.5 kg m^{-2} s^{-1} and the direction of impact was 90° to the target surface. The test duration was 1 second so that individual sites of impact could be studied in order to elucidate damage mechanisms. The eroded materials were examined using optical and electron microscopy.

9.9.2 Results and Discussion

In order to study the degree of fragmentation of the diamond grit following impact samples of used diamond grit were collected after the tests and examined for signs of degradation after impact. Figure 9.37 shows that the EMB grit had undergone significant degradation on impact. This can be compared with Figure 9.38, which shows that the extent of fragmentation of the blocky PDA999 grit, while still apparent, was much reduced. This highlights the difference in characteristics of the various grades of diamond grits, notably strength [46]. Nevertheless, the diamond sample impacted by the EMB grit still exhibited radial and lateral crack networks at impact sites, examples of which can be seen in Figures 9.39 and 9.40, though the sizes of the damage features were smaller than those generated by the PDA999 grit, which can be found in Figures 9.41 and 9.42.

In both samples features resembling radial and lateral cracks surrounding the impact site can be seen, which are similar to the "elastic-plastic" damage observed in studies of brittle ceramics [44]. This suggests that the target has undergone plastic deformation, which is not often observed in diamond at room temperature. However, Brookes [45] has shown that plastic flow is possible in diamond at room temperature. In the present case, it is thought that the high stresses generated, together with the short duration of impact may have contributed to this apparent plasticity.

In addition to these features, the diamond impacted by blocky (synthetic) diamond grit also other square shaped cracks. Examples of these cracks can be seen in Figures 9.43 to 9.46. Other partial cracks could also be seen; examples are shown in Figures 9.47 and 9.48. The dimensions of these cracks were measured and compared with Hertz

theory: the figures are listed in Table 9.11. Both complete and partial cracks are similar in scale to the Hertzian contact diameter. This mirrors the work of Telling and Field [3] and Feng *et al* [16], which found good agreement between the ring crack diameter and the Hertz theory. However, the ring cracks in both those studies were circular, whereas those in Figures 9.43 to 9.46 were of a square morphology.

There are two possible causes for these square cracks. The first is particle morphology: Figure 9.35 shows that the synthetic diamond grit particles are cubo-octahedral, rather than spherical, in shape. It could be that the "ring cracks" were generated by particles impacting the surface on one of its facets. In contrast, a particle impacting the surface on one of its corners or edges would generate higher contact pressures, which could generate the radial-lateral cracks. An alternative explanation is that the square cracks are Hertzian ring cracks that have been distorted by the propensity of diamond to cleave easily on the (111) plane. The large grain size (approximately 200μm) of diamond samples 600μm in thickness means that particles impacting on one single grain may cause the diamond target to behave as a single crystal thereby distorting shape of the ring cracks. This has been seen in both indentation [47] as well as erosion studies [48].

The impact parameters calculated from Hertz theory are listed in Table 9.11. For comparison the impact parameters for sand on diamond are also listed. This comparison helps to explain why Hertzian ring cracks were not seen on diamond when sand was used as the erodent at the same velocity. One of the reasons for this is that the contact pressure and tensile stress generated by the diamond grit is approximately 7 times greater than impact of the sand particles at the same velocity. It is the tensile stresses at the surface that are responsible for the initiation of the ring cracks. The greater density of the diamond compared to the sand, means that the kinetic energy of impact is also greater. However, the most significant reason for the increased contact pressure and tensile stress is the fact that the diamond particles did not undergo the same level of fragmentation on impact.

The maximum sub-surface shear stress of the target has also been calculated and is listed in Table 9.11. It can be seen that the thickness of the diamond is between 38 and

78 times greater than the depth at which maximum shear stress occurs. For this reason, the influence of shear stress can be ignored in the present case.

Parameter	Diamond on Diamond	Sand on Diamond
Thickness of diamond, C_T (μm)	700	500
Velocity V (m s^{-1})	268	268
Diamond grit size $2R$ (μm)	200	194
Calculated Contact Radius a_m (μm)	28	41
Calculated Contact Diameter d_m (μm)	56	82
Mean Measured Crack Diameter (μm)	61	No cracks
Range of Crack Diameters (μm)	30÷86	No cracks
Calculated Impact Load, F_m (N)	169	54
Calculated Contact Pressure, P_m (GPa)	69.8	10.6
Calculated Tensile Stress, σ_m (GPa)	29.7	4.6
Particle Kinetic Energy, E_k (μJ)	539	395
Calculated Contact Time, t_e (μs)	0.08	0.19
Maximum Shear Stress, τ_m (GPa)	49.2	7.5
Depth of Maximum Shear Stress, z_τ (μm)	9.0	13.1
z_τ / C_T	0.013	0.026

Table 9.11: Parameters for the impact of diamond particles on diamond compared with those of sand on diamond.

9.10 Conclusions

This chapter has examined the damage features generated in diamond coatings by the impact of high velocity silica sand and diamond particles. These features have been examined in detail in order to identify the mechanisms by which these features are formed.

The low hardness and fracture toughness of the sand particles prevented any radial and lateral cracks from being generated in the coatings. High-speed photography, electron microscopy and sieving of used sand demonstrated that the sand undergoes extensive fragmentation on impact with the diamond surfaces. No evidence of plastic deformation of the coatings was seen at the conditions employed during this programme.

The micrographs have shown a number of pin-holes on a single sample and the damage accumulation process caused by impact from sand particles. They also provide important information on the stages involved in their development. The figures show that the following steps occur in the development of a pin-hole:

- Formation of a circumferential crack;
- Initiation of damage in the central region within the circumferential crack;
- Growth of central damaged region both vertically (towards the coating-substrate interface) and laterally (towards the circumferential crack)

The circumferential cracks and pin-holes are seen at all the angles at which the tests were conducted. Moreover, the diameter and aspect ratio of the circumferential cracks do not appear to be dependent on impact angle.

The diameters of the circumferential cracks do not agree with Hertz impact theory, with many cracks being 2 to 4 times larger than the Hertzian contact diameters. Furthermore, a clear trend of increasing crack diameter with coating thickness, which is not predicted by Hertz, is observed. The circumferential crack diameters show good agreement with stress wave reinforcement theory over the range of coating thicknesses tested. This suggests that the cracks are formed by the stress wave reflection and reinforcement at locally debonded regions of the coatings.

The greater hardness and strength of the diamond grit compared to the silica sand means that on impact with a diamond surface, greater contact pressures and tensile stresses are generated, resulting in different damage features. They consisted of radial and lateral cracks as well as square "ring" cracks. The presence of the radial and lateral cracks suggests that plastic deformation of the diamond target may occur on impact. The size of the square cracks is close to the Hertzian contact diameter, which indicates that the Hertzian ring cracks may be generated when the hardness and fracture toughness of the erodent is sufficient to prevent significant fragmentation on impact. No Hertzian ring cracks are seen on diamond surfaces that were impacted by sand particles at the same velocity.

This chapter has shown the evolution of the surface damage features observed in CVD diamond coatings when they are subjected to high velocity sand erosion. However, they do not explain the cause of coating failure. The most likely cause for this is the accumulation of damage at sub-surface locations, for instance the coating-substrate interface. The development of sub-surface damage during the erosion process will be explored in Chapter 10.

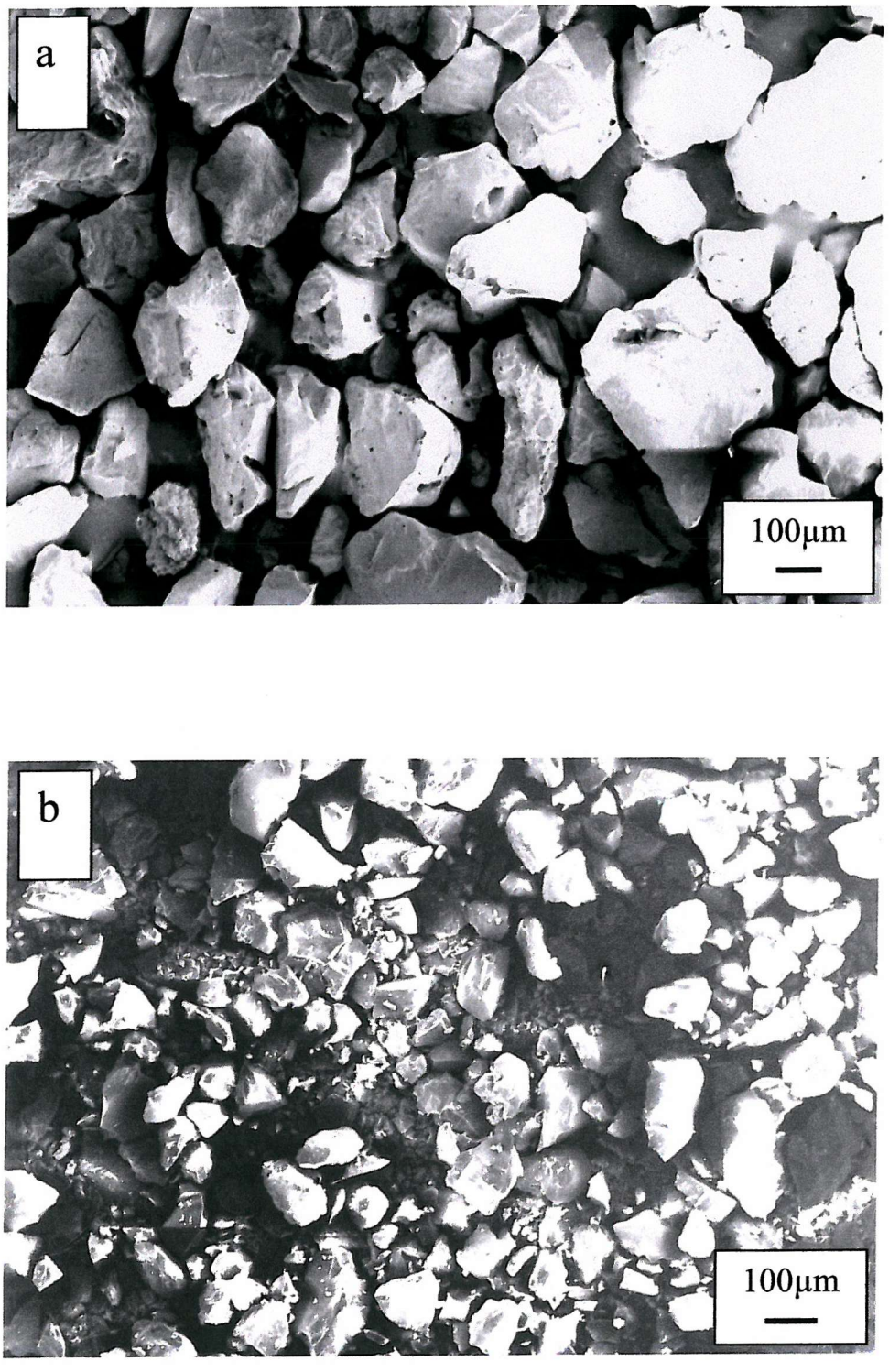

Fig. 9.1: Micrographs of quartz silica sand erodent in (a) the unused condition and (b) after impact with a diamond surface at 268 m s^{-1}. The sand sample seen in (b) was a 50:50 mixture of sand collected from the erosion chamber and the baffle box.

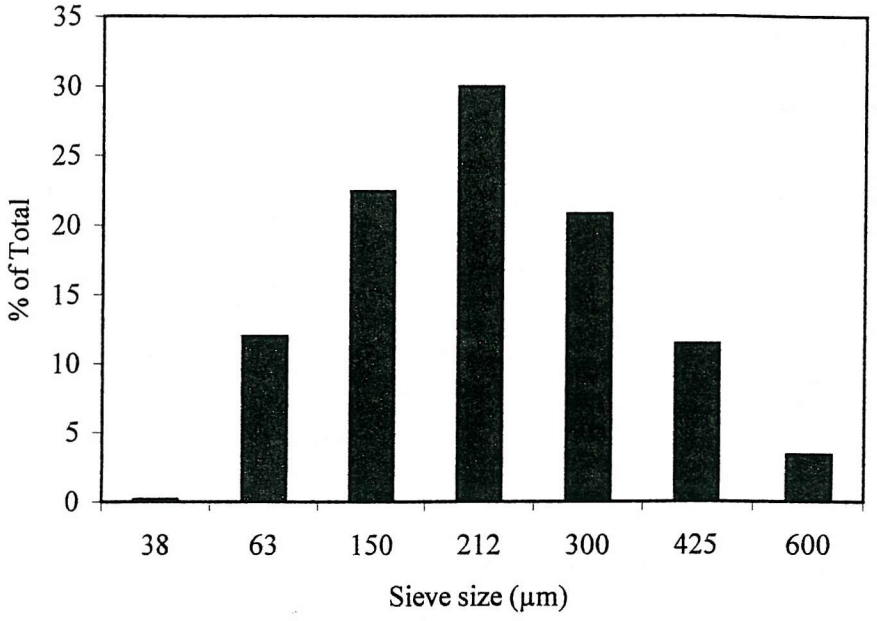

Fig. 9.2: Size distribution of unused quartz silica (Redhill Mix).

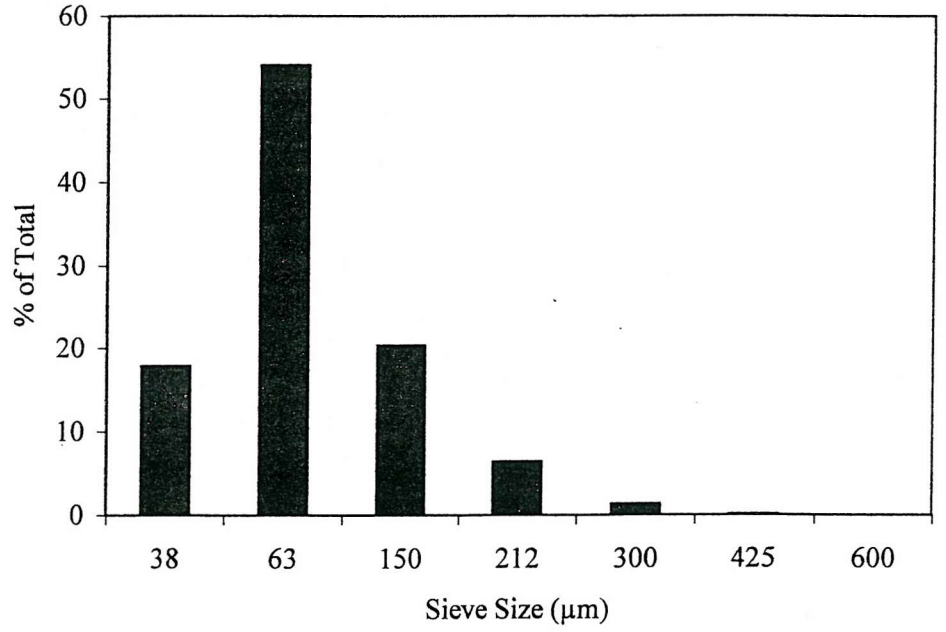

Fig. 9.3: Size distribution of Redhill Mix sand after impact with diamond at 268 m s^{-1}.

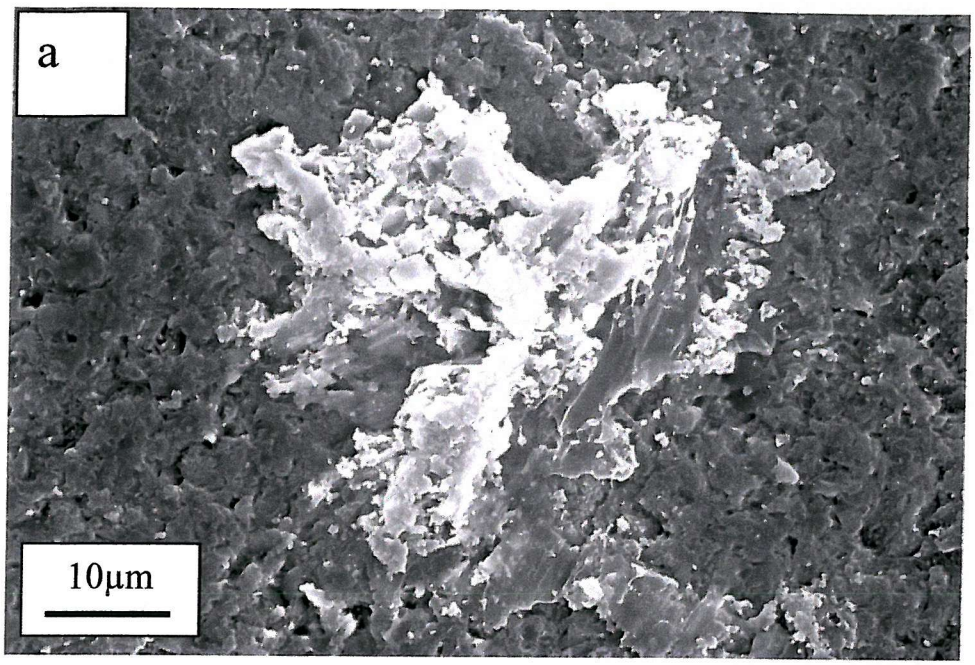

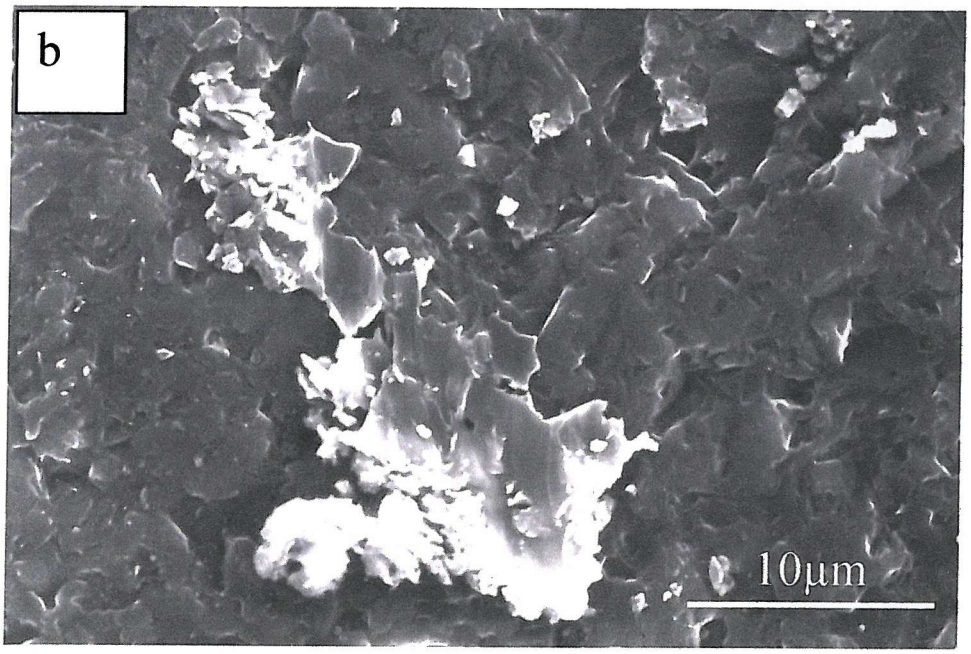

Fig. 9.4: Micrograph of a smeared silica sand particle on the surface of the 60μm diamond coating tested at 268 m s^{-1}, at (a) 30° impact, and (b) 90° impact. Particles below a certain size cannot fragment but fail by plastic flow.

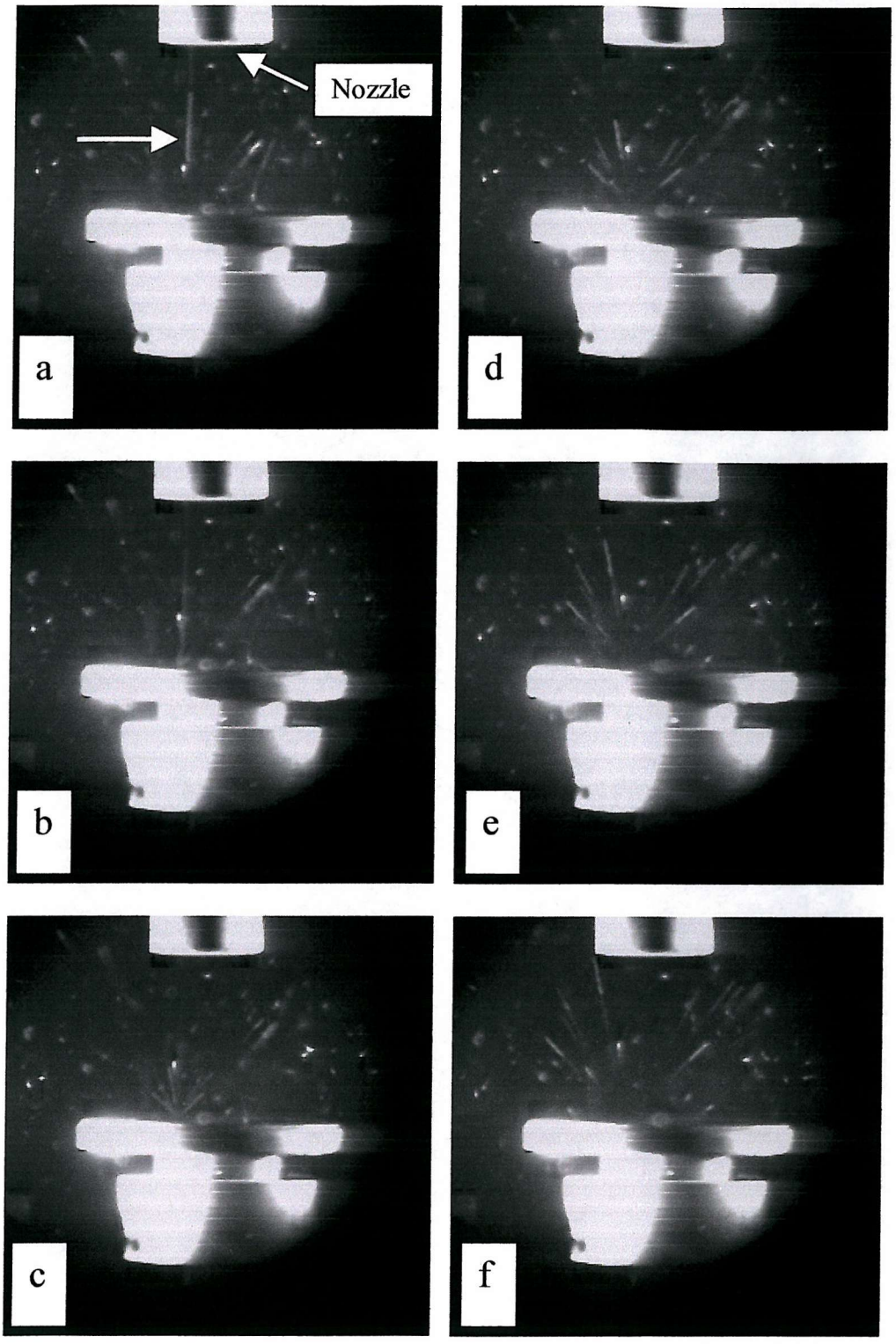

Fig. 9.5: High speed photographic sequence showing the fragmentation of a 500-710μm sand particle (arrowed) following impact at 49 m s^{-1} onto the surface of a 160μm lapped diamond coating. The stand-off distance between the nozzle and the target is 30mm and the particle flux is 0.5 kg m^{-2} s^{-1}. Framing rate 4500 fr sec^{-1}.

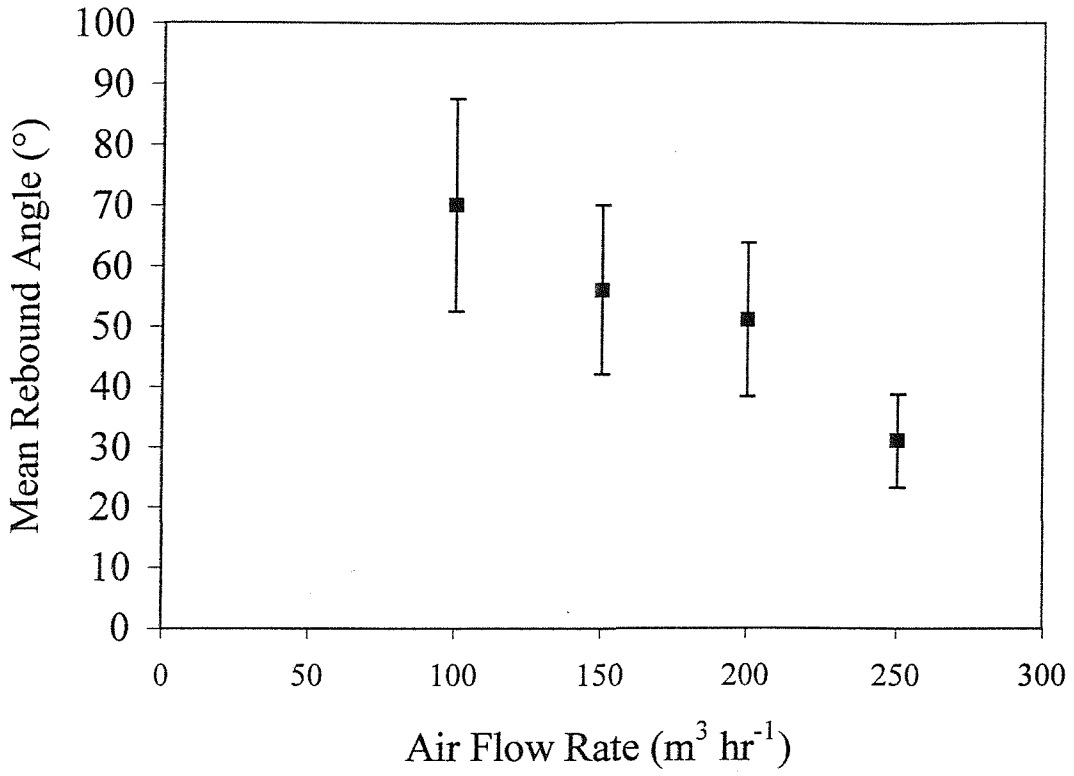

Fig. 9.6: Graph of Mean Rebound Angle vs. Air Flow Rate for 500-710μm sand particles measured using a Kodak 4540 high-speed camera described in Section 9.3.2. The definition of the term "Rebound angle" is shown in Figure 9.7.

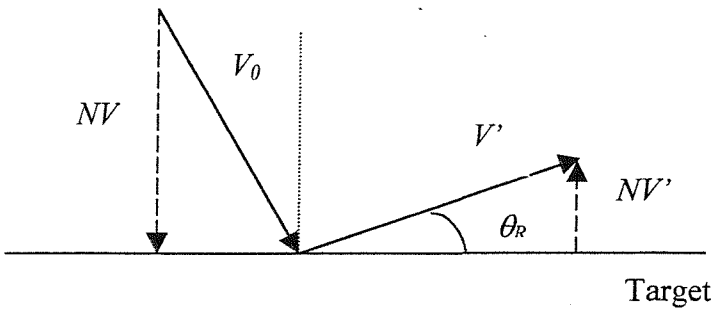

Fig. 9.7: Definition of the coefficient of restitution used in the present work. The rebound angle, θ_R, is also shown.

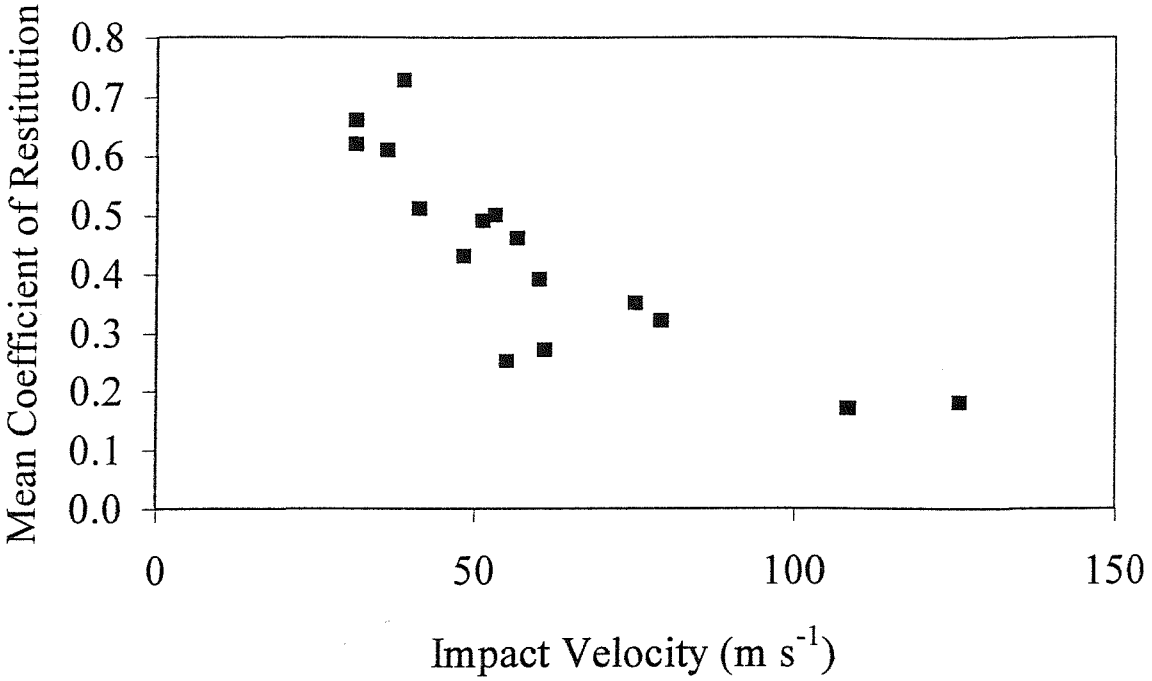

Fig. 9.8: Graph of Mean Coefficient of Restitution vs. Particle Impact Velocity for 500-710μm sand particles impacting the surface of a 160 μm diamond coating. The nozzle-target stand-off distance was 30mm and the particle flux was 0.5 kg m^{-2} s^{-1}.

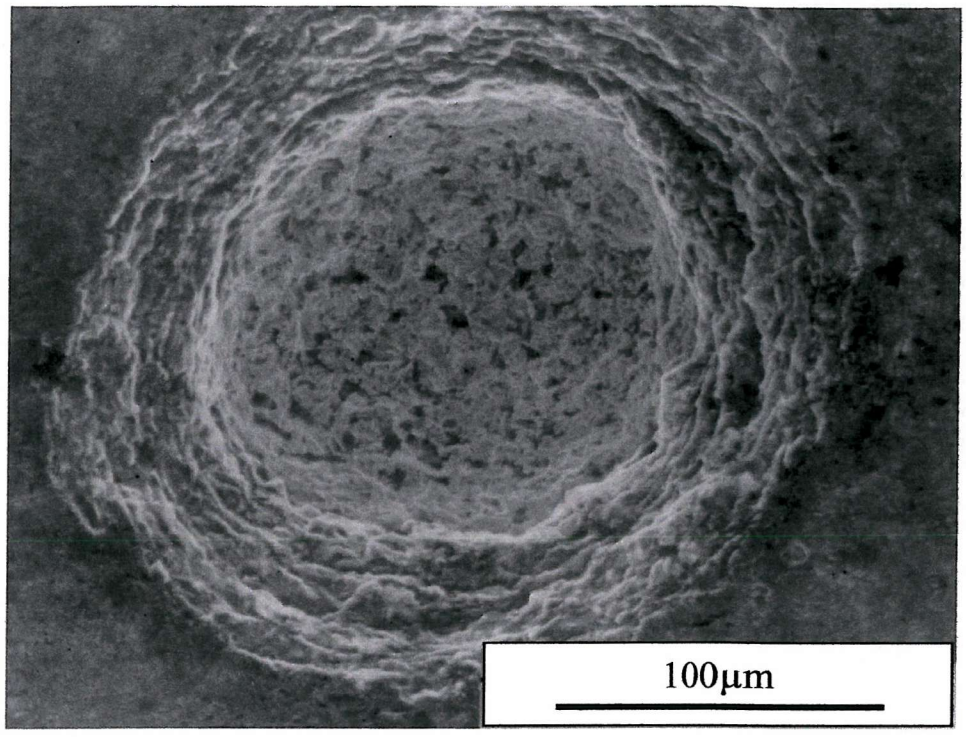

Fig. 9.9: Micrograph from a 46μm lapped diamond coating tested at 268 m s^{-1} for 3 hours showing a pin-hole that has completed penetrated the coating.

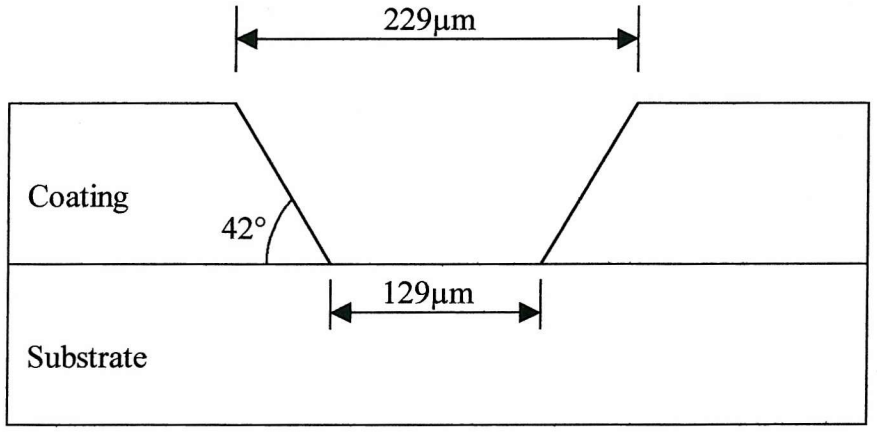

Fig. 9.10: Schematic diagram of the pin-hole shown in Figure 9.9 seen in transverse section, showing the pin-hole profile.

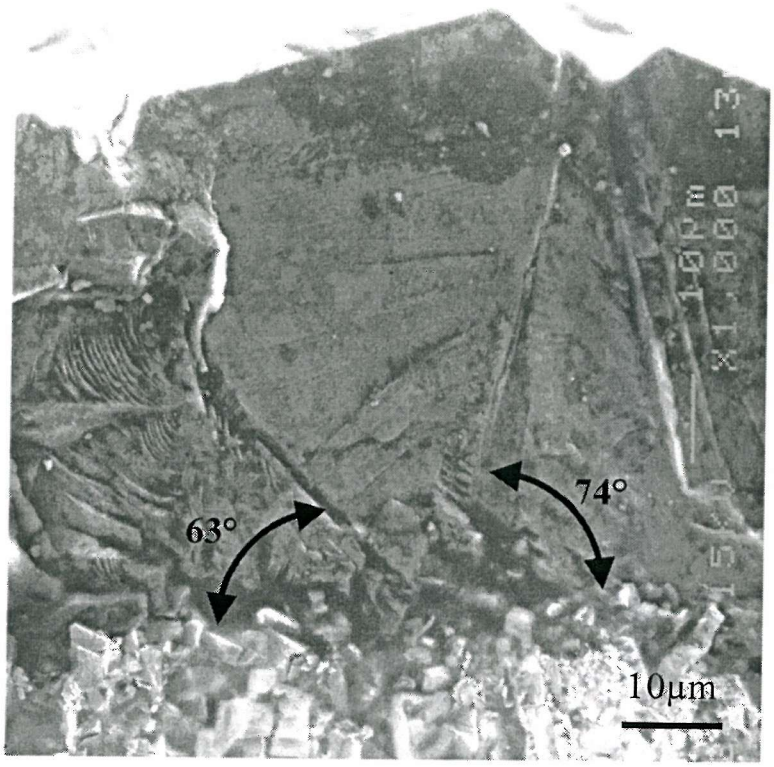

Fig. 9.11: Section from an untested 60μm as-grown coating on WC-6Co, showing the profile of a columnar grain.

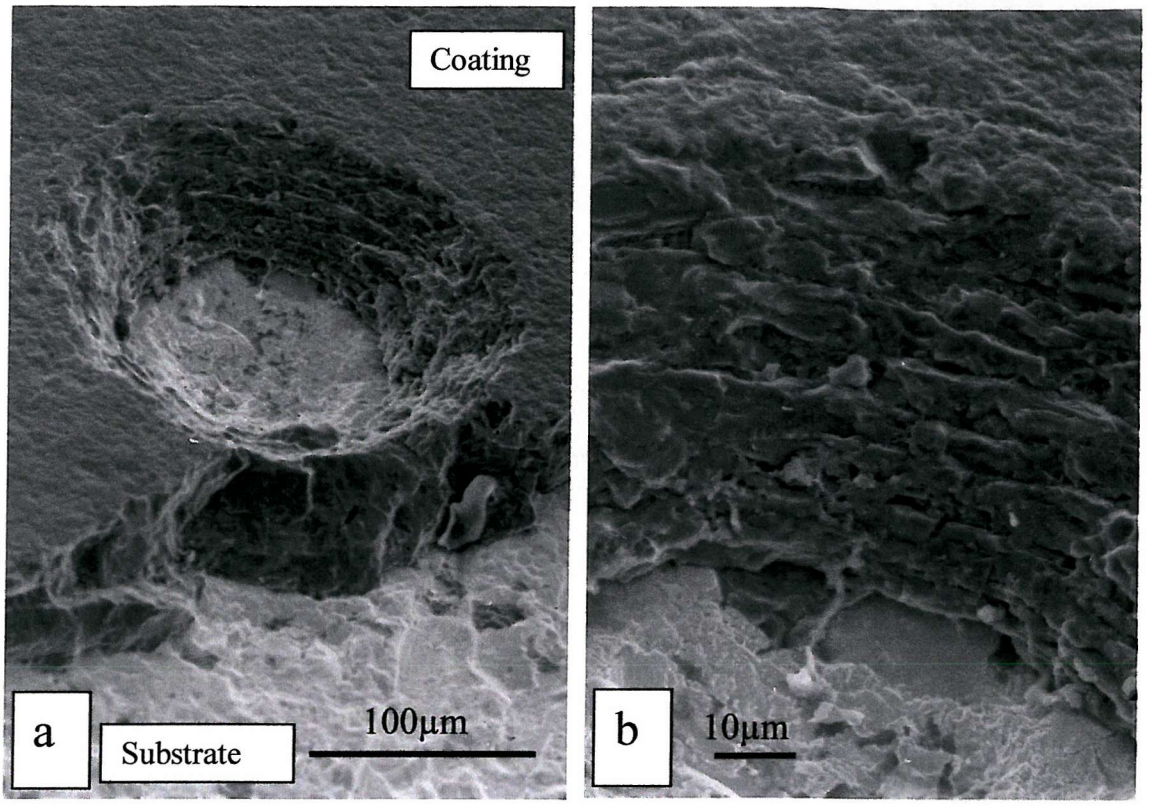

Fig. 9.12: Micrograph of 46μm coating on W, tested at 268 m s^{-1} for 3 hours, showing (a) a pin-hole at the edge of the spalled region of the coating, and (b) a detail from (a). The sample has been tilted at 45°.

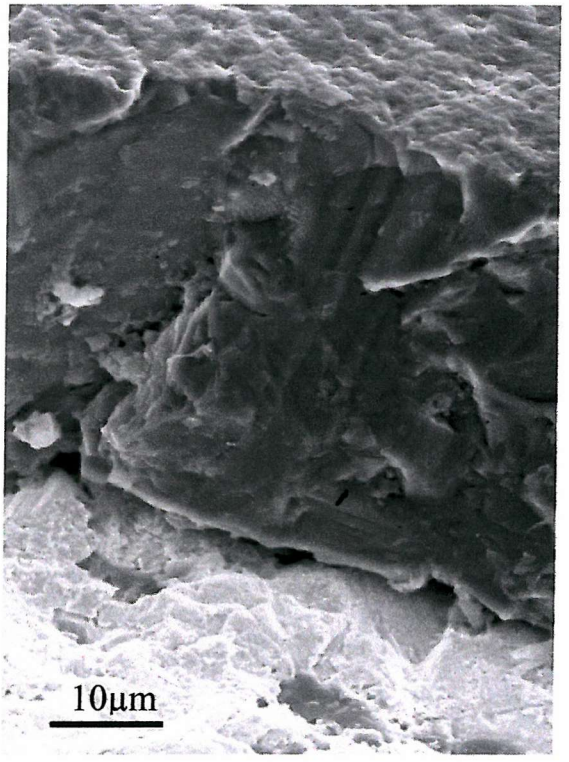

Fig. 9.13: Micrograph of a detail from the edge of the spalled region of the lapped 46μm on W coating showing debonding of the coating at the interface.

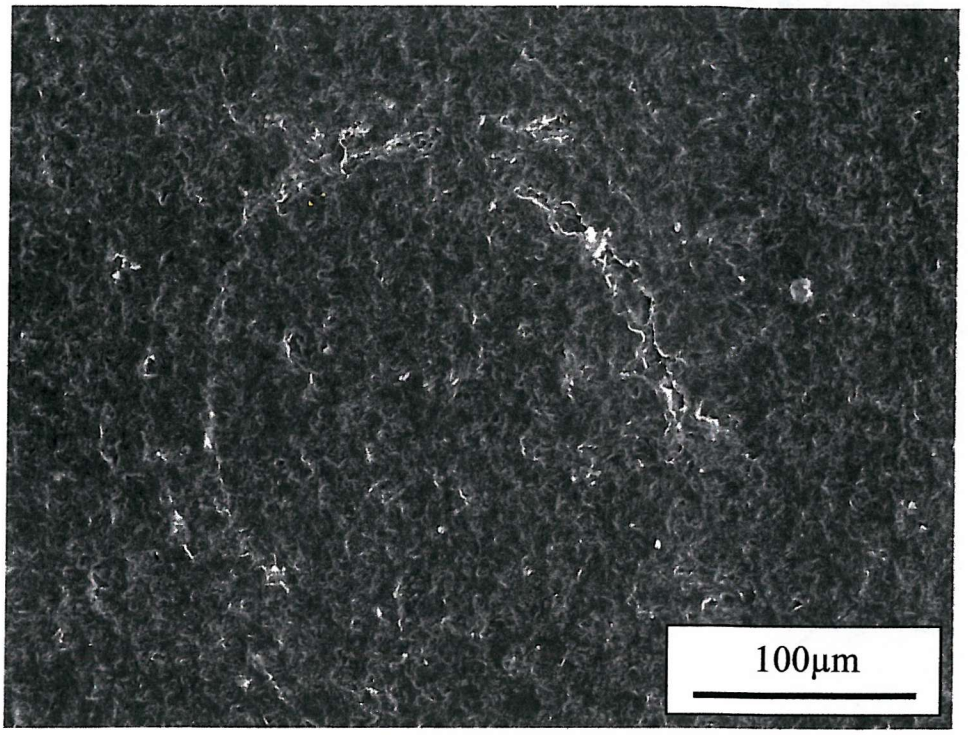

Fig. 9.14: Circumferential crack from a lapped 60μm diamond coating on W tested at 268 m s^{-1}, observed after 4 hours. Estimated total number of impacts: N (SW) = 160,048; N (Hertz) = 15,208.

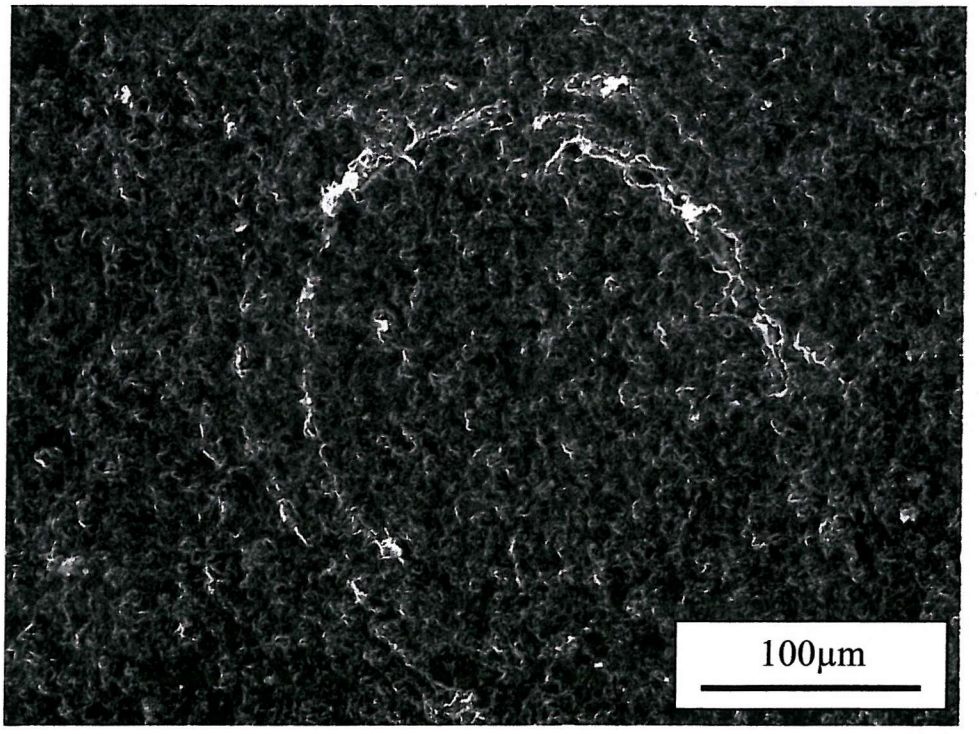

Fig. 9.15: Circumferential crack from a lapped 60μm diamond coating on W tested at 268 m s^{-1}, observed after 6 hours. N (SW) = 240,072; N (Hertz) = 22,812.

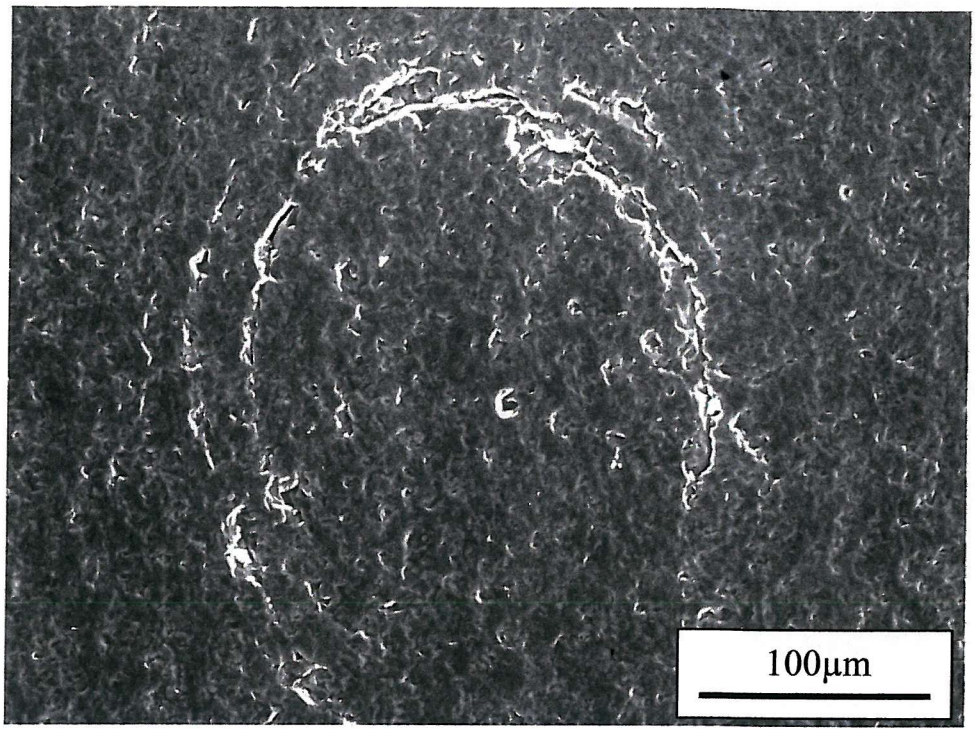

Fig. 9.16: Circumferential crack from a lapped 60μm diamond coating on W tested at 268 m s^{-1}, observed after 9 hours. N(SW) 360,108; N(Hertz) = 34,218.

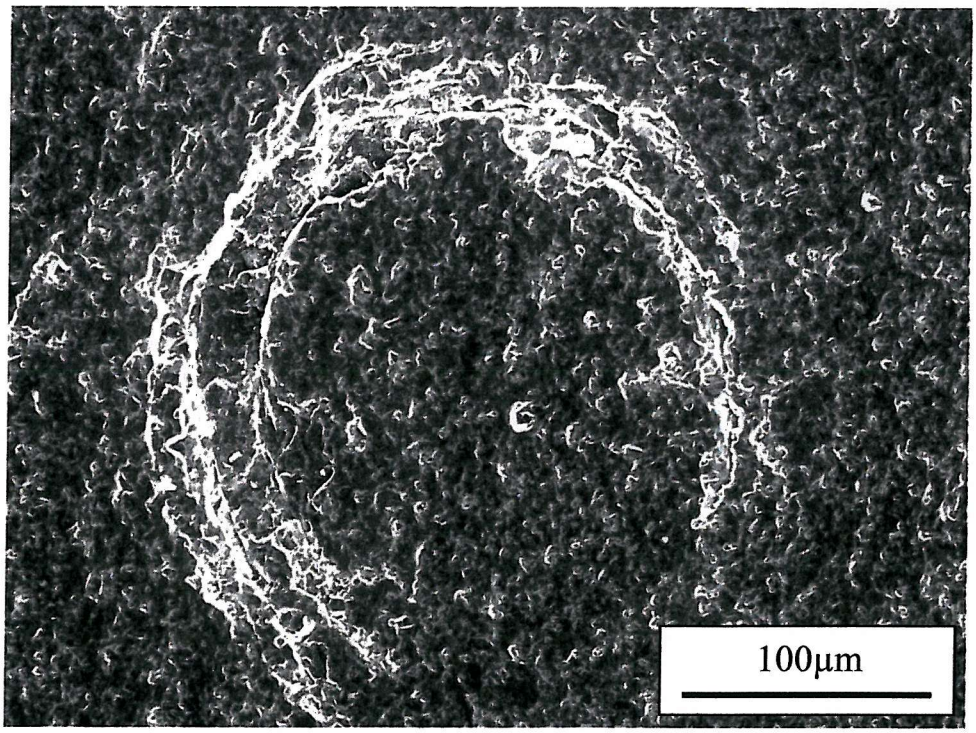

Fig. 9.17: Circumferential crack from a lapped 60μm diamond coating on W tested at 268 m s^{-1}, observed after 11 hours. N(SW) = 440,132; N(Hertz) = 41,822.

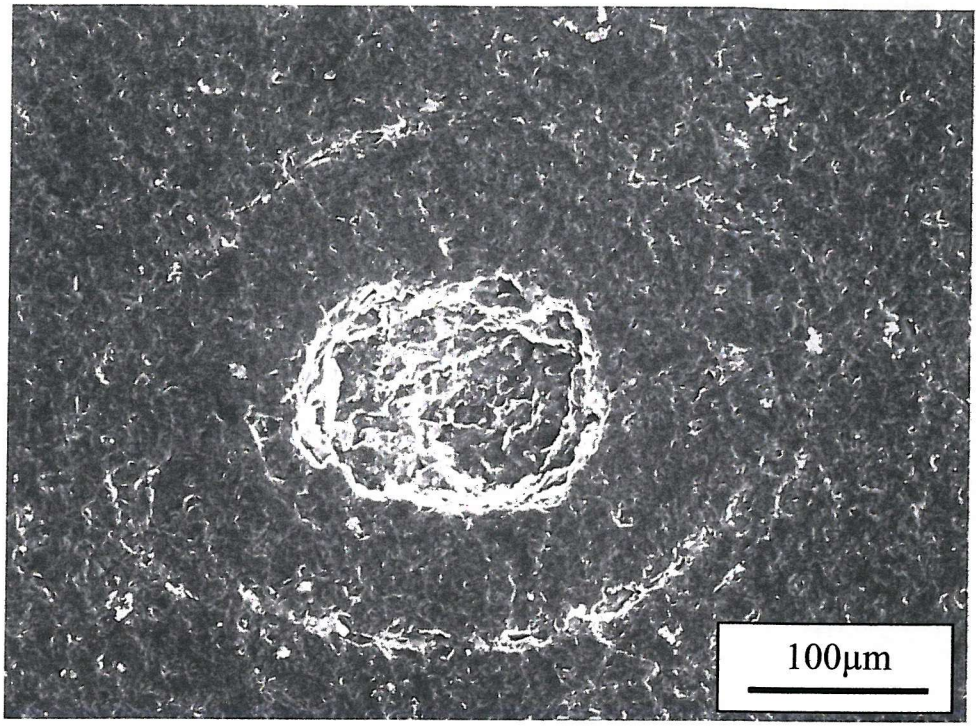

Fig. 9.18: Micrograph from the lapped 60μm diamond coating on W showing a pin-hole, observed after 6 hours at 268 m s^{-1}. N (SW) = 240,072; N (Hertz) = 22,812.

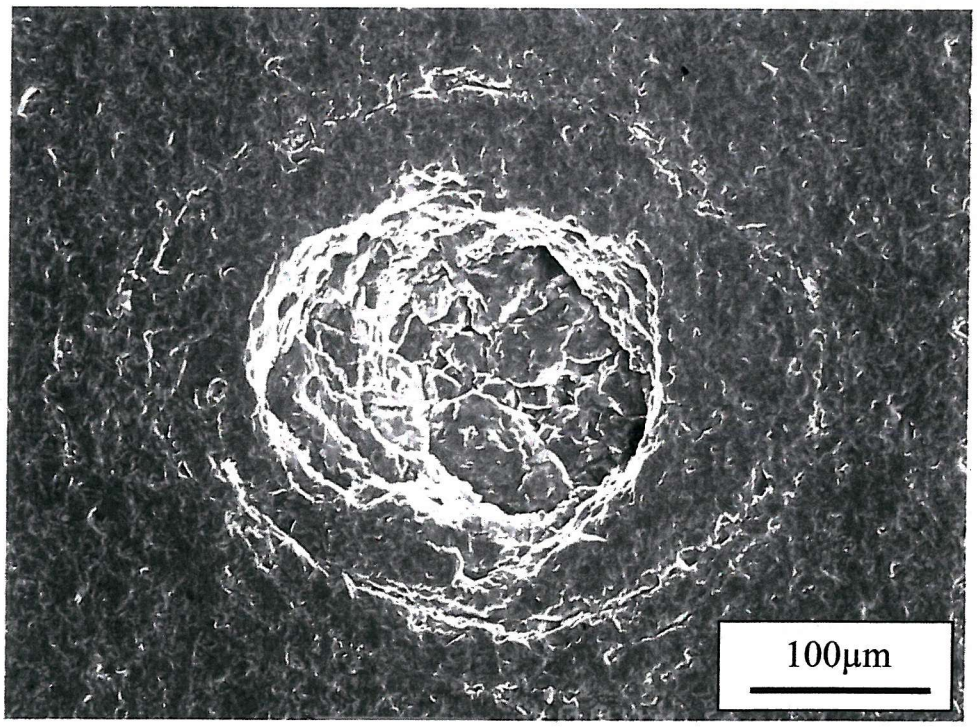

Fig. 9.19: Micrograph from the lapped 60μm coating on W showing the same pin-hole as Figure 9.18, observed after 9 hours at 268 m s^{-1}. N(SW) 360,108; N(Hertz) = 34,218.

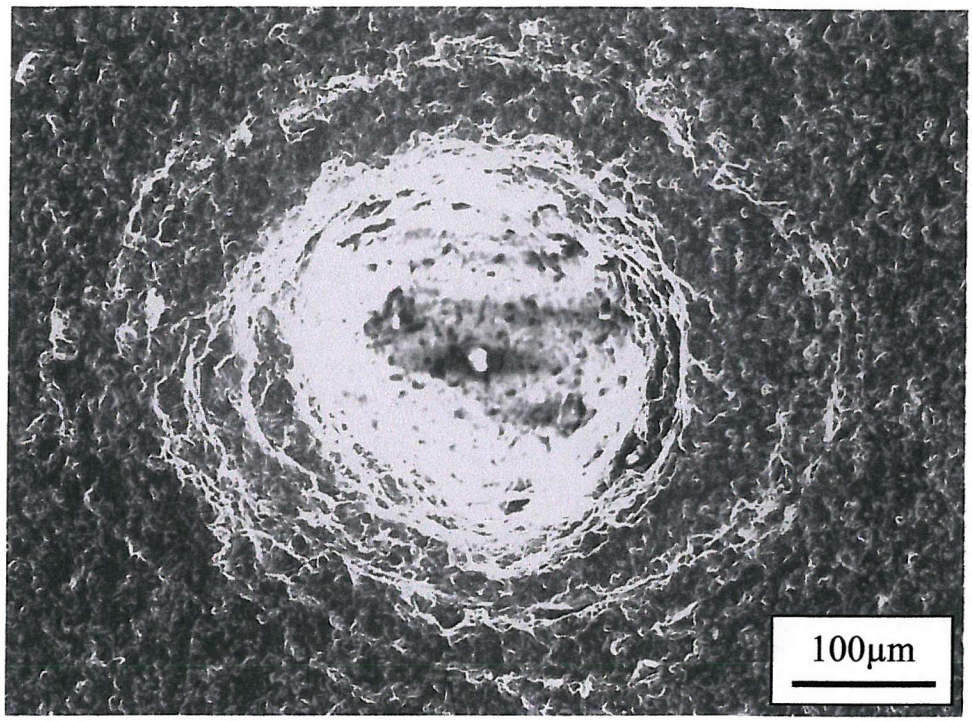

Fig. 9.20: Micrograph from the lapped 60μm coated showing the same pin-hole as Figure 9.18, observed after 11 hours at 268 m s^{-1}. N(SW) = 440,132; N(Hertz) = 41,822.

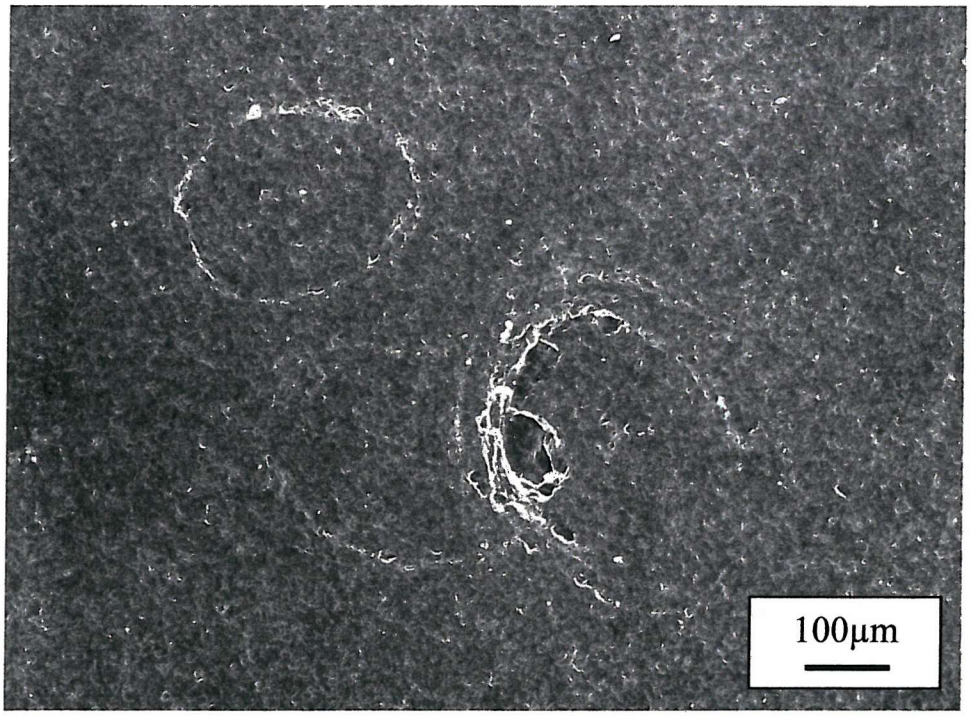

Fig. 9.21: Micrograph of three circumferential cracks from the lapped 60μm coating on W tested at 268 m s^{-1} and photographed after 4 hours. Estimated total number of impacts: N (SW) = 160,048; N (Hertz) = 15,208.

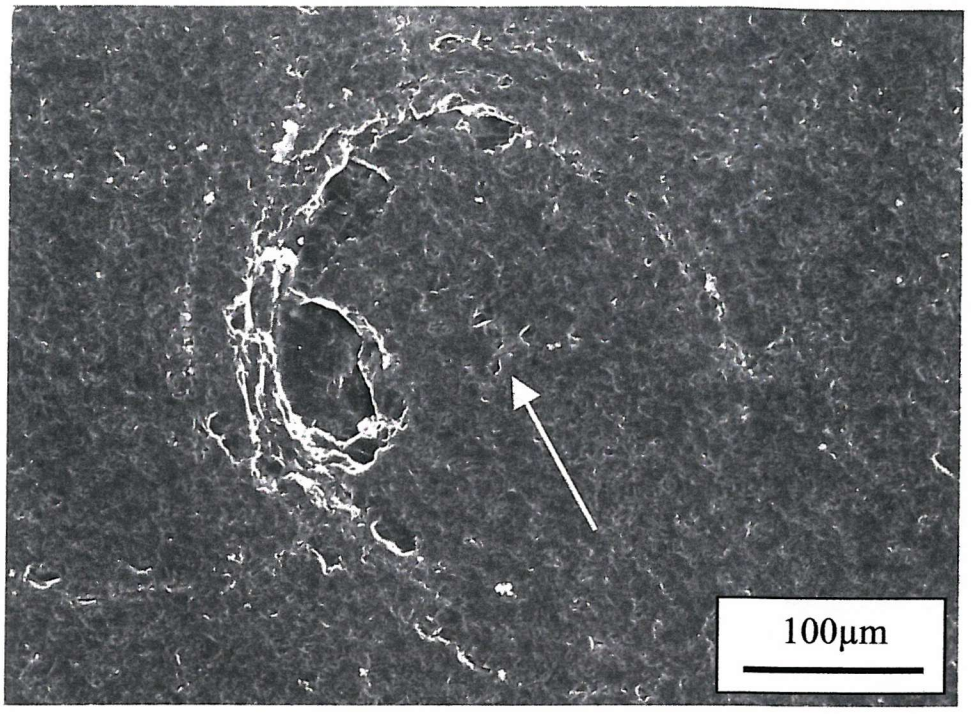

Fig. 9.22: Detail from Figure 9.21, showing the point of overlap of two circumferential cracks, where material has been ejected. Some microscopic damage can be seen in the centre of the circumferential crack (marked by the arrow), which could be the precursor of greater damage, leading to a fully-fledged pin-hole.

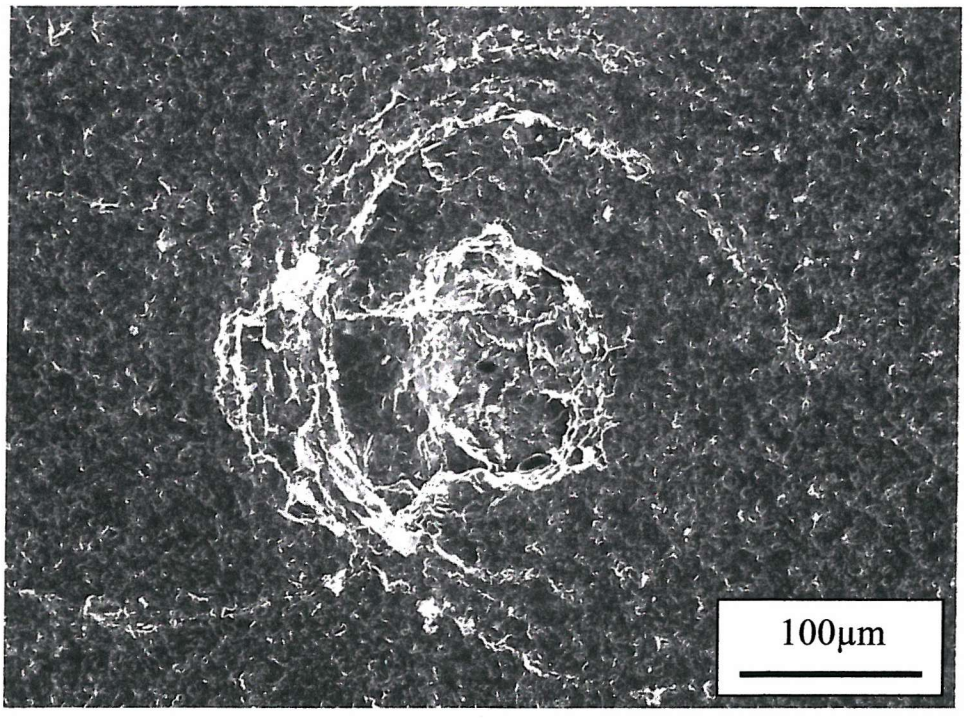

Fig. 9.23: Micrograph of the same location as Figure 9.22, taken after 6 hours at 268 m s^{-1}, showing increased damage in the centre of the circumferential crack. N (SW) = 240,072; N (Hertz) = 22,812.

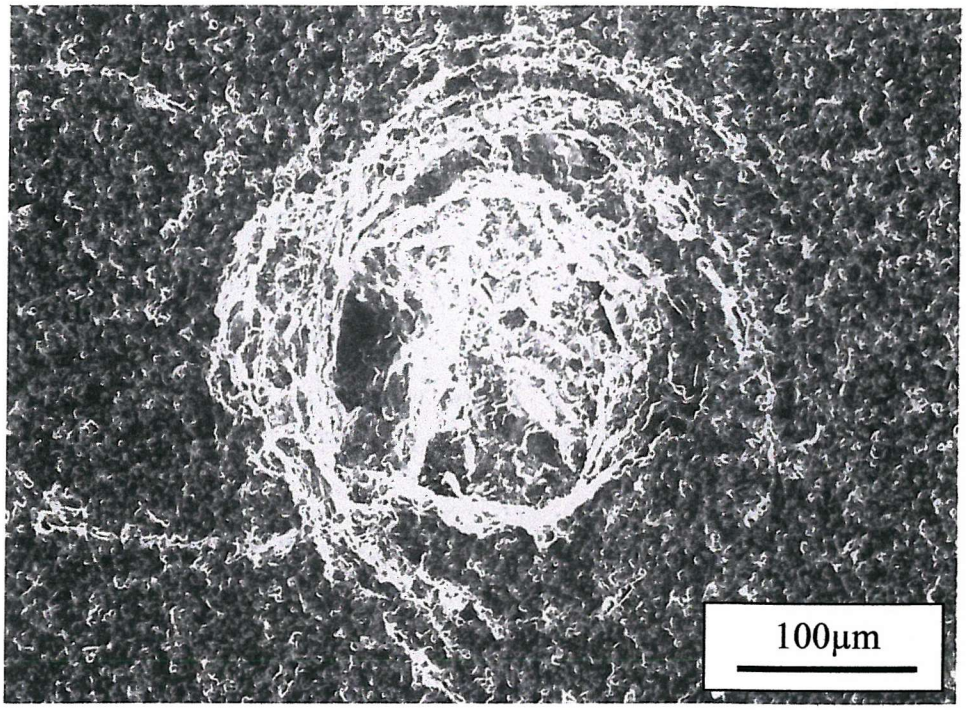

Fig. 9.24: Micrograph of the same location as Figures 9.22 and 9.23, taken after 11 hours at 268 m s^{-1}, showing further damage in the centre of the circumferential crack. N(SW) = 440,132; N(Hertz) = 41,822.

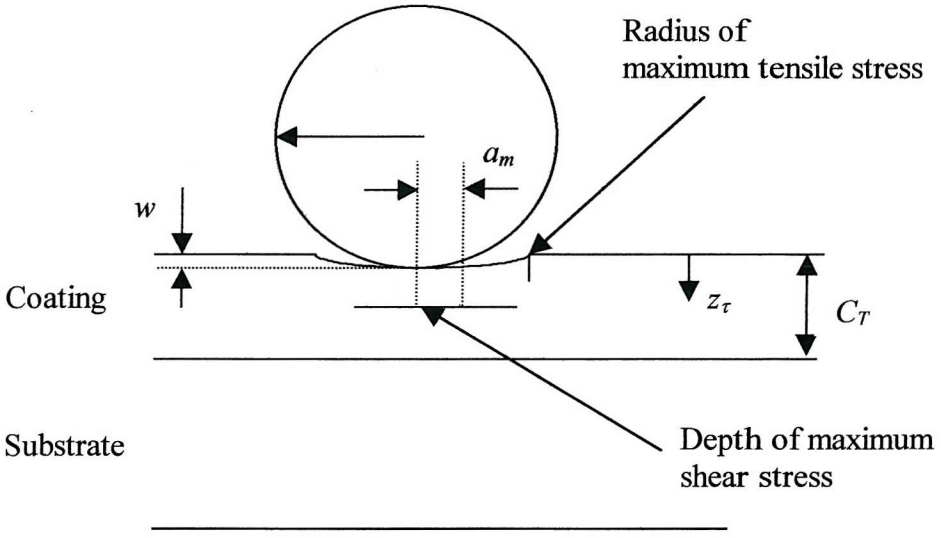

Fig. 9.25: Schematic diagram of the parameters in the Hertzian contact of a sphere on a coated material. Hertzian contact assumes that the particle is spherical and that the contact is purely elastic. For the purposes of illustration, the radius at which the maximum tensile stress occurs has been exaggerated.

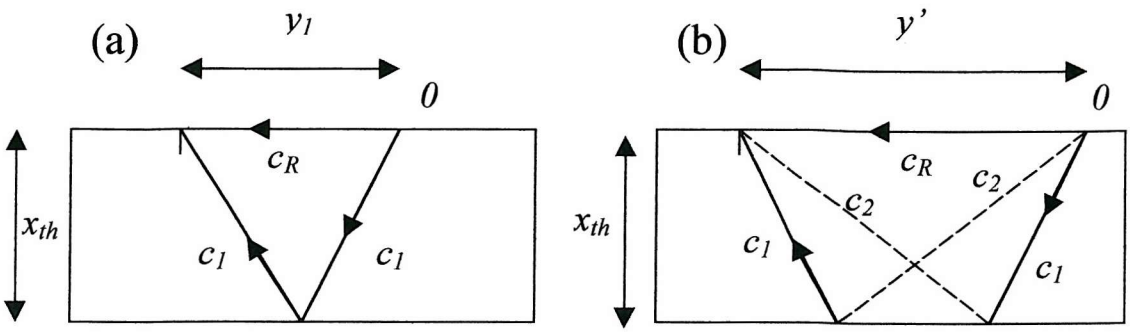

Fig 9.26: Two possible processes of stress wave reinforcement to generate circumferential cracks in CVD diamond [26].

Key: c_1 = compression wave; c_2 = shear wave; c_R = Rayleigh wave; 0 = Origin of impact. The thickness, x_{th}, has been replaced by C_T, the coating thickness, in the present work.

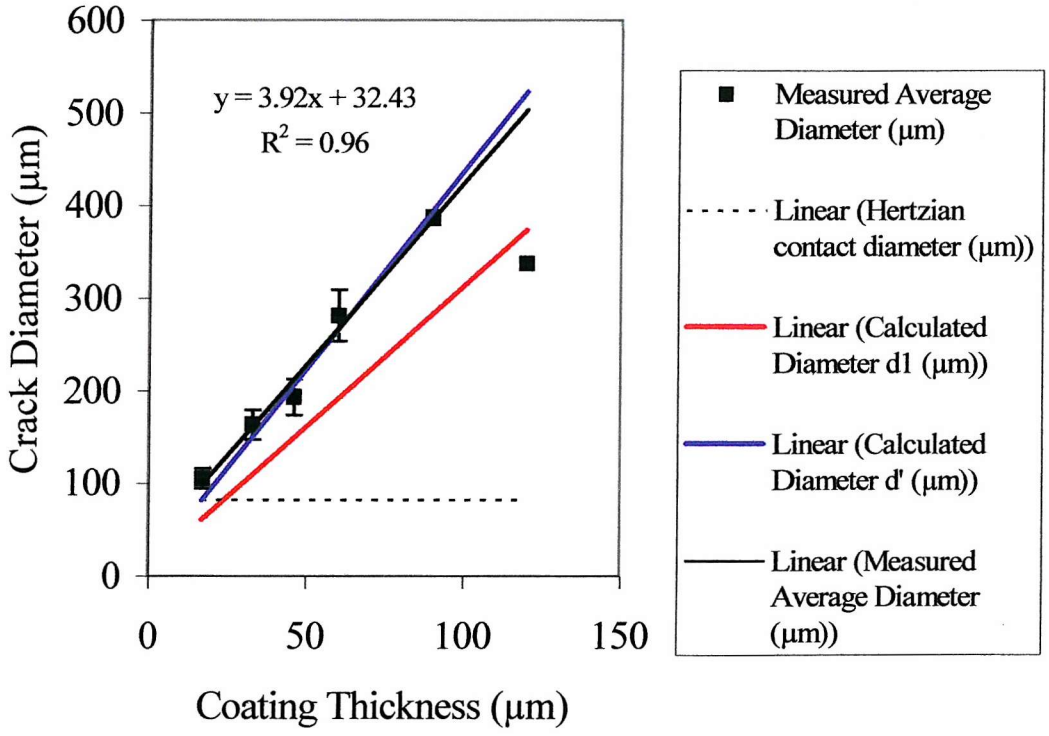

Fig. 9.27: Graph of measured average Circumferential Crack diameter vs Coating Thickness for lapped diamond coatings on tungsten which were erosion tested at 268 m s^{-1}. The calculated stress wave reinforcement diameter and Hertzian contact diameter have also been included for comparison.

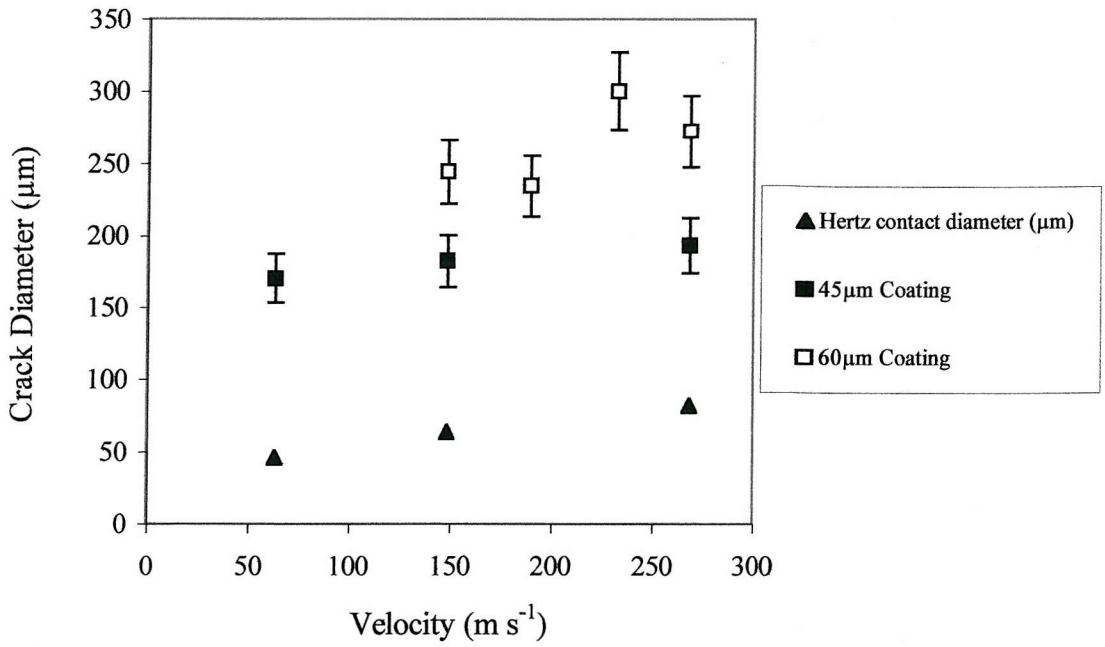

Fig. 9.28: Graph showing the relationship between Circumferential Crack Diameter and Particle Velocity for lapped diamond coatings. The Hertzian contact diameter is also included for comparison.

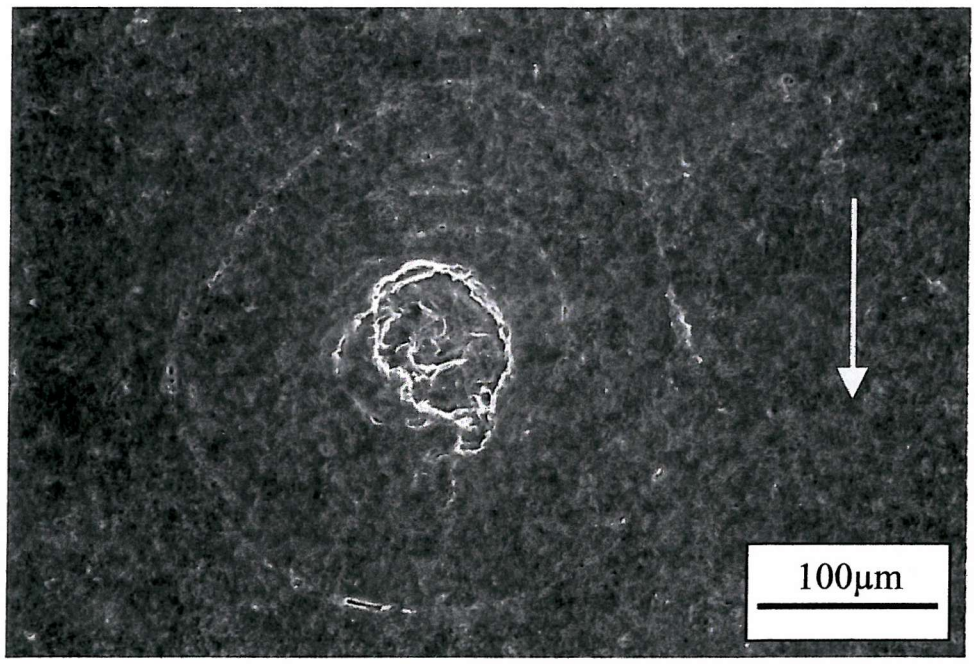

Fig. 9.29: Micrograph of a circumferential crack and pin-hole taken from a 60μm diamond coating tested at 268 m s^{-1} 30° impact.

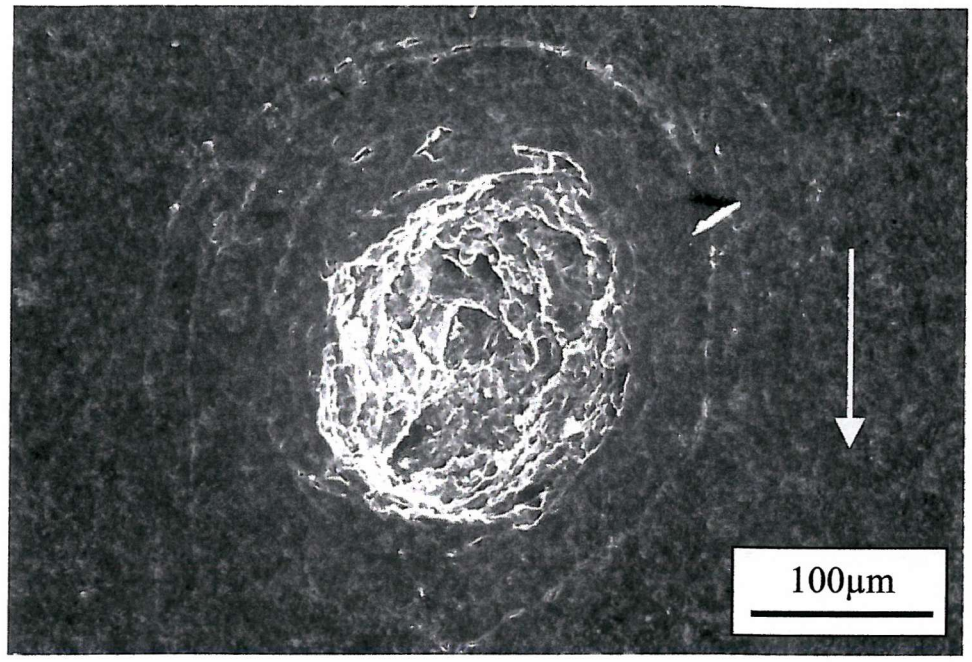

Fig. 9.30: Micrograph of a circumferential crack and pin-hole taken from a 60µm diamond coating tested at 268 m s^{-1} 60° impact.

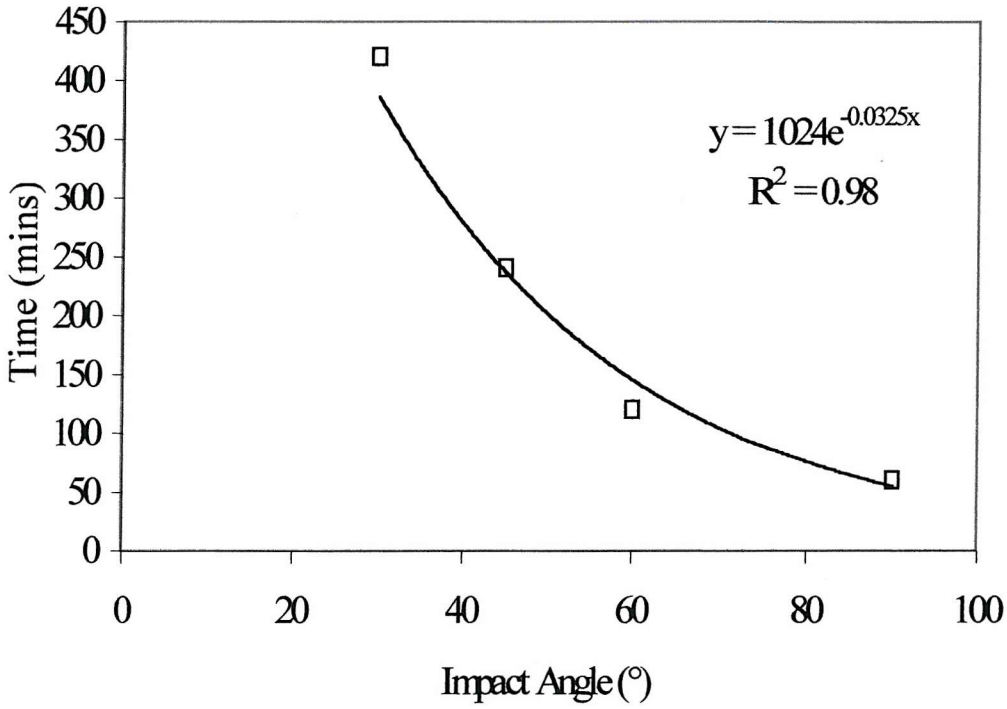

Fig. 9.31: Graph showing the relationship between Impact Angle and the Time at which the first pin-hole was observed for 60µm diamond coatings on tungsten at 268 m s^{-1}.

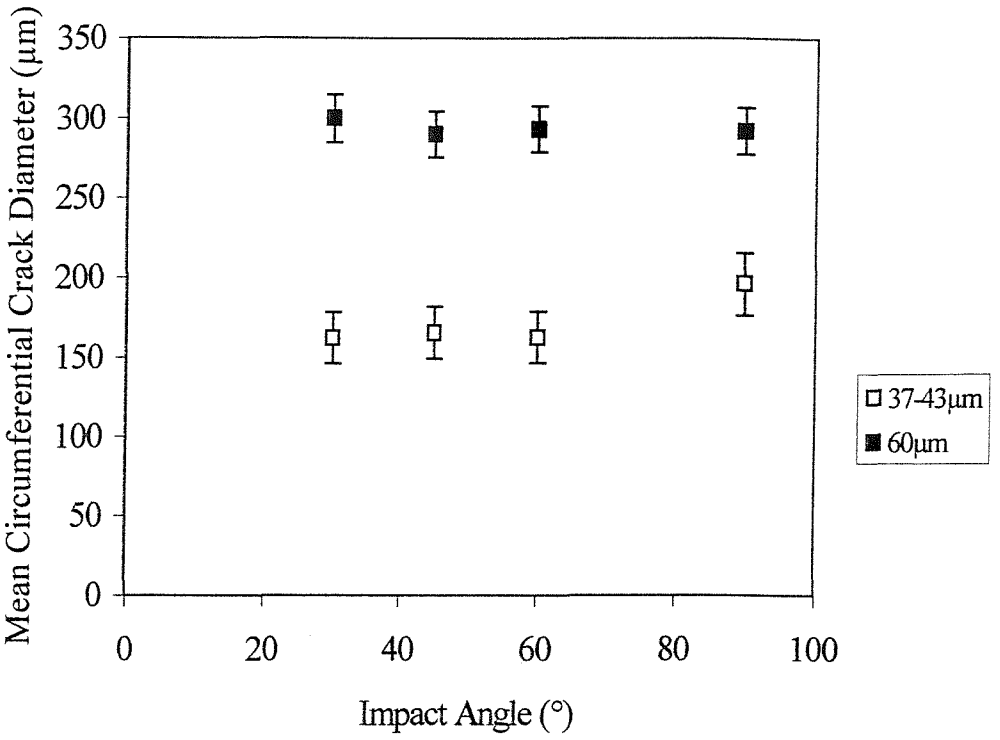

Fig. 9.32: Graph of Mean Circumferential Crack Diameter vs Impact angle for 37-43µm and 60µm lapped diamond coatings tested at 268 m s^{-1}.

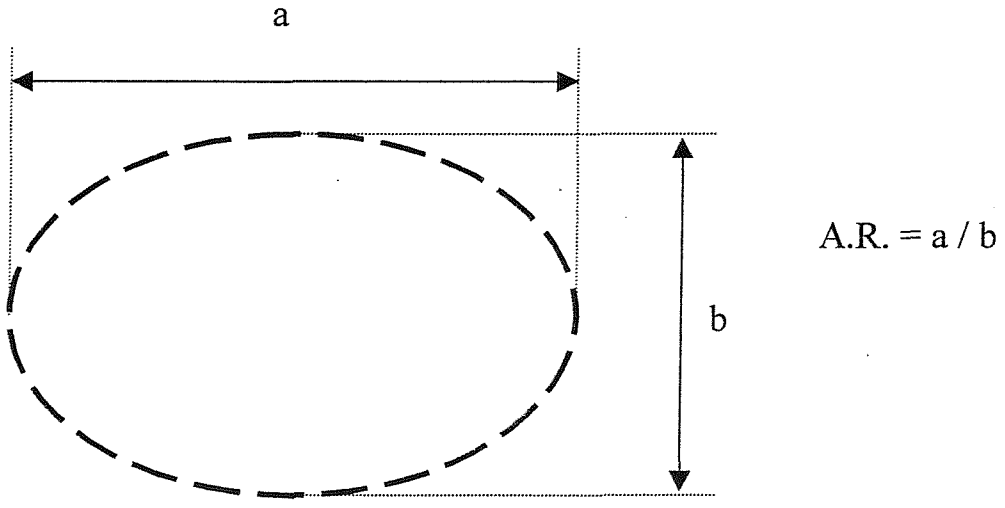

Fig. 9.33: Definition of the term "aspect ratio" (A.R) used in describing the circumferential crack shape.

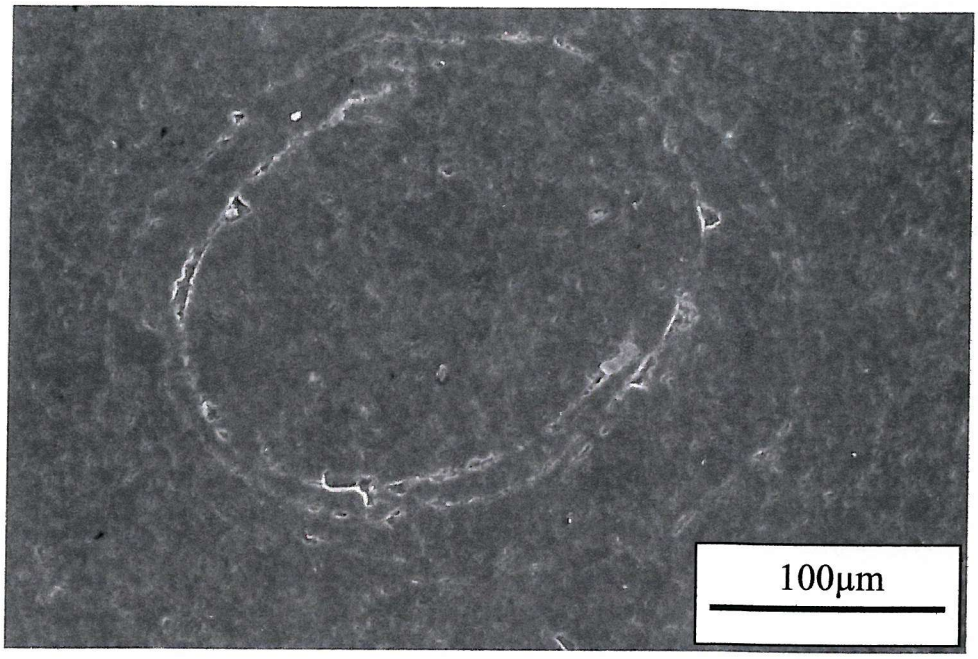

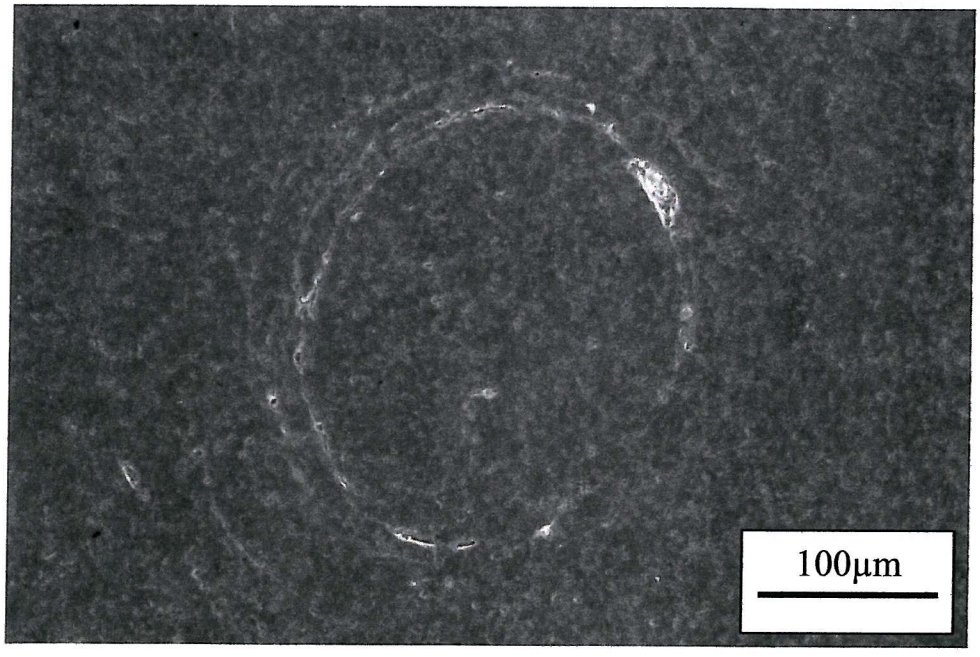

Fig. 9.34: Micrographs of two circumferential cracks seen on a 60μm lapped diamond coating tested at 268 m s^{-1} for 5 hours at 90° impact.

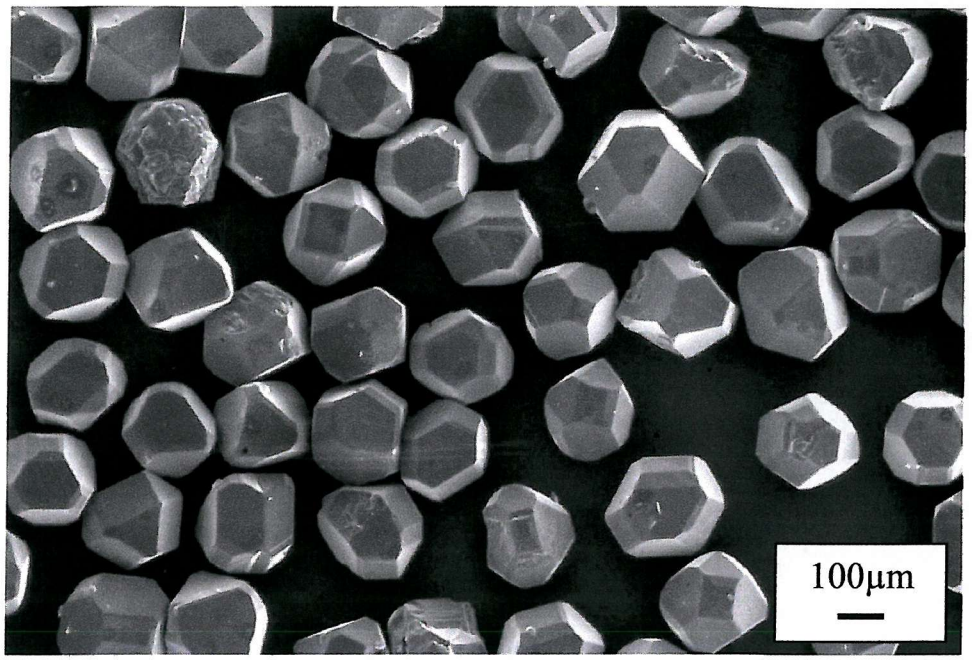

Fig. 9.35: Micrograph of unused PDA999 synthetic diamond grit.

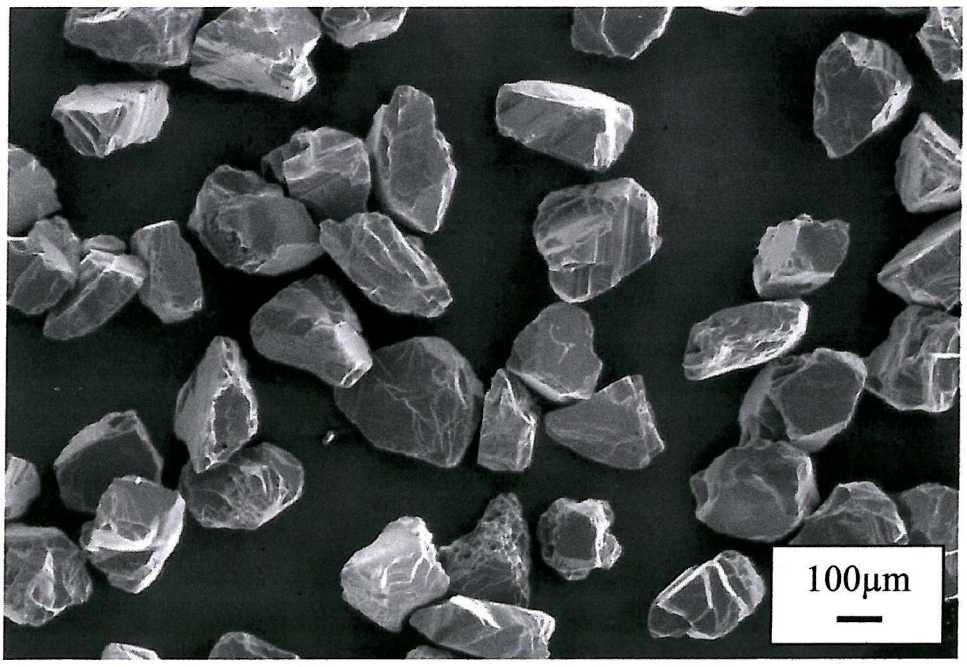

Fig. 9.36: Micrograph of unused EMB natural diamond grit.

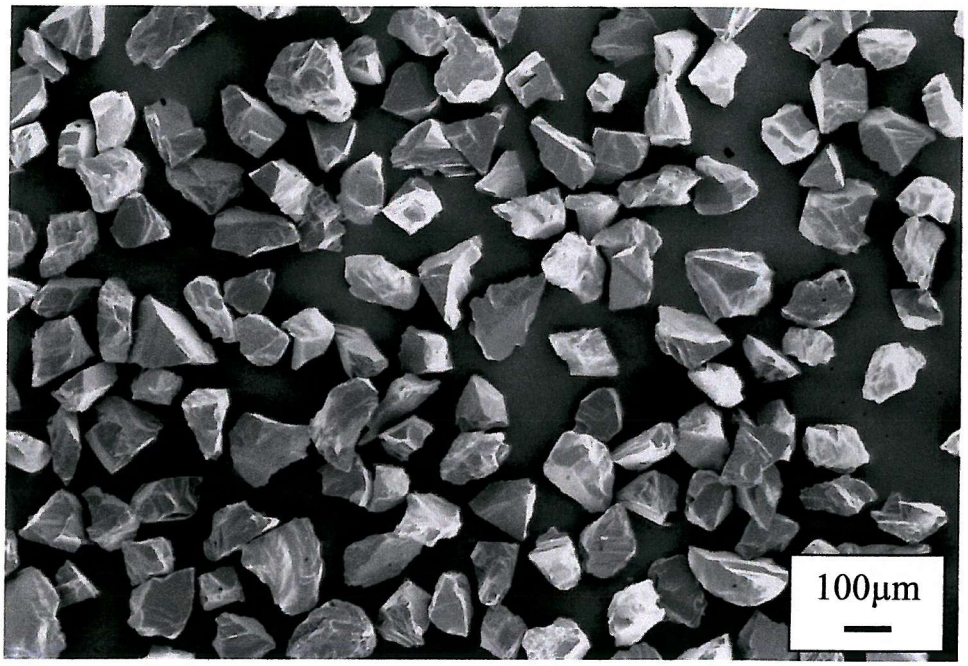

Fig. 9.37: Scanning electron micrograph of used EMB natural diamond grit following impact with a diamond surface at 268 m s^{-1}.

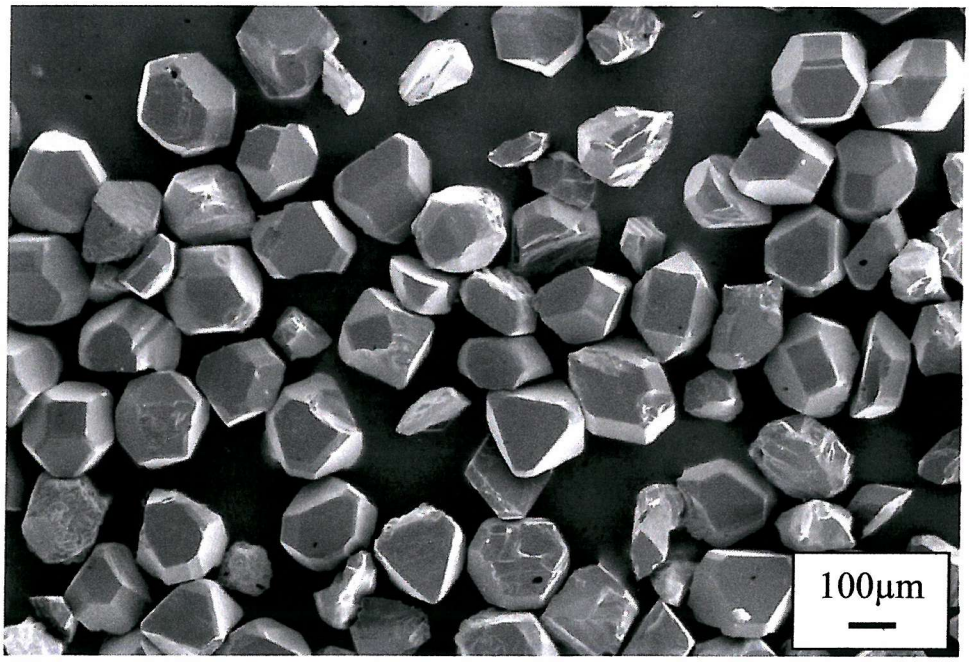

Fig. 9.38: Scanning Electron micrograph of used PDA999 natural diamond grit following impact with a diamond surface at 268 m s^{-1}.

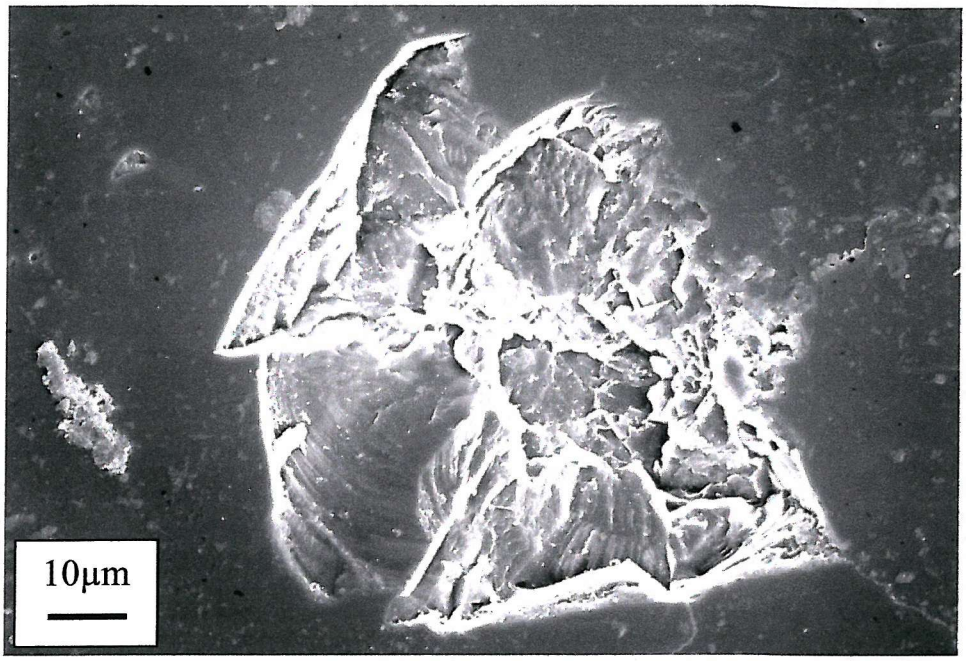

Fig. 9.39: Scanning electron micrograph of the surface of the diamond target impacted by EMB angular natural diamond grit at 268 m s^{-1}.

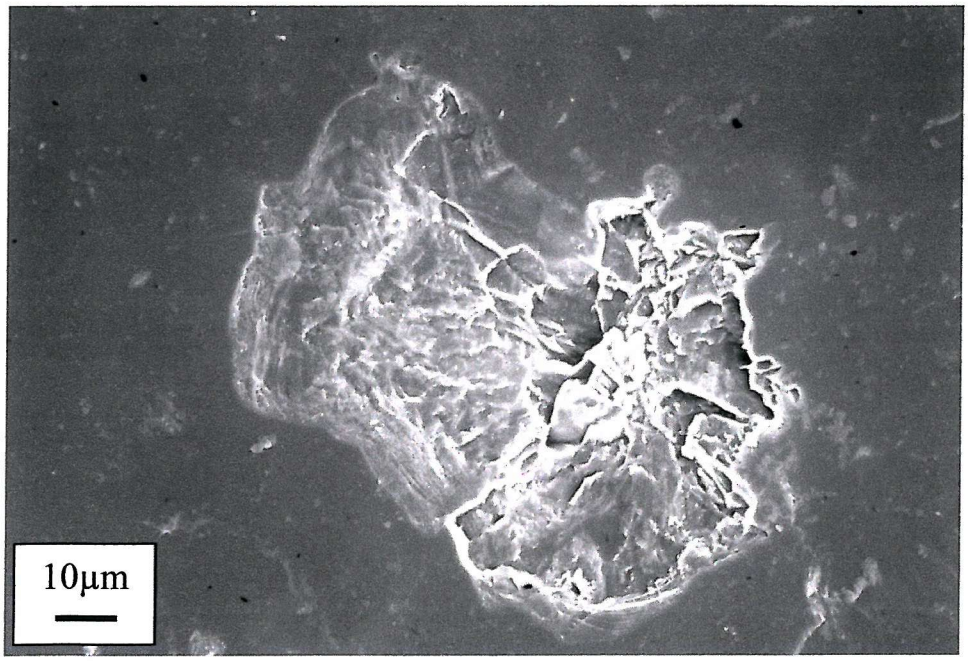

Fig. 9.40: Scanning electron micrograph of the surface of the diamond target impacted by EMB angular natural diamond grit at 268 m s^{-1}.

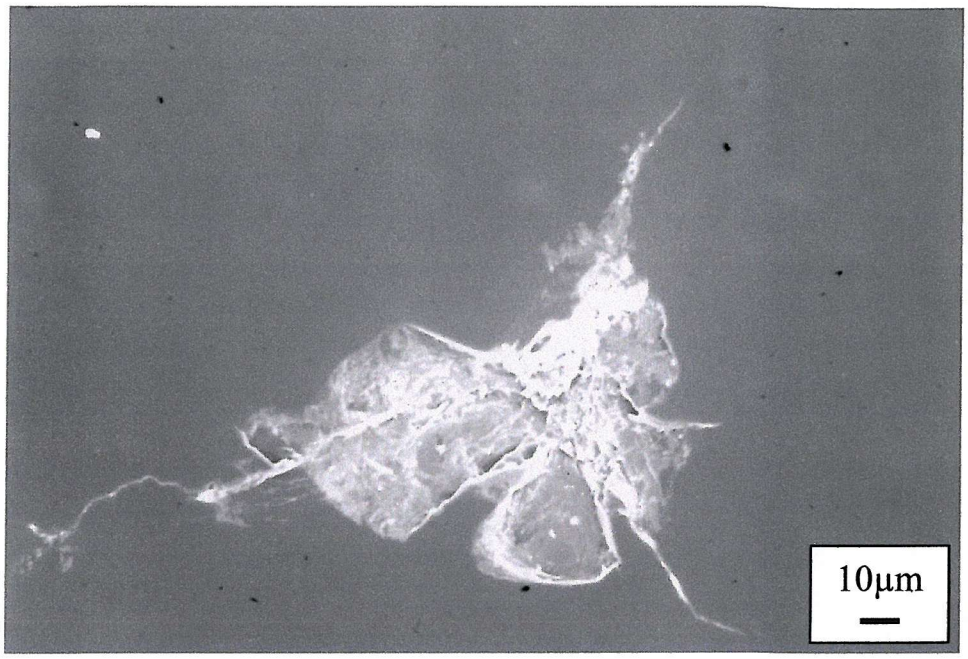

Fig. 9.41: Scanning electron micrograph of the surface of the diamond target impacted by PDA999 (blocky) synthetic diamond grit at 268 m s^{-1}.

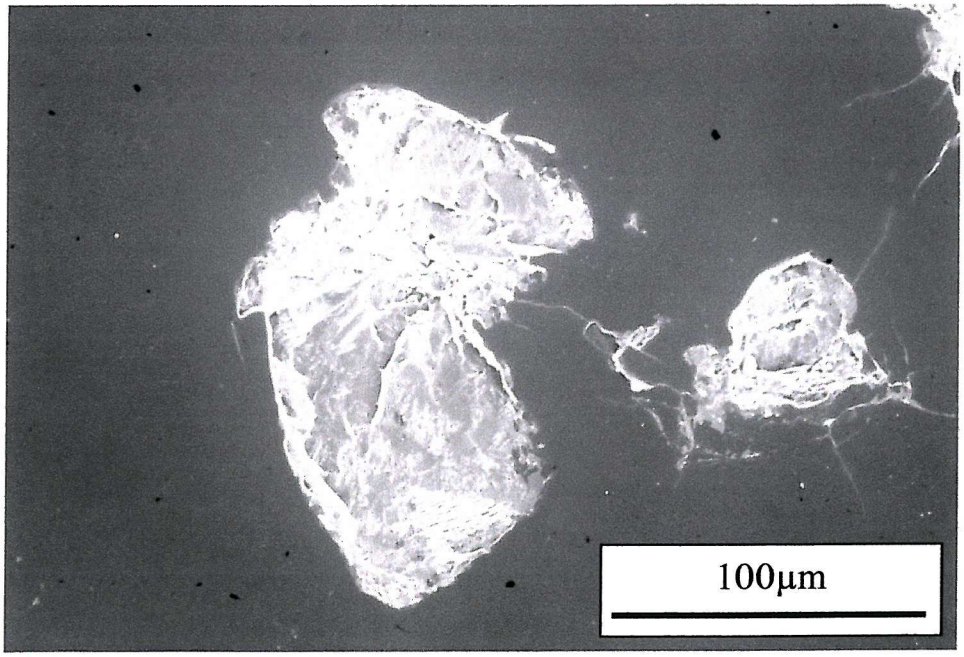

Fig. 9.42: Scanning electron micrograph of the surface of the diamond target impacted by PDA999 (blocky) synthetic diamond grit at 268 m s^{-1}.

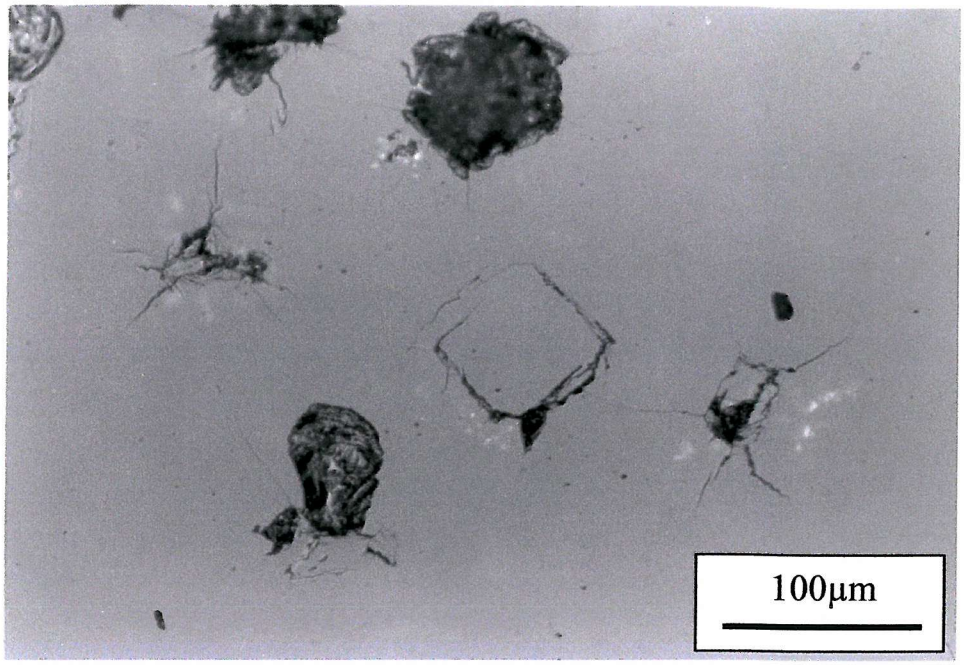

Fig. 9.43: Optical micrograph of diamond surface impacted with PDA999 synthetic diamond grit.

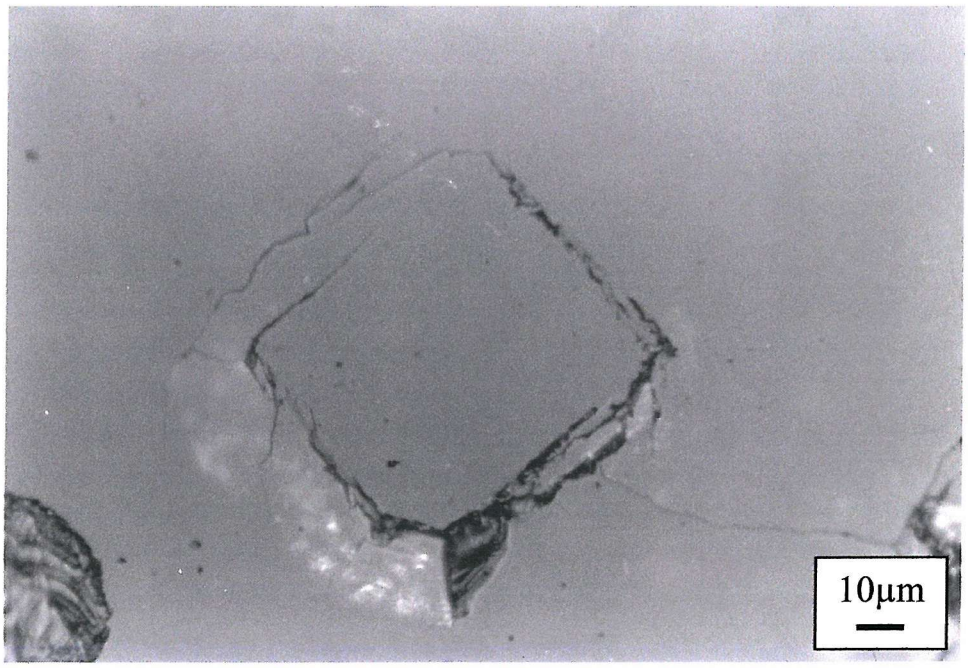

Fig. 9.44: Detail from Figure 9.43 showing a distorted ring crack.

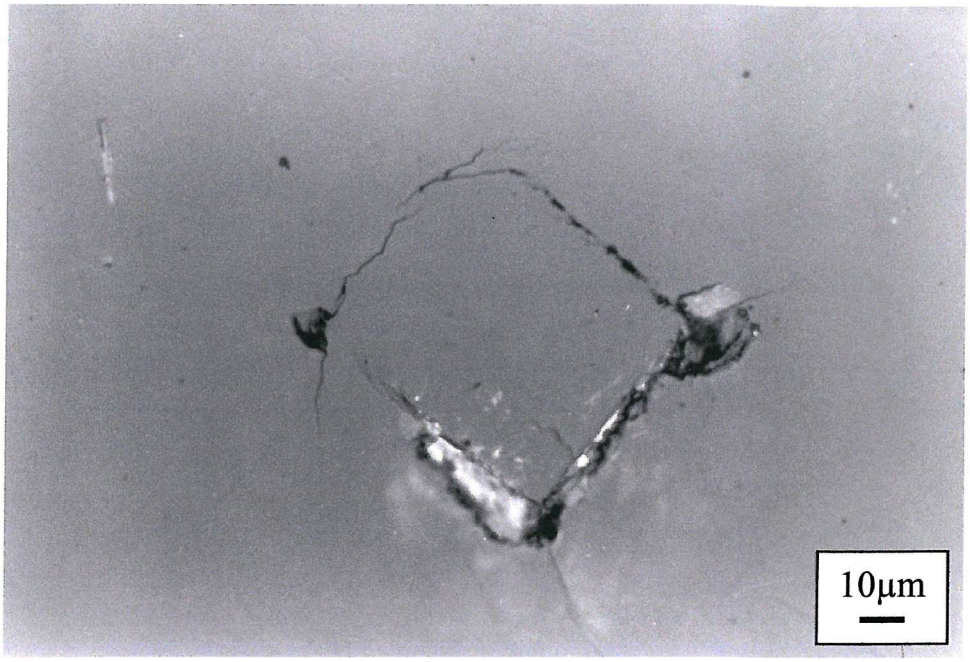

Fig. 9.45: Optical micrograph of diamond surface impacted with PDA999 synthetic diamond grit showing a distorted ring crack.

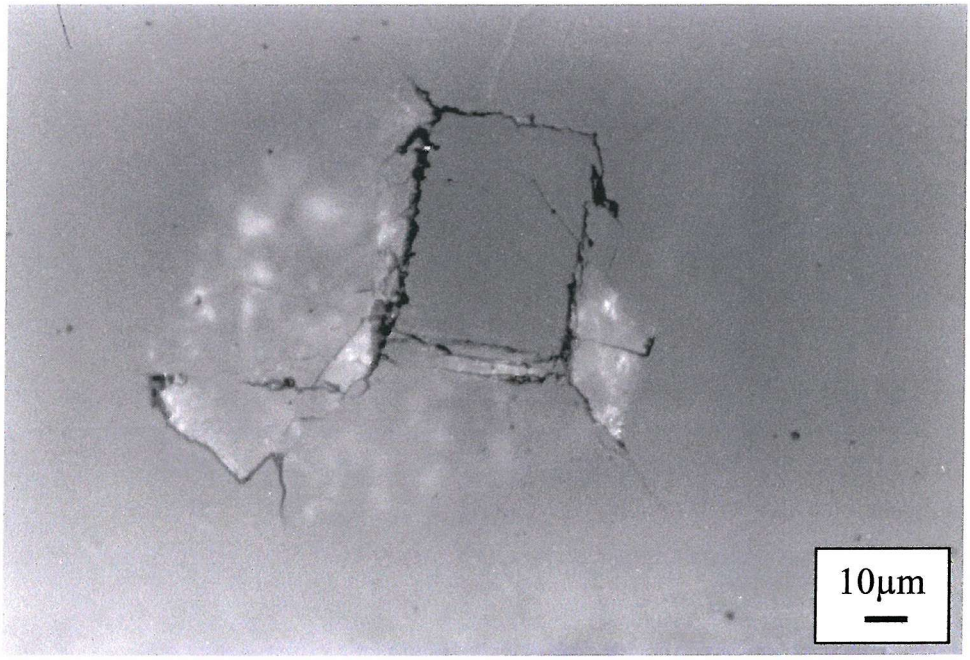

Fig. 9.46: Optical micrograph of diamond surface impacted with PDA999 synthetic diamond grit showing a distorted ring crack.

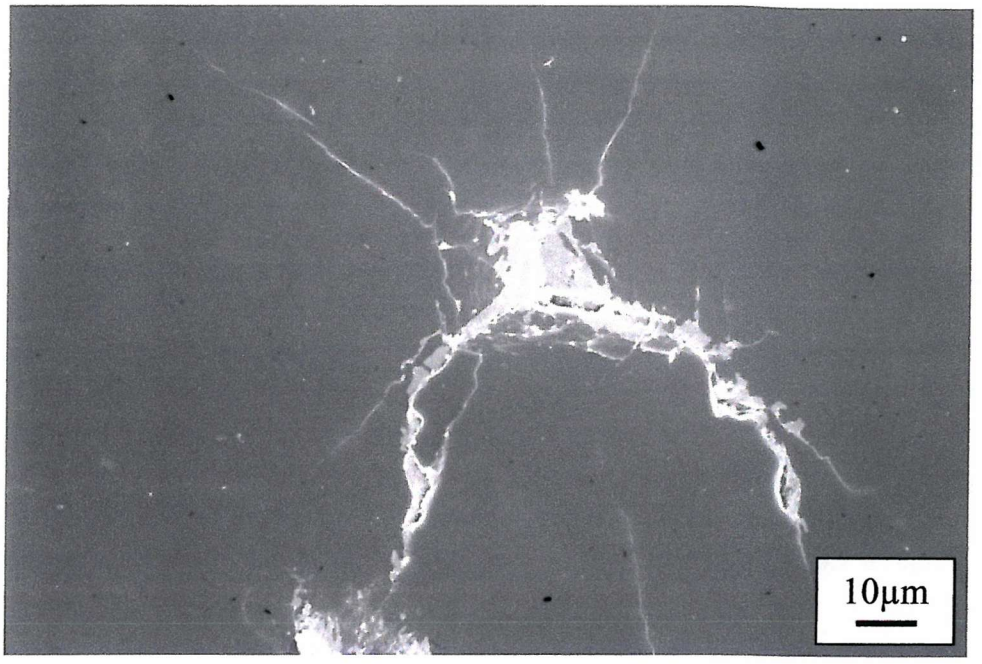

Fig. 9.47: Scanning electron micrograph of the surface of the diamond target impacted by PDA999 (blocky) synthetic diamond grit at 268 m s^{-1}.

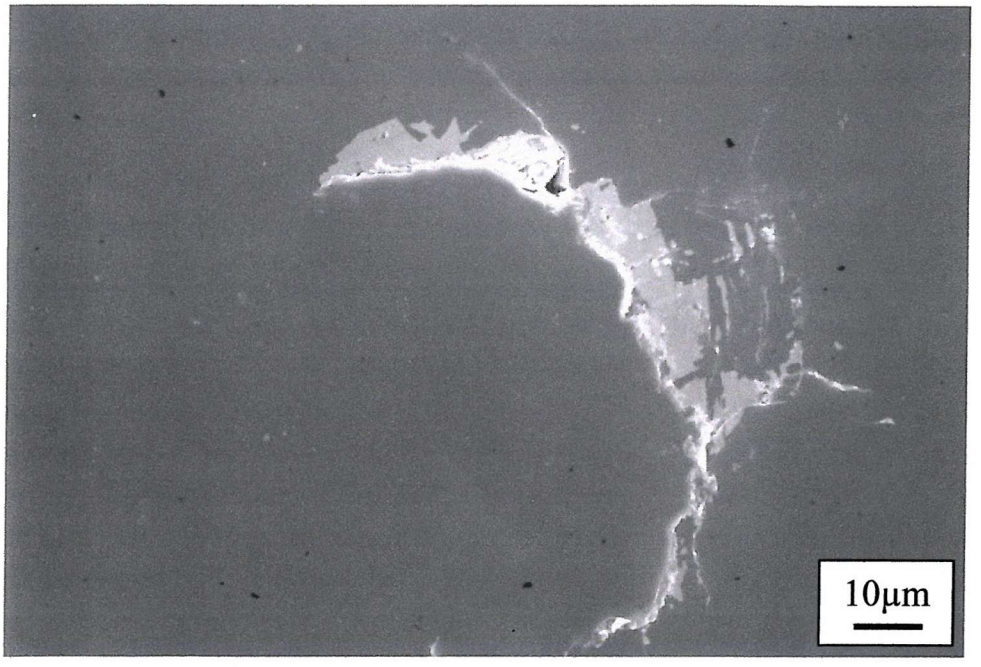

Fig. 9.48: Scanning electron micrograph of the surface of the diamond target impacted by PDA999 (blocky) synthetic diamond grit at 268 m s^{-1}.

10

SUB-SURFACE EROSION DAMAGE

10.1 Introduction

In some erosion tests, for instance that of the 120μm coating, failure of the coating had occurred before many pin-holes were seen. This suggests that sub-surface damage processes may be taking place. Some of the damage features described in this chapter take place before pin-holes form.

As has already been stated, when coating failure occurs it is sudden and catastrophic, leading to rapid delamination of the coating from the substrate. In some cases, there may be no warning that failure is imminent. Visual examination of the substrate following failure of the 120μm coating showed that the surface scratches introduced by substrate pre-treatment prior to deposition were visible. This indicates that the coating has delaminated at the interface. Furthermore, the lack of significant damage features at the surface prior to coating failure point to the accumulation of damage at the interface, which leads to coating debonding once it has reached a critical extent. Raman spectroscopy of the nucleation side of the delaminated coating revealed that while the 1333 cm^{-1} diamond peak is the dominant feature a further peak at ~1580 cm^{-1} was also prominent. This latter peak, indicative of the presence of graphitic sp^2 bonding, suggests that the coating close to the substrate contains significantly higher levels of graphite compared to the coating as a whole. In contrast, the growth surface of the coating is a purely diamond deposit. The inferior mechanical properties of graphite, compared with diamond, would also make the propagation of cracking / debonding easier. Figure 10.1 shows Raman spectra taken on the nucleation and growth surfaces of a fragment of delaminated coating.

The opaque nature of the diamond means that sub-surface damage cannot be seen without resort to other techniques. In order to obtain a better understanding of these processes it is necessary to find ways in which the sub-surface damage can be

observed. However, as with many hard materials, such preparation is difficult. Cutting techniques, such as electric discharge machining, induce damage of their own. Conventional metallographic procedures, such as cutting, sectioning and polishing, also introduce additional damage and differentiating the existing damage (i.e. erosion-related) from that introduced by the preparation process is difficult. Attempts to section a coating by spark eroding caused chipping of the diamond in the immediate vicinity of the cut. In order to minimise the problem of preparation-induced damage taper polishing and ultrasonic imaging were used to evaluate the extent and propagation of sub-surface damage.

A fragment of a 120μm coating that had spalled off the substrate was examined in the scanning electron microscope. Figure 10.2 shows a micrograph taken from the nucleation surface of this fragment. It is interesting to observe the presence of porosity at the grain boundaries. These could act as local stress raisers and lead to the initiation of coating debonding at the interface in a similar manner to porosity and cracking in thermal sprayed coatings and bulk ceramics. In addition to the diamond the micrograph also shows areas of well-adhered tungsten, approximately 15% of the interface in the figure, which have been removed from the substrate along with the coating. Energy Dispersive Spectroscopy (EDS) of the tungsten substrate following removal of the coating showed no traces of remaining diamond adhered to the substrate, with the spectrum consisting entirely of tungsten.

10.2 Taper Polish Investigations

The 90μm lapped diamond coating on tungsten was eroded for four hours at 268 m s^{-1}. The central area of the sample containing the erosion scar was then laser cut into three strips approximately 6mm wide. These strips were polished at angle of 45° to produce a taper section on one side, which consisted of the substrate, coating and the erosion scar. The taper polishing process enables the sub-surface microstructure to be viewed with minimal preparation damage. Details from the taper section of this coating can be seen in Figure 10.3. At the interface debonding is apparent; Figure 10.3 also shows cracking which can be seen extending from the interface into the substrate to a depth of approximately 10μm. This may partially explain the presence of tungsten on the nucleation side of the spalled fragment seen in Figure 10.2. It suggests that in well-bonded areas diamond spallation is dependent on the intersection of cracks in the

substrate. No sub-surface cracking was evident in the coating. The causes of the interfacial damage will be discussed in greater detail below.

10.3 Ultrasonic examination

Another lapped 120μm coating was erosion tested at 268 m s^{-1} and ultrasonically scanned at intervals in order to see if the erosion process generated any sub-surface damage. These were compared with a scan of the same sample prior to testing. The ultrasonic scanning was carried out on an amplitude-scanning C-scan system. It uses a 50 MHz probe and Krautkramer USIP-12 and USH-100 flaw detectors; the spatial resolution of the system is approximately 50μm. The scanning takes place in a water-filled tank and the set-up is controlled by a Newport x-y controller. The transmitter and receiver are housed in the same probe. The process is controlled by a software-driven PC and is capable of scanning up to 50 discs, of 50mm diameter, at a time.

Figure 10.4 shows the change in ultrasonic scans for the 120μm coating taken at different stages of the test. The ultrasonic beam is focused on the coating-substrate interface and these show that as the test proceeds there is a progressive increase in the incidence of interfacial discontinuities; this suggests that the impact of the sand particles causes debonding of the coating at the diamond-tungsten interface. In erosion tests of thick free-standing films 510-570μm thick, Field *et al* [1] found that an extensive network of cracks on the rear surface of the specimens had formed which resulted in a deterioration in the infra-red transmission of the samples. This damage was thought to be caused by tensile stresses. The possible reasons for this will be explored in more detail below.

The cause of this interfacial damage is unclear. The ultrasonic scan of the 120μm lapped coating prior to the erosion test indicates that the coating may not be completely bonded to the surface in some areas; these may act as nucleation sites for the propagation of further debonding. Moreover the driving force for debonding could be provided by stress waves generated by particle impact. Stress wave induced fracture has been observed in liquid droplet impact [2-4] and with impact by soft particles [5]. The present study could be considered to fall under the latter case, considering the low hardness of the silica sand relative to diamond. In other solid particle erosion studies of free-standing diamond, cracking at the rear surface has been suggested by Pickles *et al*

to be caused by reflection at the rear surface of the compression wave [6]. However, it is not known whether this would happen in a coating, where the difference in acoustic impedance between coating and substrate materials is smaller than between diamond and air.

10.4 Correlation of Ultrasonic Data with Microstructure

To examine the sub-surface microstructure further, another lapped 120μm coating that had been tested for 10 hours at 268 m s^{-1} (no pin-holes were observed) was fractured through the erosion scar and the resultant through-thickness section examined in the SEM. Figure 10.5 shows a micrograph taken close to the centre of the erosion scar. It shows that the coating had become debonded from the substrate. This feature was not seen either at the edge of, or outside, the erosion scar. This fact, taken with the ultrasonic data, leads the author to conclude that it is likely the debonding in Figure 10.5 is erosion-related and not caused by the fracture process. Figure 10.6 shows an ultrasonic scan taken of the fractured sample. It is interesting to note that in Figure 10.5 no other significant sub-surface microstructural damage is apparent apart from the interfacial damage.

The usefulness of ultrasonic scanning could be further enhanced if the spatial resolution could be improved and the ultrasonic scans correlated with actual microstructural features, i.e. coating debonding. At present the cracking beneath the interface, as seen in Figure 10.3, and the areas of tungsten still bonded to the fragment, as seen in Figure 10.2, are beyond the detection limit (the resolution of the system is ±50μm). As a result, the ultrasonic scan may indicate that disbondment is complete where in some areas the coating may actually still be partially adhered.

10.5 Preliminary Summary of Erosion Mechanisms

On the basis of the preliminary investigations - taper polish investigations, examination of spalled coatings and ultrasonic scanning - it is possible to say that the steady state erosion mechanisms are micro chipping of the coating surface, the accumulation of damage at the coating-substrate interface and the formation of pin-holes. It is the sub-surface damage that appears to cause catastrophic failure of the coating along the interface. Examination of the sub-surface indicates that the delamination process consists of two stages. Stage 1 is a process of tungsten-diamond interfacial debonding

leaving "islands" of well-adhered coating. Stage 2 is the growth of cracks into the substrate at these island locations leading to complete spallation when these cracks intersect. Consequently the final catastrophic failure of these coatings could well be controlled by the fracture toughness of the substrate rather than the coating-substrate adhesion strength. The remainder of this chapter will be devoted to more detailed study of the sub-surface damage, in particular to elucidating their contribution to the formation of circumferential cracks and pin-holes.

10.6 Substrate etching investigations

The taper polishing and ultrasonic examinations have shown the progression of sub-surface damage. However, the value of this work would be enhanced if some of these damage features could be observed directly. This was achieved by dissolving the tungsten substrate by immersion in a solution of HF and HNO_3 in a 2:1 ratio (by volume) to leave a free-standing film. This film could be sectioned later by snapping to observe microstructural damage in the interior of the film. This was considered to be less damaging to the diamond compared to the other methods of sectioning, for instance laser cutting or electric discharge machining.

Examination using optical microscopy revealed no circumferential cracks, partial or complete, on the nucleation surface of the diamond film. The only pin-holes that could be observed were those that had completely penetrated the coating. The area of particle impact was examined by optical microscopy on both the nucleation and growth surfaces. The number of pin-holes was counted on each surface and the results are summarised in Table 10.1 below.

Feature	Nucleation surface	Growth surface
Partial circumferential crack	0	5
Complete circumferential crack	0	7
Partially penetrated pin-hole	0	9
Completely penetrated pin-hole	6	6

Table 10.1: Summary of damage on the two sides of the free-standing film after 5 hours at 268 m s^{-1}.

The lack of features on the nucleation surface suggests that the circumferential cracks nucleate on the growth surface. This is consistent with the argument that the circumferential cracks are formed by stress wave reflection and reinforcement.

Figures 10.7 and 10.8 show micrographs of pin-holes on the nucleation surface. It is interesting to note that the area immediately surrounding the pin-hole is of a different shade to the surrounding diamond. Energy Dispersive Spectroscopy (EDS) indicated that the white areas in the micrograph are tungsten, which suggests that remnants of the substrate remained adhered to the nucleation surface of the coating. Examination of this sample in transverse revealed that the tungsten layer is approximately 10μm thick. The fact that the areas surrounding the pin-holes on the nucleation surface are free of tungsten provides further evidence to support the proposition that circumferential cracks and pin-holes are formed on debonded areas of the coating. On the nucleation surface, all completely penetrated pin-holes were surrounded by a "halo" of tungsten-free diamond. The pin-holes that have penetrated through the coating range from 160-330μm, with the mean diameter being 228μm. The tungsten-free regions surrounding these completely penetrated pin-holes range from 238μm to 675μm, with the mean diameter being 450μm.

There are also smaller areas of tungsten-free diamond present on the nucleation surface of the diamond film. These can be seen in Figures 10.9 to 10.12. These tungsten-free regions are of irregular shape, being approximately 40μm, though range in size from 25 to 50μm. These regions are large enough to be detected by acoustic microscopy.

The other significant feature was the presence of networks of large interconnecting cracks, which were seen radiating away from the area surrounding the pin-holes as well as other non-tungsten areas. These cracks are too small to be detected by scanning acoustic microscopy. An example is shown in Figure 10.10. This micrograph supports the hypothesis that stress raisers associated with grain boundary porosity at the coating-substrate interface provided initiation sites for the propagation of interfacial cracks, which later led to coating failure.

Both Pickles *et al* [6] and Telling *et al* [7] have reported rear surface cracking of free-standing diamond. They suggested that reflection of the compression wave at the rear

surface resulted in a phase change of the wave putting the rear surface into tension, the amplitude of which exceeded the local strength of the material. This type of damage is particularly prevalent in thin films, where the compression wave has not attenuated sufficiently by the time it has reached the rear surface. Telling *et al* [7] observed this type of damage in 500 μm thick free-standing diamond, though none was seen on free-standing diamond 1 mm thick. However, the present case differs from those two studies as the cracking is in the substrate, to which the coating is still adhered; therefore, reflected stress waves are unlikely to be the cause of the substrate cracking. A more likely cause is that of interfacial cracks that have become diverted into the substrate. This crack diversion could have been assisted by the presence of surface scratches introduced into the substrate by the pre-deposition treatment.

The nucleation surface cracking was seen predominantly in the centre of the area of particle impingement, declining in concentration at greater radii from the centre. No cracking of this type was seen outside the area of particle impingement. Figures 10.13 and 10.14 show micrographs taken from outside this area. The absence of cracking and/or tungsten-free regions supports the suggestion that this cracking is impact related and not generated by the relief of residual stresses following removal of the substrate.

Figure 10.15 shows a micrograph of a circumferential crack in section through the coating. It is interesting that it appears to take a tortuous path through the coating. This could partly explain the "layered" appearance of the sides of the pin-hole in, for example, Figure 8.11. Furthermore, it appears to take a trans-granular path through the coating. This is consistent with the observations of Telling and Field [8] who have stated that grain boundaries do not represent an easy route for crack propagation.

10.7 Substrate characteristics

As described in Chapter 2, the coating debonding processes, as driven by the particle impacts, are also dependent on the mechanical properties of the substrate. A softer substrate will provide less support for the coating than a harder one. However, it is also important to examine the homogeneity of the substrate to see if the deposition process has affected the microstructure in the near-surface region. The coating deposition procedure is not known but 900°C is not an unreasonable assumption. However, the plasma temperature is considerably higher than this (approximately 2000°C).

Therefore, as the substrate is located in the after-glow region of the plasma (see Chapter 3) it is possible that these high temperatures could alter the microstructure of the near-surface region of the substrate.

A transverse section of the substrate, from which the coating had been removed, was mounted and polished metallographically and examined in the scanning electron microscope. This section was not from the area of the sample subjected to particle impingement. Energy Dispersive Spectroscopy (EDS) spectrum of the substrate revealed the substrate to be exclusively tungsten with no other elements present. Figure 10.16 shows a scanning electron micrograph of the substrate close to the top surface of the interface. This can be compared with a micrograph of the same sample in Figure 10.17, from a location close to the opposite surface; the two figures are very similar. The most prominent feature in the microstructure is the presence of microscopic pores, approximately spherical in shape. The mean diameter is approximately 0.25μm. The estimated level of porosity was found to be identical in both cases, being approximately 0.3%. The pores were evenly distributed across the substrate.

Depth from upper surface (mm)	Mean hardness (H_v)	Standard deviation
0.05	397	24.5
0.65	421	16.4
1.65	444	9.0
2.65	450	17.6
3.65	460	18.1
4.65	464	16.3

Table 10.2: Results summarising the hardness variation across the tungsten substrate.

A Matsuzawa Seiki micro-hardness tester, using a Vickers indenter at a load of 1 kgf., was used to measure the variation of hardness across the substrate. Ten measurements were made at each position. A typical indent is shown in Figure 10.18. The shape of the indent is typical of the sort seen in ductile materials, with pile-up surrounding the indent. The absence of radial cracks emanating from the corners of the indent prevented the fracture toughness from being measured. However, the results showed a gradient in hardness through the thickness of the substrate. The mean hardness of the region closest to the deposition surface (397 H_v) is approximately 50H_v lower than the bulk

hardness value (465 H_v). The variation of hardness through the substrate is shown in Table 10.2 and in graphical form in Figure 10.19.

The lower hardness of the near-surface region of the substrate suggests that the microstructure has been affected by contact with the plasma during the deposition process. This will exacerbate coating debonding when the coating is subjected to high velocity particle impact. Work by Wuttiphan *et al* [9] has shown that coatings deposited onto softer substrates demonstrated a tendency to greater debonding and substrate plastic deformation when subjected to indentation from a 6mm diameter WC sphere.

10.8 Scanning acoustic microscopy

10.8.1 Introduction

The ultrasonic scanning showed that coating debonding is an important damage feature of damage in diamond coatings in erosive environments. However, the spatial resolution (approximately 50μm) was unable to resolve individual pin-holes. In order to understand the mechanisms responsible for circumferential crack and pin-hole formation a technique with greater spatial resolution was used for more localised examination: Scanning Acoustic Microscopy (SAM).

Scanning acoustic microscopy (SAM) was first developed in the 1970s, though it is only within the last decade that its use has become widespread. The technique employs high frequency (up to 2 GHz) ultrasonic waves, which are propagated into the material under examination. The waves can interact with the interior of the material in a number of ways, including absorption, scattering and reflection. At an interface between two materials of different elastic properties the ultrasonic waves can be reflected. This is shown in schematic form in Figure 10.20.

At any interface, part of the incident wave is reflected back along the incident path, while the remainder is transmitted through material 2. The extent of this reflection is determined by the difference in acoustic impedance between the two materials. Acoustic impedance (Z) is defined as the product of density (ρ) and longitudinal wave velocity (c_l):

$$Z = \rho c_l \tag{10.1}$$

The proportion of reflected energy at the interface is described by the reflection coefficient, R:

$$R = I\frac{Z_2 - Z_1}{Z_2 + Z_1} \tag{10.2}$$

In general, ultrasonic waves cannot travel through a vacuum. Therefore, regions where the two materials are not perfectly bonded can be identified by the near-total reflection of the ultrasound. It is this characteristic that is exploited in scanning acoustic microscopy and which makes it a potentially attractive tool for the examination of coatings for the detection of debonding at the coating-substrate interface. In the same way, defects within the coating, for instance porosity, can be detected.

Scanning acoustic microscopy is used extensively in the micro-electronics industry for the detection of defects in micro-chips and integrated circuits [10]. It has also been used to detect porosity in thermally sprayed ceramic coatings [11] and delamination in composite materials [12-14]. In another study [15], it has been used to examine 0.7mm thick polycrystalline diamond, bonded to tungsten carbide. The acoustic microscope enabled the detection of delamination and thermal cracks of between 20 and 150μm in size.

The objective of the work described in this chapter was to use SAM to examine sub-surface damage present in CVD diamond coatings on tungsten when subject to high velocity sand erosion.

10.8.2 Experimental

Lapped diamond coatings on tungsten 60 to 160μm in thickness, which had been erosion tested under the conditions described in the previous chapters, were examined by acoustic microscopy. A number of coatings were also examined prior to testing in order to provide a comparison with the eroded coatings.

The coatings were examined using a Sonoscan C-SAM series D-9000 scanning acoustic microscope. The microscope was equipped with a Sonoscan SK230/MP transducer, which operated at a frequency of 230 MHz. The spatial resolution of the probe is quoted at less than 10μm in the x and y directions, while in the z (vertical) direction an air gap or delamination of greater than 0.1μm can be detected.

The acoustic beam was focused at the growth surface of the coating and an electronic gate was used to only consider return echoes within a defined time window to produce the image. Echoes from outside this window (i.e. higher and lower within the sample) were ignored. To ensure adequate acoustic coupling between probe and sample, the sample was immersed in a tank filled with distilled water for the scanning process. Any air bubbles present on the sample surface were brushed away prior to scanning. The probe was scanned across the sample at a constant rate of 50 mm s^{-1} to create the acoustic image. The stand-off distance between the probe and sample corresponded to the focal length of the transducer in water; for a 230 MHz probe this distance was 9.5mm.

The width of the gate was 0.05 μs. As the compression wave velocity in diamond is 17,470 m s^{-1}, this corresponds to a depth of approximately 0.9mm. This depth far exceeds the coating thickness of all the samples used in the present study. However, the gate width was chosen so as to maximise the signal in order to obtain greater discrimination between an area of coating delamination and an area of well-bonded coating. The reduced contrast, which is a consequence of a smaller gate width, would make this task more difficult.

10.8.3 Development of coating debonding

The ultrasonic scanning, described in Section 10.3, demonstrated a progressive increase in interfacial discontinuities, suggesting the development of debonding at the coating-substrate interface, as the erosion proceeded. Scanning acoustic microscopy enables this debonding to be studied at greater resolution. Figure 10.21 shows an acoustic micro image of an untested 120μm coating. The black spots in the figure are not artefacts on the sample, but are in fact air bubbles in the coupling medium. It is instructive to compare this figure with Figure 10.22, which shows a 120μm coating after being eroded at 268 m s^{-1} for 8 hours. The area of scanning is the same for both figures.

The scale on the left of the figures relates to the amplitude of the acoustic echo. The pale areas, indicative of the highest amplitude reflections, are the areas where the coating has delaminated. Therefore, the figures confirm the findings of the ultrasonic study in Section 10.3, which showed an increase in coating debonding. The mechanism of coating debonding will be discussed in Chapter 11. The debonding process is assisted by the presence of grain-boundary porosity, which is present at the nucleation surface of the coating close to the interface. This porosity will act as local stress raisers to provide nucleation sites for interfacial crack propagation.

The average size of this porosity has been calculated, from electron micrographs, to be 9.3 μm, though the range of measured pores was approximately 3 to 18μm. From electron micrographs the pore density was estimated to be between 1485 and 2260 per mm^2. Examples of these were shown in Figure 10.2. The acoustic microscope did not detect features on this scale. For this reason none can be observed in Figure 10.21. However, Figure 10.21 does not show any gross delamination of the coating in its untested condition.

The image in Figure 10.22 shows the whole area of particle impact, which is approximately 16mm in diameter. It is notable that the delamination is present at more than 50 discrete locations, rather than originating from one location. This indicates that it is initiated at local defects, for instance grain boundary porosity, as described above. The same sample was re-examined after further erosion and is shown in Figure 10.23, after 22 hours at 268 m s^{-1}. It shows that the area of coating debonding has significantly increased and is more contiguous compared with Figure 10.22. The findings, therefore, suggest that the debonding proceeds by interfacial crack propagation from grain boundary porosity, later coalescing with other interfacial cracks that have initiated from other grain boundary pores. It is thought that when the debonding reaches a critical coverage, the coating will fail catastrophically by spalling; coatings subject to a compressive residual stress are susceptible to spalling. Conditions at the interface crack involve a combination of opening (mode I) and shearing (mode II) components [16]. Spalling occurs at a critical radius a_c, when K_{II} becomes zero and the crack is deflected up to the surface causing the film to spall from the surface [17]. This takes place when:

$$\frac{a_c}{C_T} \approx 1.6\left(\frac{E_f}{\sigma_{rs}}\right)^{1/2} \tag{10.3}$$

Assuming an elastic modulus (E_f) of 1157 GPa and a residual stress (σ_{rs}) of 0.87 GPa (this value was calculated from the mean Raman peak shift described in Chapter 7) the critical radius for spalling has been calculated for the diamond coatings on tungsten. The results are plotted in Figure 10.24 and it shows that the critical radius is increased with the coating thickness. For coatings with a greater residual stress the critical radius for spalling is reduced. This indicates the desirability of reducing the residual stress in the coating.

On the 46 μm lapped coating, spalling had begun, the fragment of spalled coating - approximately 6 mm in diameter - is very close to the critical diameter (5 mm) for a diamond coating of that thickness, assuming a residual stress of 0.87 GPa. Equation 10.3 and Figure 10.24 also help to explain the extensive delamination on the 120μm coating, which was still intact after 22 hours erosion at 268 m s^{-1}. Equation 10.3 predicts a critical diameter of 14 mm.

Scanning Acoustic Microscopy could be used in conjunction with image analysis to measure the percentage of debonding on a more quantitative basis. The rate of debonding over the course of a test could be used to determine the critical level of debonding necessary to cause catastrophic failure of the coating. This should be the subject of further work.

Figure 10.25 shows a SAM image of a lapped 160μm coating tested at 268 m s^{-1} for 22 hours. It is interesting to compare this with Figure 10.23, which showed the 120μm coating tested under the same conditions for the same duration. In contrast to Figure 10.23, Figure 10.25 does not show any significant delaminated regions. It is thought that this is due to the greater thickness, which results in the coating-substrate interface being further from the region of maximum shear stress. This assumes that the size and density of grain boundary porosity is the same as the 120μm coating. No spalled fragment of 160μm coating is available to confirm this assumption. The influence of sub-surface shear stresses on coating integrity will be discussed in detail in Chapter 11.

10.8.4 Examination of circumferential cracks and pin-holes

Figure 10.26 shows two SAM images taken from an eroded lapped 60μm coating, tested at 268 m s^{-1} for 5 hours. They show significant delamination (denoted by the white areas) over the area of examination. The scale of the delamination is of the same scale to the tungsten-free areas observed on the nucleation surface of another 60μm diamond coating, the substrate of which had been dissolved (see Figures 10.7 to 10.12). These two samples (i.e. one featured in Figures 10.7 to 10.12 and the other in Figure 10.26) are of the same thickness and were erosion tested under the same conditions (268 m s^{-1} for 5 hours). A direct comparison is, therefore, valid. In Figure 10.26, the pin-holes are the circular purple features. It is also interesting to note that they are located on areas of coating delamination. The significance of this finding will be explored in the next section.

The usefulness of these SAM images can be enhanced if corroborated by actual microstructural features. This has been done in Figures 10.27 and 10.28, which were taken from another lapped 60μm diamond coating, tested at 268 m s^{-1} for 6 hours. Figure 10.27 shows a detail from Figure 10.26, which shows two circumferential cracks and a pin-hole. This is complemented by a scanning electron micrograph (Figure 10.28) of this area, which shows features observable from the surface. It is interesting to note that in the SAM image the amplitude of the pin-hole on the right is lower than the circumferential cracks. It is thought this is a result of scattering of the acoustic beam by the walls of the pin-hole. In contrast, there is reduced potential for scatter by the circumferential crack resulting in a greater proportion of the incoming acoustic waves. This is shown schematically in Figure 10.29.

A similar feature can be seen in Figures 10.30 and 10.31, also from the same sample. Figure 10.30 shows a partial circumferential crack; again, it is located on a region of debonded coating. This crack is shown in greater detail in the SEM micrograph in Figure 10.31, which shows the shape of the circumferential crack is identical to that seen in Figure 10.30. These figures therefore demonstrate the good correlation between acoustic and electron microscopy.

In considering the formation of the circumferential cracks, it is necessary to determine whether they are initiated at the surface of the coating or sub-surface. Figure 10.32

shows the same area as Figure 10.30; however, the transducer was changed to a 230 MHz surface wave transducer. This transducer emits ultrasound in a wide, short cone. Acoustic waves at the edge of the cone meet the surface at a low angle: under these conditions the ultrasound does not penetrate the sample. Instead, it travels laterally at and just below the surface. Some of the ultrasound is continually reflected upwards towards the transducer [18]. The presence of surface cracking will cause the ultrasound to be refracted, thereby preventing the echoes from returning to the transducer.

The advantage of the surface wave transducer is that it probes the near-surface region of the sample down to a depth of only 1 wavelength. Figure 10.32 shows that the partial circumferential crack is still present, while the sub-surface debonding seen in Figure 10.30 is not seen in Figure 10.32. The surface wave velocity in diamond is 10,688 m s^{-1}. Therefore, the depth corresponding to one wavelength is approximately 46μm. At this depth, the wave energy is about 4% of the wave energy at the surface, and the amplitude of oscillation decreases sharply to a negligible value at greater depths. As the coating thickness is 60μm, it seems likely that the circumferential crack in Figure 10.32 is confined to the near-surface region of the sample.

Chapter 9 showed generally good agreement between the circumferential crack diameters and the diameters at which stress reinforcement occurs. It also showed that Hertz theory could not explain the formation of circular ring cracks in the present study. The suggestion that reflected stress waves are responsible for the circumferential cracks is supported by these SAM images, which have shown circumferential cracks and pin-holes to be located at areas of localised coating delamination. Therefore, stress wave reinforcement appears to provide a more plausible explanation for the formation of circumferential cracks.

10.9 Circumferential Crack Formation

The previous section showed that coating delamination was an essential prerequisite for circumferential crack and pin-hole formation. However, as the acoustic images show, pin-holes are not found on every delaminated region. The reason for this is that for circumferential cracks to form, it is necessary for microstructural flaws to be present in the microstructure. Moreover, these flaws have to be large enough to present a stress

intensity of sufficient magnitude. These stress intensities can then be activated by the stress waves to form circumferential cracks.

By estimating the stresses generated by the impacts it is possible to calculate the critical flaw size needed to form a circumferential crack. In quasi-static loading, the critical flaw size, c_{cr}, may be calculated using the following expression:

$$c_{cr} = 0.188\left\{\frac{K_{1c}}{\sigma}\right\}^2 \tag{10.4}$$

K_{1c} is the fracture toughness and σ the applied stress. In the absence of any definite figures, certain values must be assumed in this calculation. If the stress is assumed to be the Hertzian maximum tensile stress at the contact edge (4.6 GPa at an impact velocity of 268 m s^{-1}) and the fracture toughness of CVD diamond is 6.0 MPa$\sqrt{m}$, then the minimum flaw size, c_{cr}, becomes 0.33μm. However, the extensive particle fragmentation on impact means that this stress is unlikely in the present case. It also ignores the compressive residual stress in the coating, which constitutes an additional barrier to overcome before any flaws are activated.

An alternative way of looking at it is to assume a flaw size and calculate the stress required to activate that flaw. This is done by the equation below:

$$\sigma = \frac{K_{1c}}{1.3\sqrt{\pi c_{cr}}} \tag{10.5}$$

In Chapter 4 it was discussed that the flaws controlling fracture were of similar size to the grains. Therefore, for a 150μm coating, flaws of up to 60μm can be expected. The critical stress required to activate a flaw of this size is 336MPa. For thinner coatings, the grain sizes are smaller: for instance, for a 10μm grain, the critical stress is increased to 823MPa. Thus, the stresses required are considerably lower than the Hertzian tensile stress. However, the overall numbers of pin-holes on the thicker coatings were lower than on the thinner ones. Moreover, the flaws controlling fracture are located predominantly in the bulk of the material and not at the surface. Therefore, it is doubtful if they are playing any part in the formation of the circumferential cracks, which are thought to be formed at the surface. Microscopic examination has not

revealed any defects of this scale at the surface of untested coatings. Therefore, the defects responsible for the circumferential cracks are likely to be considerably smaller.

As the circumferential cracks resemble those generated by liquid impact, the impact pressure, P_i, (the so-called "water hammer pressure") can be calculated using the following expression:

$$P_i = \rho_e c_e V \tag{10.7}$$

Where ρ_e is the density of the projectile, c_e the speed of sound in the erodent and V the impact velocity. The values used in this calculation were: ρ_e = 2650 kg m^{-3}; c_e = 5940 m s^{-1}; V = 268 m s^{-1}. Using these values an impact pressure of 4.2 GPa is generated. This figure is close to the maximum tensile stress at the contact edge obtained using the Hertzian approach. However, this figure is unlikely to be the true pressure owing to the sand fragmentation on impact; therefore, the true figure is likely to be considerably lower. A more realistic figure can be obtained using a modified form of the above expression given by Jackson and Field [19]. This states that the peak height of the simplified triangular wave pulse, by analogy with Hertz, is:

$$\sigma_{max} = \beta^* \rho_e c_e V \tag{10.8}$$

Where β^* is a function dependent on Poisson's ratio, ν_1, of the target material, which is:

$$\beta^* = \frac{1}{2}(1 - 2\nu_1) \tag{10.9}$$

Assuming ν = 0.07 for diamond this gives a value of σ_{max} of 1.81GPa. The decay of the Rayleigh wave is proportional to $r^{-1/2}$. Therefore, at a particular distance from the centre of impact, the magnitude of the Rayleigh wave can be calculated. In the case of a 60μm coating, where the radius of reinforcement is 133μm, σ_{max} will have declined from 1.81GPa to approximately 0.16GPa. For a stress of this magnitude the critical flaw will be 264μm. For simplicity, this calculation ignores any contribution from compression or shear waves reflected from the delaminated interface. No flaws of this size have been observed in the coatings; to place this figure in context, it is approximately 10

times greater than the average grain size in a coating of this thickness. In the absence of known parameters (for instance impact stresses), estimating critical flaw sizes can be little more than speculation. For this reason, studying the impact process using finite element modelling could provide further insight into what is a complex issue and one in which much remains to be understood.

Examination of the diamond coatings in their untested condition did not reveal any cracks and the cracks that are present might be smaller than the resolution of the microscope. In addition, the coating, though lapped (R_a 0.2μm), may be too rough to prevent the defects from being observed. As could be seen in Figures 8.14 to 8.16, the paths of the circumferential cracks do not appear to be deflected or altered by the grain boundaries. This suggests that the defects responsible for the circumferential crack formation may be considerably smaller than the grain size. One new technique that could be used to examine sub-micron defects could be ultrasonic force microscopy (UFM). UFM has the potential to image surface and sub-surface cracks at nanoscale resolution [20,21].

Fewer circumferential cracks and pin-holes were seen on thicker coatings. For example, after 3 hours at 268 m s^{-1}, 29 pin-holes were counted on a 46μm coating; on a 60μm coating tested under the same conditions, the equivalent figure was 12. There are two possible reasons for this. The first is that as the thickness is increased the magnitude of the shear stress at the interface is reduced, thus increasing the rate of coating delamination. As Chapter 11 will show, there appears to be a threshold interfacial shear stress, below which no delamination will take place. In the absence of delamination, circumferential cracks and pin-holes cannot form. The second reason is the decay of the compression, shear and surface waves generated by the particle impacts: as the coating thickness increases a greater proportion of the energy associated with the stress waves has reduced. The result is that, in many cases, the amplitude will have reduced to below the critical stress needed for circumferential crack initiation. The compression and shear waves attenuate in proportion to r^{-2} on the surface and r^{-1} in the bulk of the target material while the rate of decay of the surface wave is in proportion to $r^{-1/2}$ [22]. This could explain the low number of circumferential cracks and pin-holes on the 120μm coating, despite the extensive delamination, as shown by the acoustic images.

Acoustic microscopy could also be used in a quantitative way to evaluate the residual stresses and the crack distributions of the coatings. The presence of surface cracks can lead to the attenuation of the Rayleigh (surface) wave, causing a reduction of the Rayleigh wave velocity [23]. Increases in the crack depth and/or density will cause increased attenuation [24,25]. The presence of compressive residual stresses can cause the partial closure of surface-breaking cracks, which can reduce the attenuation of the surface wave velocity [26]. Pecorari *et al* [27] have recently used line-focus acoustic microscopy to characterise the surface damage in Al_2O_3 induced by polishing. They found that high crack densities could reduce the surface acoustic wave velocity by up to 10%; the accuracy of the acoustic microscope was approximately 0.1%. This technique could potentially yield valuable information on both the residual stress and the crack distributions in diamond coatings.

10.10 Conclusions

The techniques used in this section have shown that, under repeated particle impacts, there is a progressive build-up of sub-surface damage at the coating-substrate interface. It is this damage that determines the lifetime of the coating and not the steady-state erosion rate, which is only a function of surface micro-chipping. The debonding of the coating leads to catastrophic failure of the coating by spalling when the delamination reaches a critical extent. Therefore, improved coating adhesion appears to be the most important influence on the overall life of the coating.

Raman spectroscopy has indicated that the levels of graphite in the coating are significantly higher in the region close to the coating-substrate interface. The presence of graphite is thought to reduce the adhesion of the coating as well as the interfacial fracture toughness. Reductions in these values will make interfacial crack propagation easier, thus diminishing the life of the coating. At present, the location of the graphite is not known; Raman mapping of the nucleation surface could provide useful information on the location and distribution of areas containing higher levels of graphite.

The initiation sites for this debonding appear to be grain-boundary porosity, which is present at the nucleation surface. These act as local stress raisers, leading to the propagation of coating debonding. The debonded regions also lead to the development, at the growth surface, of circumferential cracks and pin-holes. The reduction of the size

and number of the interfacial pores could increase the fracture toughness of the interface and reduce the extent of coating debonding: this would then inhibit the nucleation of circumferential cracking and pin-holes. One way in which this could be achieved is to increase the nucleation density by reducing the initial crystal size during deposition. The use of a harder substrate (for example WC or SiC) to provide greater support to the coating could also inhibit coating delamination.

Crack propagation in the substrate has also been revealed via taper polishing as well as examination of a diamond film, where the substrate had been dissolved in acid. The crack propagation in the substrate is also assisted by the nature of the tungsten substrate, where the region closest to the coating-substrate interface has undergone further softening, thought to be caused by heating during the deposition process, which has weakened the near-surface region of the substrate.

Dissolving the substrate enables examination of the nucleation surface of the coating. It is significant that the fully penetrated pin-holes are surrounded by a "halo" of tungsten-free diamond. This further suggests that the pin-holes are formed on areas of localised delamination.

Scanning acoustic microscopy has been used to image sub-surface damage on CVD diamond coatings that have been subjected to solid particle erosion. In particular, it has been used to investigate localised debonding of the coating.

The acoustic micro-images show that the amount of coating delamination increases as the number of particle impacts increases. It is thought that this is caused by sub-surface shear stresses, which interact with porosity at the grain boundaries to promote further debonding. The debonded regions grow in size until the coating fails catastrophically by spalling.

The results indicate that the pin-holes are situated on areas of localised coating debonding. This suggests that the circumferential cracks, the precursor to pin-holes, are formed by stress wave reflection and interaction at these regions. Comparison of the average pin-hole diameter with the diameter at which stress wave reinforcement occurs has already shown close agreement with this theory.

Scanning acoustic microscopy has been shown to be a useful technique for the examination of sub-surface damage on a more localised scale than the previously used ultrasonic scanning. The resolution of individual pin-holes has provided important evidence for identifying the mechanism responsible for the formation of circumferential cracks, the precursor to the pin-holes.

The results of this study have shown that scanning acoustic microscopy is a valuable tool in the detection of sub-surface damage on a more localised scale than ultrasonic scanning. It enables individual pin-holes to be resolved, the results of which provide important evidence for identifying the mechanism responsible for the formation of circumferential cracks, the precursor to the pin-holes.

Care must be taken in the interpretation of the SAM images in order to differentiate between genuine defects and extraneous features. This has been done in the present case by corroboration of surface damage with electron micrographs.

This chapter has provided further evidence for the proposition that circumferential cracks and are formed by stress wave reflections at locally delaminated regions of the coatings. The next stage is to identify the mechanism by which the coating becomes debonded. This is investigated in the next chapter.

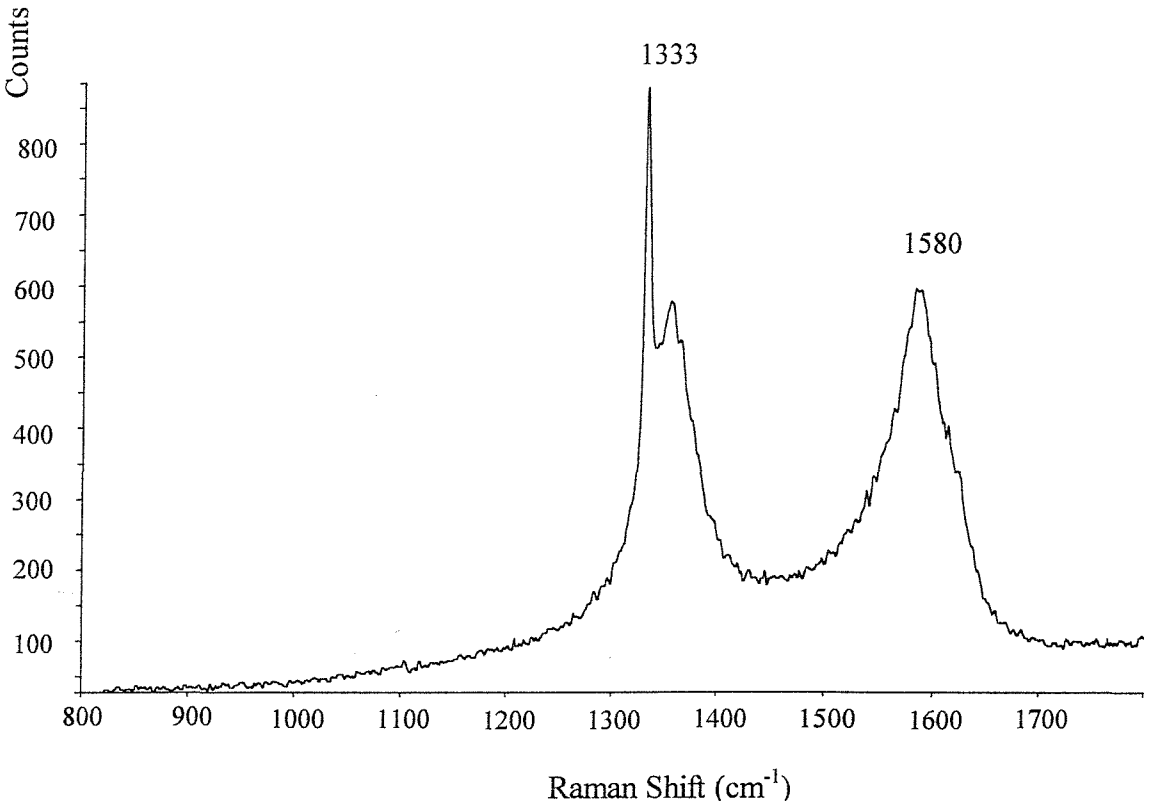

Fig. 10.1a: Raman spectrum of the nucleation side of 120μm diamond fragment, which had spalled off the substrate after erosion for 10 hours at 268 m s^{-1}.

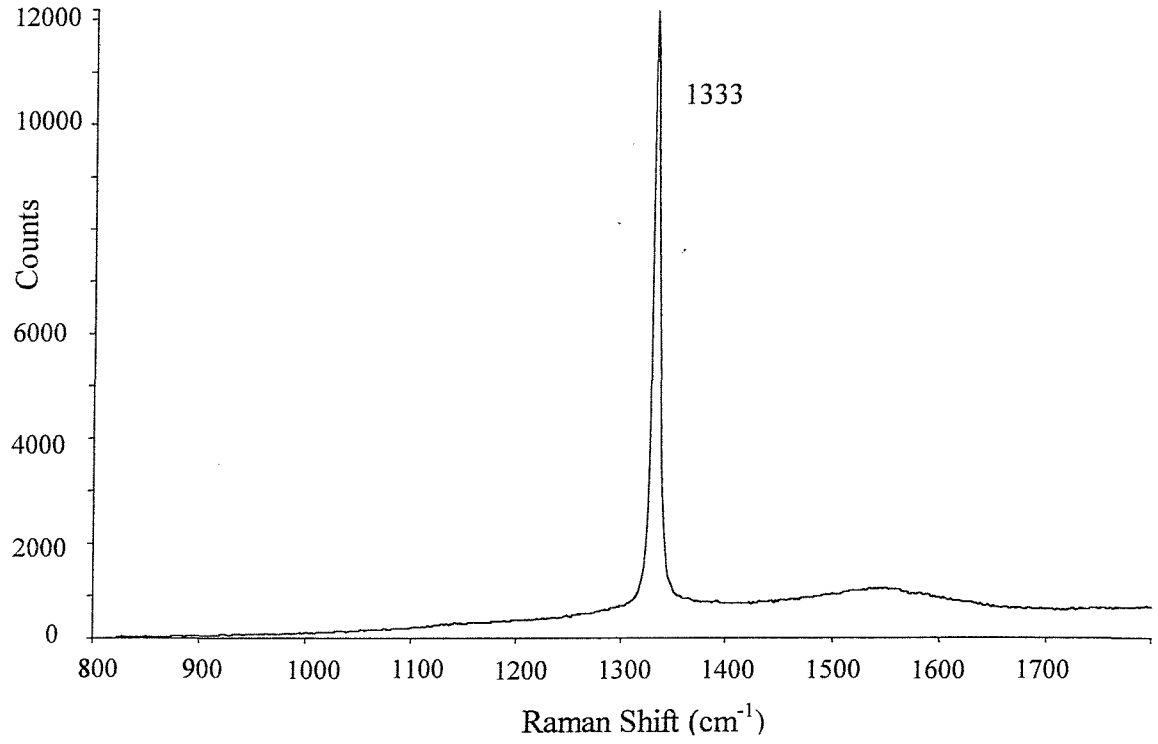

Fig. 10.1b: Raman spectrum of the growth side of 120μm diamond fragment, which had spalled off the substrate after erosion for 10 hours at 268 m s^{-1}.

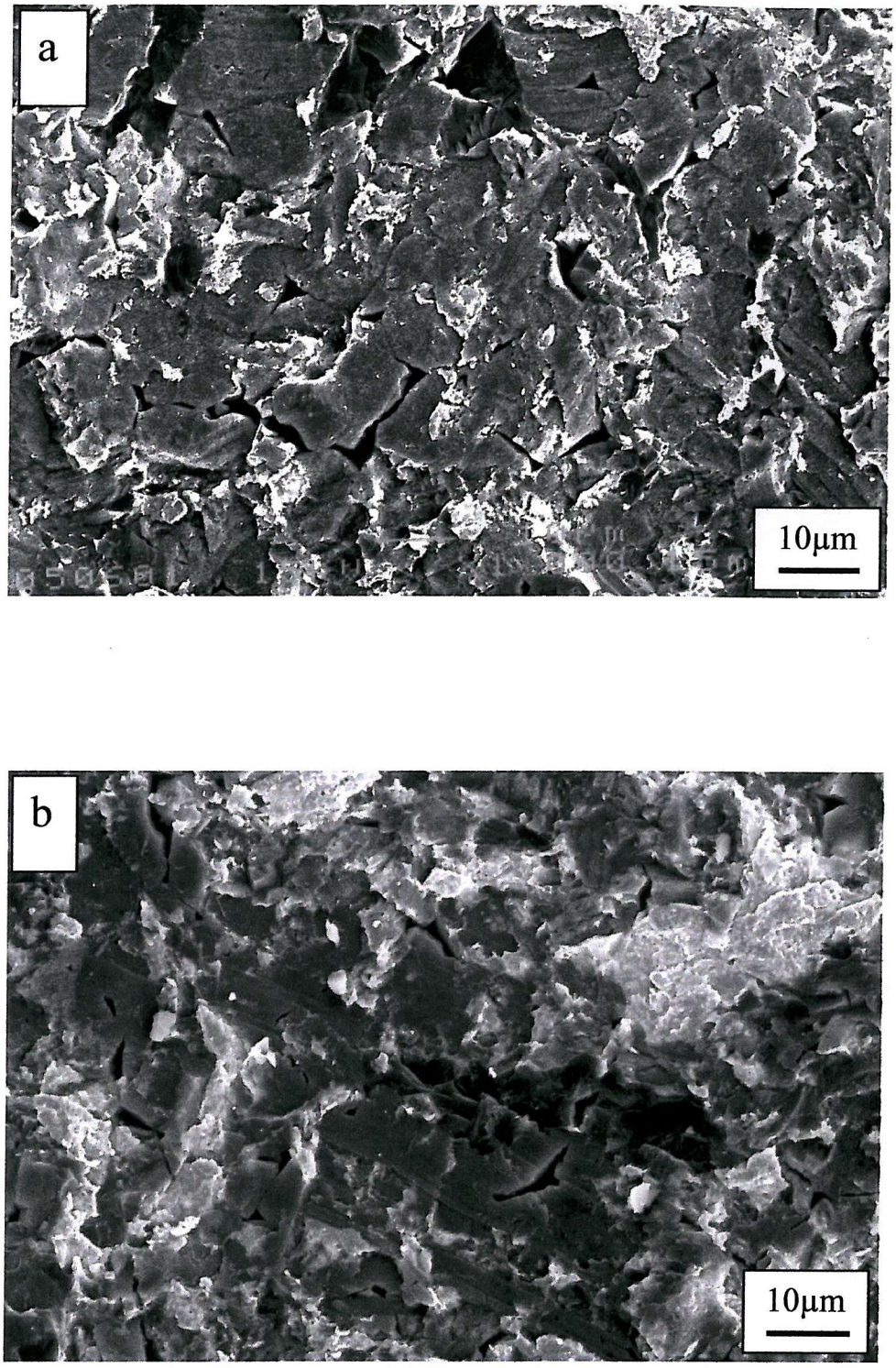

Fig. 10.2: Two SEM Micrographs of the nucleation surface of a fragment of a lapped 120μm diamond coating tested at 268 m s^{-1} for 10 hours following detachment from the substrate. Notable features include grain boundary porosity and residual tungsten from the substrate (white areas).

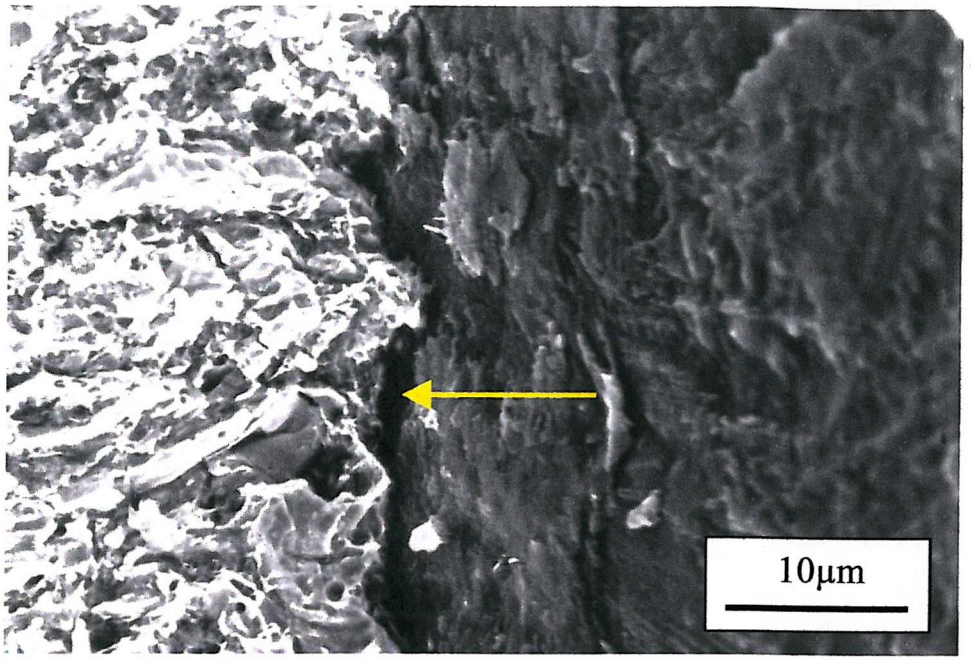

Fig. 10.3a: Micrograph of a taper section, through the erosion scar, from the 90μm lapped coating tested at 268 m s^{-1} for 4 hours, showing debonding at the coating-substrate interface. The tungsten substrate is on the left while the coating is on the right.

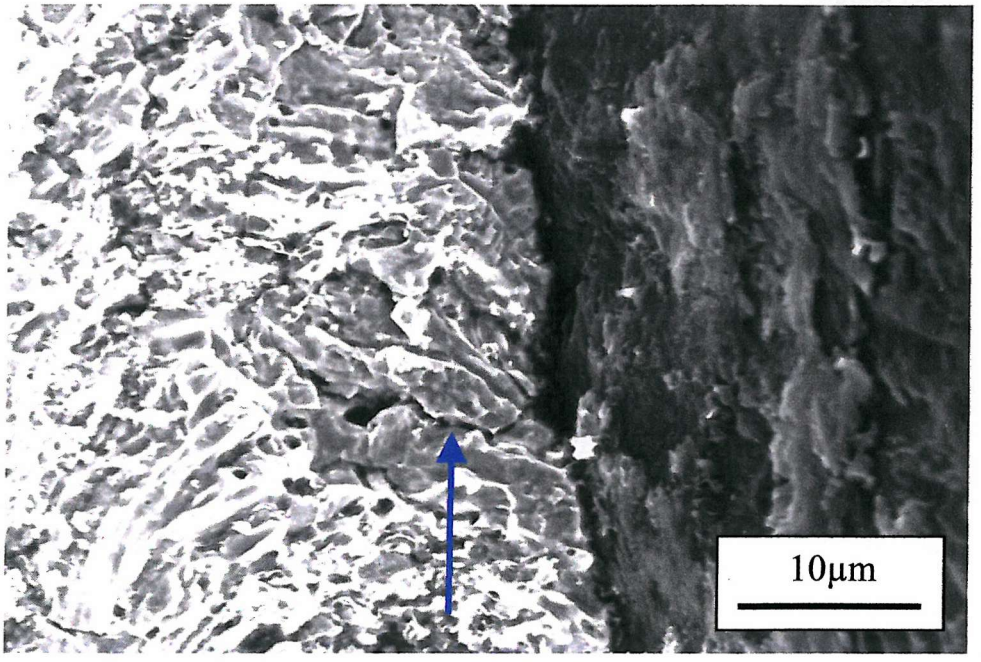

Fig. 10.3b: Micrograph of a taper section, from the same sample as Fig. 10.3a. The arrow shows cracking extending into the substrate from the interface to a depth of approximately 10μm.

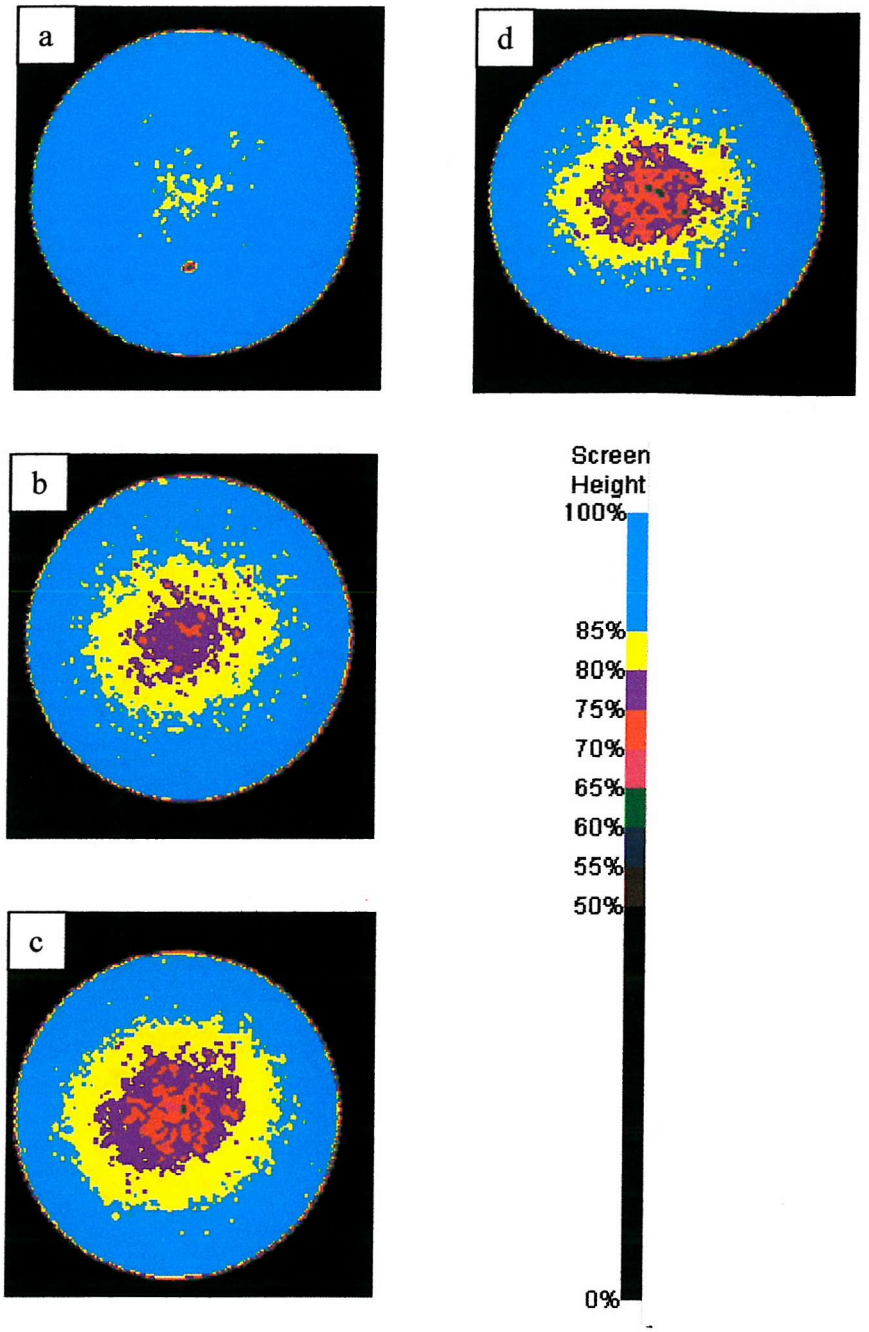

Fig. 10.4: Ultrasonic scan of a 120μm lapped CVD Diamond coating on W tested at 268 m s^{-1} for (a) 0 hrs; (b) 2 hrs; (c) 4 hrs; (d) 6 hrs. The disc is 50 mm diameter and the erosion scar corresponds to an area in the centre of the disc approximately 20 mm diameter. The "%" scale on the right hand side describes the degree of bond, i.e. complete bonding is 100%.

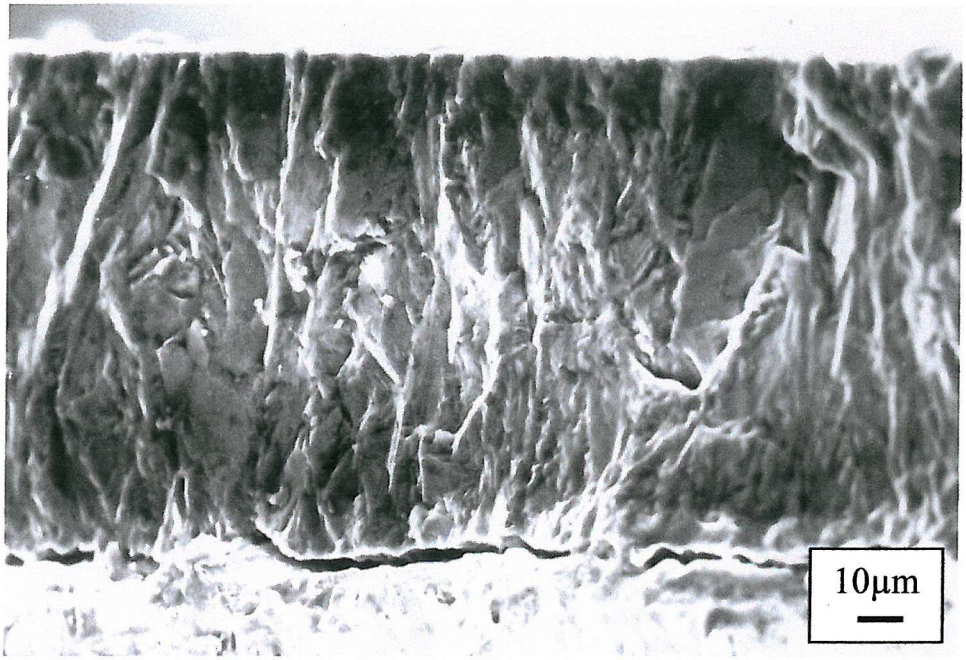

Fig. 10.5: Micrograph of a transverse section of a lapped 120μm diamond coating on W, erosion tested at 268 m s^{-1} for 10 hours, showing debonding at the coating-substrate interface.

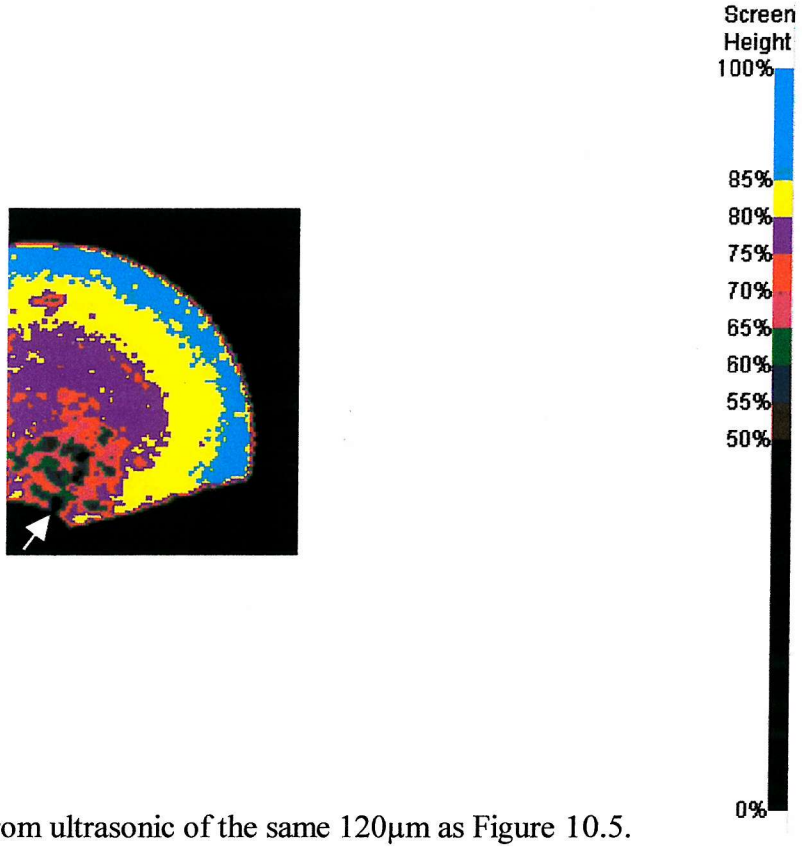

Fig. 10.6: Detail from ultrasonic of the same 120μm as Figure 10.5. The arrow marks the location of Figure 10.5.

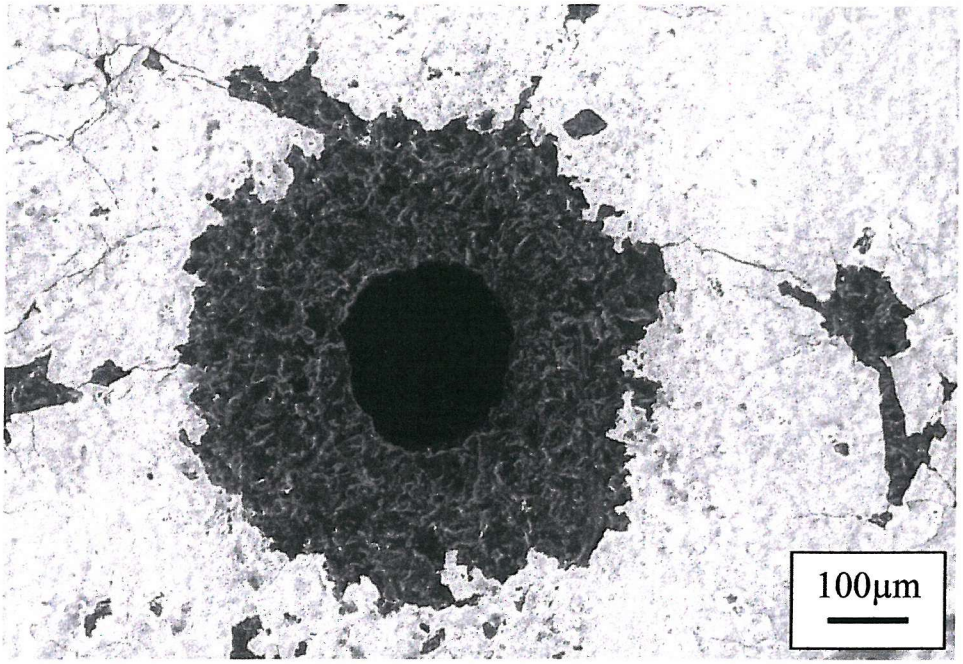

Fig. 10.7: Micrograph of the nucleation surface of a 60μm diamond coating, tested at 268 m s^{-1} for 5 hours showing a pin-hole that has completely penetrated the coating surrounded by tungsten-free diamond. The light areas are coated with a layer of residual tungsten approximately 10μm thick.

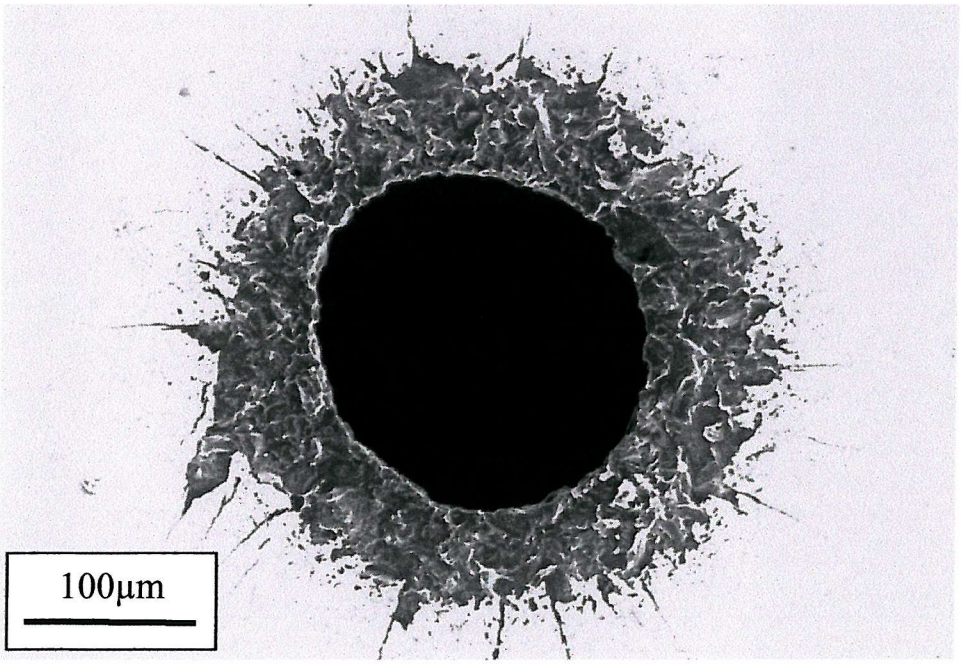

Fig. 10.8: Micrograph of the nucleation surface of the same sample as was displayed in Figure 10.7 showing a pin-hole that has completely penetrated the coating surrounded by tungsten-free diamond.

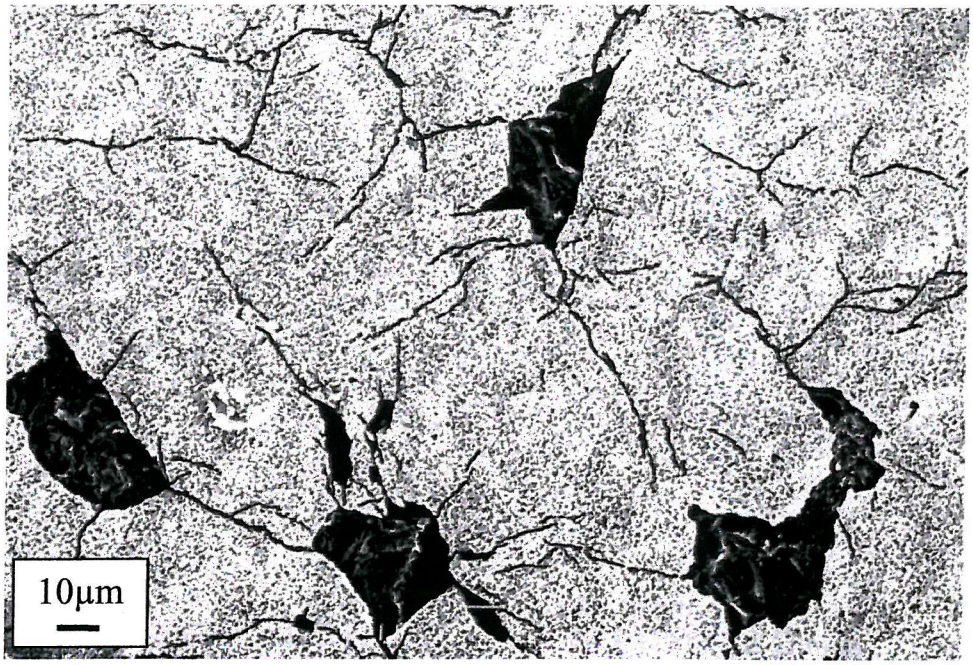

Fig. 10.9: Micrograph of the nucleation surface of the same sample as Figures 10.7 and 10.8, showing cracks propagating away from tungsten-free areas, which were thought to be delaminated regions of the coating prior to dissolution of the substrate.

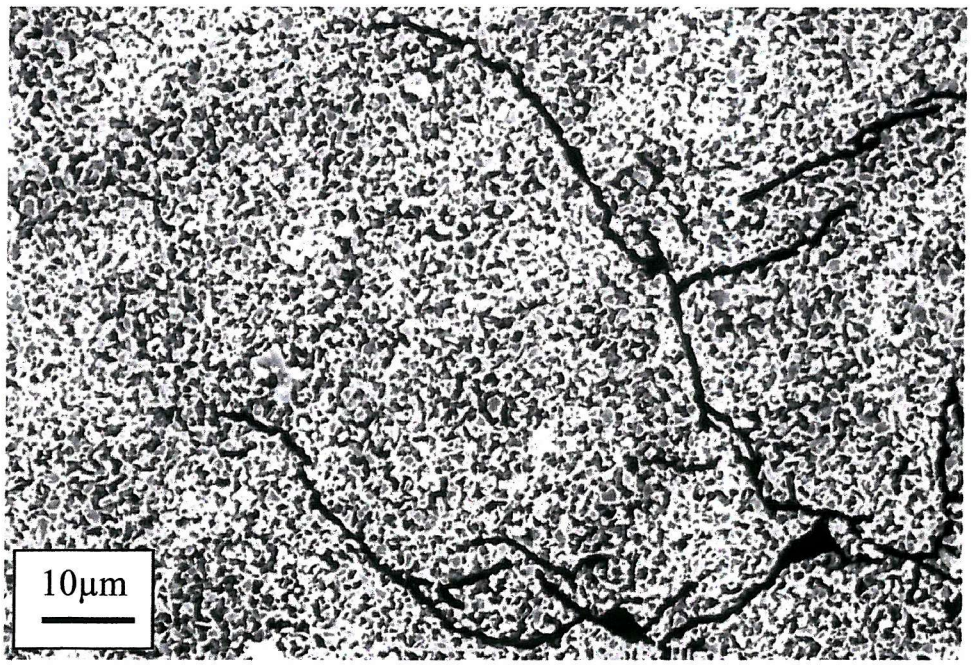

Fig. 10.10: Micrograph of the same sample as the previous figures showing a detail of cracking in the residual tungsten remaining adhering to the nucleation face of the diamond coating following dissolution of the substrate.

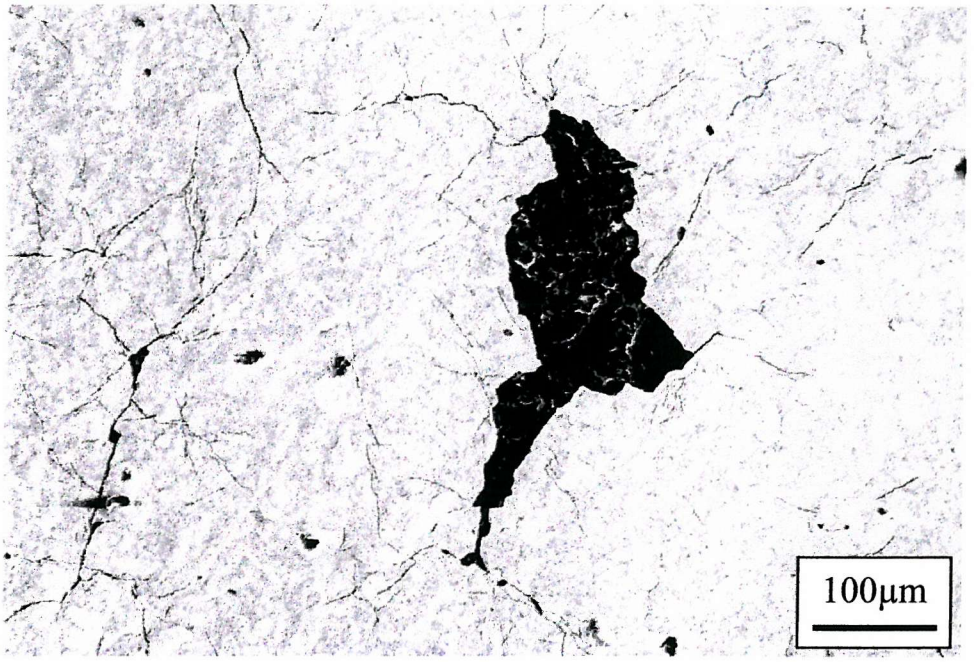

Fig. 10.11: Micrograph of the nucleation surface of the same sample as Figures 10.7 and 10.8, showing cracks propagating away from tungsten-free areas, which were thought to be delaminated regions of the coating prior to dissolution of the substrate.

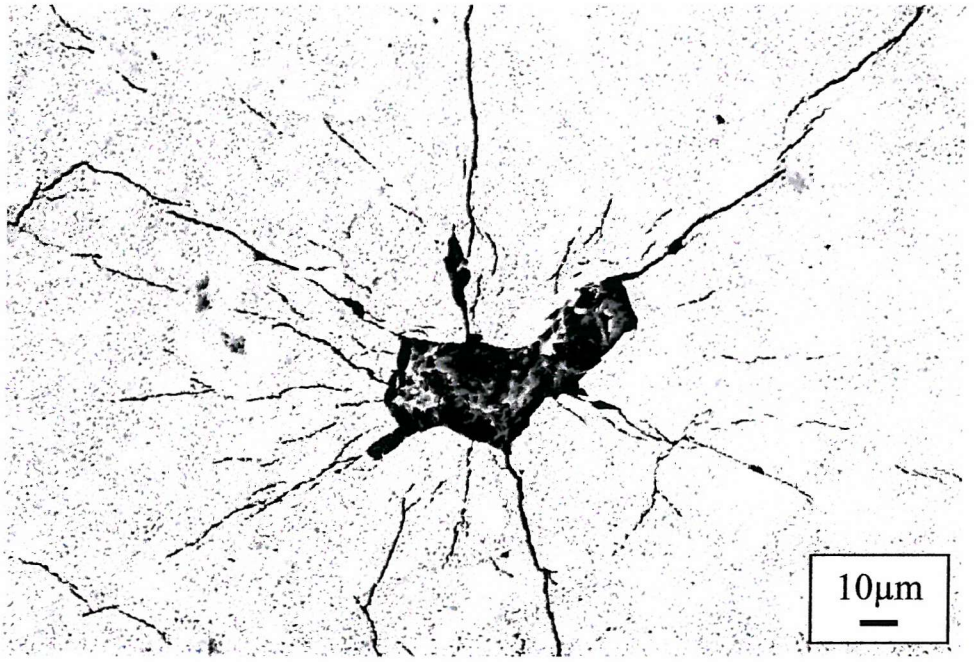

Fig. 10.12: Micrograph of the nucleation surface of the same sample as Figures 10.7 and 10.8, showing cracks propagating away from tungsten-free areas, which were thought to be delaminated regions of the coating prior to dissolution of the substrate.

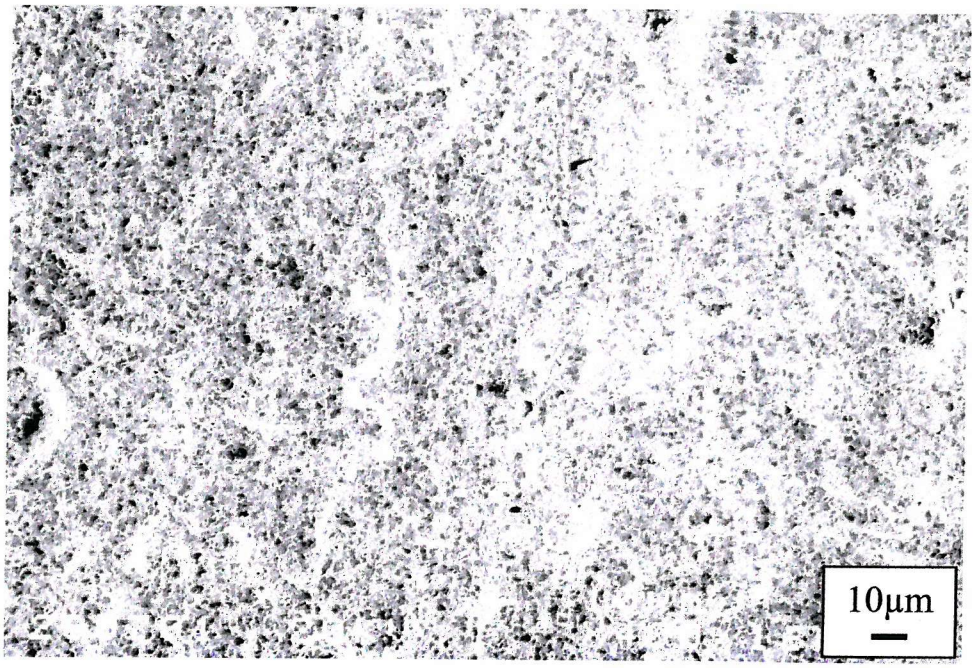

Fig. 10.13: Micrograph of residual tungsten on the nucleation surface away from the area of particle impact.

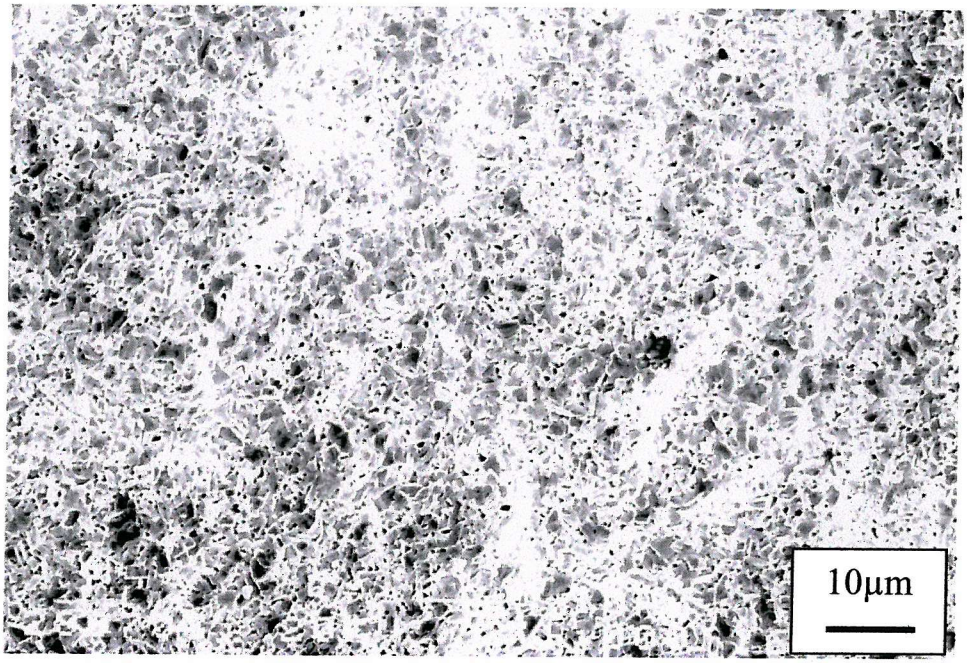

Fig. 10.14: Micrograph of residual tungsten on the nucleation surface away from the area of particle impact.

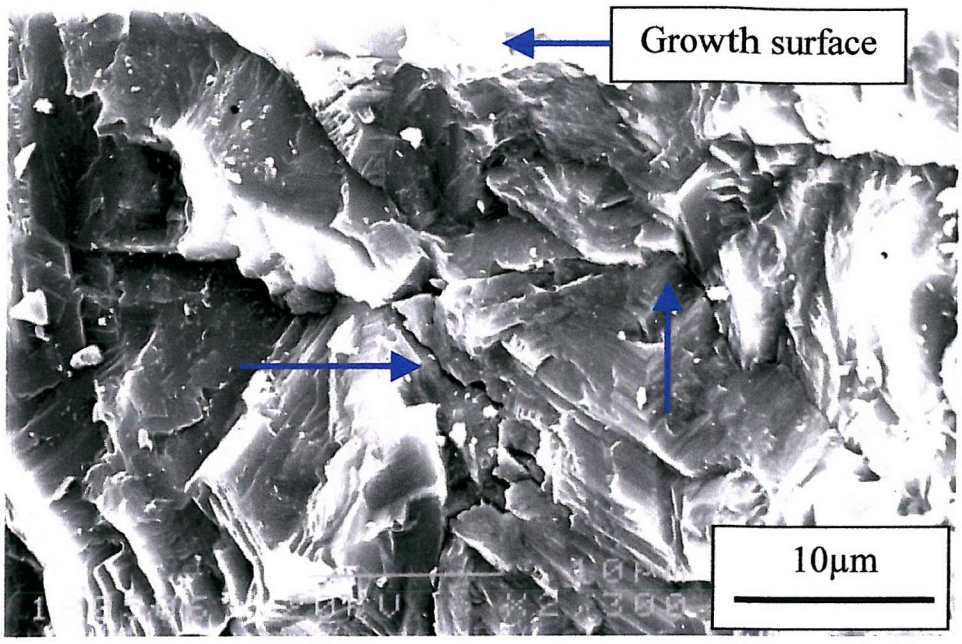

Fig. 10.15: Micrograph of the 60μm coating in Figures 10.7 to 10.14 showing a circumferential crack (arrowed) extending through the coating in the direction of the coating-substrate interface. The crack can also be seen branching into two at a depth of approximately 15μm.

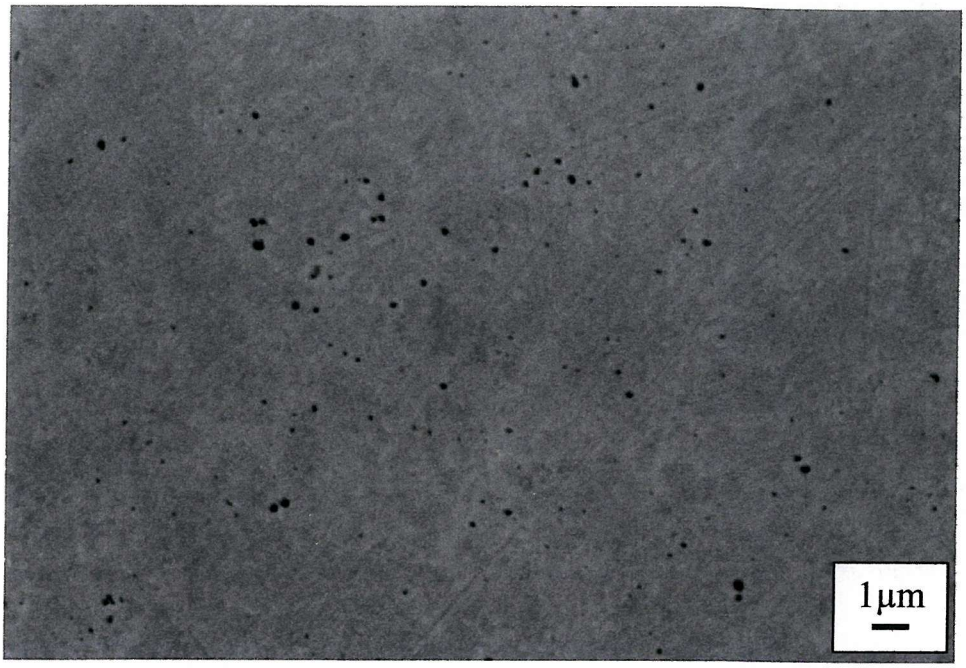

Fig. 10.16: Micrograph of a transverse section of polished tungsten substrate showing the microstructure close to the top surface.

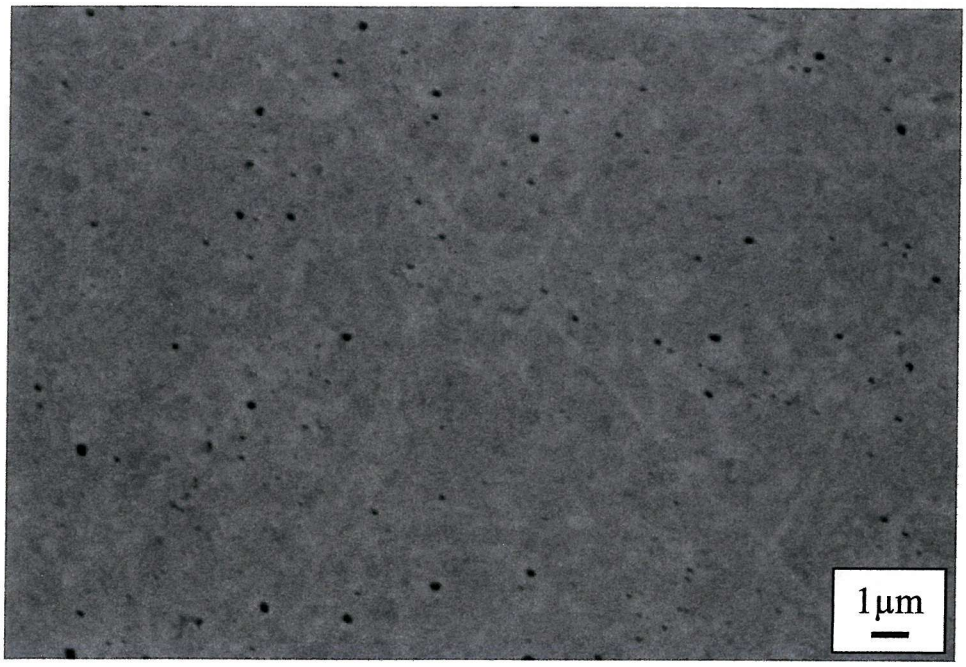

Fig. 10.17: Micrograph of a transverse section of polished tungsten substrate showing the microstructure close to the bottom surface.

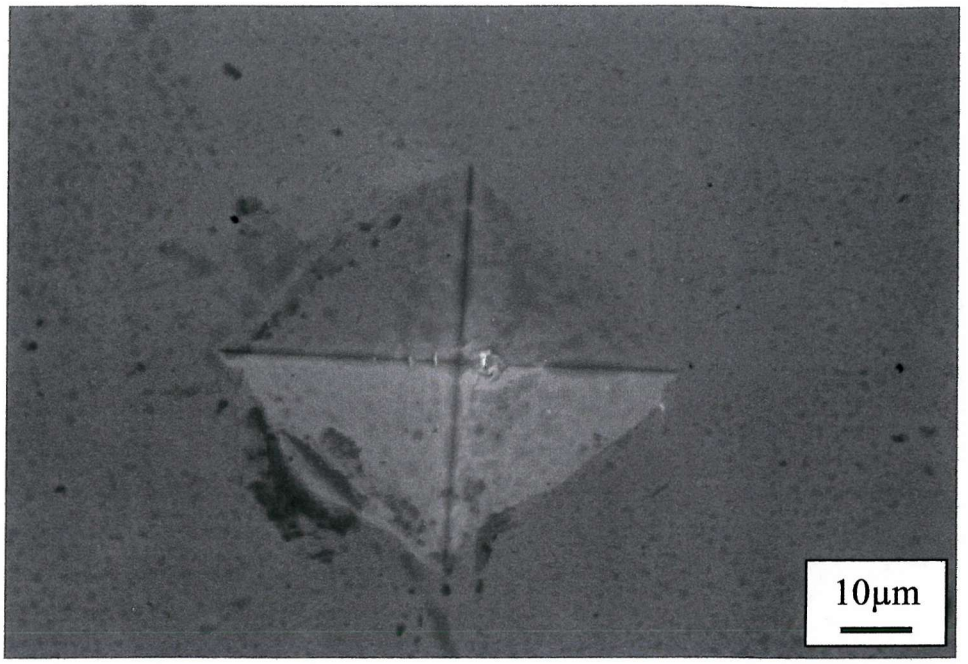

Fig. 10.18: Micrograph showing a Vickers indent in a transverse section of the tungsten substrate.

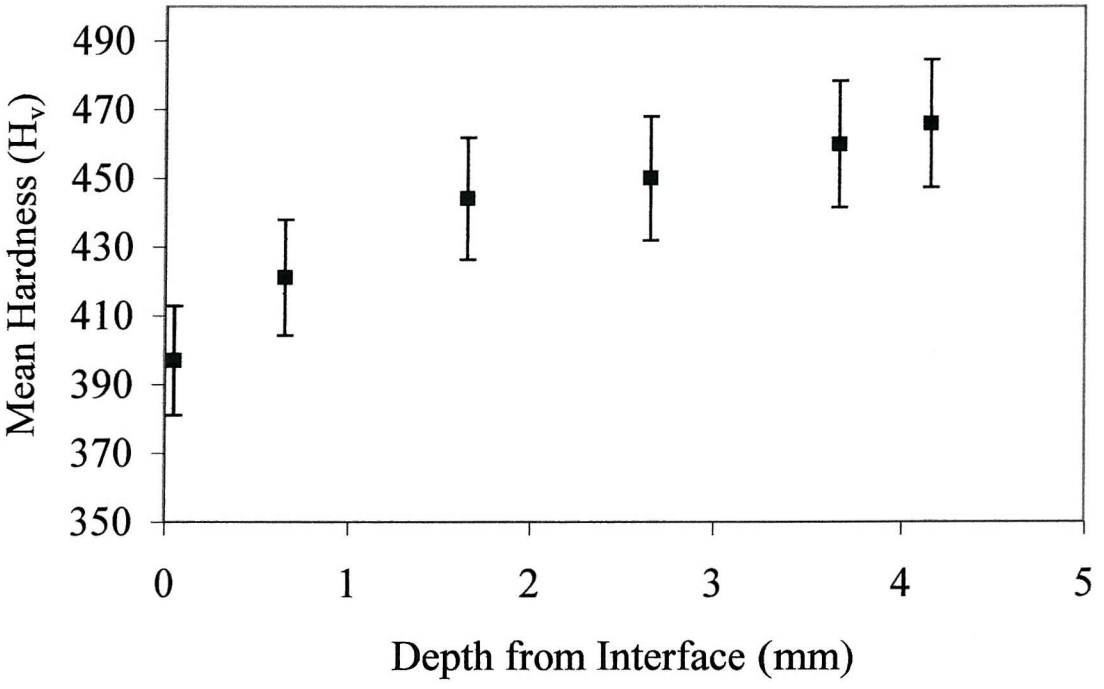

Fig. 10.19: Graph of hardness vs depth of the tungsten substrate. The error bars denote one standard deviation.

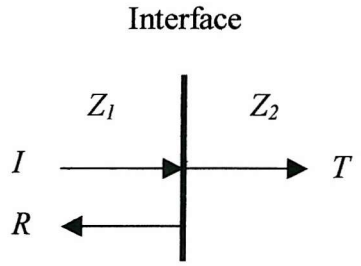

Figure 10.20: Schematic diagram showing a beam of plane acoustic waves incident normally at a plane boundary between 2 semi-infinite isotropic homogeneous materials. Key: I = incident wave; R = reflected wave; T = transmitted wave; Z_1 = acoustic impedance of material 1; Z_2 = acoustic impedance of material 2.

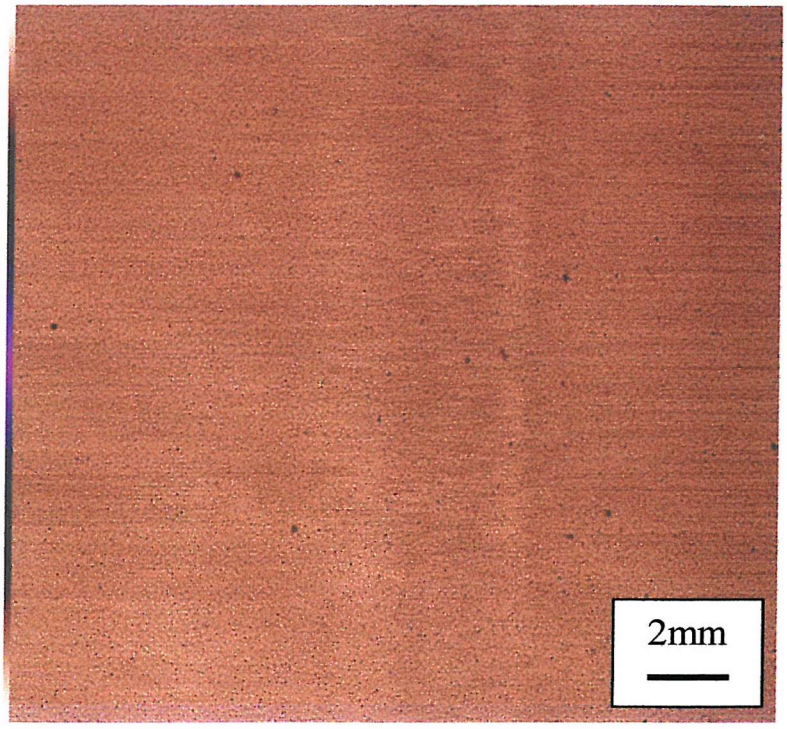

Fig. 10.21: SAM image of an untested 120μm diamond coating.

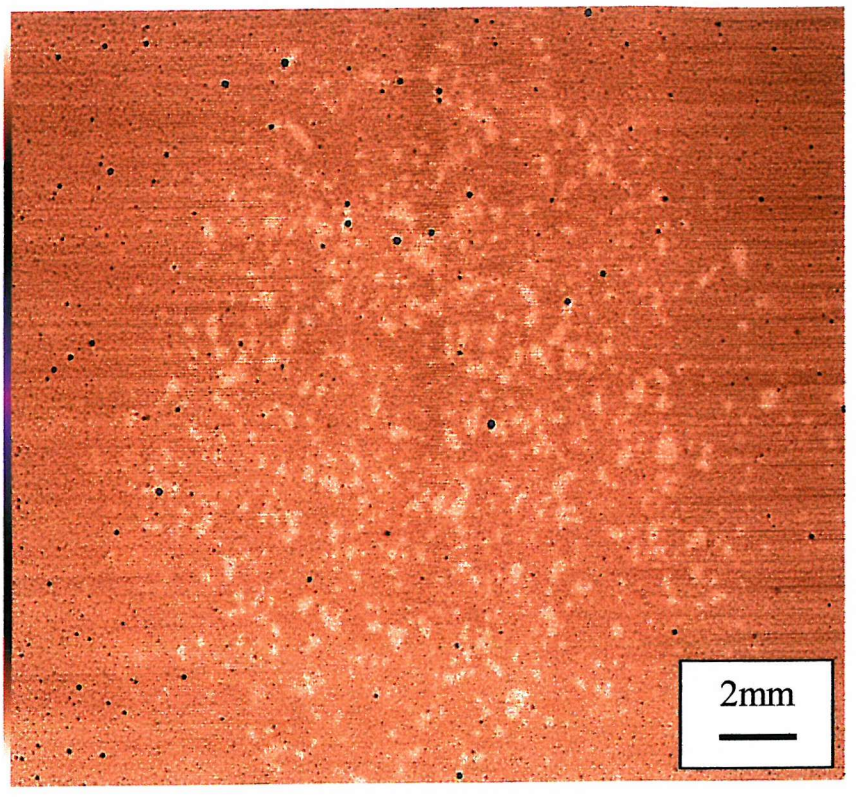

Fig. 10.22: SAM image of a 120μm diamond coating, tested for 8 hours at 268 m s^{-1}, showing delamination (light areas) in the erosion scar.

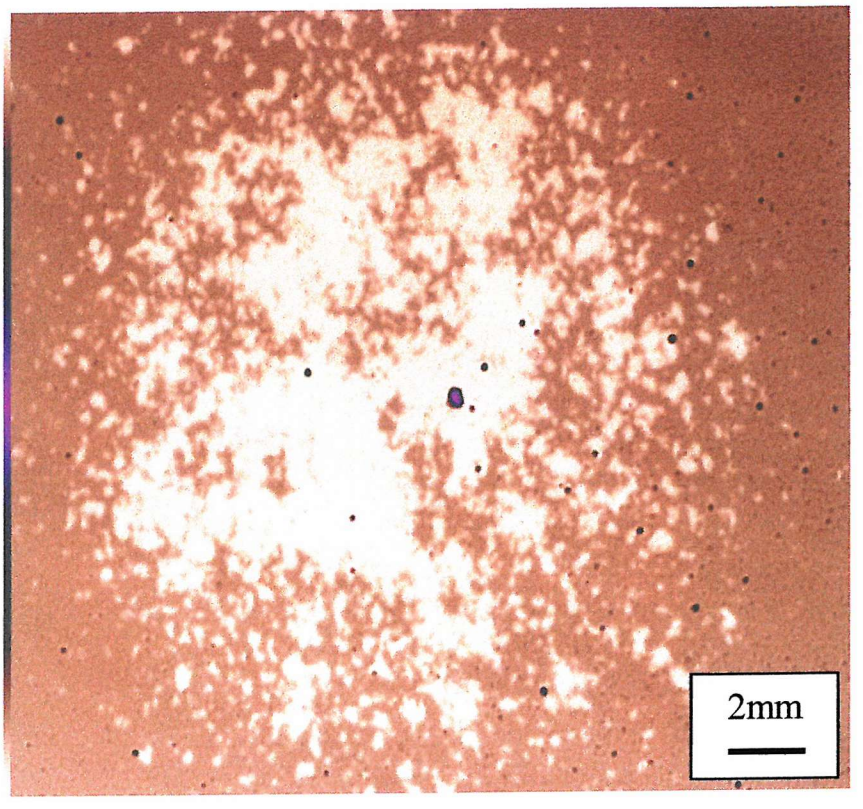

Fig. 10.23: SAM image of a 120μm diamond coating, tested for 22 hours at 268 m s^{-1}, showing extensive delamination.

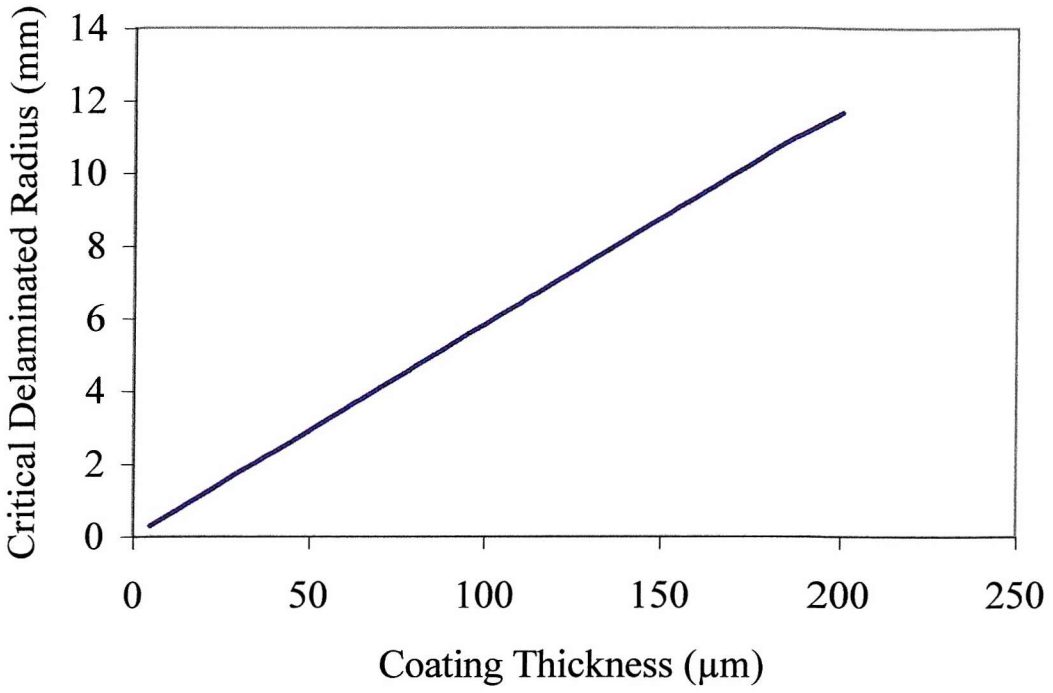

Fig. 10.24: Graph of equation 10.3, showing the dependence of Critical Delaminated Radius for coating spallation vs Coating Thickness for diamond coatings on tungsten assuming a residual stress of 0.87 GPa.

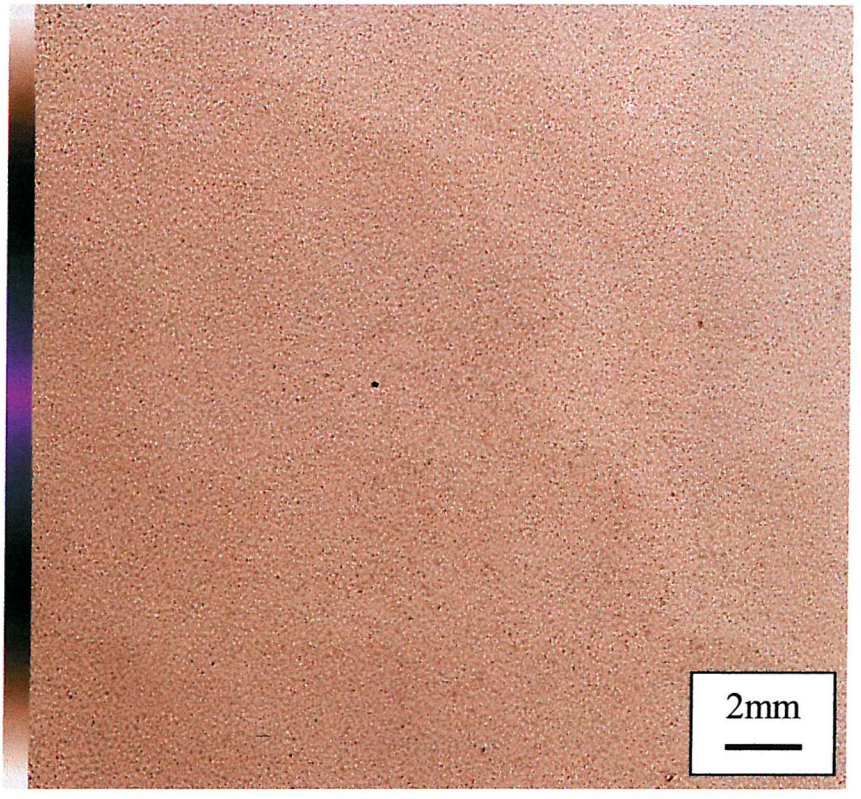

Fig. 10.25: SAM image of a lapped 160μm diamond coating, tested for 22 hours at 268 m s^{-1}, showing no delamination.

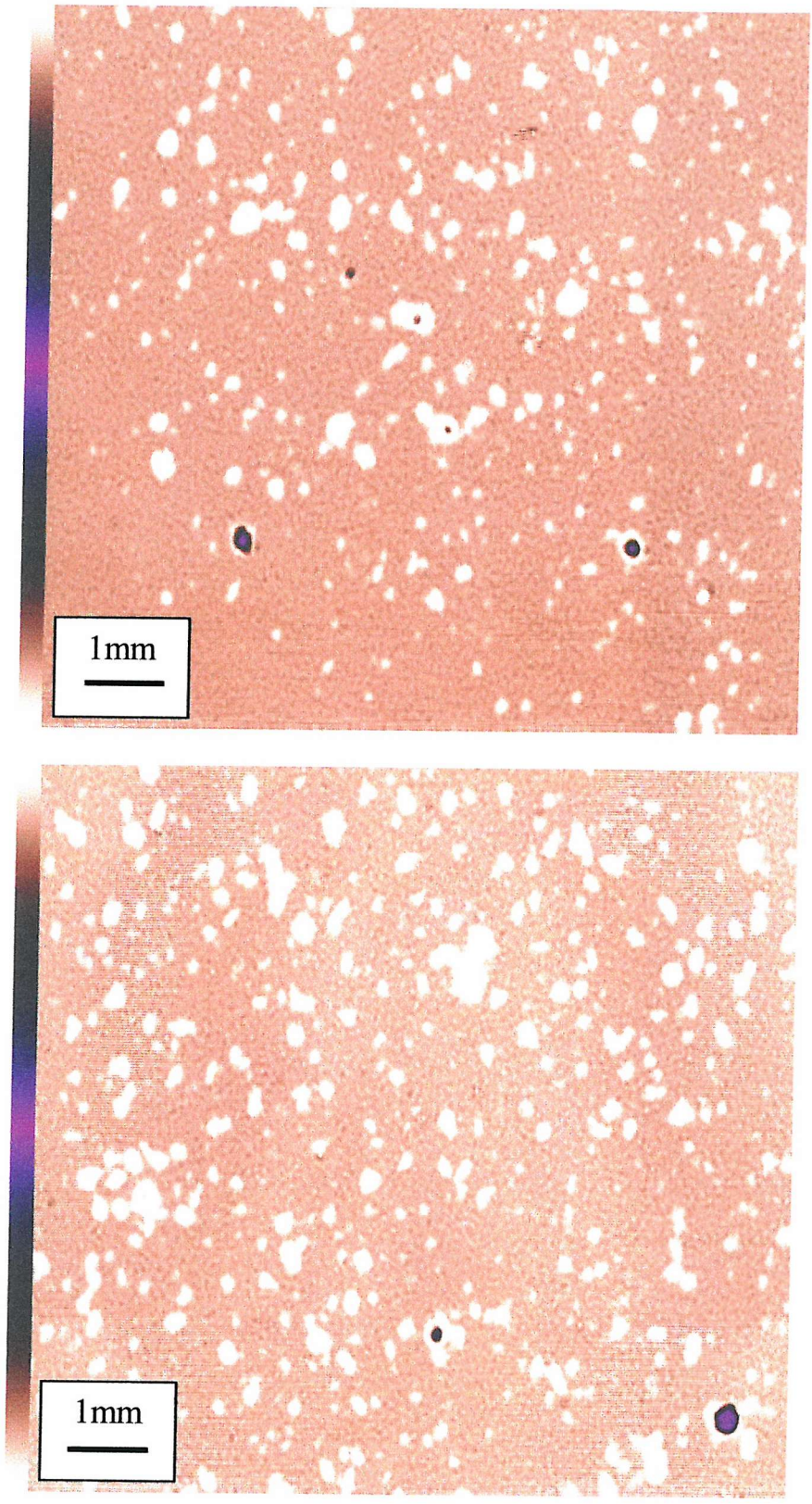

Fig. 10.26: Two SAM images of a 60μm diamond coating erosion tested at 268 m s^{-1} for 5 hours showing coating delamination (white areas) and pin-holes (circular purple features) located on delaminated regions of the coating.

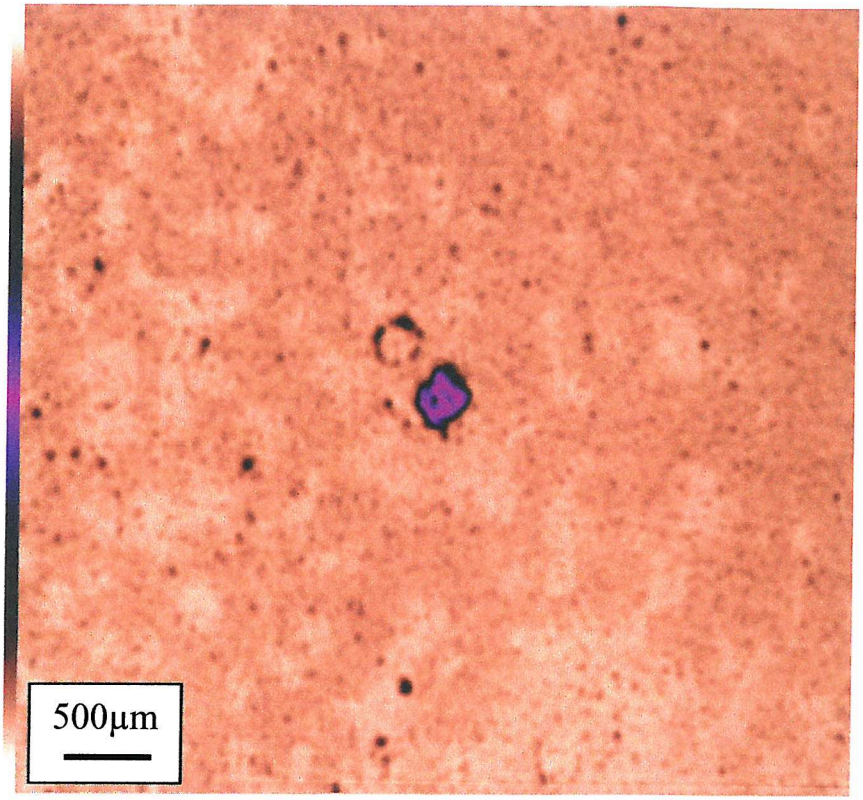

Fig. 10.27: SAM image of the centre of the erosion scar of a 60µm diamond coating, tested for 6 hours at 268 m s^{-1}, showing two circumferential cracks and a pin-hole.

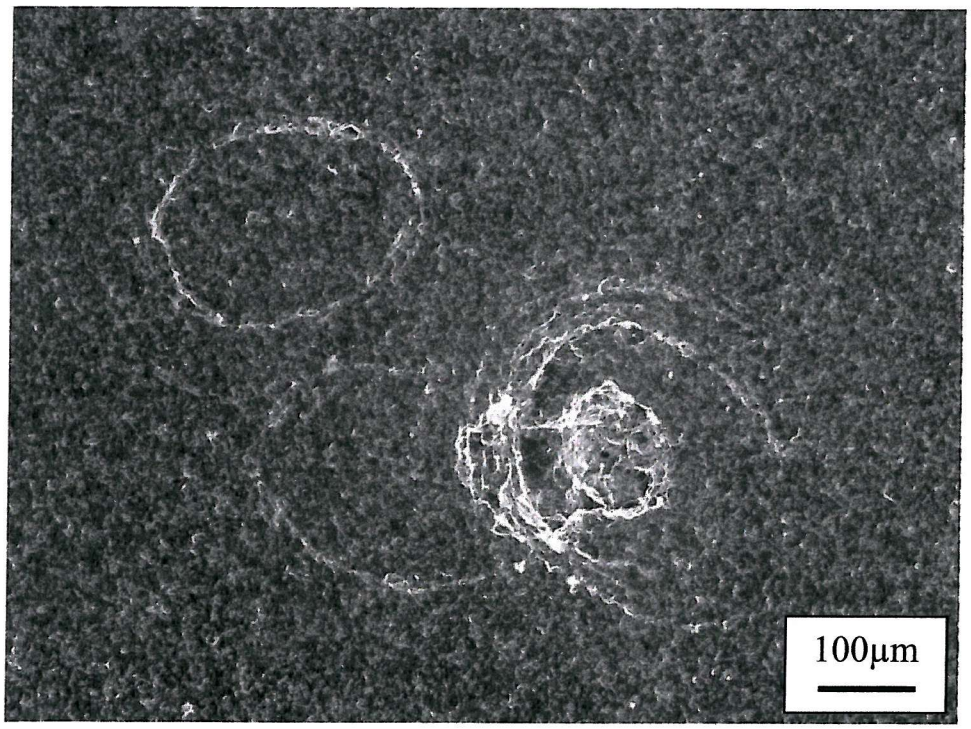

Fig. 10.28: SEM micrograph of the central feature shown in Figure 10.27.

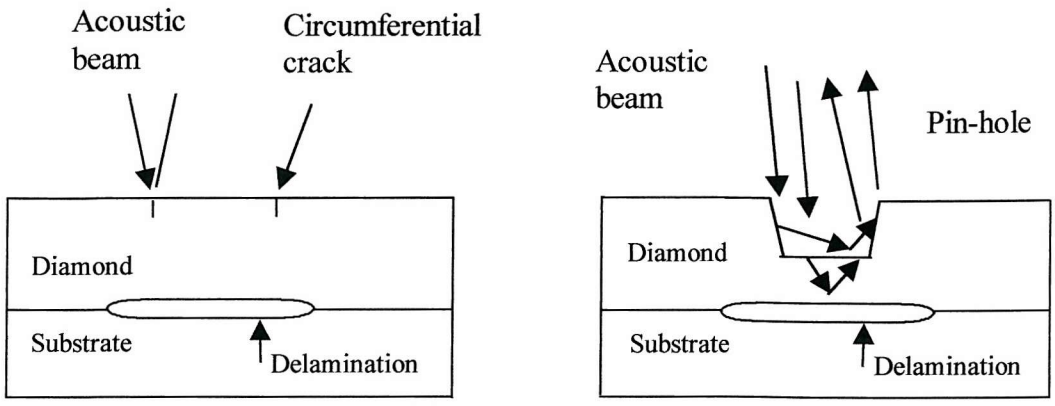

Fig. 10.29: Schematic diagram showing the interaction of the acoustic beam with circumferential cracks and pin-holes.

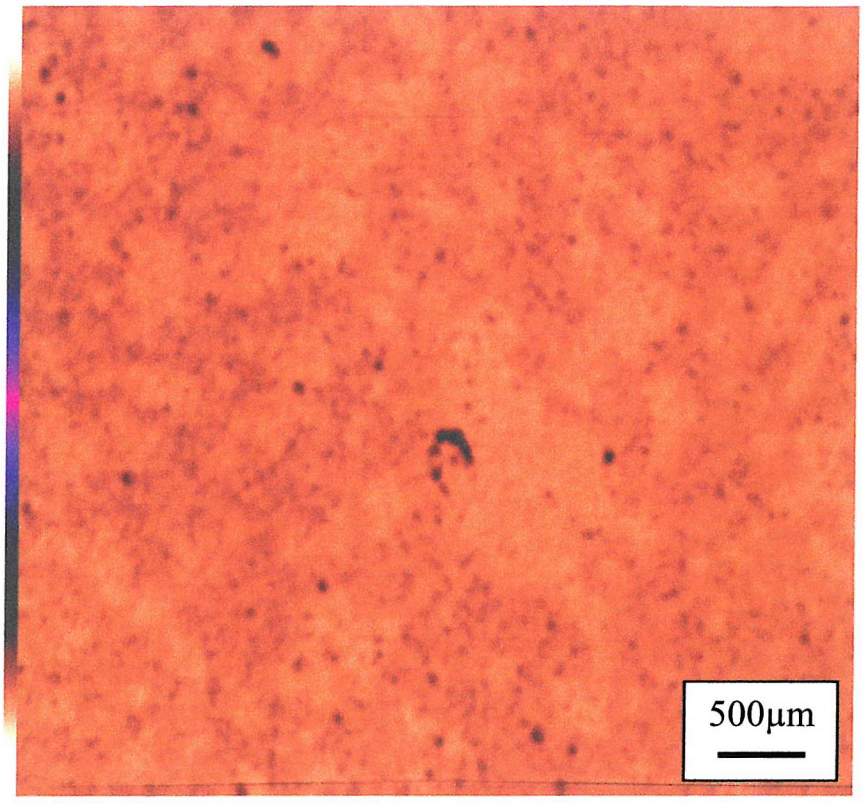

Fig. 10.30: SAM image taken from a 60µm diamond coating a partial circumferential crack located on a region of debonded coating.

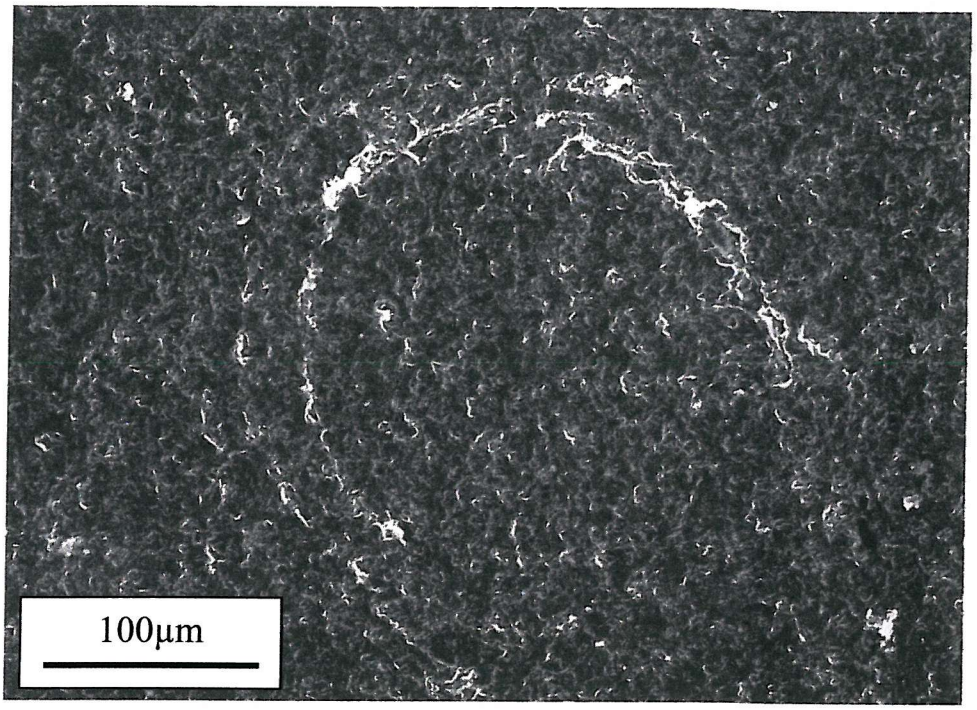

Fig. 10.31: SEM micrograph of a lapped 60µm diamond coating, tested for 6 hours at 268 m s^{-1}, showing the partial circumferential crack seen in Figure 10.30.

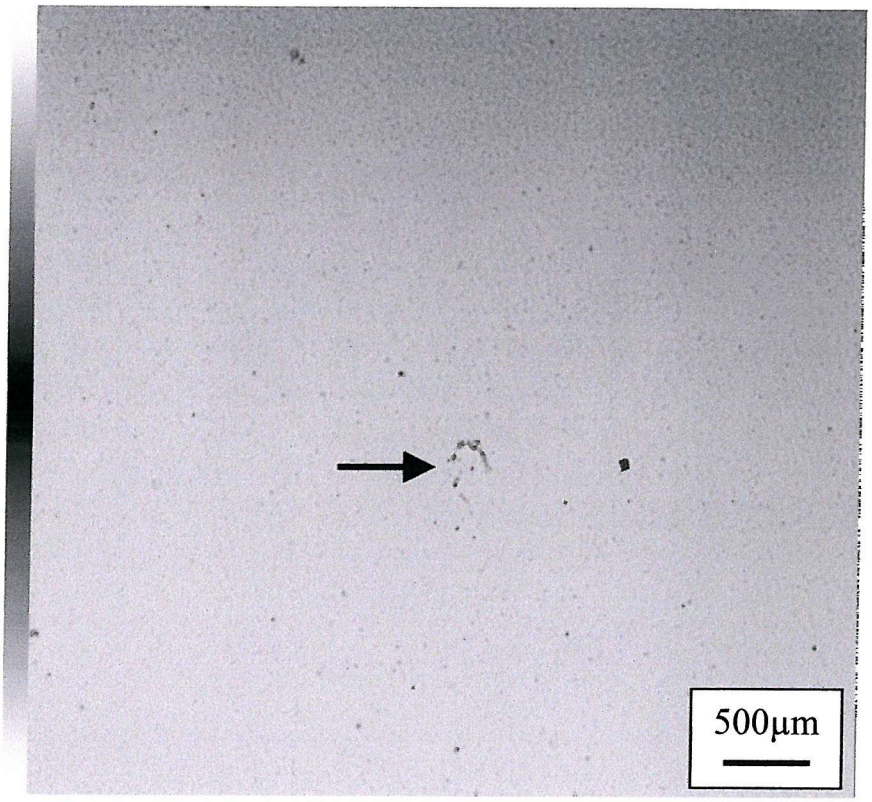

Fig. 10.32: SAM image of the 60 µm diamond coating, obtained using a surface wave transducer, showing the same circumferential crack (arrowed) as Figures 10.30 and 10.31.

11

THE INFLUENCE OF STRESS FIELD ON COATING INTEGRITY

11.1 Introduction

The previous chapter demonstrated that circumferential cracks and pin-holes were only situated on areas of the coating that had become delaminated. This supported the suggestion that they were formed by reflected stress waves rather than Hertzian stresses. However, the next stage in this work is to establish the cause of the coating debonding prior to circumferential crack formation, as well as identify the conditions under which debonding does not occur. This information can assist in the application of these coatings in real situations. It has already been seen in Chapter 8 that CVD diamond coatings can fail catastrophically, in some cases without visible indications of deterioration, in an erosive environment. Chapter 10 described the use of ultrasonic scanning and acoustic microscopy to show that, under repeated particle impact, there is a progressive increase in the incidence of interfacial discontinuities. This suggests that the sand particle impact causes debonding of the coating at the coating-substrate interface. However, further investigations are necessary in order to identify the mechanism by which this debonding occurred.

Another aspect of Hertzian contact, in addition to ring cracking, is the occurrence of shear stresses that are generated in the region beneath the contact. In a coating system these shear stresses can cause debonding via the propagation of cracks at the coating-substrate interface. The extent of this debonding is determined by the shear strength of the interface and the shear stresses caused by the applied load [1]. The propagation of interfacial cracks is known to be a mixed mode event, consisting of both mode I (tensile) and mode II (shear) components [2]. However, analysis by Comninou [3] has suggested that the growth of an interface crack is more intimately connected with failure in shear, rather than in tension.

Therefore, it is important to understand the role played by shear stresses in the delamination process.

Parameter	CVD Diamond	SiO_2
Elastic modulus, E_f (GPa)	1157	87
Poisson's ratio, ν	0.07	0.25
Density, ρ_e (kg m^{-3})	3520	2650
Hardness, H (GPa)	80	11
Fracture toughness, K_{Ic} (MPa$\sqrt{m}$)	6.0	1.3

Table 11.1: Table of relevant mechanical properties for CVD diamond and SiO_2 [4-6].

11.2 Calculation of the stress field

Table 11.1 lists the relevant material properties of both the diamond coating and the silica sand erodent used in this study. Some of these values are used in the calculations described below. The expressions for the maximum load, F_m, mean contact pressure, P_m, maximum contact radius, a_m the duration of elastic impact, t_e, have already been given in Chapter 9.

One of the limitations of the Hertzian approach is that it is only strictly applicable in cases where $a_m / R < 0.1$, where R is the radius of the spherical indenter, in this case the particle radius. Use of this theory can give rise to errors, which can increase with increasing a_m/R ratio and are particularly marked in materials of low Poisson's ratio. Under the conditions employed in this study (see section 11.3 for details) the a_m/R ratio was calculated to be 0.4. For this reason, the modified expressions proposed by Yoffe for $a_m/R > 0.1$ [7] were used in calculating the principal stresses σ_z, σ_θ and σ_r, the axial, circumferential and radial stresses respectively; the definitions of the principal stress directions are shown in Figure 11.1 [8]. In the calculations of the principal stresses the following expressions were used:

$$\sigma_r = \sigma_\theta = \frac{2F_m}{\pi a_m^4}\left[(3+2\nu_1)z\left(a^2+z^2\right)^{1/2} - (3+2\nu_1)z^2 - (1+2\nu_1)a^2/2 - a^2 z\left(a^2+z^2\right)^{-1/2}\right] \tag{11.1}$$

$$\sigma_z = \frac{2F_m}{\pi a_m^4}\left[2z^2 - a_m^2 - 2z\left(a_m^2+z^2\right)^{1/2} + 2a_m^2 z\left(a_m^2+z^2\right)^{-1/2}\right] \tag{11.2}$$

At the surface of the target material, the maximum tensile stress at the contact circle, σ_m, can also be calculated, using the following expression:

$$\sigma_m = \frac{1}{2}(1-2\nu_1)P_m \tag{11.3}$$

In considering the stresses acting on the coating it is important to remember that the stress ratio σ / P_o (where P_o is the maximum contact pressure) is dependent upon ν, the Poisson's ratio of the material concerned. The depth, z_τ, at which the maximum shear stress occurs, usually quoted as $z_\tau = 0.48a_m$, is for a material having a Poisson's ratio of 0.3. However, the Poisson's ratio of diamond, though dependent upon crystallographic orientation, is considerably lower than 0.3. The aggregate value is usually quoted as 0.07 [4] and it is this figure that was used in recalculating the values of principal stresses.

Using σ_z from equation (11.2) and σ_θ from equation (11.1) the shear stress, τ_1, was calculated using the following expression [9]:

$$\tau_1 = \frac{1}{2}|\sigma_z - \sigma_\theta| \tag{11.4}$$

Figure 11.2 shows the plot of τ_1 / P_o with depth using $\nu = 0.07$. It shows that the shear stress has a maximum value below the surface:

$$\tau_m = 0.47P_o \tag{11.5}$$

The depth, z_τ, at which this occurs, is $0.32a_m$. The final parameter in this section, the vertical displacement, w, of the coating in the centre of the impact site is given by:

$$w = \frac{3(1-\nu_1)F_m}{16G_1 a_m}\left(2 - R^2/a_m^2\right) \tag{11.6}$$

where G_1 is the shear modulus of the target.

Once again, it should be stressed that in the current calculations, the magnitude and location of the maximum shear stress for a coating system the assumption is made that the influence of the substrate on the stress field is negligible. In a theoretical analysis, El-Sherbiney and Halling [10] have stated that the effect of the substrate can be ignored if the $C_T / a_m > 0.5$, i.e. it can be treated as a homogeneous material. However, for thin coatings where $C_T / a_m <$ 0.5 finite element analysis is required in order to overcome the complications presented by the substrate. For simplicity, the influence of the substrate is neglected in all calculations described in this chapter.

11.3 Experimental Details

The diamond coatings used in the present study were deposited on tungsten substrates and were between 26 and 33μm in thickness; the surface roughness (R_a) was 0.2 ±0.03μm. Figure 11.3 shows a micrograph of the untested surface. They were erosion tested using silica sand at a constant velocity of 250 m s^{-1} and the flux rate was 0.5 kg m^{-2} s^{-1}. The nominal impact angle in all tests was 90 ±2°.

Range of sand sizes (μm)	Mean sand diameter (μm)	a_m (μm)	C_T (μm)	z_τ (μm)	z_τ / C_T	*N (Hertz)* (h^{-1})
125-180	152	31	33	9.9	0.30	4440
180-250	215	44	33	14.1	0.43	3124
250-355	303	62	30	19.8	0.66	2220
355-500	428	87	26	27.8	1.06	1556

Table 11.2: Details of the tests conducted. Note: C_T = coating thickness.

The sand was sieved to achieve a narrow size distribution so that the contact conditions could be more accurately defined. At a constant impact velocity, the depth at which the maximum shear stress, τ_m, occurs, z_τ is dependent on the particle size. Because z_τ is related to the contact radius it can be seen that larger particles will generate τ_m at greater depths. Therefore the test conditions in the present study were chosen so the effect of z_τ on the coating life could be examined. The exact details of the tests are listed in Table 11.2. The duration of each test was varied in order to ensure that the number of particle impacts

remained constant. The equation used to calculate the number of impacts per Hertzian zone, *N (Hertz)*, was introduced in Chapter 9.

11.4 Results

The results of the tests are listed in Table 11.3. They show that at a velocity of 250 m s^{-1} the larger sand particles had a considerably greater influence on the integrity of the coating. The coating impacted by the 428μm sand, where τ_m is close to the interface, failed after 2 minutes. In contrast the coating impacted by the 152μm sand, where τ_m is closer to the coating surface than to the interface, failed after 18 hours. Figure 11.4 displays the time to failure, t_f, of the coatings in graphical form. It can be seen that there is an approximately exponential relationship between t_f and mean particle diameter.

Examination, prior to failure of all coatings, revealed a number of microscopic pin-holes in the surface, many of which had completely penetrated the coatings. An example of one of these features, from the coating impacted by the 125-180μm sand, is shown in Figure 11.5. Examples of pin-holes from the coatings eroded by the 180-250μm, 250-355μm and 355-500μm sands can be seen in Figures 11.6 to 11.8. The significance of these pin-holes will be explored in more detail in the following section.

Sand size range (μm)	t_{PH} (mins)	N (pin-holes)	t_f (mins)	N (failure)
125-180	462	34188	1080	79920
180-250	120	6248	300	18744
250-355	15	555	45	1665
355-500	0.5	13	2	52

Table 11.3: Effect of sand size on the number of impacts for pin-hole formation and coating failure. Note: t_{PH} = time for pin-hole formation; t_f = time to coating failure; N = Number of particle impacts.

In all four tests, the pin-holes were first observed after approximately one-third of the overall coating life. This suggests that they could represent an early indication of coating

failure. For this reason the time for pin-hole formation, t_{PH}, has also been plotted in Figure 11.4.

The results show that, in the present tests, sand particle impacts generating shear stresses close to the coating-substrate interface will result in rapid coating debonding leading to complete catastrophic failure of the coating. For particle impacts where the maximum shear stress is within the coating, but away from the interface, the damage to the coating is minimal. Therefore for practical applications where diamond coatings are employed it is necessary for the coating to be of sufficient thickness so that the stress field generated by particle impacts is contained within the coating.

11.5. Comparison of circumferential crack / pin-hole diameters with Hertz theory

Chapter 9 showed the evolution of circumferential cracks and pin-holes: initially, the circumferential crack is formed, followed by ejection of material bounded by the crack. The ejection of the central material creates the pin-hole. In this chapter, the most of the pin-holes had fully formed, i.e. the diameter of the central material removed was the same as the circumferential crack. In order to be consistent with previous chapters, the term "circumferential crack diameter" is retained, even though many of the diameters are of pin-holes (see Figures 11.5 to 11.8).

The diameters of the circumferential cracks / pin-holes were measured and compared with the contact diameter, which was predicted by Hertz theory. The results are listed in Table 11.4. It can be seen that although the Hertz theory appears to explain the effect of the shear stress on the coating integrity it does not appear to explain the formation of the circumferential cracks / pin-holes. With the exception of the tests conducted using 125-180μm and 180-250μm sand, the mean crack diameters are significantly smaller than the Hertzian contact diameter, d_m. Moreover, Table 11.4 shows that there is no significant dependence of crack diameter on the sand size used in the different tests.

Figure 11.9 shows mean circumferential crack diameter plotted against sand size. To enable easy comparison the dependence of Hertzian contact diameter is also plotted. It can be seen that the size range within which all circumferential crack / pin-hole diameters fall is essentially the same, irrespective of erodent particle diameter.

Chapter 9 showed that the diameters of the circumferential cracks did not agree with Hertz theory. However, most of the tests conducted in that study employed a sand blend that contained a wide distribution in sizes. At the time, it was thought that the large sand particles in the blend were responsible for generating the pin-holes. However, the present results appear to confound that supposition as pin-holes of similar diameter have been observed in tests using finely sieved sand with narrow size distribution.

Range of sand sizes (μm)	Mean sand diameter (μm)	Mean Hertzian contact diameter d_m (μm)	Mean crack diameter (μm)	Standard Deviation (crack diameter) (μm)	No. of pin-holes
125-180	152	62	93	16	6
180-250	215	88	92	10	4
250-355	303	124	93	11	12
355-500	428	174	106	24	13

Table 11.4: Comparison of Measured crack diameters with Hertz theory at 250 m s^{-1}.

11.6 Effect of shear stresses on pin-hole formation

The calculations indicate that high shear stresses are generated by the particle impacts reaching a maximum value, τ_m, of 7.3GPa. The data in Figure 11.4 has been re-plotted in Figure 11.10 to show the relationship between *N(pin-holes)* and *N(failure)* with the depth of maximum shear, z_τ normalised to the coating thickness, C_T. As z_τ/C_T is reduced there is an exponential increase in the number of impacts for both pin-hole formation and failure. This mirrors the trend seen in Figure 11.4.

It is necessary to account for this exponential increase in N as z/C_T is reduced. For each of the four impact conditions the variation of τ/P_o as a function of z/C_T was plotted; these are

shown in Figure 11.11. Once again, the influence of the substrate is ignored. They show that the normalised shear stress, τ/P_o, at the coating-substrate interface, when $z/C_T = 1$, is 0.26 for the 125-180μm sand and 0.38 for the 180-250μm sand. They are significantly lower than the figures for the other two sand sizes (0.45 – 0.47). The level of τ/P_o as a function of z/C_T is summarised in Table 11.5.

The data listed in Table 11.5 has been plotted in graphical form in Figure 11.12. It shows an approximately exponential relationship between N and τ/P_o at $z/C_T = 1$. It is significant that this closely mirrors Figure 11.10; therefore, this supports the suggestion that the formation of pin-holes is linked to the coating debonding process.

Sand size range (μm)	*N(pin-hole)*	*N(Failure)*	τ/P_o at $z/C_T = 1$	τ at $z/C_T = 1$ (GPa)
125-180	34188	79920	0.29	4.4
180-250	6248	18744	0.38	5.8
250-355	555	1665	0.45	6.9
355-500	13	52	0.47	7.2

Table 11.5: Number of impacts for pin-hole initiation as a function of τ/P_o at the coating-substrate interface at 250 m s^{-1}.

The initiation of cracking in brittle materials usually occurs from intrinsic flaws present in the microstructure. As shown in Figure 10.2 the microstructure of the nucleation surface of CVD diamond contains significant amounts (up to 5%) of grain boundary porosity. The size of these flaws can be as large as 18μm. They therefore constitute nucleation sites, which will assist the debonding process, if the stress is sufficiently high.

Interfacial crack propagation (i.e. delamination) can also be driven by the presence of residual stresses in the coating. When the residual stress is compressive in nature, as is the present case, it can induce buckling of the film above if the stress is sufficiently high. This can provide an additional driving force for interfacial crack growth [11].

Although there appears to be a correlation between Hertz theory and the location of sub-surface shear stresses it has already been demonstrated in Chapter 9 that Hertz theory does not explain the formation of the circumferential cracks and pin-holes. This apparent logical inconsistency can be reconciled by recalling that shear stresses have also been attributed to being the cause of sub-surface damage in non-Hertzian impact conditions, for instance liquid impact in liquid impact studies, even though the assumption that the erodent and target are not deformed is plainly not the case. In studies of liquid impact on PMMA targets, Bowden and Brunton [14] found evidence of damage below the surface at a depth of approximately half the contact radius. This location is close to where the maximum shear stress occurs for elastic contact as predicted by Hertz. However, the shear stress is also likely to be augmented by the interaction of release waves from the contact periphery to give a net tension. This has been demonstrated experimentally in liquid impact studies of PMMA [15,16]. Therefore, in the present case there appear to be two competing stress fields (i.e. Hertzian and stress wave) created by the particle impacts, which together are responsible for the circumferential cracks and pin-holes.

In theoretical work, shear stress as a result of liquid impact has also been predicted. In a finite element model of liquid impact onto a silicon sample coated with a 30μm diamond film, de Botton [17] found that the model predicted the existence of an intensive peak of in-plane shear stresses just beneath the point at which the load terminates. This mirrors the quasi-static analysis as described by van der Zwaag and Field [1].

11.7 Effect of stress field on coating performance

The results show that the coatings exhibiting the greatest resistance to debonding are those in which the stress field is contained within the coating. This is of great importance in the design of coating systems exposed to erosive particles in service and shows that coatings less than a certain thickness offer little resistance to sand particle impacts. However, it does not automatically follow that increasing the thickness of the coating confers enhanced erosion resistance. In certain circumstances residual stresses present in the coating may be of sufficient magnitude to be detrimental to both the erosion resistance and the coating

adhesion. Therefore, there is a point beyond which any further increase in coating thickness will not procure any extra benefit in terms of coating performance.

Parameter	125-180μm sand	180-250μm sand	250-355μm sand	355-500μm sand
F_m (N)	30.5	61.2	120.3	241.6
P_m (GPa)	10.2	10.2	10.2	10.2
P_o (GPa)	15.5	15.5	15.5	15.5
a_m(μm)	31	44	61	87
d_m (μm)	62	88	122	174
t_e (μs)	0.15	0.21	0.29	0.42
σ_m (GPa)	4.4	4.4	4.4	4.4
τ_m (GPa)	7.3	7.3	7.3	7.3
w (μm)	0.79	1.10	1.57	2.22
w / C_T	0.02	0.04	0.05	0.09
z_τ / C_T	0.30	0.43	0.66	1.06

Table 11.6: Impact calculations for the different sand at a velocity of 250 m s^{-1}impacting diamond coatings of 30μm in thickness.

In order to explore further the reasons for the superior performance of the coatings where the z_τ / C_T ratio is very low, it is necessary to consider the impact conditions. These are summarised in Table 11.6. It shows that the impact force, F_m, with the 355-500 μm sand particles is approximately 8 times that of the 125-180μm sand. Moreover, the vertical deflection at the centre of impact is approximately 5 times greater than that generated using the 125-180μm particles. This will lead to an increased in-plane strain, as well as bending, becoming an important influence on coating behaviour. Komvopoulos [18] suggested that for thin coatings ($C_T / a_m < 0.45$) deformation was likely to be dominated by surface microcracking, while for thicker coatings ($C_T / a_m > 0.45$) interfacial crack initiation caused by sub-surface shear stresses was likely to be the dominant degradation mechanism. The experimental results described in this chapter support this analysis.

Table 11.6 shows that high impact pressures (P_o) and shear stresses (τ_m) are predicted. However, it is thought that particle fragmentation on impact may prevent stresses of this magnitude from being generated in which case the actual stresses will be considerably lower. Finite element modelling of the impact conditions could help in further understanding of the stress field.

11.8 Erodent Characteristics

One aspect of the impact conditions that has not been considered is that of particle morphology. The shape of sand particles is known to vary with size. Smaller diameter particles are predominantly angular while larger particles assume a more spherical morphology. Table 11.7 below lists the characteristics of the sand used in the present tests. Micrographs of the four erodent sizes are shown in Figures 11.13 to 11.16.

Sand size Range (μm)	Angularity	Sphericity	Particle Roundness Factor
125-180	Angular	Low	0.1-0.3
180-250	Sub-angular	Medium	0.4-0.7
250-355	Sub-rounded	Medium	0.7-0.9
355-500	Sub-rounded	Medium	0.7-0.9

Table 11.7: Characteristics of the silica sand erodent

Table 11.7 shows that over the range of sand sizes used in the present tests there is a wide variation in the characteristics of the silica sand erodent. They range from the angular (125-180μm) to the sub-rounded (250-355μm and 355-500μm). For a perfect sphere, the roundness factor (RF) will be equal to one [19]. It can be seen that all grades of sand listed in Table 11.7 represent, by varying degrees, a departure from a perfect sphere. In the case of the smallest particles (125-180μm) this deviation in considerable.

It is, therefore, significant that the change in sand morphology with diameter is not matched by variations in pin-hole shape or diameter. The average pin-hole diameter appears to be independent of both particle diameter and shape. This represents a further departure from Hertz theory. The Hertzian contact diameter, d_m, is dependent on the radius of the indenter /

particle. Moreover, it is also based on a linear elastic half space subjected to normal loading by a *smooth, spherical,* indenter [20]. The departure from a purely spherical shape means that the *actual* contact radius, is likely to be considerably less than that predicted by Hertz. This would bring the contact radius closer to that of the pin-holes produced by the two larger sand sizes (see Figure 11.9). However, an even greater reduction in contact radius would be seen for the highly angular 125-180μm sand particles, the contact radius is already approximately 30% lower than that of the measured pin-hole diameter. Therefore, this does not explain the small variation in shape and diameter of the pin-holes generated in all four tests.

11.9 Comparison with other erosion studies of CVD diamond

In comparing the results of this project with the work of other workers [21-23] it is important to understand why Hertzian ring cracks were seen in those studies and not in the present one. Table 11.8 summarises the details of the two cases in order to aid comparison. There are three major differences:

- Particle velocity;
- Sand morphology;
- Nature of the coating-substrate system;

Each of these will be considered in turn.

11.9.1 Particle Velocity

The particle impact velocity in the present case is much higher (250 m s^{-1}) than those used by Feng *et al* [21], where the velocities were 34 and 59 m s^{-1}. As a consequence the contact time, t_e, is considerably reduced, thereby decreasing the time available for ring crack formation. The contact times may be further reduced by particle fragmentation, leading to actual contact times that are significantly lower than those listed in Table 11.7.

Particle fragmentation is also more prevalent at higher velocities owing to the greater stresses on impact and the high levels of intrinsic flaws in silica, especially in the larger particles. As previously described in Chapter 9, the mean sand particle diameter decreased by approximately 65% following impact with a diamond surface at 268 m s^{-1}. Evidence of plastic flow of some sand particles, thought to be generated by high strain rates on impact, has also been described in Chapter 9. Thus, another assumption of Hertzian contact, that both the indenter and target material remain undeformed, is no longer applicable.

Parameter	Feng *et al* [21]	This study
Surface roughness R_a (μm)	0.008	0.2
Substrate material	Si_3N_4	W
Coating thickness C_T (μm)	15	26-33
Sand size (μm)	300-600	125 – 500
Impact velocity V (m s^{-1})	34	250
Contact time, t_e (μsec)	0.65	0.15 – 0.42
Contact radius a_m (μm)	27-54	31 – 87
Max tensile stress σ (GPa)	2.2	4.4
Max shear stress τ_m (GPa)	3.5	7.2
Depth of max shear z_τ (μm)	8.6-17.2	9.96-27.8
z_τ / C_T	0.57-1.15	0.29-1.07

Table 11.8: Comparison of impact conditions between the present study and those of other workers [21].

11.9.2 Sand Morphology

The morphology of the sand is significant, as ring cracks are more likely to be generated by impact from spherical or near-spherical sand particles. This was the case for the work of Feng *et al* [21], though was not true for the present case. However, Figure 11.16 shows the 355-500μm sand used in one of the tests which is approximately the same size as that use by Feng *et al* and yet no ring cracks were observed. This suggests that another factor could be significant.

11.9.3 Nature of the coating-substrate system

One major difference is the nature of the coating-substrate system itself. In the case of the work by Telling and Field [22,23] there was no substrate as the target was free-standing diamond 0.5mm thick. The diamond coatings investigated by Feng *et al* [21] were deposited upon Si_3N_4 substrates. The choice of substrate is known to affect the performance of coatings. In indentation tests of plasma sprayed ZrO_2 coatings with a WC sphere Wuttiphan *et al* [24] showed that greater interfacial delamination and more extensive yielding on softer substrates. This is a consequence of the larger elastic-plastic mis-match stresses between the coating and the substrate.

As can be seen in Table 11.9, the hardness of Si_3N_4 is approximately 3.5 times that of W. Moreover, the maximum shear stress in [21] is less than half that of the present case. Therefore, the driving force for interface crack propagation is lower, even though the depth at which the maximum shear stress acts is close to the interface. For the large sand particles the maximum shear stress is acting within the substrate. Therefore, the diamond coatings on tungsten are likely to be more susceptible to delamination and substrate yielding when the sub-surface stresses are of sufficient magnitude.

Property	Sintered Silicon Nitride	Tungsten
Elastic modulus, E_s (GPa)	260-330	411
Yield strength, σ_y (MPa)	-	725
Tensile strength σ_t (MPa)	600-1200	900
Poisson's ratio, ν	0.25	0.28
Hardness (H_{v30})	1400	460
Coefficient of thermal expansion α_s ($\mu m\ m^{-1}\ K^{-1}$)	3.0	4.5
E_c / E_s	3.5	2.6

Table 11.9: Comparison in the mechanical properties between Si_3N_4 and tungsten.

11.9.4 Residual stress

The mis-match in thermal expansion coefficient between coating and substrate can be a significant influence on the nature and magnitude of residual stress in a coating system. Work by Rats *et al* [25] has shown that for diamond coatings on metallurgical substrates the thermal expansion mis-match is the dominant influence on the magnitude of the residual stress. The coefficient of thermal expansion for diamond is 0.9 $\mu m\ m^{-1}\ K^{-1}$ at 300 K [26]. Therefore, the mis-match for diamond on Si_3N_4 is significantly lower than for diamond on tungsten.

The nature of the residual stress in the coating will also influence the behaviour of the coating. Chapter 7 has already shown that the overall level of residual stress is approximately constant for coatings >10μm, the aggregate stress being approximately 0.8 GPa (compressive). In contrast, work by Rats *et al* [25] has shown that the thermal stress for diamond on Si_3N_4 is slightly tensile. It is interesting to note that on studying the edge of the delaminated coating, Feng *et al* noted that the fractured edge of the coating appeared to curve away from the substrate, which they attributed to the presence of residual stresses in the film [21]. This tendency to peel away from the surface was also observed in a study of Cr films on glass substrates by Hu *et al* [27]. The nature of this coating system (a brittle film on a brittle substrate and containing tensile residual stresses) mirrors the case of Feng *et al* [21].

It is thought that the compressive nature of the residual stress for diamond on tungsten could inhibit crack initiation on the surface of the coatings used in the present study. In contrast, the slightly tensile nature of the diamond coatings on silicon nitride may assist crack initiation on the coatings used by Feng *et al* [21]. The absence of compressive residual stresses may have had the same effect in the erosion studies by Telling and Field [22,23] who conducted their work on free-standing diamond. Studies of free-standing diamond have shown the overall residual stress to be negligible [28]. Again, the absence of a compressive stress may have rendered it more susceptible to surface ring cracking.

11.10 Use of erosion data to assist coating design

The finding that there appears to be a critical normalised depth of maximum shear stress (z_τ / C_T), below which the life of the coating can be considered to be almost infinite, could be used to assist the coating design process. The data from this chapter has been used to construct a map, shown in Figure 11.17, of velocity against sand radius showing the regions where pin-holes are found (z_τ / C_T $\geq$ 0.3), where they have not been seen (z_τ / C_T < 0.3), and where rapid failure of the coating occurs (z_τ / C_T $\geq$ 1). This map only applies to diamond coatings on tungsten 30μm in thickness. This work should be extended to cover coatings of greater thickness and on different substrates.

Other information that would assist the design process would be maps showing *N(pin-hole)* and *N(failure)* against velocity for a given coating thickness. Such information could be used to identify critical velocities, below which pin-holes are not seen, in a similar manner to Damage Threshold Velocity curves, used in liquid impact studies [29]. An example of this is shown in Table 11.10, which lists *N (pin-hole)* against velocity for 39-47μm lapped diamond coatings on tungsten. Originally listed in Table 9.3 (Chapter 9), this data is plotted in graphical form in Figure 11.18. The absence of pin-holes on the coating tested at 33m s^{-1}, despite being tested for 25 hours, may be because z_τ / C_T < 0.3 for all particle impacts; therefore, coating delamination will not be generated, thus preventing the formation of pin-holes. However, further tests are needed to confirm this.

Velocity, V (m s^{-1})	33	63	148	268
Coating Thickness, C_T (μm)	40	39	47	46
Time required to form 1st pin-hole (hrs)	-	12.0	3.0	1.0
N (pin-hole) (Hertz)	-	14362	6948	3802
Maximum shear stress τ_m (GPa)	2.1	2.7	3.9	4.9
Depth of τ_m, z_τ (μm)	5.4	7.4	10.2	12.2
z_τ/C_T	0.14	0.19	0.22	0.27

Table 11.10: Summary of Table 9.3 showing the relationship between velocity and *N(pin-hole)*. Erodent used: Redhill Mix.

Although the present data is limited, when it is extended to cover other thicknesses and sand sizes it could provide valuable information for the design process. Table 11.10 also lists the normalised depth of maximum shear stress z_τ / C_T. Although they appear to contradict earlier statements made above (they indicate that pin-holes were formed when z_τ / C_T < 0.3) these z_τ / C_T figures relate to the average sand diameter (194μm). The large range of sand diameters in the Redhill Mix (approximately 90-500μm) make analysis of this kind complicated. The pin-holes are thought to have been caused by larger sand particles in the Redhill Mix blend, where z_τ / C_T > 0.3. For example, a 355-500μm particle at 250 m s^{-1} would generate a maximum shear stress at a depth of 26μm; for a 46μm coating, z_τ / C_T = 0.57, placing it within the range in which pin-holes are seen. The influence of the wide distribution in the Redhill Mix on erosion damage features is addressed in section 11.11.

11.11 Comparison of Redhill Mix with sieved sand

11.11.1 Damage Features and Coating Delamination

Previous tests described in Chapters 8 and 9 used Redhill Mix, which has a large distribution in particle diameters. However, this leads to wide variations in the contact conditions, thus complicating the task of modelling the damage. The work described in this section was undertaken in order to evaluate the influence of the wide size distribution on the damage features.

Two 60μm lapped diamond coatings were erosion tested: in one, Redhill Mix was the erodent and in the other sieved 180-250μm sand. In both cases the velocity (268 m s^{-1}) was nominally identical, as were the flux (0.5 kg m^{-2} s^{-1}), stand-off distance (30mm) and impact angle (90°). The test duration was 5 hours. The mean particle diameter of the Redhill Mix (194μm) is close to that of the sieved sand (215μm). Therefore, the *mean* velocity was assumed to be the same. However, for the Redhill Mix sand, it was recognised that the air stream in the erosion rig may accelerate particles <180μm to a higher velocity, while particles >250μm may be travelling slower, than the mean value of 268 m s^{-1}.

Examination of the coating impacted with Redhill Mix revealed 12 circumferential cracks and pin-holes and an overall mass loss over 5 hours of 0.86 mg. For the coating eroded by the 180-250μm sieved sand no mass loss was recorded and no circumferential cracks or pin-holes were observed. Therefore, both the steady state erosion rate (a function of micro-chipping) and pin-hole formation appear to be generated by the presence of the large particles (>250μm) present in the Redhill Mix.

Both samples were examined using scanning acoustic microscopy to examine the extent of sub-surface delamination. The procedure was identical to that described in Chapter 10. The area scanned was 20.8mm x 15.6mm, which encompasses the entire area of particle impact on each coating. Acoustic images of each sample are shown in Figures 11.19 and 11.20. On the diamond coating eroded by the Redhill Mix (Figure 11.19), delamination is present over the area of particle impact, as indicated by the white areas in the figure. In contrast, there is no delamination present in the coating eroded by the sieved sand (Figure 11.20). This suggests that, in the present case, the large (>250μm) sand particles in the Redhill Mix are responsible for coating delamination, as it is not seen when these particles are absent. Moreover, the large particles make up less than 40% of the overall sand blend. It is thought that the sub-surface shear stresses generated by the 180-250μm sand are of insufficient magnitude to cause delamination. This is borne out by comparison of the normalised depth of maximum shear stress, z_τ / C_T, with the data in Figure 11.10. For a 60μm diamond coating impacted by 180-250μm sand at 268 m s^{-1}, z_τ / C_T is 0.25. It can be seen that this is within the region where pin-holes are predicted to be absent. This supports the findings of section 11.6.

While it is recognised that the number of impacts in each case is not identical, and that the velocity of particles in the Redhill Mix is dependent upon their size, the acoustic images highlight the influence of large particles, where the depth of maximum shear stresses is greater, on coating behaviour under erosive conditions.

11.11.2 Circumferential Crack Diameter

It is instructive to compare the circumferential crack diameters of the 26-33μm coatings eroded by sieved sand in this chapter with the 33μm coating described in Chapter 9, where the erodent was Redhill Mix. The results are listed in Table 11.11 and in Figure 11.21. It can be seen that there is a large difference in the crack diameters in the two cases. The crack diameters for the 26-33μm are closer to the stress wave reinforcement diameter d_1, which is more common for materials of high Poisson's ratio. The other crack diameters mirror the findings of Chapter 9, which showed closer agreement with the stress wave reinforcement diameter d'. The terms d_1 and d', including the mathematical equations, were introduced in Chapter 9.

C_T (μm)	Erodent (μm)	Velocity (m s^{-1})	Mean Crack Diameter (μm)	Range of Crack diameters (μm)	SW diameter d' (μm)	SW diameter d_1 (μm)
33	90-500*	268	163	110-200	150	109
33	125-180	250	93	80-125	148	107
33	180-250	250	92	80-112	151	107
30	250-355	250	93	70-112	142	104
26	355-500	250	106	73-148	130	98
46	90-500*	268	193	150-245	206	149
40	355-500	250	178	130-220	190	140

Table 11.11: Comparison of circumferential crack diameters as a function of erodent.
Key: * = Redhill Mix. All other sand listed in the table was sieved. Note: see Chapter 9 for explanation of the stress wave reinforcement diameters d' and d_1.

The reasons for this lack of agreement between crack diameter and stress wave reinforcement diameter d' for the 26-33μm coatings are not clear. As mentioned in Chapter 9, Bowden and Field [12] have stated that many analyses of wave motion become less applicable as the origin is approached. This could be the reason for the discrepancy; it is notable that Table 11.11 shows better agreement in the case of the thicker 40μm coating. Moreover, comparison between a lapped 46μm coating eroded by Redhill Mix and a lapped

40μm coating eroded by sieved 355-500μm sand, which was described in Chapter 9, showed considerably less disagreement. Further tests using different sized sand on thicker coatings could further assist in understanding this matter.

Another factor to consider is the high stress wave velocity in diamond: the compression wave velocity is ~18,000 m s^{-1}. Thus, for a 30μm coating, a stress wave will travel through the coating and back to the growth surface in approximately 3ns. This figure is approximately 100 times less than the time of impact as predicted by Hertz (0.2μs at 268 m s^{-1}), though this figure is reduced by particle fragmentation on impact. However, the experimental evidence has demonstrated that the stress wave theory provides a plausible explanation for circumferential crack formation. Nevertheless, there are aspects of this work that remain to be fully understood. Computer modelling may provide further understanding of this topic.

11.12 Conclusions

This study has looked at the effect of varying the depth of maximum shear stress on the integrity of CVD diamond coatings subjected to high velocity erosion by silica sand. This was done by using finely sieved sand of different diameters at a constant velocity.

Erosion experiments indicate that sub-surface shear stresses, generated by the impact of the sand particles, are responsible for the generation of coating debonding. When the maximum shear stress occurs close to the coating-substrate interface, the coating fails rapidly and catastrophically. For this reason diamond coatings used in erosive environments must be sufficiently thick to ensure that τ_m is contained within the coating and is away from the interface.

The results suggest that, for 30μm coatings tested at 250 m s^{-1}, when $z_T/C_T < 0.3$ pin-holes are not generated as the maximum shear stress, τ_m, is insufficient to generate coating delamination. In these cases the life of the coating can be considered to be almost infinite.

Under these conditions, the critical shear stress required to promote delamination, appears to be approximately 3.9 GPa.

Sub-surface shear stresses, as predicted by Hertz theory, explains the integrity of diamond coatings subjected to impact from sand particles. However, the mean circumferential crack and pin-hole diameters do not agree with the contact diameter as predicted by the Hertz theory. Furthermore, the measured pin-hole diameters appear to be independent of particle size and morphology.

The number of impacts necessary to generate pin-holes has been observed to increase exponentially as the mean particle diameter, and hence the z/C_T ratio, is reduced. This provides further evidence that pin-holes represent visible evidence that coating delamination is taking place at the interface, which may result in catastrophic failure of the coating.

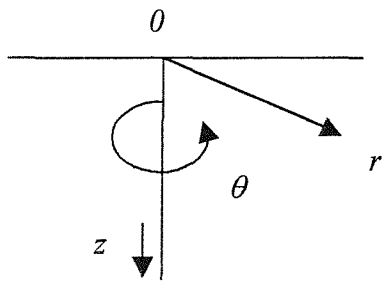

Figure 11.1: Schematic diagram showing the axial (z), circumferential (θ) and radial (r) directions referred to in this chapter [8]. Key: 0 = Centre of contact.

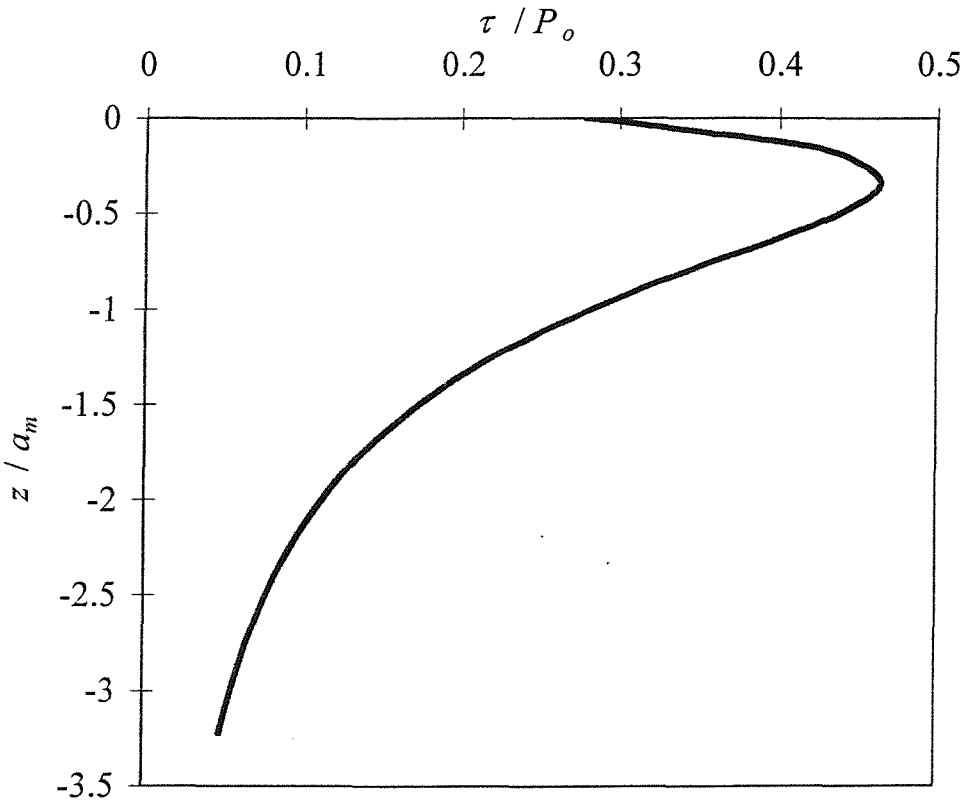

Fig. 11.2: Graph showing the variation of normalised shear stress (τ / P_o) with depth at the central axis of contact for 152μm diameter silica sand impacting on diamond at 250 m s^{-1}.

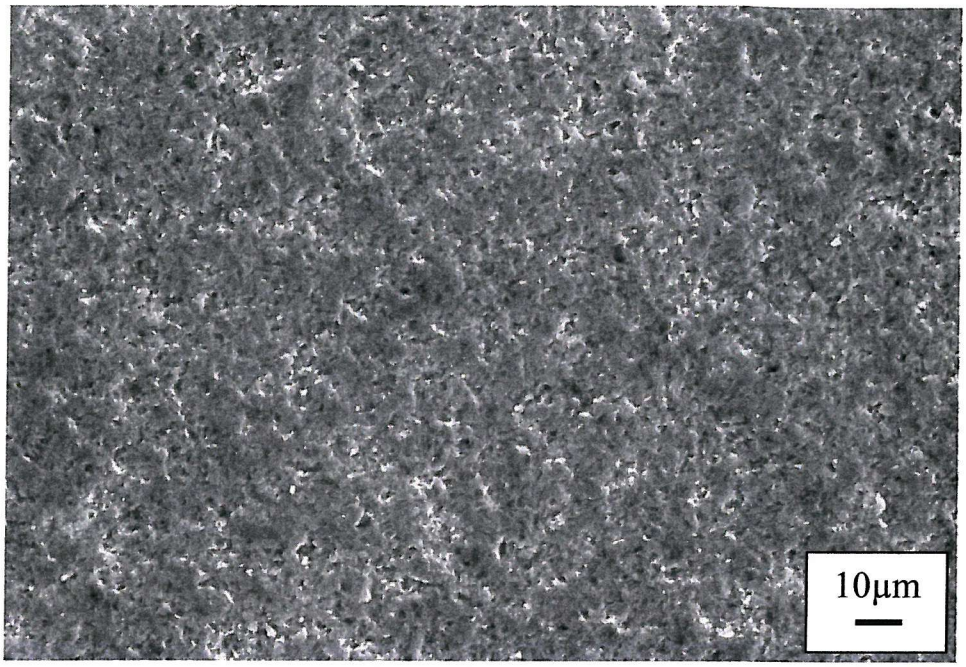

Fig. 11.3: Micrograph of the untested surface of a 30μm lapped diamond coating.

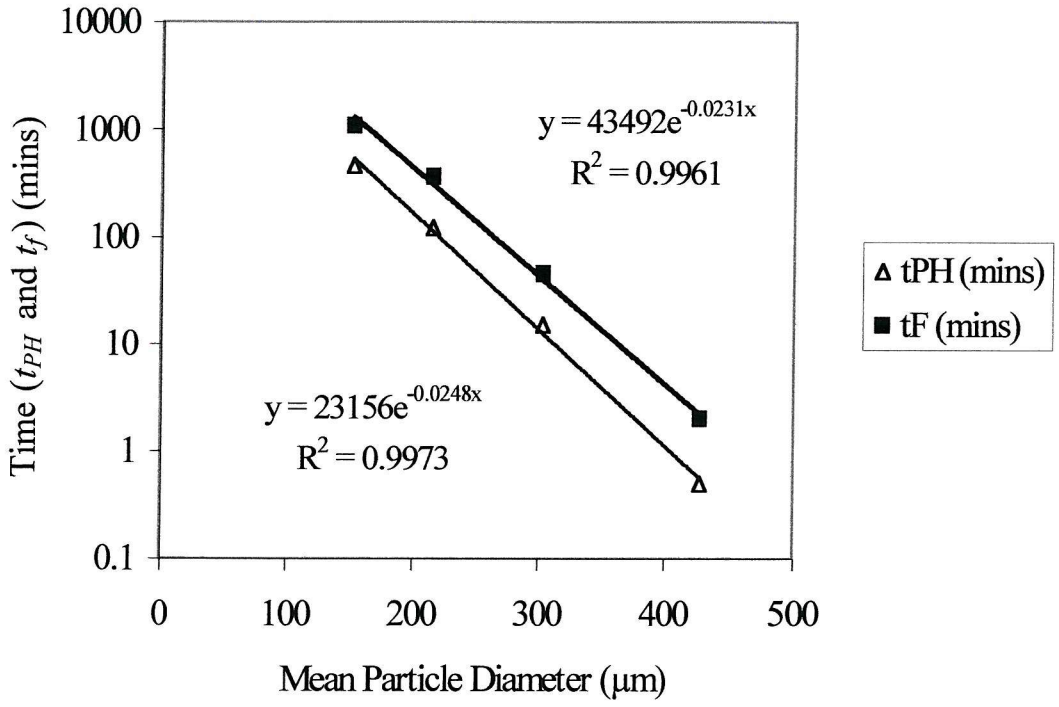

Fig. 11.4: Graph showing the relationship between mean particle diameter and the time for pin-hole formation (t_{PH}) and failure (t_f).

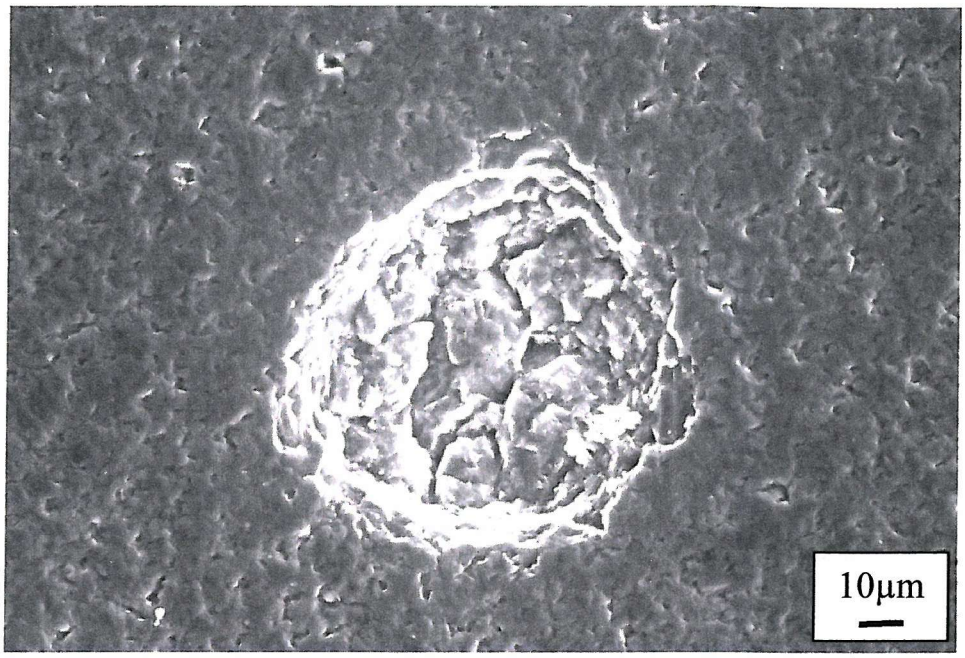

Fig. 11.5: Micrograph from the same sample as Figure 11.3, tested at 250 m s^{-1} for 8 hours using 125-180μm sand, showing a pin-hole.

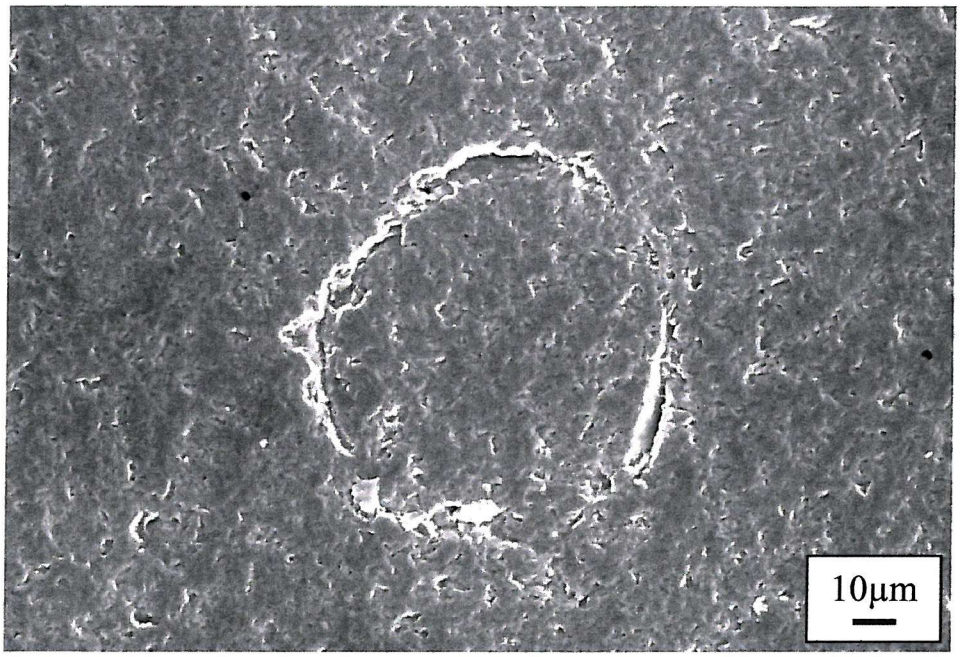

Fig. 11.6: Micrograph taken from a 30μm diamond coating tested at 250 m s^{-1} using 180-250μm sand for 2 hours showing a circumferential crack.

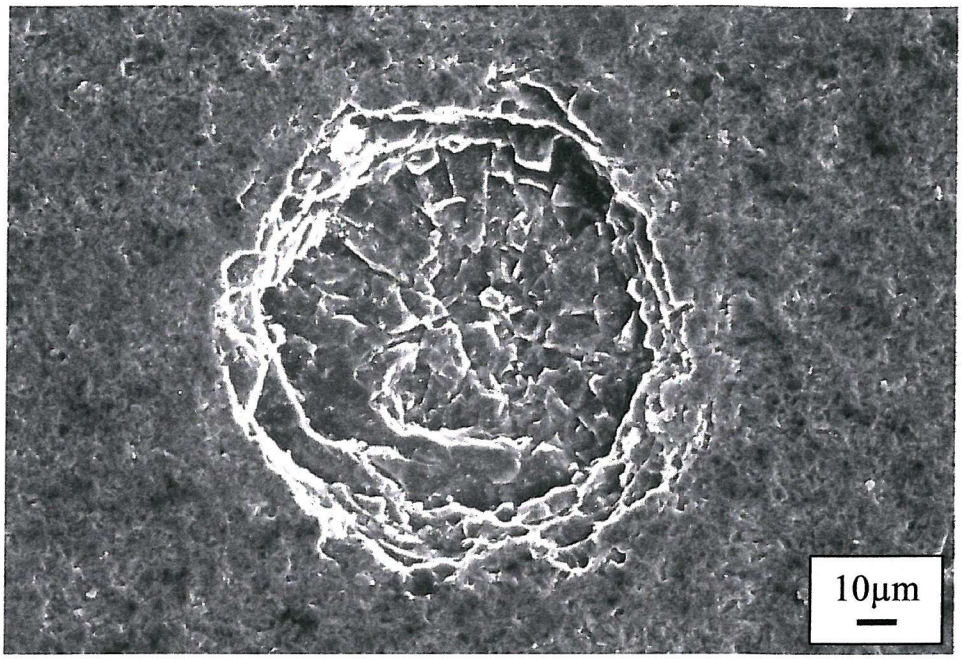

Fig. 11.7: Micrograph taken from a 26μm diamond coating tested at 250 m s^{-1} using 355-500μm sand for 1 minute showing a pin-hole.

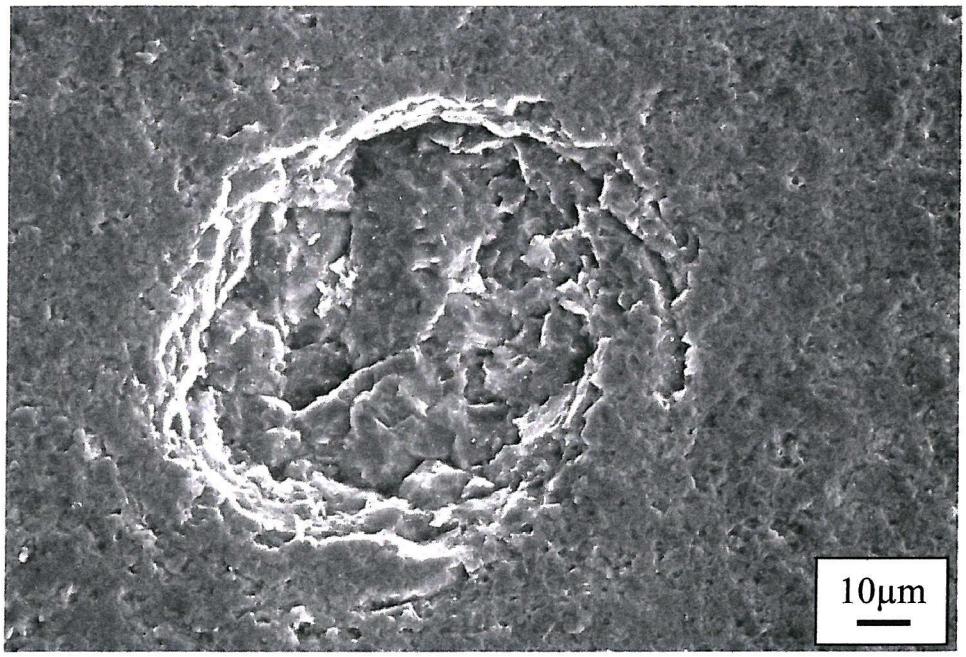

Fig. 11.8: Micrograph taken from a 30μm diamond coating tested at 250 m s^{-1} using 250-355μm sand for 30 minutes showing a circumferential crack.

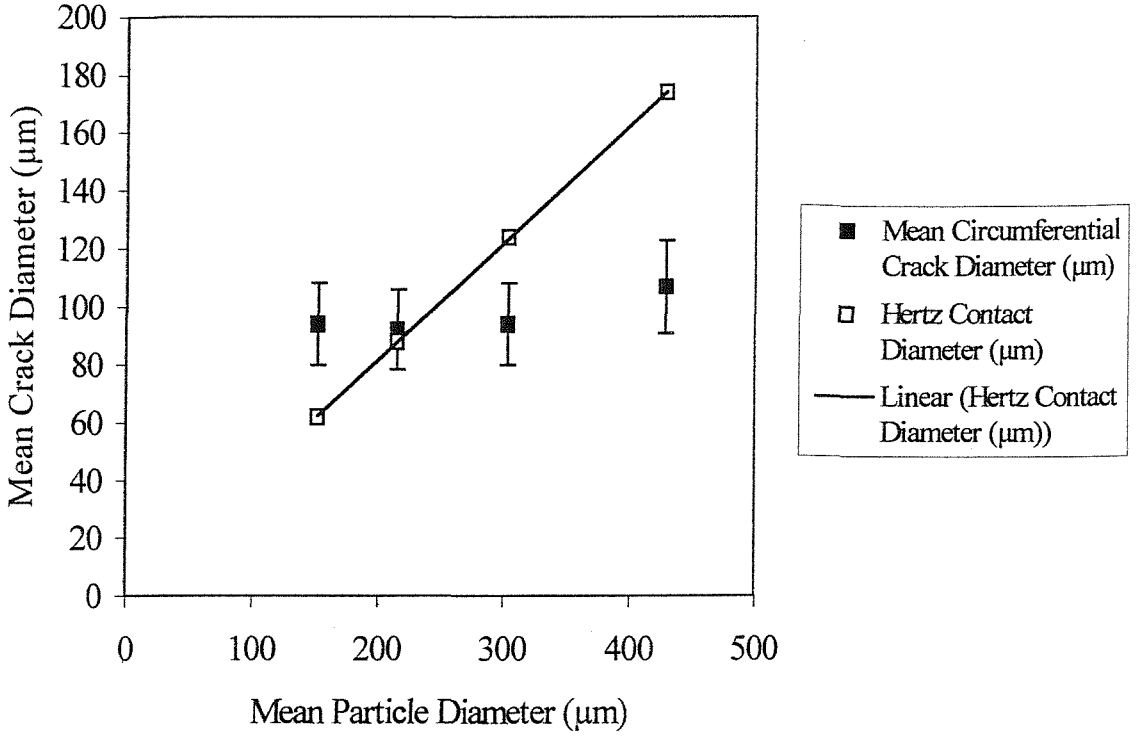

Fig. 11.9: Graph showing the relationship between Mean Particle Diameter and the Mean Circumferential Crack Diameter for 26-33μm diamond coatings on tungsten tested at 250 m s^{-1}. The Hertz contact diameter is also included for comparison. The error bars denote 1 standard deviation.

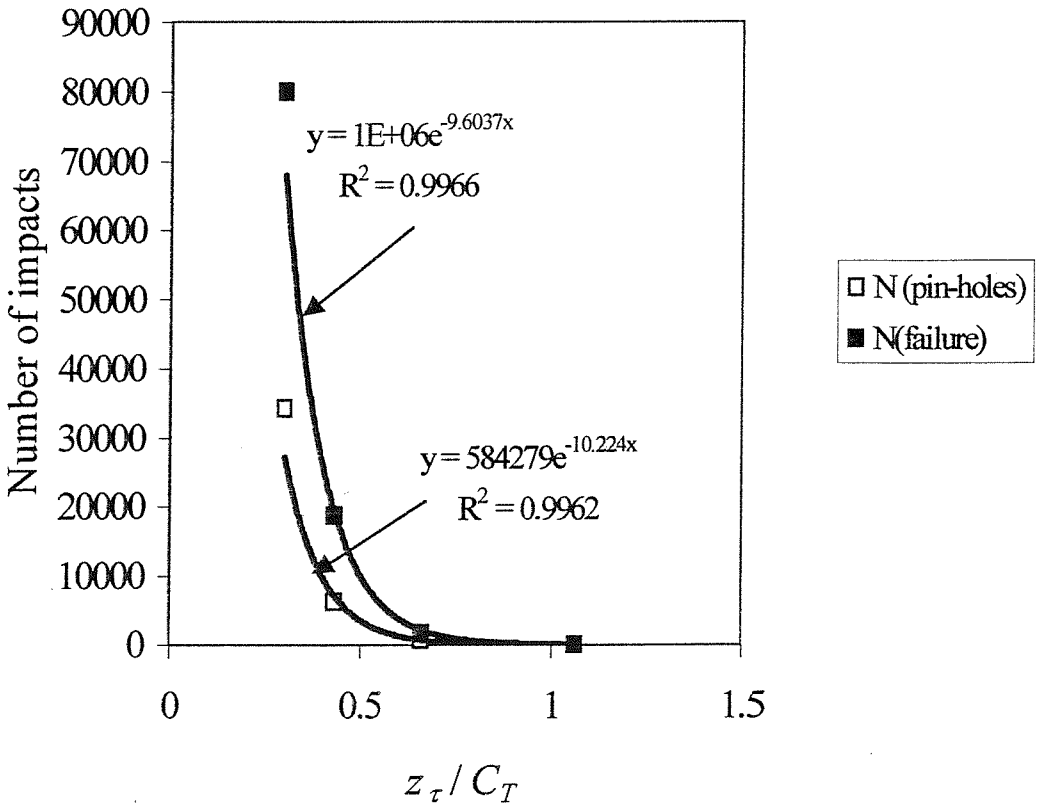

Fig. 11.10: Graph showing the effect of z_τ / C_T on the number of impacts for pin-hole formation and coating failure.

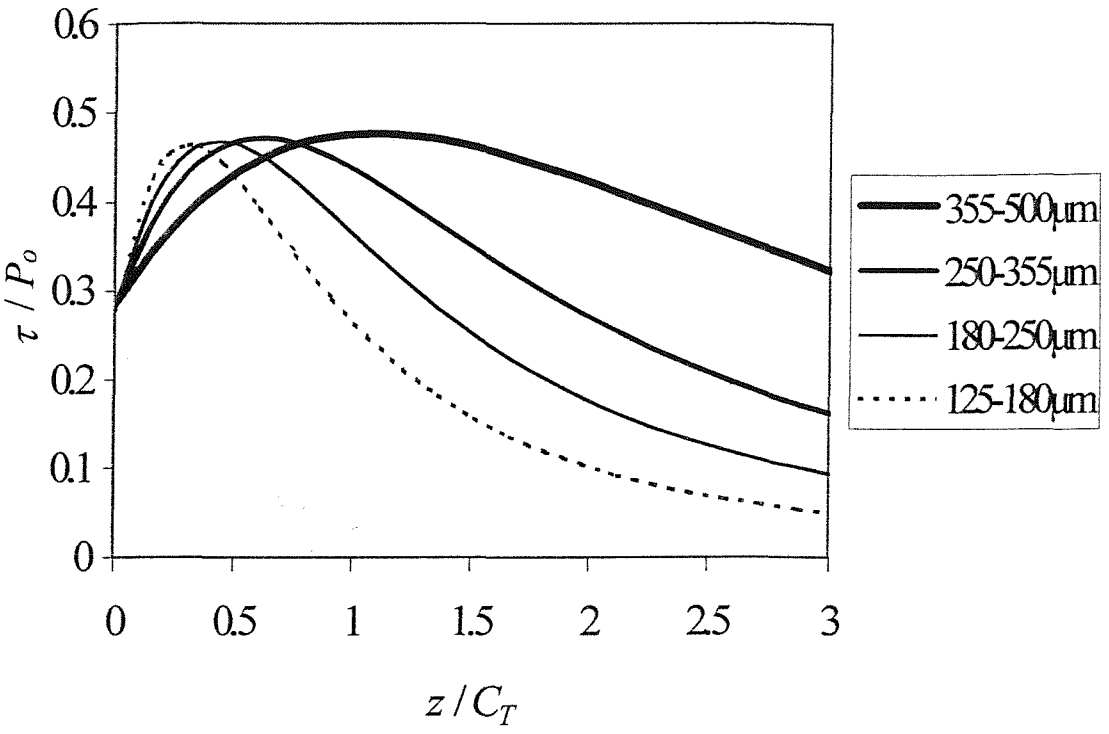

Fig. 11.11: Graph showing the variation of normalised shear stress τ_m / P_o, with normalised depth, z / C_T, for 26-33μm diamond coatings on tungsten erosion tested at 250 m s^{-1}. The four curves represent the four different diameter sand particles used in the erosion tests.

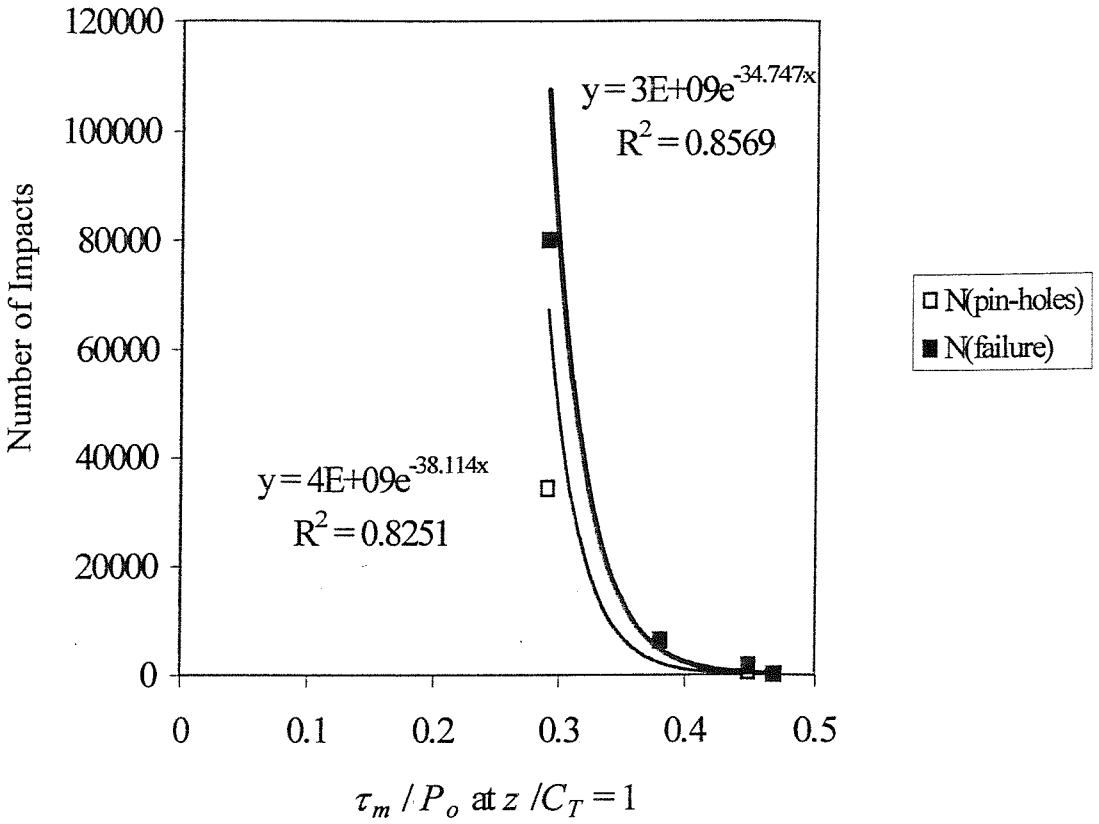

Fig. 11.12: Graph showing the relationship between Number of Impacts and τ_m / P_o at $z / C_T = 1$ for 26-33μm lapped diamond coatings erosion tested at 250 m s^{-1}.

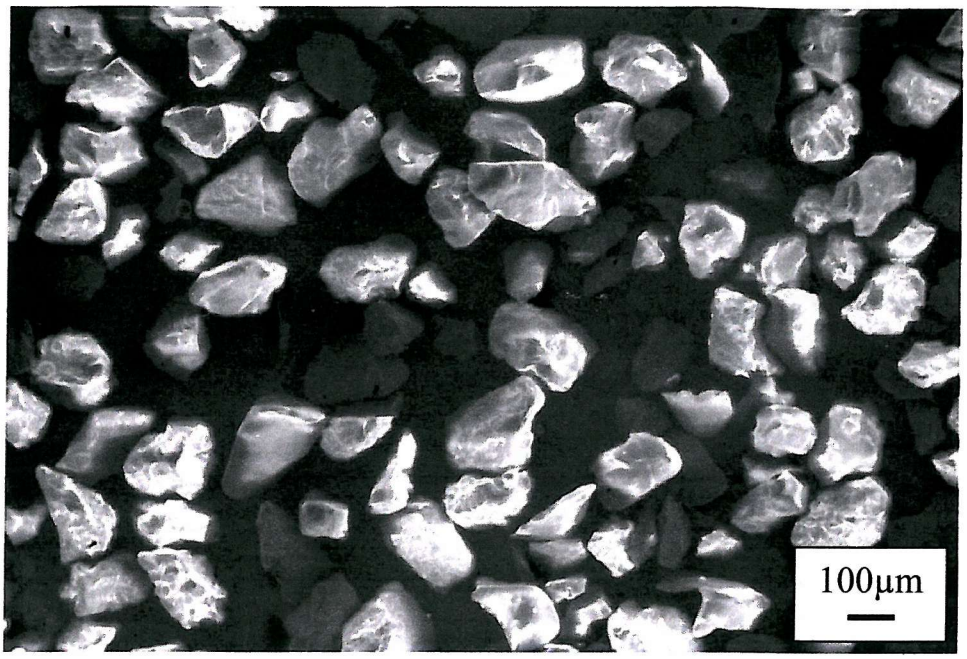

Fig. 11.13: Micrograph of unused 125-180μm sand.

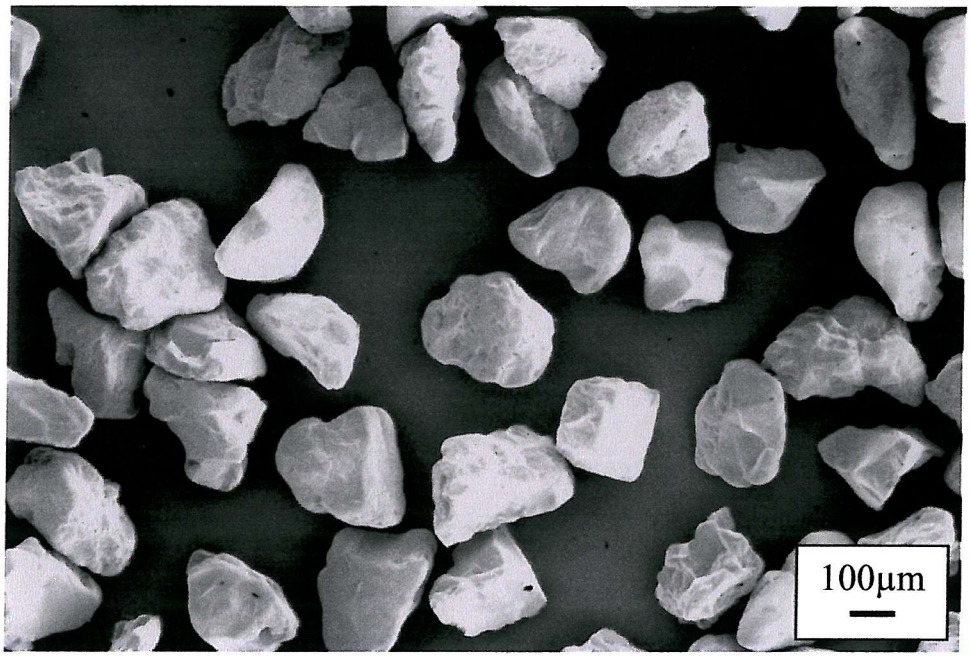

Fig. 11.14: Micrograph of unused 180-250μm sand.

Fig. 11.15: Micrograph of unused 250-355µm sand.

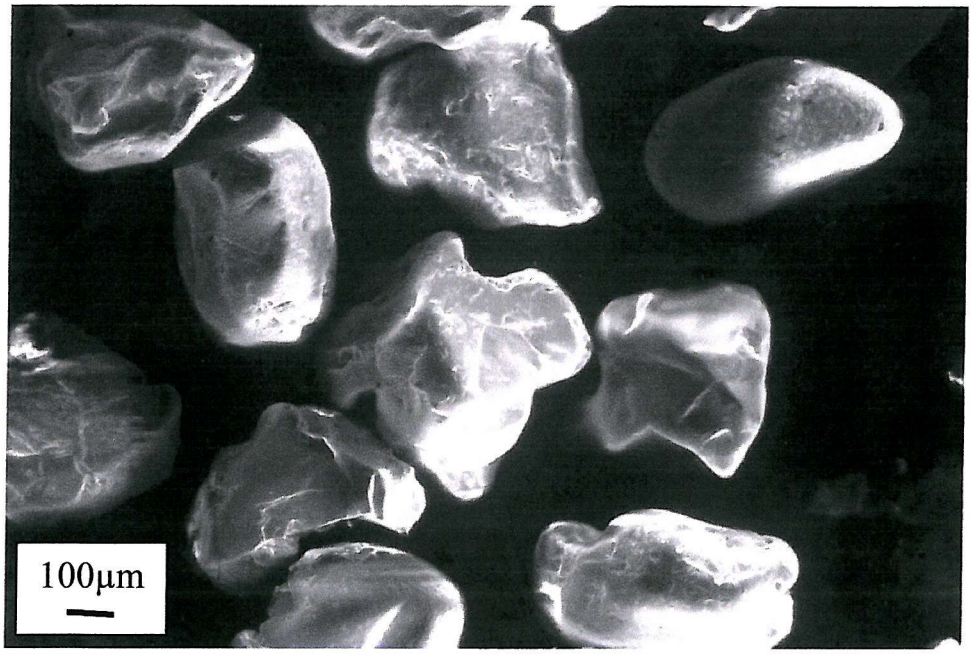

Fig. 11.16: Micrograph of unused 355-500µm sand.

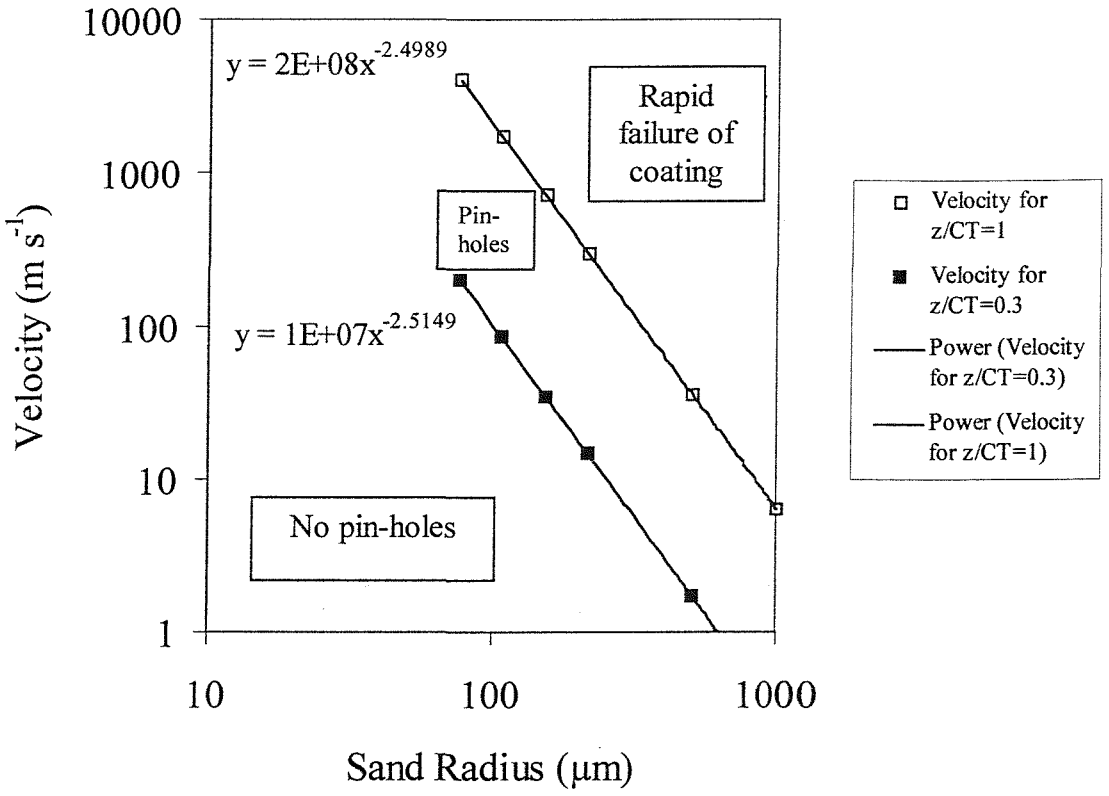

Fig. 11.17: Graph of Particle Impact Velocity vs Sand Radius for lapped 30μm diamond coatings on tungsten showing the theoretical velocities required for z_τ / C_T = 0.3 and 1.

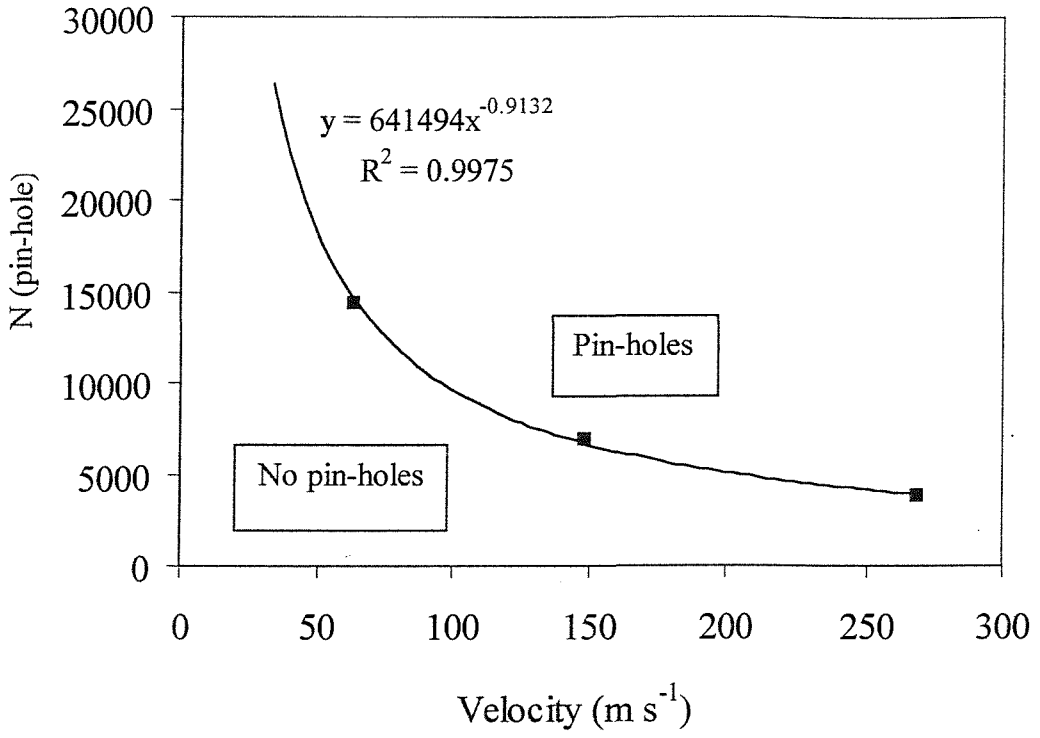

Fig. 11.18: Graph of particle velocity vs. the number of impacts per Hertzian zone required to generate pin-holes (*N (pin-hole)*) for 39-47μm lapped diamond coatings on tungsten.

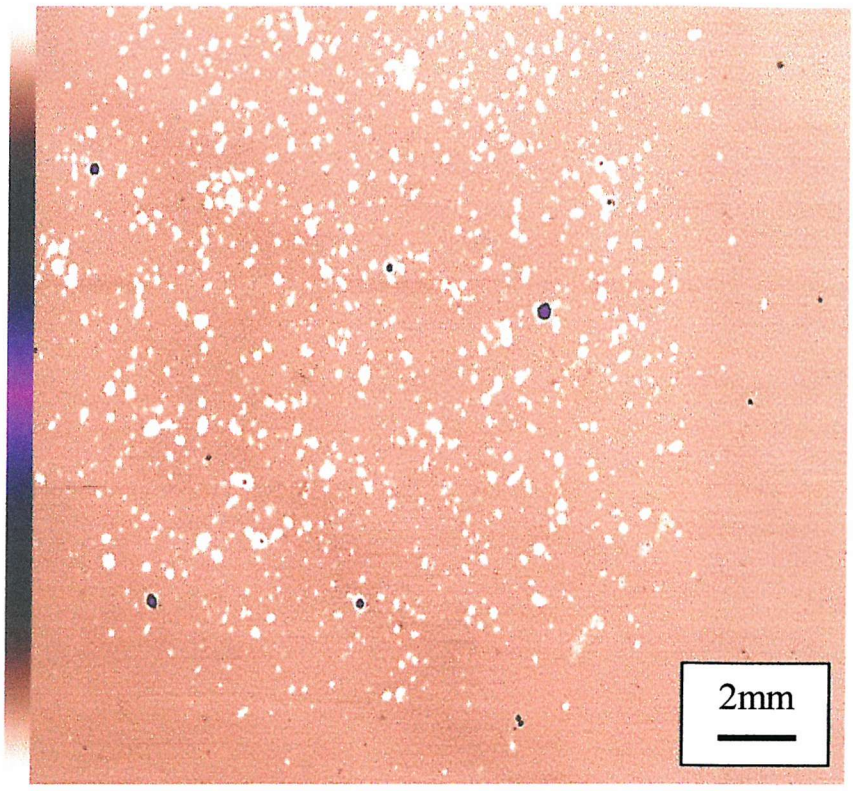

Fig. 11.19: SAM image of a lapped 60μm diamond coating erosion tested at 268 m s^{-1} for 5 hours at 268 m s^{-1} using Redhill Mix (mean diameter 194μm) sand.

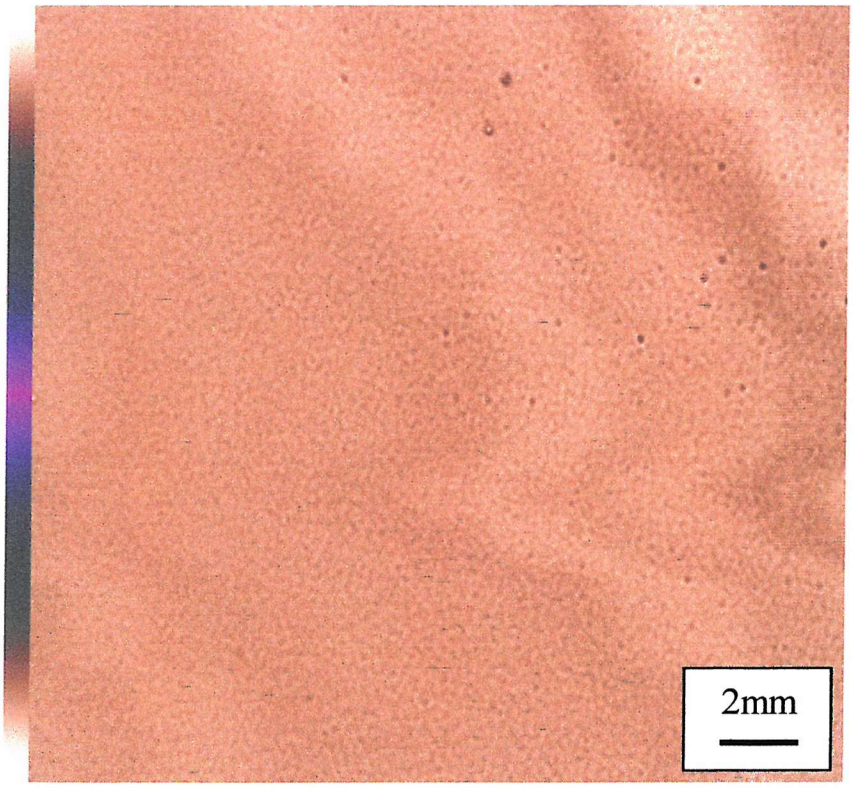

Fig. 11.20: SAM image of a lapped 60μm diamond coating erosion tested at 268 m s^{-1} for 5 hours at 268 m s^{-1} using 180-250μm sieved sand.

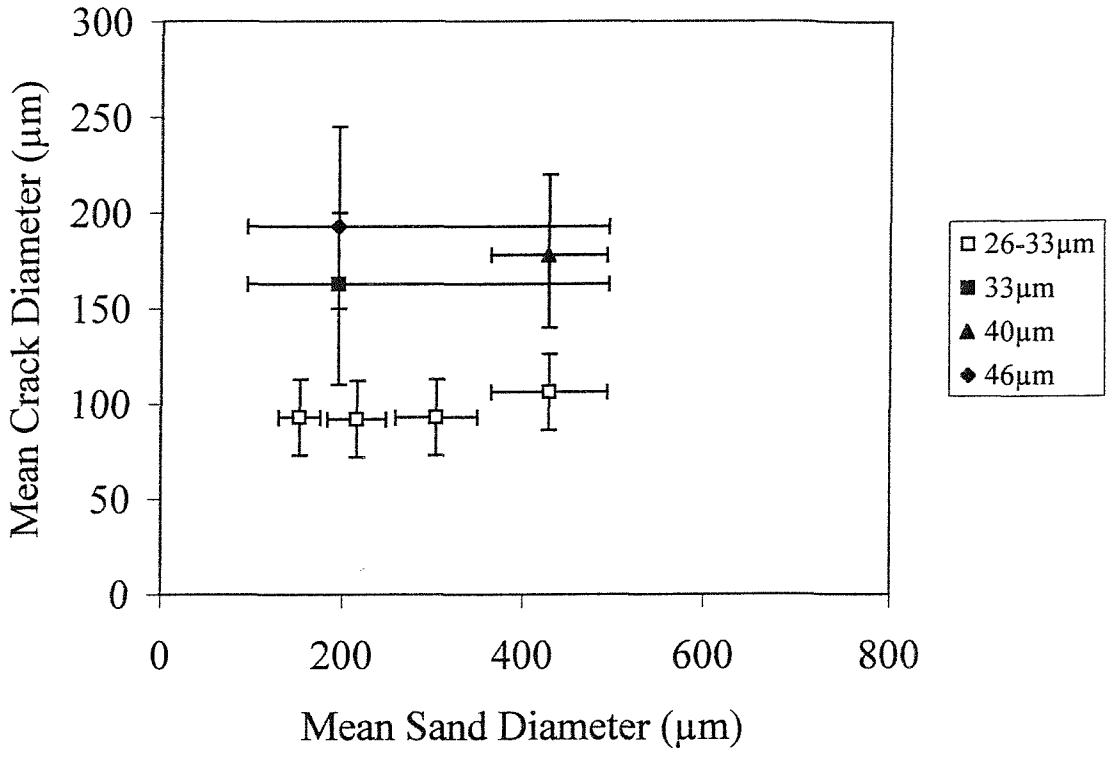

Fig. 11.21: Graph showing the influence of sand size on the mean circumferential crack diameter of diamond coatings eroded at velocities of 250 m s^{-1} (26-33µm and 40µm samples) and 268 m s^{-1} (33µm and 46µm coatings). The error bars denote the range of sand sizes (*x* axis) and the range of circumferential crack diameters (*y* axis).

12

CONCLUSIONS AND FURTHER WORK

This thesis has described the work carried out in investigating the performance and behaviour of CVD diamond coatings, 10-200μm in thickness, when subject to solid particle erosion. This work originated from a project evaluating the suitability of CVD diamond as an erosion-resistant hard facing on components such as choke valve trims. Some choke valve trims are susceptible to high velocity sand erosion, especially on high-pressure gas wells. For this reason, most of the work described has focused on high velocity erosion, the highest velocity being 268 m s^{-1}.

12.1 Characterisation

Characterisation of the coatings prior to testing has shown that the hardness and elastic modulus values of the diamond coatings are close to those of natural diamond. The mean values of these parameters are 80 GPa and 1157 GPa respectively; therefore they lie within the range of values normally quoted for diamond. Moreover, Raman spectroscopy of the growth surfaces of the coatings indicates that, on a purely qualitative basis, the amount of graphitic sp^2 bonding is almost negligible.

The Raman spectra also indicate the presence of compressive residual stresses in the coatings. For coatings greater than 60μm in thickness the mean residual stress is approximately 0.87 ±0.19GPa. Moreover, the results indicate that the variation of Raman peak shift over the thickness of interest is small and, therefore, the influence of residual stress on coating performance does not appear to be significant. This is mirrored in the erosion tests, which revealed that as the coating thickness is increased from 10 to 120μm, the time to failure increases significantly. This stress does not appear to be deleterious to coating adhesion or erosion resistance, and may actually be beneficial in preventing the nucleation of cracking at the surface. The residual stress is also thought to be the cause of the recorded fracture toughness values, which are almost double the average values recorded in the literature.

12.2 Performance

The erosion rates for lapped coatings between 60μm and 160μm in thickness are at least six to ten times lower than cemented tungsten carbide at a particle velocity of 268 m s^{-1}. The optimum coating thickness at 268 m s^{-1}, using 194μm diameter sand, appears to be in the region of 120μm where the erosion rate, V_u, was 1.31 ± 0.15 μm^3 $impact^{-1}$. This compares favourably with WC-7Ni, the most erosion–resistant grade of sintered tungsten carbide, which had a V_u of 25.6 μm^3 $impact^{-1}$. The test results also show good repeatability, being typically within the range of ±10%. However, the coatings had a tendency to fail catastrophically when large pieces became detached at the coating-substrate interface. The weakest part of the system is not the coating, but rather the bond between the coating and the substrate. Therefore, under erosive conditions, if the stress field generated by impacting particles extends to the interface, then debonding is likely to be the preferred mode of coating degradation. This emphasises the importance of the interface on coating behaviour.

The results also show that the erosion resistance of a lapped diamond coating is approximately three to four times greater than an as-grown coating for the same thickness. Moreover, the erosion rate is seen to increase with coating thickness for the as-grown coatings while the erosion rate is essentially independent of thickness for the lapped coatings over the range 60 to 160μm. The reason for this difference is that the surface roughness and grain size increase with thickness for the as-grown coatings. The higher contact stresses and the larger intrinsic flaws associated with these increases are thought to account for the higher erosion rates.

The superior mechanical properties of the diamond, particularly hardness, compared to the sand erodent meant that the damage to the particles exceeded that of the target material. This was confirmed by sand sieving, which showed that at 268 m s^{-1} the mean sand diameter reduced by 65% following impact with CVD diamond at 268 m s^{-1}. Evidence of plastic flow of the sand has also been recorded, which shows sand particles that have become smeared across the surface of the diamond. High-speed photography was also used to study the impact of the erodents onto the diamond surface. It enabled the impact event to be visualized, in particular allowing observation of sand fragmentation.

At the highest velocity employed, 268 m s^{-1}, diamond films ≤33μm in thickness are insufficient to withstand the stresses generated by sand particle impact at all velocities and fail rapidly and catastrophically. As the velocity is increased from 28 m s^{-1} to 268 m s^{-1}, the minimum coating thickness required to confer sufficient erosion resistance is increased. For instance, a 33μm coating was adequate at 28 m s^{-1}, though it began to fail before steady state erosion conditions were established at 268 m s^{-1}.

12.3 Erosion Mechanisms

In the high velocity erosion tests, the coatings are thought to erode by a three-stage mechanism. The stages are: (i) Initial period prior to steady state erosion where erosion of the coatings proceeds by a gradual chipping of grains; (ii) Steady state period where the micro-chipping is augmented by the nucleation of pin-holes and development of debonded areas at the coating-substrate interface; (iii) Failure of the coating.

No evidence of plastic deformation was seen on the coatings eroded by sand particles at any conditions employed during this programme. However, on samples impacted with diamond grit, damage features resembling elastic-plastic radial and lateral cracks were observed. Distorted Hertzian cracks were also seen on samples impacted with cubo-octahedral diamond grit. This indicates that Hertzian damage can be generated at these velocities when the properties of the erodent are closer to those of the target. Fragmentation of the diamond grit erodent occurred on impact; however, the extent of the degradation was much reduced compared with the silica sand erodent.

The most significant erosion features seen on eroded diamond coatings are the generation of microscopic "pin-holes". These are seen to nucleate during the test and grow and multiply with time until coating failure. Scanning Electron Microscopy studies have shown a number of pin-holes on a single sample and how they develop during an erosion test. They also provide important information on the stages involved in their formation. The figures show that the following steps occur in the development of a pin-hole:

- Formation of a circumferential crack on the growth (impact) surface of the coating;
- Initiation of damage in the central region within the circumferential crack;

- Growth of central damaged region both vertically (towards the coating-substrate interface) and laterally (towards the circumferential crack)

The pin-holes are parallel or conical in shape, having convergent sides, rather than divergent, as is seen with Hertzian cone cracks. The shape of the pin-holes resemble that of individual columnar grains in the diamond coatings. However, they can be as much as 10 times the size of individual grains. The circumferential cracks do not appear to be influenced by the grain boundaries in the diamond coatings.

The steady state erosion values are a function of the surface chipping process but it is the sub-surface damage, which leads to catastrophic failure of the coating along the interface. This appears to be a two-stage process with diamond-tungsten debonding leaving islands of well-bonded coating. Coating removal appears to be controlled by crack intersection in the substrate below the well-bonded islands. Therefore, the fracture toughness of the substrate may also influence the time to failure of the coating. Improved coating adhesion is likely to improve coating life.

Ultrasonic examination of coatings prior to erosion testing has revealed areas of imperfect bonding in the coating. This takes the form of porosity at the grain boundaries. It is thought that these can act as localised stress raisers and nucleation sites for further debonding during erosion.

Experimental work has indicated that the driving force for the debonding process is sub-surface shear stresses, which are generated in the coatings by particle impacts. The tests indicate that when the ratio of depth of maximum shear stress to coating thickness, z_τ / C_T, is less than 0.30, the time to produce pin-holes appears to be almost infinite.

Ultrasonic scanning proved to be a useful macroscopic tool in erosion studies of CVD diamond as it enabled non-destructive detection of sub-surface damage during the test. However, its resolution is insufficient to study smaller areas on a microscopic scale. For more localized examination, scanning acoustic microscopy (SAM), offered better resolution enabling individual pin-holes to be imaged. SAM images showed pin-holes to be located on localized areas of coating delamination. This provides supporting

evidence that they are formed by stress wave reflection and reinforcement rather than Hertzian stresses.

Coating delamination appears to be driven by sub-surface shear stresses, which are generated by the impact of the sand particles. When the maximum shear stress, τ_m, occurs close to the coating-substrate interface ($z_\tau / C_T \approx 1$), the coating fails rapidly and catastrophically. For this reason diamond coatings used in erosive environments must be sufficiently thick to ensure that τ_m is contained within the coating and is remote from the interface.

Tests conducted on 30μm diamond coatings at 250 m s^{-1}, demonstrated that when $z_\tau / C_T < 0.3$ pin-holes were not observed as the shear stress was insufficient to generate coating delamination. In these cases the life of the coating can be considered to be almost infinite. Under the erosion conditions employed, the critical shear stress required to promote delamination, appeared to be approximately 3.9 GPa.

The number of impacts necessary to generate pin-holes increased exponentially as the mean particle diameter, and hence the z/C_T ratio, was reduced. This provided further evidence that pin-holes represent visible evidence that coating delamination is taking place at the interface, which may result in catastrophic failure of the coating.

To summarise the main damage features seen in eroded CVD diamond coatings, Figure 12.1 shows a schematic diagram of the main features in the context of the coating microstructural features.

12.4 Modelling

The diameters of the circumferential cracks and pin-holes have been compared with the diameters predicted by Hertzian impact theory. The measured circumferential crack diameters are 2 to 4 times larger than the diameter predicted by Hertz. Moreover, a trend of increasing circumferential crack diameter with coating thickness, which is not predicted by Hertz, has also been noted. The measured pin-hole diameters appear to be independent of particle size and morphology. These findings, together with the SAM

images, suggest that the formation of circumferential cracks, the precursor to pin-holes, is related to stress wave reflection and interaction.

In attempting to model the erosion of diamond coatings, this study has shown that the multiplicity of parameters involved make this no small task. The SAM work has shown that circumferential cracks and pin-holes only form on regions of the coating that have become delaminated from high velocity sand particle impact. Without delamination, pin-holes cannot form. Therefore, the critical factor is maintaining the bond between coating and substrate. However, the SAM images have also shown that the absence of pin-holes does not always indicate that the coating remains well bonded to the substrate, especially for the thicker coatings, for instance the 120μm coating, where only one pin-hole was observed, though delamination was extensive.

The stress field in the coating resulting from an impact event is likely to consist of several constituent parts: these include the Hertzian contact stress, stress waves and the residual stress present in the coating. The adhesion strength and its variation with coating thickness, not measured as part of the present work, may also influence the stress field.

From a practical perspective, the work described in this thesis has suggested that the following factors are important in assessing the suitability of diamond coatings for use in erosive environments:

- Residual stress in the coating;
- Adhesion strength;
- Coating thickness – Thicker coatings will provide greater resistance to impact-induced delamination so long as the adhesion is adequate and residual stresses are not sufficient to assist coating delamination;
- Particle size and velocity – this will determine the size of the stress field;
- z_τ / C_T - should be as low as possible, ideally < 0.3. Conditions of $z_\tau / C_T \approx 1$ should be avoided;
- Porosity at interface (size and density) – a function of nucleation density;
- Surface roughness – lapped surfaces provide greater erosion resistance;

- Property mismatch between coating and substrate.

Alternatively, the list of factors affecting the integrity of diamond coatings subjected to sand erosion can be expressed by the following equation:

$$\text{Coating Integrity} = f(\sigma_t,\ \Gamma_c,\ N,\ z_\tau / C_T,\ P_o,\ E_s,\ K_{(inter)},\ a_{f(inter)},\ \theta)$$

Where σ_t is the total residual stress in coating, Γ_c is the Interfacial toughness, N is the number of impacts, z_τ / C_T is the normalised depth of maximum shear stress (itself a function of particle size and velocity), P_o is the maximum contact pressure, E_s is the elastic modulus of the substrate, $K_{c\ (inter)}$ stress intensity at coating-substrate interface (itself a function of defect size and shape), $a_{f(inter)}$ is the defect size at the interface and θ is the Impact angle. $\psi_{(inter)}$ is the defect density at the coating-substrate interface.

In the same way, the factors affecting the formation of circumferential cracks on the growth surface of the diamond coatings can also be summarised in the form of an equation:

$$\text{Circumferential Crack Formation} = f(d_g,\ C_T,\ \rho_e c_e V,\ K_{1c},\ \theta,\ N,\ \psi_c,\ \chi)$$

Where d_g, is the grain size, C_T, is the coating thickness, $\rho_e c_e V$ is the impact pressure similar to the water hammer pressure, K_{1c} the fracture toughness of the coating (itself a function of the flaw size), ψ_c is the defect density in the coating and χ is the area of delamination

12.5 Novelty

Overall, the work contained in this thesis represents an advance in understanding the erosion behaviour of CVD diamond coatings, In particular it is the first time that thick (>20μm) coatings deposited directly onto substrates, as opposed to free-standing diamond, have been investigated under the conditions of solid particle erosion. More importantly, tests on these thicker coatings have revealed damage features, (circumferential cracks and pin-holes) that have not been reported in the literature. The author has attempted to explain the causes for the formation of these pin-holes and has

found a trend of increasing pin-hole diameter with coating thickness. This cannot be explained by Hertzian theory and appears to be closer to that predicted by stress wave interaction, which has been used to explain damage features observed in liquid impact studies.

This thesis has also described the use of new techniques, taper polishing, ultrasonic scanning and scanning acoustic microscopy, which have not previously been used for this purpose. These three methods have enabled advances to be made in understanding the development of sub-surface damage during the erosion process.

12.6 Further Work

The nature of scientific research is that it often poses as many questions as it answers. This situation is also true in the present case. Therefore, the final section in this thesis seeks to highlight subjects that could not be explored in the current work but are, nevertheless, worth considering by future researchers.

The behaviour of diamond coatings on other substrates, for instance SiC, should be investigated. This should provide more information on the influence of the substrate on the erosion performance; of particular interest is the question of whether the circumferential cracks and pin-holes are observed. Further work using different erodents should also be continued, for instance extended tests using diamond grit. This should provide more information on diamond coatings and their response to high velocity particle impact.

The circumferential cracks, the precursors to pin-holes, have been shown to be formed on the growth surfaces of the coating. However, it would be of interest to identify the measure the size and distribution of surface flaws. Moreover, it is also desirable to measure the size of the grain boundary pores at the coating-substrate interface in the untested condition. This task could not be accomplished with the scanning acoustic microscope. It is thought that it could be done ultrasonic force microscopy (UFM). Transmission electron microscopy (TEM) could also be used to study the microstructure and defects in the interior of the coatings.

The scanning acoustic microscope has been found to be a useful technique in the detection of sub-surface damage at the coating-substrate interface. However, a more quantitative analysis of the progression of debonding under repeated particle impacts would be useful in order to determine if there is a critical amount of debonding, for each thickness, which can lead to catastrophic coating failure. A series of acoustic images of coatings could be taken and the percentage of debonding calculated by image analysis.

Quantitative acoustic microscopy could also be used to evaluate the size and population of surface flaws in the coatings. This work could also be used to evaluate the residual stress.

The role of reflected stress waves (from delaminated regions of the coating) in the formation of circumferential cracks has been shown in this thesis. However, there are still unknown aspects of the impact process. Modelling the process using Finite Element Analysis could assist in the task of understanding the stress fields present in the coating.

Single impact studies using a variety of particles from sand to diamond could also yield more information on the damage features. In order that the damage sites be more easily observed this work should be performed on a polished, rather than a lapped, surface.

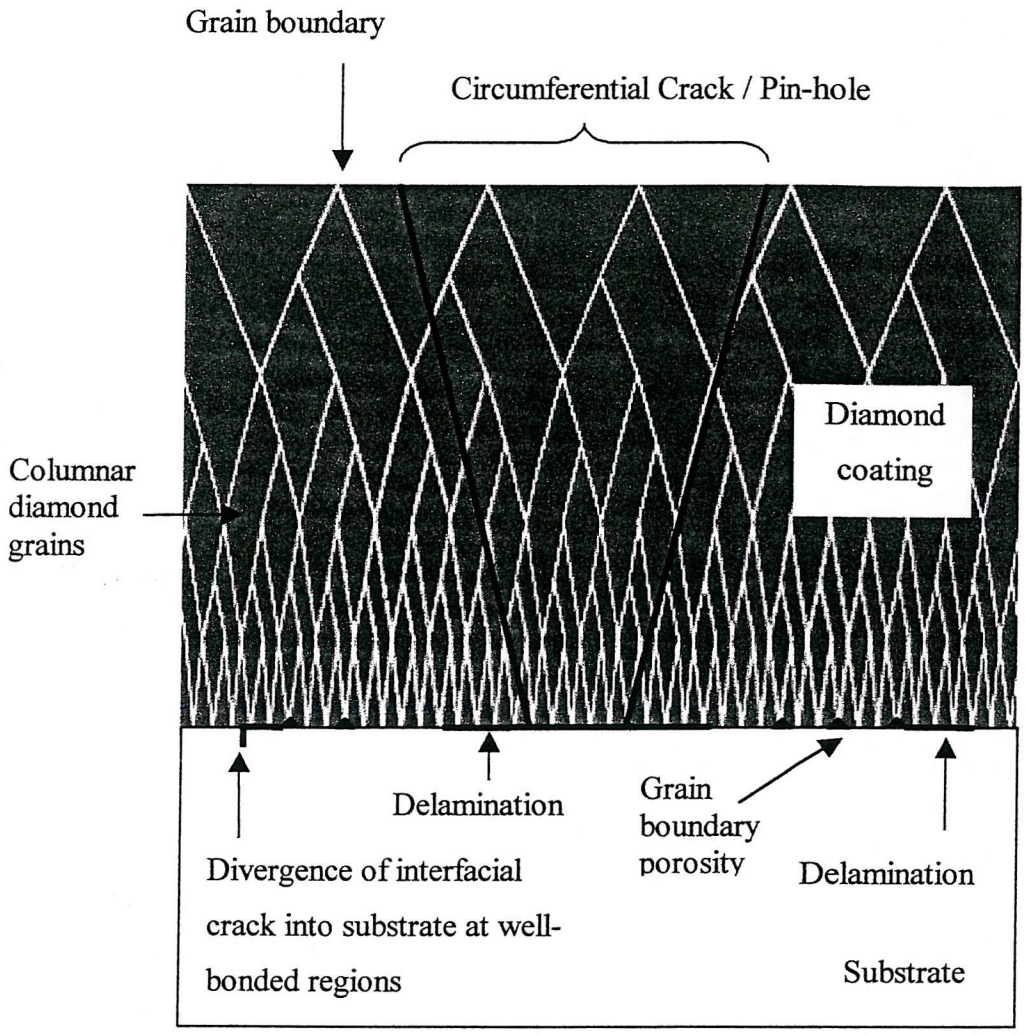

Fig. 12.1: Schematic diagram summarising the main damage features seen in eroded CVD diamond coatings in the context of the coating microstructure.

REFERENCES

CHAPTER 1

1. *Encyclopaedia Britannica*, 15th ed., Vol. 3 (1979), 519-520.
2. G.E. Harlow (ed), *The Nature of Diamonds*, Cambridge University Press (1998).
3. R.M. Hazen, *The Diamond Makers*, Cambridge University Press (1999).
4. D.W. Wheeler, R.J.K. Wood, S. Atwell, D. Harrison, "Application of CVD diamond to enhance choke valve life in erosive duties", to be submitted to *Wear*.

CHAPTER 2

1. ASTM G40 *Standard Terminology Relating to Wear and Erosion.*
2. T.S. Eyre, "Friction and wear control in industry", *Met. Mater.*, 7, (1991), 143-148.
3. S. Maw, "Industrial Wear Survey: Guide to wear testing requirements", Presented at UK Forum on Friction and Wear Testing, NPL, Teddington, 29th Oct. 1997.
4. N.K. Bourne, J.E. Field, "A high-speed photographic study of cavitation damage", *J. Appl. Phys.*, 78 (1995), 4423-4427.
5. J.E. Field, "Liquid impact erosion", *Phys. Bull.*, 37 (1986), 70-72.
6. M.B. Lesser, J.E. Field, "The impact of compressible liquids", *Ann. Rev. Fluid Mech.*, 15 (1983), 97-122.
7. J.E. Field, "High-speed photography", *Contemp. Phys.*, 24 (1983), 439-459.
8. J.P. Dear, J.E. Field, "High-speed photography of surface geometry effects in liquid / solid impact", *J. Appl. Phys.*, 63 (1988), 1015-1021.
9. J.E. Field, "Physics of liquid impact, shock wave interactions with cavities, and the implications to shock wave lithotripsy", *Phys. Med. Biol.*, 36 (1991), 1475-1484.
10. J.E. Field, D.A. Gorham, D.S. Rickerby, "High speed liquid jet and drop impact on brittle targets", *Erosion: Prevention and Useful Applications*, ASTM STP 664 (1979), 298-319.
11. F.P. Bowden, J.E. Field, "The brittle fracture of solids by liquid impact, by solid impact, and by shock", *Proc. R. Soc. Lond.*, A282 (1964), 331-352.
12. J.E. Field, I.M. Hutchings, "Impact erosion processes", Paper presented at 3rd Conf. Mech. Prop. High Rates of Strain, Oxford, *Inst. Phys. Conf. Ser.*, 70 (1984), 349-371.

13. A.A. Fyall, "Single impact studies with liquids and solids", *Proc. 2nd Int. Conf. On Rain Erosion and Allied Phenomena*, Meersburg, ed. A.A. Fyall, R.B. King (1967), 563-591.
14. L.L. Wang, J.E. Field, Q. Sun, J. Liu, "Surface damage of polymethylmethacrylate plates by ice and nylon ball impacts", *J. Appl. Phys.*, 78 (1995), 1643-1649.
15. R.H. Telling, G.H. Jilbert, J.E. Field, "The erosion of aerospace materials by solid particle impact", *Proc. SPIE*, 3060 (1997), 56-67.
16. A.G. Evans, T.R. Wilshaw, "Dynamic solid particle damage in brittle materials: an appraisal", *J. Mater. Sci.*, 12 (1977), 97-116.
17. A.J. Moore, R.J.K. Wood, "The erosive wear behaviour of pipeline materials in slurry flow streams", Unpublished.
18. H. M. Clark, "On the impact rate and impact energy of particles in a slurry pot erosion tester", *Wear*, 147 (1991), 165-183.
19. J.E. Goodwin, W. Sage, G.P. Tilly, "Study of erosion by solid particles", *Proc. Instn. Mech. Engrs.*, 184 (1969-70), 279-289.
20. R.A. Vaughan, A. Ball, "Erosion processes for hard materials subjected to impact impact by different erodents", *J. Hard Mater.*, 2 (1991), 257-269.
21. I.M. Hutchings, *Tribology: Friction and Wear of Engineering Materials*, Edward Arnold (1992).
22. M.E. Gulden, "Correlation of experimental erosion data with elastic-plastic impact models", *J. Am. Ceram. Soc.*, 64 (1981), C59-C60.
23. P.H. Shipway, I.M. Hutchings, "The role of particle properties in the erosion of brittle materials", *Wear*, 193 (1996), 105-113.
24. S. Wada, "Effects of hardness and fracture toughness of target materials and impact particles on erosion of ceramic materials", *Erosion of Ceramic Materials* (ed. J.E. Ritter), Trans Tech (1992), 51-74.
25. I.M. Hutchings, "Transitions, threshold effects and erosion maps", *Erosion of Ceramic Materials* (ed. J.E. Ritter), Trans Tech (1992), 75-92.
26. B.J. Hockey, S.M. Wiederhorn, H. Johnson, "Erosion of brittle materials by solid particle impact", *Fracture Mechanics of Ceramics*, 3 (1978), 379-402.
27. J.L. Routbort, R.O. Scattergood, E.W. Kay, "Erosion of silicon single crystals", *J. Am. Ceram. Soc.*, 63 (1980), 635-640.
28. J.E. Field, Q. Sun, H. Gao, G.H. Jilbert, "Solid particle erosion of IR-transmitting materials and diamond composites", *Wear*, 186-187 (1995), 195-202.

29. A. Franco, S.G. Roberts, "The effect of impact angle on the erosion rate of polycrystalline α-Al_2O_3", *J. Eur. Ceram. Soc.*, 18 (1998), 269-274.
30. I.M. Finnie, "Erosion of surfaces by solid particles", *Wear*, 3 (1960), 87-103.
31. R.J.K. Wood, D.W. Wheeler, "Design and performance of a high velocity air-sand jet impingement erosion facility", *Wear*, 220 (1998), 95-112.
32. P.H. Shipway, I.M. Hutchings, "A method for optimising the particle flux in erosion testing with a gas-blast apparatus", *Wear*, 174 (1994), 169-175.
33. S. Turenne, M. Fiset. J. Masounave, "The effect of sand concentration on the erosion of materials by a slurry jet", *Wear*, 133 (1989), 95-106.
34. I.G. Wright, D.K. Shetty, A.H. Clauer, "Slurry erosion of WC-Co cermets and its relationship to materials properties", *Proc. 6th Int. Conf. Erosion by Liquid and Solid Impact*, Cambridge (1983), paper 63.
35. R.C. Pennefather, R. Hutchings, A. Ball, "Erosion mechanisms in cemented carbides subjected to solid particle erosion", *Proc. 7th Int. Conf. Erosion by Liquid and Solid Impact*, Cambridge (1987), paper 60.
36. I.M. Finnie, J. Wolak, Y. Kabil, "Erosion of metals by solid particles", *J. Mater.*, 2 (1967), 682-700.
37. H. Reshetnyak, J. Kuybarsepp, "Mechanical properties of hard metals and their erosive wear resistance", *Wear*, 177 (1994), 185-193.
38. A.W. Ruff, S.M. Wiederhorn, "Erosion by solid particle impact", *Treatise on Materials Science,* 16 (1979) (ed. C.M. Preece), 69-126.
39. R.J. Anton, G. Subhash, "Dynamic Vickers indentation of brittle materials", *Wear*, 239 (2000), 27-35.
40. S. van der Zwaag, J.E. Field, "The effect of thin hard coatings on the Hertzian stress field", *Phil. Mag.*, A46 (1982), 133-150.
41. P. Hedenqvist, M. Olsson, "Solid particle erosion of titanium carbide coated high speed steel", *Tribol. Int.*, 23 (1990), 173-181.
42. C.A. Brookes, L. Y. Zhang, P.W. May, "On the mechanical integrity ratio of diamond coatings", *Diamond Relat. Mater.*, 6 (1997), 348-352.
43. S. van der Zwaag, J.E. Field, "Indentation and liquid impact studies on coated germanium", *Phil. Mag.*, A48 (1983), 767-777.
44. A. Pajares, L. Wei, B.R. Lawn, C.C. Berndt, "Contact damage in plasma-sprayed alumina-based coatings", *J. Am. Ceram. Soc.*, 79 (1996), 1907-1914.

45. K. Komvopoulos, "Finite element analysis of a layered elastic solid in normal contact with a rigid surface", *J. Tribol.*, 110 (1988), 477-485.
46. K. Komvopoulos, "Elastic-plastic finite element analysis of indented layered media", *J. Tribol.*, 111 (1989), 430-439.
47. C.S.J. Pickles, J.R. Brandon, S.E. Coe, R.S. Sussmann, "Factors influencing the strength of chemical vapour deposited diamond", *Diamond Films* (1999), 435-454.
48. M. Godet, Y. Berthier, M.C. Dubourg, L. Vincent, "Contact mechanics: needs for broader applications", *J. Phys. D: Appl. Phys.*, 25 (1992), A273-A278.
49. J. Valli, " A review of adhesion test methods for thin hard coatings", *J. Vac. Sci. Technol.*, A4 (1986), 3007-3014.
50. P.J. Burnett, D.S. Rickerby, "The erosion behaviour of TiN coatings on steels", *J. Mater. Sci.*, 23 (1988), 2429-2443.
51. S.Wuttiphan, A. Pajares, B.R. Lawn, C.C. Berndt, "Effect of substrate and bond coat on contact damage in zirconia-based plasma-sprayed coatings", *Thin Solid Films*, 293 (1997), 251-260.
52. U. Wiklund, J. Gunners, S. Hogmark, "Influence of residual stresses on fracture and delamination of thin hard coatings", *Wear*, 232 (1999), 262-269.
53. A.G. Evans, J.W. Hutchinson, "On the mechanics of delamination and spalling in compressed films", *Int. J. Solids Structures*, 20 (1984), 455-466.
54. A.G. Evans, M.D. Drory, M.S. Hu, "The cracking and decohesion of thin films", *J. Mater. Res.*, 3 (1988), 1043-1049.
55. P.C. Jindal, D.T. Quinto, G.J. Wolfe, "Adhesion measurements of chemically vapour deposited and physically vapour deposited hard coatings on WC-Co substrates", *Thin Solid Films*, 154 (1987), 361-375.
56. J. Gunners, A. Alahelisten, "Thermal stresses in diamond coatings and their influence on coating wear and failure", *Surf. Coat. Technol.*, 80 (1996), 303-312.
57. H. Windischmann, K.J. Gray, "Stress measurement of CVD diamond films", *Diamond Relat. Mater.*, 4 (1995), 837-842.
58. S.R. Sails, D.J. Gardiner, M. Bowden, "Raman spectroscopy of diamond films - spatial variations of diamond quality", *Proc. SPIE*, 2286 (1994), 239-246.
59. D.S. Knight, W.B. White, "Characterisation of diamond films by Raman spectroscopy", *J. Mater. Res.*, 4 (1989), 385-393.
60. H. Boppert, J. Van Straaten, I.F. Silvera, "Raman spectra of diamond at high pressures", *Phys. Rev.*, B32 (1985), 1423-1425.

61. N.C. Burton, J.W. Steeds, G.M. Meaden, Y.G. Shreter, J.E. Butler, "Strain and microstructure variation in grains of CVD diamond film", *Diamond Relat. Mater.*, 4 (1995), 1222-1234.

62. C.D.O. Pickard, T.J. Davis, W.N. Wang, J.W. Steeds, "Mapping crystalline quality in diamond films by micro-Raman spectroscopy", *Diamond Relat. Mater.*, 7 (1998), 238-242.

63. C.D.O. Pickard, T.J. Davis, A.C. Gilmore, P. Greenwood, C.A. Brookes, E.J. Brookes, J.E. Butler, J.W. Steeds, "Mapping damage profiles in diamond with Raman spectroscopy", Diamond Conference, Royal Holloway (1998) unpublished.

64. R. Ramesham, R.F. Askew, M.F. Rose, "Adhesion and Young's modulus of CVD diamond thin films grown on various substrates", *Mat. Res. Soc. Symp. Proc.*, 383 (1995), 217-221.

65. S.S. Chiang, D.B. Marshall, A.G. Evans, "A simple method for adhesion measurements", *Surfaces and Interfaces in Ceramic and Ceramic-Metal Systems*, (ed. J. Pask, A.G. Evans), Plenum Press, New York (1981), 603-617.

66. P.K. Mehrota, D.T. Quinto, "Techniques for evaluating mechanical properties of hard coatings", *J. Vac. Sci. Technol.*, A3 (1985), 2401-2405.

67. P.R. Chalker, S.J. Bull, D.S. Rickerby, "A review of the methods for the evaluation of coating-substrate adhesion", *Mater. Sci. Eng.*, A140 (1991), 583-592.

68. M.D. Drory, J.W. Hutchinson "An indentation test for measuring adhesion toughness for thin films under high residual compression with application to diamond films", *Mat. Res. Soc. Symp. Proc.*, 383 (1995), 173-182.

69. K. Mallika, R. Komanduri, "Diamond coatings on cemented tungsten carbide tools by low pressure microwave CVD", *Wear*, 224 (1999), 245-266.

70. M.D. Drory, J.W. Hutchinson, "Measurement of the adhesion of a brittle film on a ductile substrate", *Proc. R. Soc. Lond.*, A452 (1996), 2319-2341.

71. D. Schneider, B. Schultrich, P. Burck, H-J Scheibe, G. Jorgensen, M. Lahres, J. Karner, "Non-destructive characterisation of CVD diamond films on cemented carbide cutting tools", *Diamond Relat. Mater.*, 7 (1998), 589-596.

72. H. Liu, D.S. Dandy, "Studies on nucleation process in diamond CVD: an overview of recent developments", *Diamond Relat. Mater.*, 4(1995), 1173-1188.

73. H. Makita, T. Yara, N. Jang, K. Nishimura, A Hatta, T. Ito, A. Hiraki, "Seeding with purified ultrafine diamond particles for diamond synthesis by CVD",

Applications of Diamond Films and Related Materials: 3rd Int. Conf. (1995), 333-336.

74. R. Stockel, M. Stammler, K. Janischowsky, J. Ley, M. Albrecht, H.P. Strunk, "Diamond nucleation under bias conditions", *J. Appl. Phys.*, 83(1) (1998), 531-539.
75. C.R. Shi, Y. Avygal, S. Dirnfeld, A. Hoffman, A. Fayer, R. Kalish, "Growth of a well-adhering diamond coating on sintered tungsten", *Diamond Relat. Mater.*, 4 (1995), 1079-1087.
76. B. Zhang, L. Zhou, "Effect of sandblasting on adhesion strength of diamond coatings", *Thin Solid Films*, 307 (1998), 21-28.
77. R.K. Singh, D.R. Gilbert, J. Fitzgerald, S. Harkness, D.G. Lee, "Engineered interfaces for adherent diamond coatings on large thermal expansion coefficient mismatched surfaces", *Science*, 272 (1996), 396-398.
78. B. Spitsyn, L.L. Bouilov, B.V. Derjaguin, "Vapour growth of diamond on diamond and other surfaces", *J. Cryst. Growth.*, 52 (1981), 219-226.
79. M. Nesladek, K. Vandierendonck, C. Quaeyhaegens, M. Kerkhofs, L.M. Stals, "Adhesion of diamond coatings on cemented carbides", *Thin Solid Films*, 270 (1995), 184-188.
80. I.Y. Konyashin, M.B. Guseva, "Thin films comparable with WC-Co cemented carbides as underlayers for hard and superhard coatings: the state of the art", *Diamond Relat. Mater.*, 5 (1996), 575-579.
81. M. Nesladek, J. Spinnewyn, C. Asinari, R. Lebout, R. Lorent, "Improved adhesion of CVD diamond films to steel and WC-Co substrates", *Diamond Relat. Mater.*, 3 (1993), 98-104.
82. M. Kohzaki, K. Higuchi, S. Noda, K. Uchida, "Large area diamond deposition and brazing of the diamond films on steel substrates for tribological applications", *Diamond Relat. Mater.*, 2 (1993), 612-616.
83. J.S. Hansen, "Relative erosion resistance of several materials", *Erosion: Prevention and Useful Applications, ASTM STP664* (ed. W.F. Adler), American Society for Testing and Materials (1979), 148-162.
84. D. Rats, L. Bimbault, L. Vandenbulcke, R. Herbin, K.F. Badawi, "Crystalline quality and residual stresses in diamond layers by Raman and x-ray diffraction analyses", *J. Appl. Phys.*, 78(8) (1995), 1-8.
85. H.C. Meng, K.C. Ludema, "Wear models and predictive equations: their form and content", *Wear*, 181-183 (1995), 443-457.

86. B.R. Lawn, M.V. Swain, "Microfracture beneath point indentations in brittle solids", *J. Mater. Sci.*, 10 (1975), 113-122.

87. S.P. Timoshenko, J.N. Goodier, *Theory of Elasticity*, McGraw-Hill, New York, 3rd ed. (1970).

88. S.C. Hunter, "Energy absorbed by elastic waves during impact", *J. Mech. Phys. Solids*, 5 (1957), 162-171.

89. Z. Feng, Y. Tzeng, J.E. Field, "Solid particle impact on CVD diamond films", *Thin Solid Films*, 212 (1992), 35-42.

90. K.L. Johnson, J.J. O'Connor, A.C. Woodward, "The effect of indenter elasticity on the Hertzian fracture of brittle materials", *Proc. R. Soc. Lond.*, A334 (1973), 95-117.

91. S.M. Wiederhorn, B.R. Lawn, Strength degradation of glass resulting from impact with spheres", *J. Am. Ceram. Soc.*, 60 (1977), 451-458.

92. M.M. Chaudhri, S.M. Walley, "Damage to glass surfaces by the impact of small glass and steel spheres", *Phil. Mag.*, A37 (1978), 153-165.

93. J.E. Field, Q. Sun, D. Townsend, "Ballistic impact of ceramics" Paper presented at Int. Conf. Mech. Prop. Materials at High Rates of Strain, Oxford, *Inst. Phys. Conf. Ser.*, 102 (1989), 387-394.

94. R.H. Telling, J.E. Field, "The fracture and erosion of diamond", Diamond Conference, Royal Holloway (1998), unpublished.

95. R.H. Telling, *The Fracture of Natural and Synthetic Diamond*, PhD thesis, University of Cambridge (1999).

96. M.M. Chaudhri, C. Liangyi, "The orientation of the Hertzian cone crack in soda-lime glass formed by oblique dynamic and quasi-static loading with a hard sphere", *J. Mater. Sci.*, 24 (1989), 3441-3448.

97. Y. Akimune, "Oblique impact of spherical particles onto silicon nitride", *J. Am. Ceram. Soc.*, 73 (1990), 3607-3610.

98. A.G. Evans, M.E. Gulden, M. Rosenblatt, "Impact damage in brittle materials in the elastic-plastic response regime", *Proc. R. Soc. Lond.*, A361 (1978), 343-365.

99. S.M. Wiederhorn, B.R. Lawn, "Strength degradation of glass impacted with sharp particles: I Annealed surfaces", *J. Am. Ceram. Soc.*, 62 (1979), 66-70.

100. S.M. Wiederhorn, B.J. Hockey, "Effect of material parameters on the erosion resistance of brittle materials", *J. Mater. Sci.*, 18 (1983), 766-780.

101.J.L. Routbort, R.O. Scattergood, A.P.L. Turner, "The erosion of reaction-bonded SiC", *Wear*, 59 (1980), 363-375.

102.J.E. Ritter, "Erosion damage in structural ceramics", *Mater. Sci. Eng.*, 71 (1985), 195-201.

103.G.L. Sheldon, I.M. Finnie, "The mechanism of material removal in the erosive cutting of brittle materials", *Trans ASME: J. Eng. Ind.*, 88 (1966), 393-400.

104.G.T. Camacho, M. Ortiz, "Computational modelling of impact damage in brittle materials", *Int. J. Solids Structures*, 33 (1996), 2899-2938.

105.A.C. Fisher-Cripps, B.R. Lawn, A. Pajares, L. Wei, "Stress analysis of elastic-plastic contact damage in ceramic coatings on metal substrates", *J. Am. Ceram. Soc.*, 79 (1996), 2619-2625.

106.M.J. Fagan, S.J. Park, L. Wang, "Finite element analysis of the contact stresses in diamond coatings subjected to a uniform normal load", *Diamond Relat. Mater.*, 9 (2000), 26-36.

107.B.M. Liaw, A.S. Kobayashi, "Computer impact damage model for ceramics and ceramic coatings", *Erosion of Ceramic Materials* (ed. J.E. Ritter), Trans Tech (1992), 121-136.

CHAPTER 3

1. S. Tennant, "On the nature of diamond", *Phil. Trans. R. Soc. Lond.*, 87 (1797), 97-99.
2. J.C. Angus, A. Argoita, R. Gat, Z. Li, M. Sunkara, L. Wang, Y. Wang, "Chemical vapour deposition of diamond", *Phil. Trans. R. Soc. Lond.*, A342 (1993), 195-208.
3. A.Y. Liu, M.L. Cohen, "Prediction of new low compressibility solids", *Science*, 245 (1989), 841-842.
4. H. Pierson, *Handbook of Carbon, Graphite, Diamond and Fullerenes*, Noyes Publishers (1993).
5. J. Chin, P.K. Gantzel, R.G. Hudson, "The structure of chemical vapour deposited silicon carbide", *Thin Solid Films*, 40 (1977), 57-72.
6. J. Schlichting, "Chemical Vapour deposition of silicon carbide", *Powder Metall. Int.*, 12 (1980), 141-147.
7. J. Schlichting, "Chemical Vapour deposition of silicon carbide", *Powder Metall. Int.*, 12 (1980), 196-200.

8. R. Brutsch, "Chemical vapour deposition of silicon carbide and its applications", *Thin Solid Films*, 126 (1985), 313-318.
9. N.J. Archer, "The plasma-assisted chemical vapour deposition of TiC, TiN and TiC_xN_{1-x}", *Thin Solid Films*, 80 (1981), 221-225.
10. H.E. Rebenne, D.G. Bhat, "Review of CVD TiN coatings for wear-resistant applications: deposition processes, properties and performance", *Surf. Coat. Technol.*, 63 (1994), 1-13.
11. J.M. Mackowski, B. Cimma, R. Pignard, P. Colardelle. P. Laprat, "Rain erosion behaviour of germanium carbide films grown on ZnS substrates", *Proc. SPIE*, 1760 (1992), 201-209.
12. U. Jansson, J-O Carlsson, "Chemical vapour deposition of boron carbides in the temperature range 1300-1500 K and at a reduced pressure", *Thin Solid Films*, 125 (1985), 101-107.
13. V. Cholet, R. Herbin, L. Vandenbulcke, "Chemical vapour deposition of boron carbide from BBr_3-CH_4-H_2 mixtures in a microwave plasma", *Thin Solid Films*, 188 (1990), 143-155.
14. D.R. Gibson, E.M. Waddell, K.L. Lewis, "Advances in ultradurable phosphide-based broadband anti-reflection coatings for sand and rain erosion protection of infrared windows and domes", *Proc. SPIE*, 2286 (1994), 335-346.
15. E.M. Waddell, C.C. Clark, "Boron phosphide films on new substrate materials", *Proc. SPIE*, 3705 (1999), 152-162.
16. B. Spitsyn, L.L. Bouilov, B.V. Derjaguin, "Vapour growth of diamond on diamond and other surfaces", *J. Cryst. Growth.*, 52 (1981), 219-226.
17. M. Kamo Y. Sato, S. Matsumoto, N. Setaka, "Diamond synthesis from gas phase in microwave plasma", *J. Cryst. Growth*, 62 (1982), 642-645.
18. S. Matsumoto, Y. Sato, M. Tsutsumi, N. Setaka, "Growth of diamond particles from methane-hydrogen gas", *J. Mater. Sci.*, 17 (1982), 3106-3112.
19. P.W. May, "Diamond thin films: a 21st century material", *Phil. Trans. R. Soc. Lond.*, A358 (2000), 473-495.
20. Y. Saito, S. Matsuda, S. Nogita, "Synthesis of diamond by decomposition of methane in microwave plasma", *J. Mater. Sci. Lett.*, 5 (1986), 565-568.
21. E. Sideras-Haddad, D.B. Rebuli, S.H. Connell, J.P.F. Sellschop, B.P. Doyle, R.D. Maclear, T.E. Derry, "Oxygen on diamond", Diamond Conference, Royal Holloway, London (1998), unpublished.

22. J.C. Angus, F.A. Buck, M. Sunkara, T.F. Groth, C.C. Hayman, R. Gat, "Diamond growth at low pressures", *MRS Bull.*, 14(10) (1988), 38-47.
23. J.E. Butler, "Surface chemical mechanisms of diamond chemical vapour deposition", Diamond Conference, Royal Holloway, London (1998), unpublished.
24. C.C. Chiu, Y. Liou, Y-D Juang, "Elastic modulus of and residual stresses in diamond films", *Thin Solid Films*, 260 (1995), 118-123.
25. D. Rats, L. Bimbault, L. Vandenbulcke, R. Herbin, K.F. Badawi, "Crystalline quality and residual stresses in diamond layers by Raman and x-ray diffraction analyses", *J. Appl. Phys.*, 78(8) (1995), 1-8.
26. D.S. Knight, W.B. White, "Characterisation of diamond films by Raman spectroscopy", *J. Mater. Res.*, 4 (1989), 383-393.
27. S.E. Coe, J.L. Collins, C.S.J. Pickles, R.S. Sussmann, "Mechanical applications of CVD diamond", Presented at 11th European Conf. Diamond, Diamond-like Materials, Carbon Nanotubes, Nitrides and Silicon Carbide, Porto, Portugal, 3-8 Sept. 2000.
28. J.A. Smith, K.N. Rosser, H. Yagi, M.N.R. Ashfold, "Diamond film deposition using a DC plasma jet system", Diamond Conference, Oxford (1999), unpublished.
29. A. Lammer, "Mechanical properties of polycrystalline diamond", *Mater. Sci. Technol.*, 4 (1989) 949-955.
30. A.H. Lettington, "Applications of diamond-like carbon thin films", *Phil. Trans. R. Soc. Lond.*, A342 (1993), 287-296.
31. J.L. Collins, "Diamond-like carbon (DLC) – a review", *Ind. Diamond Rev.*, 58 (1998), 90-92.
32. L. Chandra, M. Allen, R. Butter, N. Rushton, I.M. Hutchings, T.W. Clyne, "The effect of biological fluids on the response of DLC films to a novel erosion durability test", *Diamond Relat. Mater.*, 5 (1996), 410-414.
33. R.H. Telling, G.H. Jilbert, JE. Field, "The erosion of aerospace materials by solid particle impact", *Proc. SPIE*, 3060 (1997), 56-67.
34. R.J.K. Wood, "Erosion resistance of advanced hard facings for production equipment", Unpublished report, October 1992.
35. J.E. Field (ed.), *The Properties of Natural and Synthetic Diamond*, Academic Press (1992).

36. A. Lammer, "Syndite as a wear-resistant material: an assessment" *Diamonds in Industry: Syndite PCD wear-resistant parts*, De Beers Industrial Diamond Division (UK) Ltd., 2-5.
37. Data from Boart Longyear.
38. Data from De Beers Industrial Diamonds (UK) Ltd.
39. X. Jiang, K. Reichelt, B. Stritzker, "Mechanical properties of a-C:H films prepared by plasma decomposition of C_2H_2", *J. Appl. Phys.*, 68 (1990), 1018-1022.
40. H.O. Juchem, "Diamond abrasives in the machining of ceramics", *Ind. Diamond Rev.*, 57 (1997), 114-118.
41. M.W. Cook, "Diamond machining of MMC engineering components", *Ind. Diamond Rev.*, 58 (1998), 15-18.
42. J.L. Collins, "New CVD diamond products", *Ind. Diamond. Rev.*, 59 (1999), 212-213.
43. J.E. Butler, H. Windischmann, "Developments in CVD diamond synthesis during the past decade", article on Norton web-site www.nortondiamondfilm.com (2000).

CHAPTER 4

1. J.E. Field, E. Nicholson, C.R. Seward, Z. Feng, "Strength, fracture and erosion properties of CVD diamond", *Phil. Trans. R. Soc. Lond.*, A342 (1993), 261-275.
2. G.H. Jilbert, C.S.J. Pickles, E.J. Coad, J.E. Field, "Diamond: an erosion resistant aerospace material", *Applications of Diamond Films and Related Materials: 3rd Int. Conf.* (1995), 561-564.
3. I.P. Hayward, J.E. Field, "Solid particle erosion of diamond", *J. Hard Mater.*, 1 (1990), 53-64.
4. Z. Feng, J.E. Field, "Solid particle erosion of diamond, a polycrystalline diamond composite and a polycrystalline boron nitride composite", *J. Hard Mater.*, 1 (1991), 273-287.
5. Z. Feng, Y. Tzeng, J.E. Field, "Solid particle impact on CVD diamond films", *Thin Solid Films*, 212 (1992), 35-42.
6. A.Alahelisten, P. Hollman, S. Hogmark, "Solid particle erosion of hot-flame deposited diamond coatings on cemented carbide", *Wear*, 177 (1994), 159-165.
7. T. Grogler, E. Zeiler, A. Franz, O. Plewa, S.M. Rosiwal, R.F. Singer, "Erosion resistance of CVD diamond coated titanium alloy for aerospace applications", *Surf. Coat. Technol.*, 112 (1999), 129-132.

8. M.V. Kral, J.L. Davidson, J.J. Wert, "Erosion resistance of diamond coatings", *Wear*, 166 (1993), 7-16.
9. R.J.K. Wood, "Erosion resistance of advanced hard facings for production equipment", Unpublished report, October 1992.
10. J.E. Field, Q. Sun, H. Gao, G.H. Jilbert, "Solid particle erosion of IR-transmitting materials and diamond composites", *Wear*, 186-187 (1995), 195-202.
11. R.H. Telling, J.E. Field, "The fracture and erosion of diamond", Diamond Conference, Royal Holloway, London (1998), Unpublished.
12. R.A. Vaughan, A. Ball, "Erosion processes for hard materials subjected to impact impact by different erodents", *J. Hard Mater.*, 2 (1991), 257-269.
13. P.L. Kaye, J.E. Field, "Solid particle erosion of stainless steel, tungsten carbide and a polycrystalline diamond composite", *J. Hard Mater.*, 4 (1993), 167-175.
14. A.G. Evans, T.R. Wilshaw, "Dynamic solid particle damage in brittle materials: an appraisal", *J. Mater. Sci.*,12 (1977), 97-116.
15. C.S.J. Pickles, J.R. Brandon, S.E. Coe, R.S. Sussmann, "Factors influencing the strength of chemical vapour deposited diamond", *Diamond Films* (1999), 435-454.
16. G.Savage, "Ceramic armour", *Met. Mater.*, 6(8) (1990), 487-492.
17. E.J. Coad, C.S.J. Pickles, G.H. Jilbert, J.E. Field, "The erosion resistance of infrared transparent materials", *Proc. R. Soc. Lond.*, A454 (1998), 213-238.
18. C.R. Seward, J.E. Field, E.J. Coad, "Liquid impact erosion of bulk diamond, diamond composites and diamond coatings", *J. Hard Mater.*, 5 (1994), 49-62.
19. C.R. Seward, E.J. Coad, C.S.J. Pickles, J.E. Field, "The rain erosion resistance of diamond and other window materials", *Proc. SPIE*, 2286 (1994), 285-300.
20. C.R. Seward, C.S.J. Pickles, R. Marrah, J.E. Field, "Rain erosion data on window and dome materials", *Proc. SPIE*, 1760 (1992), 280-290.
21. J.E. Field (ed.), *The Properties of Natural and Synthetic Diamond*, Academic Press (1992).
22. C.A. Brookes, "Plastic deformation and anisotropy in the hardness of diamond", *Nature*, 228 (1970), 660-661.
23. C.J. McHargue, "Surface mechanical properties using nanoindentation", *Micro / Nanotribology and its applications*, (ed. B. Bhushan), Kluwer Academic Publishers (1997), 467-492.

24. C.J. McHargue, "Mechanical properties of diamond and diamond-like films", *Proc. Int. Conf. Applications of Diamond Films and Related Materials*, (1991), 113-120.
25. E.D. Nicholson, C.S.J. Pickles, J.E. Field, "The mechanical properties of thin films for aerospace applications", *Proc. SPIE*, 2286 (1994), 275-284.
26. N.M. Everitt, A.M. Cock, P.W. May, K.N. Rosser, M.N.R. Ashfold, "Hardness testing of diamond and diamond-like carbon films", *Proc. 3rd Int. Symp. On Diamond Materials*, Honolulu (1993) (ed. J.P. Dismukes, K.V. Ravi), The Electrochemical Society, 955-959.
27. N. Savvides, T.J. Bell, "Microhardness and Young's modulus, of diamond and diamondlike carbon", *J. Appl. Phys.*, 72 (1992), 2791-2796.
28. E.D. Nicholson, J.E. Field, "The mechanical and thermal properties of thin films", *J. Hard Mater.*, 5 (1994), 89-132.
29. C.B. Ponton, R.D. Rawlings, "Vickers indentation fracture toughness test Part 1: Review of literature and formulation of standardised indentation toughness equations", *Mater. Sci. Technol.*, 5 (1989), 865-872.
30. C.B. Ponton, R.D. Rawlings, "Vickers indentation fracture toughness test Part 2: Applications and critical evaluation of standardised indentation toughness equations", *Mater. Sci. Technol.*, 5 (1989), 961-976.
31. M.D. Drory, C.F. Gardinier, J.S. Speck, "Fracture toughness of chemically vapor-deposited diamond", *J. Am. Ceram. Soc.*, 74(12) (1991), 3148-3150.
32. R.S. Sussman, J.R. Brandon, G.A. Scarsbrook, C.G. Sweeney, T.J. Valentine, A.J. Whitehead, C.J.H. Wort, "Properties of bulk polycrystalline CVD diamond", *Diamond Relat. Mater.*, 3 (1994), 303-312.
33. R.H. Telling, J.E. Field, "Fracture in CVD diamond", *Int. J. Refract. Met. Hard Mater.*, 16 (1998), 269-276.
34. N.V. Novikov, S.N. Dub, "Fracture toughness of diamond single crystals", *J. Hard. Mater.*, 2 (1991), 3-11.
35. N.V. Novikov, S.N. Dub, "Hardness and fracture toughness of CVD diamond films", *Diamond Relat. Mater.*, 5 (1996), 1026-1030.
36. M.D. Drory, R.H. Dauskardt, A. Kant, R.O. Ritchie, "Fracture of synthetic diamond", *J. Appl. Phys.*, 78 (1995), 3083-3088.

37. D.S. Olsen, G.J. Reynolds, G.F. Virship, F.I. Friedlander, B.G. James, L.D. Partain, "Tensile strength of synthetic chemical vapour deposited diamond", *J. Appl. Phys.*, 78 (1995), 5177-5179.
38. J.A. Savage, C.J.H. Wort, C.S.J. Pickles, R.S. Sussmann, C.G. Sweeney, M.R. McClymont, J.R. Brandon, C.N. Dodge, A.C. Beale, "Properties of free-standing CVD diamond optical components", *Proc. SPIE*, 3060 (1997) 144-159.
39. L.P. Hehn, Z. Chen, J.J. Mecholsky, P. Klocek, J.T. Hoggins, J.M. Trombetta, "Fracture surface analysis of free-standing diamond films", *J. Mater. Res.*, 9 (1994), 1540-1545.
40. J.E. Field, C.S.J. Pickles, "Strength, fracture and friction properties of diamond", *Diamond Relat. Mater.*, 5 (1996), 625-634.
41. F.P. Bowden, J.E. Field, "The brittle fracture of solids by liquid impact, by solid impact and by shock", *Proc. R. Soc. Lond.*, A282 (1964), 331-352.
42. R. Ramaseshan, "The cleavage properties of diamond", *Proc. Ind. Acad. Sci.*, A24 (1946), 114-121.
43. R.H. Telling, C.J. Pickard, M.C. Payne, J.E. Field, "Intrinsic strength anisotropy and cleavage in diamond", Diamond Conference, Oxford (1999), unpublished.
44. C.F. Kennedy, R.H. Telling, J.E. Field, "Liquid impact and fracture of free-standing CVD diamond", *Proc. SPIE*, 3705 (1999), 290-296.
45. J.E. Butler, "Surface chemical mechanism of diamond chemical vapour deposition", Diamond Conference, Royal Holloway, London (1998), unpublished.
46. B.E. Williams, H.S. Kong, J.T. Glass, "Electron microscopy of vapor phase deposited diamond", *J. Mater. Res.*, 5 (1990), 801-810.
47. S. Amirhaghi, H.S. Reehal, E. Plappert, Z. Bajic, R.J.K. Wood, D.W. Wheeler, "Growth and erosive wear performance of diamond coatings on WC substrates", *Diamond Relat. Mater.*, 8 (1999), 845-849.
48. C.J.H. Wort, J.R. Brandon, B.S.C. Dorn, J.A. Savage, R.S. Sussmann, A.J. Whitehead, "Properties of CVD diamond domes" *Applications of Diamond Films and Related Materials: 3rd Int. Conf.* (1995), 569-572.
49. J.A. Savage, C.J.H. Wort, C.S.J. Pickles, R.S. Sussmann, C.G. Sweeney, M.R. McClymont, J.R. Brandon, C.N. Dodge, A.C. Beale, "Properties of CVD diamond optical components", *Proc. SPIE*, 3060 (1997), 144-159.
50. *ASM Handbook, Vol 4: Ceramics and glasses*, ASM International (1995).
51. Data from Morton Advanced Materials.

52. R.H. Telling, G.H. Jilbert, J.E. Field, "The erosion of aerospace materials by solid particle impact", *Proc. SPIE*, 3060 (1997), 56-67.

CHAPTER 5

1. R.J.K. Wood, D.W. Wheeler, "Design and performance of a high velocity air-sand jet impingement erosion facility", *Wear*, 220 (1998), 95-112.
2. P.H. Shipway, I.M. Hutchings, "A method for optimising the particle flux in erosion testing with a gas-blast apparatus", *Wear*, 174 (1994), 169-175.

CHAPTER 6

1. R.H. Telling, J.E. Field, "The fracture and erosion of diamond", Diamond Conference, Royal Holloway, London (1998), Unpublished.
2. N. Savvides, T.J. Bell, "Microhardness and Young's modulus of diamond and diamondlike carbon films", *J. Appl. Phys.*, 72 (1992), 2791-2796.
3. C.J. McHargue, "Mechanical properties of diamond and diamond-like films", *Applications of Diamond Films and Related Materials* (ed. Y. Tzeng, M. Yoshikawa, M. Murakawa, A. Feldman), Elsevier Science Publishers (1991), 113-122.
4. M.D. Drory, C.F. Gardinier, J. Speck, "Fracture toughness of chemically vapor-deposited diamond", *J. Am. Ceram. Soc.*, 74(12) (1991), 3148-3150.
5. R.S. Sussman, J.R. Brandon, G.A. Scarsbrook, C.G. Sweeney, T.J. Valentine, A.J. Whitehead, C.J.H. Wort, "Properties of bulk polycrystalline CVD diamond", *Diamond Relat. Mater.*, 3 (1994), 303-312.
6. N.V. Novikov, S.N. Dub, "Fracture toughness of diamond single crystals", *J. Hard. Mater.*, 2 (1991), 3-11.
7. N.V. Novikov, S.N. Dub, "Hardness and fracture toughness of CVD diamond films", *Diamond Relat. Mater.*, 5 (1996), 1026-1030.
8. M.D. Drory, R.H. Dauskardt, A. Kant, R.O. Ritchie, "Fracture of synthetic diamond", *J. Appl. Phys.*, 78 (1995), 3083-3088.

CHAPTER 7

1. Y. Von Kaenel, J. Stiegler, J. Michler, E. Blank, "Stress distribution in heteroepitaxial chemical vapor deposited diamond films", *J. Appl. Phys.*, 81 (1997), 1726-1736.

2. J.A. Savage, C.J.H. Wort, C.S.J. Pickles, R.S. Sussmann, C.G. Sweeney, M.R. McClymont, J.R. Brandon, C.N. Dodge, A.C. Beale, "Properties of free-standing CVD diamond optical components", *Proc. SPIE*, 3060 (1997), 144-159.
3. R.S. Sussmann, J.R. Brandon, S.E. Coe, C.S.J. Pickles, C.G. Sweeney, A. Wasenczuk, C.J.H. Wort, C.N. Dodge, "CVD diamond: a new engineering material for thermal, dielectric and optical applications", *Ind. Diamond Rev.*, 58 (1998), 69-77.
4. C.J.H. Wort, C.G. Sweeney, M.A. Cooper, G.A. Scarsbrook, R.S. Sussmann, "Thermal properties of bulk polycrystalline CVD diamond", *Diamond Relat. Mater.*, 3 (1994), 1158-1167.
5. D. Rats, L. Bimbault, L. Vandenbulcke, R. Herbin, K.F. Badawi, "Residual stresses analysis in diamond layers deposited on various substrates", *Mater. Res. Soc. Symp. Proc.*, 383 (1995), 159-164.
6. H. Boppert, J. Van Straaten, I.F. Silvera, "Raman spectra of diamond at high pressures", *Phys. Rev.*, B32 (1985), 1423-1425.
7. A.B. Harker, D.G. Howitt, S.J. Chen, J.F. Flintoff, M.R. James, "Residual stress measurements on polycrystalline diamond", *Proc. SPIE*, 2286 (1994), 254-261.
8. H. Windischmann, M.A. Simpson, "Free-standing CVD diamond wafers fabricated by DC arc jet", article on the Norton Diamond Film web-site www.nortondiamondfilm.com.
9. P.K. Mehrota, D.T. Quinto, "Techniques for evaluating mechanical properties of hard coatings", *J. Vac. Sci. Technol.*, A3 (1985), 2401-2405.

CHAPTER 8

1. M. Hashish, "An improved model of erosion by solid particle impact" Proc. 7th Int Conf. *Erosion by Liquid and Solid Impact*, Cambridge (1987), Paper 66.
2. Z. Feng, A. Ball, "The erosion of four materials using seven erodents – towards an understanding", *Wear*, 233-235 (1999), 674-684.
3. A.R. Davies, R.H. Telling, J.E. Field, "The erosion performance of CVD diamond and the effect of impact velocity", Diamond Conference, Oxford (1999), Unpublished.
4. D.W. Wheeler, R.J.K. Wood, "Erosion of candidate hard surface coatings for gate valve applications", *Proc. 8th Int. Conf. Energy Week '97*, Houston (1997), 33-40.

5. C.F. Kennedy, M.J. Jackson, J.E. Field, "A response of CVD diamond to liquid impact", Diamond Conference, Royal Holloway, London (1998), Unpublished.
6. D. Schneider, B. Schultrich, P. Burck, H-J Scheibe, G. Jorgensen, M. Lahres, J. Karner, *Diamond Relat. Mater.*, 7 (1998), 589-596.
7. C.A. Brookes, L.Y. Zhang, P.W. May, "On the mechanical integrity ratio of diamond coatings", *Diamond Relat. Mater.*, 6 (1997), 348-352.
8. D.W. Wheeler, R.J.K. Wood, S. Atwell, D. Harrison, "Application of diamond to enhance choke valve life in erosive duties", to be submitted to *Wear.*
9. J.A. Savage, C.J.H. Wort, C.S.J. Pickles, R.S. Sussmann, C.G. Sweeney, M.R. McClymont, J.R. Brandon, C.N. Dodge, A.C. Beale, "Properties of CVD diamond optical components", *Proc. SPIE*, 3060 (1997), 144-159.

CHAPTER 9

1. R.S. Sussman, J.R. Brandon, G.A. Scarsbrook, C.G. Sweeney, T.J. Valentine, A.J. Whitehead, C.J.H. Wort, "Properties of bulk polycrystalline CVD diamond", *Diamond Relat. Mater.*, 3 (1994), 303-312.
2. P.H. Shipway, I.M. Hutchings, "The role of particle properties in the erosion of brittle materials", *Wear*, 193 (1996), 105-113.
3. R.H. Telling, J.E. Field, "The erosion of diamond, sapphire and zinc sulphide by quartz particles", *Wear*, 233-235 (1999), 666-673.
4. M.E. Gulden, "Correlation of experimental erosion data with elastic-plastic impact models", *J. Am. Ceram. Soc.*, 64 (1981), C59-C60.
5. A.W. Ruff, S.M. Wiederhorn, "Erosion by solid particle impact", *Treatise on Materials Science,* 16 (1979) (ed. C.M. Preece), 69-126.
6. S. Srinivasan, R.O. Scattergood, "Effect of erodent hardness on erosion of brittle materials", *Wear*, 128 (1988), 139-152.
7. S.C. Hunter, "Energy absorbed by elastic waves during impact", *J. Mech. Phys. Solids*, 5 (1957), 162-171.
8. Y.M. Tsai, H. Kolsky, "A study of the fractures produced in glass blocks by impact", *J. Mech. Phys. Solids*, 15 (1967), 263-278.
9. C.G. Knight, M.V. Swain, M.M. Chaudhri, "Impact of small steel spheres on glass surfaces", *J. Mater. Sci.*, 12 (1977), 1573-1586.
10. G.L. Sheldon, J. Maji, C.T. Crowe, "Erosion of a tube by gas-particle flow", *ASME J. Eng. Mater. Technol.*, 99 (1977), 138-142.

11. A.D. Salman, A. Verba, Z. Lukenics, M. Szabo, "Particle velocity after collision", *Periodica Polytechnica*, 35 (1991), 31-41.
12. D. Tabor, "A simple theory of static and dynamic hardness", *Proc. R. Soc. Lond.*, A192 (1948), 247-274.
13. D. Tabor, *The Hardness of Metals*, Clarendon Press (1951).
14. A.H. Kharaz, D.A. Gorham, "A study of the restitution coefficient in elastic-plastic impact", *Phil. Mag. Lett.*, 80 (2000), 549-559.
15. C.R. Seward, E.J. Coad, C.S.J. Pickles, J.E. Field, "The rain erosion resistance of diamond and other window materials", *Proc. SPIE*, 2286 (1994), 285-300.
16. Z. Feng, Y. Tzeng, J.E. Field, "Solid particle impact on CVD diamond films", *Thin Solid Films*, 212 (1992), 35-42.
17. S.P. Timoshenko, J.N. Goodier, *Theory of Elasticity*, McGraw-Hill, New York, 3rd ed. (1970).
18. K.L. Johnson, J.J. O'Connor, A.C. Woodward, "The effect of indenter elasticity on the Hertzian fracture of brittle materials", *Proc. R. Soc. Lond.*, A334 (1973), 95-117.
19. J.E. Field, Q. Sun, H. Gao, "Solid particle erosion of infrared transmitting materials", *Proc. SPIE*, 2286 (1994), 301-306.
20. E.H. Yoffe, "Modified Hertz theory for spherical indentation", *Phil. Mag.*, A50 (1984), 813-828.
21. J.E. Field, E. Nicholson, C.R. Seward, Z. Feng, "Strength, fracture and erosion properties of CVD diamond", *Phil. Trans. R. Soc. Lond.*, A342 (1993), 261-275.
22. C.S.J. Pickles, J.R. Brandon, S.E. Coe, R.S. Sussmann, "Factors influencing the strength of chemical vapour deposited diamond", *Diamond Films* (1999), 435-454.
23. S.G. Roberts, "Hertzian testing of ceramics", *Brit. Ceram. Trans.*, 99 (2000), 31-38.
24. S.G. Roberts, C.W. Lawrence, Y. Bisrat, P.D. Warren, D.A. Hills, "Determination of surface residual stresses in brittle materials by Hertzian indentation: theory and experiment", *J. Am. Ceram. Soc.*, 82 (1999), 1809-1816.
25. F.P. Bowden, J.E. Field, "The brittle fracture of solids by liquid impact, by solid impact, and by shock", *Proc. R. Soc. Lond.*, A282 (1964), 331-352.
26. E.J. Coad, J.E. Field, "The liquid impact resistance of CVD diamond and other infrared materials", *Proc. SPIE*, 3060 (1997), 169-180.
27. C.R. Seward, J.E. Field, E.J. Coad, "Liquid impact erosion of bulk diamond, diamond composites and diamond coatings", *J. Hard Mater.*, 5 (1994), 49-62.

28. J.E. Field (ed.), *The Properties of Natural and Synthetic Diamond*, Academic Press (1992).
29. J.E. Field, D.A. Gorham, D.G. Rickerby, "High-speed liquid jet and drop impact on brittle targets", *Erosion: Prevention and Useful Applications, ASTM STP664*, (1979), 298-319.
30. S. van der Zwaag, J.E. Field, "Liquid jet impact damage on zinc sulphide", *J. Mater. Sci.* (1982), 2625-2636.
31. D.A. Gorham, J.E. Field, "Anomalous behaviour of high velocity oblique liquid impact", *Wear*, 41 (1977), 213-222.
32. G.H. Kinner, "Some remarks on single impact studies at the Royal Aircraft Establishment", *Proc. 2nd Int. Conf. On Rain Erosion and Allied Phenomena*, ed. A.A. Fyall, R.B. King (1967), 517-533.
33. R.J. Hand, J.E. Field, D. Townsend, "The use of liquid jets to simulate angled drop impact", *J. Appl. Phys.*, 70 (1991), 7111-7118.
34. J.E. Field, "Stress waves, deformation and fracture caused by liquid impact", *Phil. Trans. R. Soc. Lond.*, A260 (1966), 86-93.
35. B.R. Lawn, "Hertzian fracture in single crystals with the diamond structure", *J. Appl. Phys.*, 39 (1968), 4828-4836.
36. L-L Wang, J.E. Field, Q. Sun, J. Liu, "Surface damage of polymethylmethacrylate plates by ice and nylon ball impacts" *J. Appl. Phys.*, 78 (1995), 1643-1649.
37. G.F. Miller, H. Pursey, "On the partition of energy between elastic waves in a semi-infinite solid", *Proc. R. Soc. Lond.*, A233 (1955), 55-69.
38. M.V. Swain, J.T. Hagan, "Rayleigh wave interaction with, and the extension of, microcracks", *J. Mater. Sci.*, 15 (1980), 387-404.
39. F.P. Bowden, J.H. Brunton, "Damage to solids by liquid at supersonic speeds", *Nature*, 181 (1958), 873-875.
40. S. van der Zwaag, J.E. Field, "Rain erosion damage in brittle materials", *Eng. Fract. Mech.*, 17 (1983), 367-379.
41. F.P. Bowden, J.H. Brunton, "The deformation of solids by liquid impact at supersonic speeds", *Proc. R. Soc. Lond.*, A263 (1961), 433-450.
42. F. Guiberteau, N.P. Padture, H Cai, B.R. Lawn, "Indentation fatigue: a simple cyclic Hertzian test for measuring damage accumulation in polycrystalline ceramics", *Phil. Mag.*, A68 (1993), 1003-1016.
43. K.L. Johnson, *Contact Mechanics*, Cambridge University Press (1985).

44. S.M. Wiederhorn, B.J. Hockey, "Effect of material parameters on the erosion resistance of brittle materials", *J. Mater. Sci.*, 18 (1983), 766-780.
45. C.A. Brookes, "Plastic deformation and anisotropy in the hardness of diamond", *Nature*, 228 (1970), 660-661.
46. H.O. Juchem, "Diamond abrasives in the machining of ceramics", *Ind. Diamond. Rev.*, 57 (1997), 114-118.
47. F.P. Bowden, D. Tabor, "Deformation, friction and wear of diamond", *Physical Properties of Diamond* (ed. R. Berman), Clarendon Press (1965), 184-220.
48. I.P. Hayward, J.E. Field, "The solid particle erosion of diamond", *J. Hard Mater.*, 1 (1990), 53-64.

CHAPTER 10

1. J.E. Field, Q. Sun, H. Gao, G.H. Jilbert, "Solid particle erosion of IR-transmitting materials and diamond composites", *Wear*, 186-187 (1995), 195-202.
2. F.P. Bowden, J.E. Field, "The brittle fracture of solids by liquid impact, by solid impact, and by shock", *Proc. R. Soc. Lond.*, A282 (1964), 331-352.
3. J.E. Field, "Stress waves, deformation and fracture caused by liquid impact", *Phil. Trans. R. Soc. Lond.*, A260 (1966), 86-93.
4. N.K. Bourne, T. Obara, J.E. Field, "High-speed photography and stress gauge studies of jet impact upon surfaces", *Phil. Trans. R. Soc. Lond.*, A355 (1997), 607-623.
5. L-L Wang, J.E. Field, Q. Sun, J. Liu, "Surface damage of polymethylmethacrylate plates by ice and nylon ball impacts" *J. Appl. Phys.*, 78 (1995), 1643-1649.
6. C.S.J. Pickles, E.J. Coad, G.H. Jilbert, J.E. Field, "The erosive behaviour of diamond" *Mater. Res. Soc. Symp. Proc.*, 383 (1995), 327-338.
7. R.H. Telling, G.H. Jilbert, J.E. Field, "The erosion of aerospace materials by solid particle impact", *Proc. SPIE*, 3060 (1997), 56-67.
8. R.H. Telling, J.E. Field, "Fracture in CVD diamond", *Int. J. Refract. Metal Hard Mater.*, 19 (1998), 269-276.
9. S. Wuttiphan, A. Pajares, B.R. Lawn, C.C. Berndt, "Effect of substrate and bond coat on contact damage in zirconia-based plasma-sprayed coatings", *Thin Solid Films*, 293 (1997), 251-260.

10. J.C. Yang, "Non-destructive identification of defects in integrated circuit packages by scanning acoustic microscopy", *Microelectronics and Reliability*, 36 (1996), 1291-1295.
11. Y.Y. Yang, Y.S. Jin, S.Y. Luo, "SAM study on plasma sprayed ceramic coatings", *Surf. Coat. Technol.*, 91 (1997), 95-100.
12. C.W. Lawrence, G.A.D. Briggs, C.B. Scruby, J.R.R. Davies, "Acoustic microscopy of ceramic-fibre composites I: Glass-matrix composites", *J. Mater. Sci.*, 28 (1993), 3635-3644.
13. C.W. Lawrence, G.A.D. Briggs, C.B. Scruby, "Acoustic microscopy of ceramic-fibre composites II: Glass-ceramic-matrix composites", *J. Mater. Sci.*, 28 (1993), 3645-3652.
14. C.W. Lawrence, G.A.D. Briggs, C.B. Scruby, "Acoustic microscopy of ceramic-fibre composites III: Metal-matrix composites", *J. Mater. Sci.*, 28 (1993), 3653-3660.
15. C. Delebarre, C. Bruneel, R. Delwiche, I de Vos, "Polycrystalline diamond cutting element control using high frequency C-scan image processing", *NDT & E Int.*, 26 (1993), 303-308.
16. A.G. Evans, J.W. Hutchinson, "On the mechanics of delamination and spalling in compressed films", *Int. J. Solids Structures*, 20 (1984), 455-466.
17. A.G. Evans, M.D. Drory, M.S. Hu, "The cracking and decohesion of thin films", *J. Mater. Res.*, 3 (1988), 1043-1049.
18. T. Adams, "Surface imaging gets cracking", *Mater. World*, 5 (1997), 199-200.
19. M.J. Jackson, J.E. Field, "Liquid impact erosion of single-crystal magnesium oxide", *Wear*, 233-235 (1999), 39-50.
20. P.D. Warren, O.V. Kolosov, S.G. Roberts, G.A.D. Briggs, "Characterization of surface damage via contact probes", *Nanotechnology*, 7 (1996), 288-294.
21. O.V. Kolosov, "UFM shakes out the details at the nanoscopic scale", *Mater. World*, 6 (1998), 753-754.
22. M.J. Jackson, J.E. Field, "Modelling liquid impact fracture thresholds in brittle materials", *Brit. Ceram. Trans.*, 99 (2000), 1-13.
23. C. Pecorari, "Attenuation and dispersion of Rayleigh waves propagating on a cracked surface: an effective field approach", *Ultrasonics*, 38 (2000), 754-760.
24. C. Pecorari, "Rayleigh wave dispersion due to a distribution of semi-elliptical surface-breaking cracks", *J. Acoust. Soc. Am.*, 103 (1998), 1383-1387.

25. P.D. Warren, C. Pecorari, O.V. Kolosov, S.G. Roberts, G.A.D. Briggs, "Characterization of surface damage via surface acoustic waves", *Nanotechnology*, 7 (1996), 295-301.
26. C. Pecorari, "On the effect of a residual stress field on the dispersion of a Rayleigh wave propagating on a cracked surface", *J. Acoust. Soc. Am.*, 103 (1998), 616-617.
27. C. Pecorari, C.W. Lawrence, S.G. Roberts, G.A.D. Briggs, "Quantitative evaluation of surface damage in brittle materials by acoustic microscopy", *Phil. Mag.*, A80 (2000), 2695-2708.

CHAPTER 11

1. S. Van der Zwaag, J.E. Field, "The effect of thin hard coatings on the Hertzian stress field", *Phil. Mag.*, A46 (1982), 133-150.
2. A.G. Evans, M.D. Drory, M.S. Hu, "The cracking and decohesion of thin films", *J. Mater. Res.*, 3 (1988), 1043-1049.
3. M. Comninou, "The interface crack", *J. Appl. Mech.*, 44 (1977), 631-636.
4. J.E. Field (ed.), *The Properties of Natural and Synthetic Diamond*, Academic Press (1992).
5. R.S. Sussmann, J.R. Brandon, G.A. Scarsbrook, C.G. Sweeney, T.J. Valentine, A.J. Whitehead, C.J.H. Wort, "Properties of bulk polycrystalline CVD diamond", *Diamond Relat. Mater.*, 3 (1994), 303-312.
6. P.H. Shipway, I.M. Hutchings, "The role of particle properties in the erosion of brittle materials", *Wear*, 193 (1996), 105-113.
7. E.H. Yoffe, "Modified Hertz theory for spherical indentation", *Phil. Mag.*, A50 (1984), 813-828.
8. B.R. Lawn, *Fracture of Brittle Solids* (2nd ed.), Cambridge University Press (1993).
9. K.L. Johnson, *Contact Mechanics*, Cambridge University Press (1985).
10. M.G.D. El-Sherbiney, J. Halling, "The Hertzian contact of surfaces covered with metallic films", *Wear*, 40 (1976), 325-337.
11. A.G. Evans, J.W. Hutchinson, "On the mechanisms of delamination and spalling in compressed films", *Int. J. Solids Structures*, 20 (1984), 455-466.
12. F.P. Bowden, J.E. Field, "The brittle fracture of solids by liquid impact, by solid impact and by shock", *Proc. R. Soc. Lond.*, A282 (1964), 331-352.
13. C.R. Seward, J.E. Field, E.J. Coad, "Liquid impact erosion of bulk diamond, diamond composites and diamond coatings", *J. Hard Mater.*, 5 (1994), 49-62.

14. F.P. Bowden, J.H. Brunton, "The deformation of solids by liquid impact at supersonic speeds", *Proc. R. Soc. Lond.*, A263 (1961), 433-450.
15. T. Obara, N.K. Bourne, J.E. Field, "Liquid jet impact on liquid and solid surfaces", *Wear*, 186-187 (1995), 388-394.
16. N.K. Bourne, T. Obara, J.E. Field, "High speed photography and stress gauge studies of jet impact upon surfaces", *Phil. Trans. R. Soc. Lond.*, A355 (1997), 607-623.
17. G. DeBotton, "The interaction of a coated target and an impinging water drop", *Wear*, 219 (1998), 60-72.
18. K. Komvopoulos, "Finite element analysis of a layered elastic solid in normal contact with a rigid surface", *J. Tribol.*, 110 (1988), 477-485.
19. S. Raadnui, B.J. Roylance, "The classification of wear particle shape", *Lubr. Eng.*, 51 (1995), 432-437.
20. B.R. Lawn, R. Wilshaw, "Review: indentation fracture: principle and applications", *J. Mater. Sci.*, 10 (1975), 1049-1081.
21. Z. Feng, Y. Tzeng, J.E. Field, "Solid particle impact of CVD diamond films", *Thin Solid Films*, 212 (1992), 35-42.
22. R.H. Telling, G.H. Jilbert, J.E. Field, "The erosion of aerospace materials by solid particle impact", *Proc. SPIE*, 3060 (1997), 56-67.
23. R.H. Telling, J.E. Field, "The fracture and erosion of diamond", Diamond Conference, Royal Holloway (1998), Unpublished.
24. S. Wuttiphan, A. Pajares, B.R. Lawn, C.C. Berndt, "Effect of substrate and bond coat on contact damage in zirconia-based plasma-sprayed coatings", *Thin Solid Films*, 293 (1997), 251-260.
25. D. Rats, L. Bimbault, L. Vandenbulcke, R. Herbin, K.F. Badawi, "Residual stresses analysis in diamond layers deposited on various substrates", *Mater. Res. Soc. Symp. Proc.*, 383 (1995), 159-164.
26. J.A. Savage, C.J.H. Wort, C.S.J. Pickles, R.S. Sussmann, C.G. Sweeney, M.R. McClymont, J.R. Brandon, C.N. Dodge, A.C. Beale, "Properties of free-standing CVD diamond optical components", *Proc. SPIE*, 3060 (1997), 144-159.
27. M.S. Hu, M.D. Thouless, A.G. Evans, "The decohesion of thin films from brittle substrates", *Acta Metall.*, 36 (1988), 1301-1307.
28. A.B. Harker, D.G. Howitt, S.J. Chen, J.F. Flintoff, M.R. James, "Residual stress measurements on polycrystalline diamond", *Proc. SPIE*, 2286 (1994), 254-261.

29. C.F. Kennedy, J.E. Field, "Damage threshold velocities for liquid impact", *J. Mater. Sci.*, 35 (2000), 5331-5339.

APPENDIX 1: LIST OF PUBLICATIONS

Publications and presentations made during the period covered by this thesis:

1. R.J.K. Wood, D.W. Wheeler, "Design and performance of a high velocity air-sand jet impingement erosion facility", *Wear*, 220 (1998), 95-112.
2. D.W. Wheeler, R.J.K. Wood, "Erosive wear behaviour of thick chemically vapour deposited diamond coatings", Presented at the 12th International Conference *Wear of Materials*, Atlanta, 25 –29 Apr. 1999; published in *Wear*, 225-229 (1999), 523-536.
3. D.W. Wheeler, R.J.K. Wood, "Solid particle erosion of CVD diamond coatings", Presented at the *International Conference on Erosive and Abrasive Wear*, Cambridge, 13-17 Sept. 1998; published in *Wear*, 233-235 (1999), 306-318.
4. R.J.K. Wood, D.W. Wheeler, D.C. Lejeau, B.G. Mellor, "Sand erosion performance of CVD boron carbide coated tungsten carbide", Presented at the *International Conference on Erosive and Abrasive Wear*, Cambridge, 13-17 Sept. 1998; published in *Wear*, 233-235 (1999), 134-150.
5. D.W. Wheeler, R.J.K. Wood, "High velocity sand impact damage on CVD diamond", *Diamond and Related Materials.*, 10 (2001), 459-462.
6. D.W. Wheeler, R.J.K. Wood, "Circumferential crack and pin-hole formation in CVD diamond coatings under multiple solid particle impacts", Presented at the *International Tribology Conference*, Nagasaki, Japan, 29 Oct. – 2 Nov. 2000. To be published in the conference proceedings, August 2001.
7. D.W. Wheeler, R.J.K. Wood, "Solid particle erosion of CVD diamond coatings at non-normal impact angles", Presented at the 13th International Conference *Wear of Materials*, Vancouver, 22-26 Apr. 2001. Accepted for publication in *Wear* (2001).
8. D.W. Wheeler, R.J.K. Wood, "Erosion of CVD diamond coatings on tungsten", Diamond Conference, Oxford (1999), unpublished.
9. D.W. Wheeler, R.J.K. Wood, "A scanning acoustic microscopy study of erosion damage features in CVD diamond coatings", Diamond Conference, Cambridge (2000), unpublished.

10. S. Amirhaghi, H.S. Reehal, Z. Bajic, E. Plappert, R.J.K. Wood, D.W. Wheeler, "Growth and erosive wear performance of diamond coatings on WC substrates", *Diamond and Related Materials*, 8 (1999), 845-849.
11. S. Amirhaghi, H.S. Reehal, R.J.K. Wood, D.W. Wheeler, "Growth and erosive wear properties of MPCVD diamond coatings on sintered tungsten carbide substrates", *Properties and Processing of Vapor Deposited Coatings, MRS Symposium Proceedings*, 555 (1999), 395-400.
12. S. Amirhaghi, H.S. Reehal, R.J.K. Wood, D.W. Wheeler, "Diamond coatings on tungsten carbide substrates and their erosive wear properties", *Surface and Coatings Technology*, 135 (2001), 126-138.

APPENDIX 2: NOMENCLATURE

A	Hertzian zone area = πd_m^2 (m^2)
a	Distance in the radial direction (m)
a_c	Critical radius for coating spallation (m)
a_m	Mean Hertzian contact radius (m)
a_f	Flaw size (m)
b	Modifying factor
C_v	Volume fraction of solid in slurry
C_T	Coating thickness (m)
c	Measure of perfection of a crystal
c_e	Compression (longitudinal) wave velocity in erodent ($m\ s^{-1}$)
c_{cr}	Crack length (m)
c_1	Compression (longitudinal) wave velocity ($m\ s^{-1}$)
c_2	Transverse (shear) wave velocity ($m\ s^{-1}$)
c_R	Rayleigh (surface) wave velocity ($m\ s^{-1}$)
d_1	Circumferential diameter (m)
d'	Circumferential diameter (m)
d_g	Grain size (m)
d_{ind}	Diameter of indentation (m)
d_p	Sand particle diameter (μm)
d_m	Mean Hertzian contact diameter (m)
d_s	Standard indentation diameter (m)
E_{er}	Erosion rate ($mm^3\ g^{-1}$)
E_f	Elastic modulus of film (Pa)
E_k	Mean kinetic energy of sand particle (J)
E_{kt}	Total energy per Hertzian zone area (J)
E_s	Elastic modulus of substrate (Pa)
E_t	Elastic modulus of target (Pa)
E_v	Erodent volume (m^3)
E_1	Young's modulus for half space or target (Pa)
E_2	Elastic modulus of indenter or erodent particle (Pa)

e	Coefficient of restitution
F	Flux rate at normal impact angle (kg m^{-2} s^{-1})
F_θ	Flux rate at impact angle θ (kg m^{-2} s^{-1})
F_m	Maximum load (N)
G_1	Shear modulus of half space or target (Pa)
G_2	Shear modulus of indenter or erodent particle (Pa)
H_m	Measured hardness (kg mm^{-2})
H_t	Hardness of target material (kg mm^{-2})
H_v	Vickers hardness (kg mm^{-2})
h_c	Indentation contact depth (m)
h_t	Indentation depth at maximum load (m)
I	Incident wave energy
IR	Integrity ratio
k	Constant
k_y	Yield stress in pure shear (Pa)
K_I	Stress intensity factor in mode I loading (tension) (MPa$\sqrt{m}$)
K_{II}	Stress intensity factor in mode II loading (shear) (MPa$\sqrt{m}$)
K_{Ic}	Critical stress intensity (fracture toughness) (MPa$\sqrt{m}$)
L_c	Critical load for coating removal in scratch test (N)
M	Ballistic figure of merit
m	Energy exponent
m_s	Sand particle mass (kg)
NV'	Normal component of rebound velocity (m s^{-1})
NV_o	Normal component of incoming velocity (m s^{-1})
$N(Hertz)$	Number of impacts per Hertzian zone
$N(SW)$	Number of impacts per stress wave reinforcement zone
n	Velocity exponent
P_{ind}	Indentation load (Pa)
P_i	Water hammer pressure (Pa)
P_s	Probability of survival
P_m	Mean contact pressure (Pa)
P'_m	Threshold pressure to initiate failure in uncoated substrate
P''_m	Threshold pressure to initiate failure in coating.

P_o	Maximum contact pressure (Pa)
$P_o(y)$	Peak contact pressure at first yield (Pa)
P_1	Upstream pressure in air-sand rig (bar)
P_2	Downstream pressure in air-sand rig (bar)
Q	Volumetric flow rate ($m^3\ s^{-1}$)
R	Sand particle radius (m)
R_a	Surface roughness (μm)
R_c	Reflection coefficient
R_g	Gas constant ($J\ K^{-1}\ mol^{-1}$)
R_p	Radius of curvature of the displaced surface (m)
r_c	Separation of impact centres (m)
r_e	Edge Radius (m)
S_T	Substrate thickness (m)
T	Temperature (K)
t	Test duration (s)
t_e	Elastic impact time (s)
t_f	Time to failure of coating (s)
t_{PH}	Time for pin-holes to form in the coating
u	Weibull exponent
u_1	Velocity of body 1 prior to collision ($m\ s^{-1}$)
u_2	Velocity of body 2 prior to collision ($m\ s^{-1}$)
V	Velocity of particle or liquid ($m\ s^{-1}$)
V_c	Critical velocity for ring crack formation ($m\ s^{-1}$)
V_e	Total erodent volume loss (m^3)
V	Impact velocity ($m\ s^{-1}$)
V_l	Volume loss (m^3)
V_o	Volume (m^3)
V_s	Specific volume loss = V_l/V_e
V_u	Volume loss per impact ($\mu m^3\ impact^{-1}$)
v_1	Volume of body 1 (Weibull analysis) (m^3)
v_2	Volume of body 2 (Weibull analysis) (m^3)
V_1	Velocity of body 1 after collision ($m\ s^{-1}$)
V_2	Velocity of body 2 after collision ($m\ s^{-1}$)

V'	Rebound velocity (m s^{-1})
V_o	Incoming velocity (m s^{-1})
W	Velocity of material removed by a given number of particles (m^3)
W_{er}	Erosion rate (mm^3 g^{-1})
w	Vertical indentation displacement (m)
x	Fraction of erodent (% wt)
x_{th}	Material thickness (m)
y_1	Stress wave reinforcement radius (m)
y'	Stress wave reinforcement radius (m)
z_τ	Depth of maximum shear (m)
Z	Acoustic impedance (kg m^{-2} s^{-1})
z	Distance in the axial direction (m)

α	Dundurs' independent variable (dimensionless)
α_f	Thermal expansion coefficient of film (K^{-1})
α_s	Thermal expansion coefficient of substrate (K^{-1})
β	Dundurs' independent variable (dimensionless)
β^*	An impact function dependent on Poisson's ratio (dimensionless)
Γ_c	Interfacial toughness
γ	Fracture surface energy (J m^{-2})
Δ	Nozzle diameter (m)
ΔT	Difference between deposition temperature and room temperature (K)
Δy	Diameter over which the high pressure phase exists (m)
ε	Indentation geometrical constant
ξ	Calibration constant
ν_1	Poisson's ratio for half space or target
ν_2	Poisson's ratio for indenter or erodent particle
θ	Particle impact angle (°)
θ_A	Semi-apex angle of cone crack (°)
ρ_l	Density of liquid (kg m^{-3})
ρ_e	Density of erodent (kg m^{-3})

ρ_t	Density of target (kg m^{-3})
ρ_2	Sand particle density (kg m^{-3})
σ	Applied stress (Pa)
σ_o	Characteristic strength (Pa)
σ_{in}	Intrinsic stress component to residual stress in coating (Pa)
σ_r	Principal stress in the radial direction (Pa)
σ_m	Maximum tensile stress at contact circle (Pa)
σ_{rs}	Total residual stress in coating (Pa)
σ_{th}	Total thermal residual stress taking into account C_T and S_T (Pa)
σ'_{th}	Thermal component of residual stress in coating (Pa)
σ_{ts}	Tensile strength (Pa)
σ_y	Yield stress in tension (Pa)
σ_z	Principal stress in the axial direction (Pa)
σ_θ	Principal stress in the circumferential direction (Pa)
σ_1	Critical stress to activate a flaw in a sample of volume v_1 (Pa)
σ_2	Critical stress to activate a flaw in a sample of volume v_2 (Pa)
τ_m	Maximum shear stress (Pa)
$\psi_{(inter)}$	Defect density at the coating-substrate interface
ψ_c	Defect density in the coating
χ	Area of delamination (m^2)